SCUOLA DI DOTTORATO

UNIVERSITÀ DEGLI STUDI DI MILANO-BICOCCA

Department of

Biotecnology and biosciences

PhD program in Life Sciences
Cycle XXIX

Use of a technological platform to screening *in vitro* and *in vivo* anti-amyloidogenic drugs able to prevent early neurodegenerative process

PhD Student: Visentin Cristina

744768

Tutor: Dott.ssa Maria Elena Regonesi

Coordinator: Marco Vanoni

ACADEMIC YEAR 2015/2016

Amyloidoses are protein misfolding diseases caused by deposition of fibrillar proteins in target organs. Nowadays, most of them are still incurable and their relevance to public health system is growing, especially as a consequence of population aging. Spinocerebellar ataxia type 3 is a member of this group of pathologies and its causative agent is ataxin-3 (ATX3). This is consists of a globular N-terminal (JD), followed by a flexible tail carrying a poly-glutamine (polyQ) tract. An expanded polyQ tract triggers the aggregation. In this work, I have investigated the capability of tetracycline (Tetra), epigallocatechin-gallate (EGCG), epigallocatechin (EGC), gallic acid (GA) and trifluoroethanol (TFE) to interfere with ATX3 amyloid deposition. Tetra is an antibiotic recently re-evaluated as anti-amyloidogenic compound. EGCG, EGC and GA, which are natural polyphenols, are already known in literature for their anti-amyloidogenic effect; finally, TFE is an osmolyte that stabilizes secondary structure, preferentially α-helix. Data obtained by aggregation assay, spectroscopic analyses (NMR, FTIR) and morphologic characterisation clearly demonstrated Tetra capability of increasing ATX3 aggregates solubility, without a substantial remodelling of the internal structure. Nevertheless, this antibiotic reduced the toxicity of the oligomeric species and ameliorated ataxic *C. elegans* phenotype. On the contrary, the analysed polyphenols were capable to interfere with ATX3 aggregation but, instead of preventing, they accelerated the aggregation rate redirecting the process towards the formation of soluble, not toxic, off-pathway aggregates. All compounds were also active against the JD in isolation, but only the polyphenols were capable to bind the monomeric form. In particular, they overlapped specific aggregation-prone regions directly involved in the fibrillation. This could explain their capability of redirecting the aggregation pathway and the different mode of action with respect to Tetra. These polyphenols showed a remarkable reduction of ATX3-mediated cytotoxicity and mitigation of ataxic phenotype in *C. elegans* and *E. coli* models. However, the compounds displayed a different efficacy, whereby EGCG was the most and GA the least effective. All data strongly support the idea that GA is the minimal functional unit of EGCG. TFE did not show the capability of preventing aggregation; in fact, even at very low concentration it promotes a faster amyloid-like aggregation. Biophysical characterization of its effect on JD aggregation, instead, provided evidence that ATX3 aggregation proceeds along a new identified pathway by which protein misfolding follows protein aggregation. In fact, TFE induces the formation of a native-like state almost indistinguishable from fully native protein, but more aggregation prone.

CHAPTER 1

Introduction

1.1 SPINOCEREBELLAR ATAXIA TYPE 3 AND ATAXIN-3

Spinocerebellar ataxia type 3 (SCA3), also known as Machado-Joseph disease (MJD), is the most common form of autosomal dominantly-inherited ataxia in the world, representing almost 45% of all SCAs (1,2). It is a neurodegenerative disorder originally described in people of Portuguese Azorean descent, but it has been reported also in Spain, Italy, Germany, China, Taiwan, Japan, Australia, Brazil, United States and Canada. SCA3/MJD is caused by an abnormal repetition of the CAG triplet in the translated region of *ATXN3* gene and for this reason it is classified as trinucleotide repeat expansion disease of class II. Neurodegeneration affects very specific neuronal populations leading to the characteristic clinical symptoms and phenotype of SCA3/MJD patients, *e.g.,* progressive ataxia and many neuromuscular complication affecting posture, breath, view and speech capability (3,4). Death usually occurs for pulmonary complications and cachexia, from 6 to 29 years after the disease onset, with an average survival of 21 years (5–7).

ATXN3 gene is located in the long arm of chromosome 14 (14q32.1) and encodes for ataxin 3 (ATX3), a polyglutammine (polyQ) containing protein (8,9). The length of polyQ tract is crucial for disease onset: between 50 and 87 repetitions are associated with disease onset, healthy population can carry from 12 to 44 repetition and between 45 and 51 repetitions both phenotypes are possible (10,11).

ATX3 is wide distributed in the eukaryotic kingdom. In humans it is expressed in almost all body tissues and cell types, despite in the pathology the neurodegeneration is highly localized and cell-specific (12–14). Even inside the cells it has a wide and heterogeneous expression, with cytoplasmic and nuclear localization, with different predominance depending on cell type. In the neurons, the cell population impaired in SCA3/MJD patients, it is mainly localized in the perikarya, but it can also be detected on proximal process, axons and nuclei. ATX3 is actively transported across the nuclear envelope, shuttling from cytoplasm to the nucleus and *vice versa* (13,15–21).

ATX3 is composed by N-terminal globular domain (Josephine domain, JD) followed by a flexible tail in the C-terminous (22). JD is highly conserved among evolution: it belongs to papain-like cysteine protease family and the catalytic triad has strong homology with ubiquitin (Ub) C-terminal hydrolases and Ub-specific processing proteases (23–26). It consists of the residue 1 to 182 and has Ub protease activity. It is composed of two subdomains: a globular subdomain and a helical hairpin (23,26). The catalytic site (C14, H119 and N134) and two Ub-binding sites, together with two nuclear export signal, are located in this domain. Two Ub-interacting domains (UIM), a nuclear

localization signal and the polyQ tract are located in the flexible tail. Downstream of polyQ tract, according to the isoform present, is possible to identify an additional third UIM. ATX3 can be phosphorylated at UIMs level and can be ubiquitinated in the lysine 117 of the JD.

This protein is involved in many cellular pathways, and in particular in the ubiquitin-proteasome pathway (UPP), one of the mechanism that regulate protein turnover (27,28). ATX3 preferentially interacts with chains of no less than four K48-linked Ub monomers; polyUb chains of four or more monomers are the ones involved in the targeting of proteins for proteasomal degradation (26,29–31), in fact, trimming or editing of K48-linked polyUb chains, *in vitro*, leads to decrease of proteasome-dependent degradation of a polyubiquitinated protein model (32). However ATX3 is able to interact with both K48- and K63-linked chains in a UIM-dependent manner and promotes the shortening of polyUb chains rather than their complete disassembly (29,30,32–35). Winborn and coauthors suggested for ATX3 a role as regulator of topologically complex polyUb chains, in fact it preferentially cleaves K63-linked chains and chains of mixed K48 and K63 linkage (30). The two UIMs have a major role in recruiting target ubiquitinated proteins and in their presentation to the catalytic site located in the JD; the role of the additional third UIM present in one ATX3 isoform for the overall ubiquitin protease activity is still not clear (26,28,36). The proteolytic activity *in vitro* is actually very slow, suggesting that external factor(s) may be required for optimal proteolysis and it lacks and that probably it requires its endogenous substrate(s) (30,37,38).

ATX3 capability to interact with p97/valosin-containing protein (VCP), HHR23A and HHR23B, the human homologs of the yeast DNA repair protein Rad23, provides another evidence of its involvement in UPP. Those ATX3-interactors are involved in many cellular process, but they have an key role in the UPP as promoter of the shuttling of polyubiquitinated substrates to the proteasome for degradation, particularly in endoplasmic reticulum-associated degradation (ERAD) (23,26,39–44). ATX3 role in ERAD is still debate: in particular it is not clear if it is associated with an increase or decrease of the degradation ERAD-mediated (42,45). There are evidence of a direct association of ATX3 with the proteasome, but the nature and the strength of this interaction is not known (27,46). However the interaction with VCP, HHR23A and HHR23B support the hypothesis as ATX3 acts shortening polyUb chains of a substrate facilitating the action of proteasome-associated DUBs, targeting the substrate for degradation editing its polyUb

chain or mediating the recognition of substrates when associated to the proteasome (39,47).

ATX3 is also associated with aggresome-autophagy pathway, in particular with aggresome formation. This structure is formed when chaperone and ubiquitin proteasome systems are overwhelmed; misfolded and aggregated proteins accumulated in aggresomes are then degraded by lysosomes (48). ATX3 co-localize with aggresome and preaggresome particles and associates with dynein, histone deacetylase 6 (HDAC6) and tubulin, constituents of the complex responsible for the transport of misfolded proteins to the MTOC. Its role could be the protection of misfolded proteins before they reach the microtubule-organizing center or the stabilization of the proteins involved in the transport. Recently it was also demonstrated that ATX3 is required for HDAC6 recruitment of protein aggregates to aggresome (32,49–51).

The involvement in aggresome formation highlights the capability of this protein to interact with cytoskeleton components, *e. g.* microtubule-associated protein 2 (MAP2) and dynein (32). Those interactions are important for cytoskeleton organization, in fact ATX3 absence leads the disorganization of the several cytoskeleton constituents (microtubules, microfilaments and intermediate filaments) and a loss of cell adhesions (52).

ATX3 action as DUBs may influence not only protein, but also transcription regulators turnover, and specifically can interfere with repressor complex formation and activity (52,53). The active role in transcription regulation is moreover exerted by inhibiting transcription activators; by decreasing histone acetylation through interaction with histone deacetylase 3 (HDAC3), nuclear receptor co-repressor (NCor) and histones (53,54).

Expanded ATX3 forms nuclear and axonal polyubiquitinated inclusion in brain, even if this protein has an ubiquitous expression in the body (55,56). The presence of this amyloid aggregates is usually associated with the pathology but it is now well demonstrated that this final aggregates are the mechanism that cells adopt as defence against cytotoxicity exerted by oligomers and early and small aggregates (57). ATX3 aggregation mechanism is still not completely clear. It has been shown that aggregation pathway consists of two steps; in fact the isolated JD has itself an intrinsic amyloidogenic potential. The first step occurs in all ATX3 variant as a consequence of aberrant interactions between monomers at JD level and gives rise to SDS-soluble oligomers and protofibrils; the second step is accessible just to variants carrying expanded polyQ and results in the formation of mature, SDS-insoluble fibrils. The latter ones are characterized

by the formation of hydrogen bonds among polyQ side-chains giving them their characteristic stability (58–61). Expanded variants display the fastest aggregation kinetics, suggesting that the polyQ tract also affects the mode of JD aggregation (60). It has recently demonstrated that this is due to the enhanced mobility of one critical α-helics in the JD if the polyQ tract is expanded; in this *scenario* the aggregation prone regions (APRs) of JD are exposed for a longer time compared to a wild type variant, increasing the probability of aberrant interaction between monomers. This evidence highlights that polyQ expansion does not impair protein stability, but its pathological role is due to the increase protein fluctuation (62,63). The APRs overlap with the ubiquitin binding sites 1 and 2 suggesting a direct link between protein function and aggregation. Intracellular interactors could therefore protect against AT3 self-assembly, in keeping with the fact that Ub reduces *in vitro* aggregation of the JD (64,65).

1.2 AIM OF THE WORK

Spinocerebellar ataxia type 3 (SCA3) is a severe neurodegenerative disease and its invariably fatal outcome, like in the case of other amyloidoses, represents a challenge for researchers. It is well reported SCA3 causative agent is ataxin-3 (ATX3) aggregation when it carries an expanded poly-glutamine tract. In spite of this, the aggregation starts from the folded domain, referred as Josephin domain. Even though several molecules have been tested as ATX3 aggregation inhibitors, only few of them are effective. Our group previously demonstrated that (-)-epigallocatechin-3-gallate (EGGC) and tetracycline hydrochloride were capable to interfere with ATX3 aggregation.

This work aims to find and characterize new molecules capable to interfere with ATX3 aggregation and to provide a deeper understanding of the mechanism of action of these two previously identified compounds. We also investigated the effect of epigallocatechin and of gallic acid, two molecules structurally related to EGCG using a multi-disciplinary approach. We performed *in vitro*, *in vivo*, and *in silico* analyses, thus identifying further compounds active against ATX3 aggregation and the minimal functional unit of EGCG responsible for its anti-amyloid action.

In parallel, we also studied the effects of very low TFE concentrations on JD aggregation, as this compound is a well-known secondary structure stabilizer. Instead, we observed an accelerated amyloid-like aggregation provide a better insight into the mechanism of amyloid aggregation of ATX3.

In conclusion, the main achievements of this thesis are a deeper insight into the

mechanism of action of tetracycline and EGCG, the identification of two new drug candidates (EGC and GA) for SCA3 treatment. Moreover, a new evidence that aggregation precedes misfolding in the ATX3 deposition is reported.

1.3 CANDIDATE'S CONTRIBUTION

The candidate wrote the introduction autonomously.

1.4 REFERENCES

1. Paulson HL. Dominantly inherited ataxias: lessons learned from Machado-Joseph disease/spinocerebellar ataxia type 3. Semin Neurol. 2007 Apr;27(2):133–42.

2. Silveira I, Lopes-Cendes I, Kish S, Maciel P, Gaspar C, Coutinho P, et al. Frequency of spinocerebellar ataxia type 1, dentatorubropallidoluysian atrophy, and Machado-Joseph disease mutations in a large group of spinocerebellar ataxia patients. Neurology. 1996 Jan;46(1):214–8.

3. Dürr A, Stevanin G, Cancel G, Duyckaerts C, Abbas N, Didierjean O, et al. Spinocerebellar ataxia 3 and Machado-Joseph disease: clinical, molecular, and neuropathological features. Ann Neurol. 1996 Apr;39(4):490–9.

4. Matos CA, de Macedo-Ribeiro S, Carvalho AL. Polyglutamine diseases: the special case of ataxin-3 and Machado-Joseph disease. Prog Neurobiol. 2011 Sep 15;95(1):26–48.

5. Sequeiros J, Coutinho P. Epidemiology and clinical aspects of Machado-Joseph disease. Adv Neurol. 1993;61:139–53.

6. Sudarsky L, Coutinho P. Machado-Joseph disease. Clin Neurosci N Y N. 1995;3(1):17–22.

7. Kieling C, Prestes PR, Saraiva-Pereira ML, Jardim LB. Survival estimates for patients with Machado-Joseph disease (SCA3). Clin Genet. 2007 Dec;72(6):543–5.

8. Takiyama Y, Nishizawa M, Tanaka H, Kawashima S, Sakamoto H, Karube Y, et al. The gene for Machado-Joseph disease maps to human chromosome 14q. Nat Genet. 1993 Jul;4(3):300–4.

9. Kawaguchi Y, Okamoto T, Taniwaki M, Aizawa M, Inoue M, Katayama S, et al. CAG expansions in a novel gene for Machado-Joseph disease at chromosome 14q32.1. Nat Genet. 1994 Nov;8(3):221–8.

10. Maciel P, Costa MC, Ferro A, Rousseau M, Santos CS, Gaspar C, et al. Improvement in the molecular diagnosis of Machado-Joseph disease. Arch Neurol. 2001 Nov;58(11):1821–7.

11. Riess O, Rüb U, Pastore A, Bauer P, Schöls L. SCA3: neurological features,

pathogenesis and animal models. Cerebellum Lond Engl. 2008;7(2):125–37.

12. Paulson HL, Das SS, Crino PB, Perez MK, Patel SC, Gotsdiner D, et al. Machado-Joseph disease gene product is a cytoplasmic protein widely expressed in brain. Ann Neurol. 1997 Apr;41(4):453–62.

13. Trottier Y, Cancel G, An-Gourfinkel I, Lutz Y, Weber C, Brice A, et al. Heterogeneous intracellular localization and expression of ataxin-3. Neurobiol Dis. 1998 Nov;5(5):335–47.

14. Ichikawa Y, Goto J, Hattori M, Toyoda A, Ishii K, Jeong SY, et al. The genomic structure and expression of MJD, the Machado-Joseph disease gene. J Hum Genet. 2001;46(7):413–22.

15. Macedo-Ribeiro S, Cortes L, Maciel P, Carvalho AL. Nucleocytoplasmic shuttling activity of ataxin-3. PloS One. 2009 Jun 8;4(6):e5834.

16. Pozzi C, Valtorta M, Tedeschi G, Galbusera E, Pastori V, Bigi A, et al. Study of subcellular localization and proteolysis of ataxin-3. Neurobiol Dis. 2008 May;30(2):190–200.

17. Reina CP, Zhong X, Pittman RN. Proteotoxic stress increases nuclear localization of ataxin-3. Hum Mol Genet. 2010 Jan 15;19(2):235–49.

18. Tait D, Riccio M, Sittler A, Scherzinger E, Santi S, Ognibene A, et al. Ataxin-3 is transported into the nucleus and associates with the nuclear matrix. Hum Mol Genet. 1998 Jun;7(6):991–7.

19. Wang G, Ide K, Nukina N, Goto J, Ichikawa Y, Uchida K, et al. Machado-Joseph disease gene product identified in lymphocytes and brain. Biochem Biophys Res Commun. 1997 Apr 17;233(2):476–9.

20. Antony PMA, Mäntele S, Mollenkopf P, Boy J, Kehlenbach RH, Riess O, et al. Identification and functional dissection of localization signals within ataxin-3. Neurobiol Dis. 2009 Nov;36(2):280–92.

21. Chai Y, Shao J, Miller VM, Williams A, Paulson HL. Live-cell imaging reveals divergent intracellular dynamics of polyglutamine disease proteins and supports a sequestration model of pathogenesis. Proc Natl Acad Sci U S A. 2002 Jul 9;99(14):9310–5.

22. Masino L, Musi V, Menon RP, Fusi P, Kelly G, Frenkiel TA, et al. Domain architecture of the polyglutamine protein ataxin-3: a globular domain followed by a flexible tail. FEBS Lett. 2003 Aug 14;549(1-3):21–5.

23. Nicastro G, Menon RP, Masino L, Knowles PP, McDonald NQ, Pastore A. The solution structure of the Josephin domain of ataxin-3: structural determinants for molecular recognition. Proc Natl Acad Sci U S A. 2005 Jul 26;102(30):10493–8.

24. Albrecht M, Hoffmann D, Evert BO, Schmitt I, Wüllner U, Lengauer T. Structural modeling of ataxin-3 reveals distant homology to adaptins. Proteins. 2003 Feb 1;50(2):355–70.

25. Scheel H, Tomiuk S, Hofmann K. Elucidation of ataxin-3 and ataxin-7 function by integrative bioinformatics. Hum Mol Genet. 2003 Nov 1;12(21):2845–52.

26. Mao Y, Senic-Matuglia F, Di Fiore PP, Polo S, Hodsdon ME, De Camilli P. Deubiquitinating function of ataxin-3: insights from the solution structure of the Josephin domain. Proc Natl Acad Sci U S A. 2005 Sep 6;102(36):12700–5.

27. Doss-Pepe EW, Stenroos ES, Johnson WG, Madura K. Ataxin-3 interactions with rad23 and valosin-containing protein and its associations with ubiquitin chains and the proteasome are consistent with a role in ubiquitin-mediated proteolysis. Mol Cell Biol. 2003 Sep;23(18):6469–83.

28. Berke SJS, Chai Y, Marrs GL, Wen H, Paulson HL. Defining the role of ubiquitin-interacting motifs in the polyglutamine disease protein, ataxin-3. J Biol Chem. 2005 Sep 9;280(36):32026–34.

29. Burnett B, Li F, Pittman RN. The polyglutamine neurodegenerative protein ataxin-3 binds polyubiquitylated proteins and has ubiquitin protease activity. Hum Mol Genet. 2003 Dec 1;12(23):3195–205.

30. Winborn BJ, Travis SM, Todi SV, Scaglione KM, Xu P, Williams AJ, et al. The deubiquitinating enzyme ataxin-3, a polyglutamine disease protein, edits Lys63 linkages in mixed linkage ubiquitin chains. J Biol Chem. 2008 Sep 26;283(39):26436–43.

31. Schmitt I, Linden M, Khazneh H, Evert BO, Breuer P, Klockgether T, et al. Inactivation of the mouse Atxn3 (ataxin-3) gene increases protein ubiquitination. Biochem Biophys Res Commun. 2007 Oct 26;362(3):734–9.

32. Burnett BG, Pittman RN. The polyglutamine neurodegenerative protein ataxin 3 regulates aggresome formation. Proc Natl Acad Sci U S A. 2005 Mar 22;102(12):4330–5.

33. Chai Y, Berke SS, Cohen RE, Paulson HL. Poly-ubiquitin binding by the polyglutamine disease protein ataxin-3 links its normal function to protein surveillance pathways. J Biol Chem. 2004 Jan 30;279(5):3605–11.

34. Donaldson KM, Li W, Ching KA, Batalov S, Tsai C-C, Joazeiro CAP. Ubiquitin-mediated sequestration of normal cellular proteins into polyglutamine aggregates. Proc Natl Acad Sci U S A. 2003 Jul 22;100(15):8892–7.

35. Nicastro G, Todi SV, Karaca E, Bonvin AMJJ, Paulson HL, Pastore A. Understanding the role of the Josephin domain in the PolyUb binding and cleavage properties of ataxin-3. PloS One. 2010 Aug 26;5(8):e12430.

36. Harris GM, Dodelzon K, Gong L, Gonzalez-Alegre P, Paulson HL. Splice isoforms of the polyglutamine disease protein ataxin-3 exhibit similar enzymatic yet different aggregation properties. PloS One. 2010 Oct 27;5(10):e13695.

37. Chow MKM, Mackay JP, Whisstock JC, Scanlon MJ, Bottomley SP. Structural and functional analysis of the Josephin domain of the polyglutamine protein ataxin-3. Biochem Biophys Res Commun. 2004 Sep 17;322(2):387–94.

38. Reyes-Turcu FE, Wilkinson KD. Polyubiquitin binding and disassembly by deubiquitinating enzymes. Chem Rev. 2009 Apr;109(4):1495–508.

39. Boeddrich A, Gaumer S, Haacke A, Tzvetkov N, Albrecht M, Evert BO, et al. An arginine/lysine-rich motif is crucial for VCP/p97-mediated modulation of ataxin-3 fibrillogenesis. EMBO J. 2006 Apr 5;25(7):1547–58.

40. Hirabayashi M, Inoue K, Tanaka K, Nakadate K, Ohsawa Y, Kamei Y, et al. VCP/p97 in abnormal protein aggregates, cytoplasmic vacuoles, and cell death, phenotypes relevant to neurodegeneration. Cell Death Differ. 2001 Oct;8(10):977–84.

41. Matsumoto M, Yada M, Hatakeyama S, Ishimoto H, Tanimura T, Tsuji S, et al. Molecular clearance of ataxin-3 is regulated by a mammalian E4. EMBO J. 2004 Feb 11;23(3):659–69.

42. Zhong X, Pittman RN. Ataxin-3 binds VCP/p97 and regulates retrotranslocation of ERAD substrates. Hum Mol Genet. 2006 Aug 15;15(16):2409–20.

43. Wang G, Sawai N, Kotliarova S, Kanazawa I, Nukina N. Ataxin-3, the MJD1 gene product, interacts with the two human homologs of yeast DNA repair protein RAD23, HHR23A and HHR23B. Hum Mol Genet. 2000 Jul 22;9(12):1795–803.

44. Wang Q, Song C, Li C-CH. Molecular perspectives on p97-VCP: progress in understanding its structure and diverse biological functions. J Struct Biol. 2004 May;146(1-2):44–57.

45. Wang Q, Li L, Ye Y. Regulation of retrotranslocation by p97-associated deubiquitinating enzyme ataxin-3. J Cell Biol. 2006 Sep 25;174(7):963–71.

46. Todi SV, Laco MN, Winborn BJ, Travis SM, Wen HM, Paulson HL. Cellular turnover of the polyglutamine disease protein ataxin-3 is regulated by its catalytic activity. J Biol Chem. 2007 Oct 5;282(40):29348–58.

47. Wang Q, Li L, Ye Y. Inhibition of p97-dependent protein degradation by Eeyarestatin I. J Biol Chem. 2008 Mar 21;283(12):7445–54.

48. Markossian KA, Kurganov BI. Protein folding, misfolding, and aggregation. Formation of inclusion bodies and aggresomes. Biochem Biokhimiia. 2004 Sep;69(9):971–84.

49. Mazzucchelli S, De Palma A, Riva M, D'Urzo A, Pozzi C, Pastori V, et al. Proteomic and biochemical analyses unveil tight interaction of ataxin-3 with tubulin. Int J Biochem Cell Biol. 2009 Dec;41(12):2485–92.

50. Bonanomi M, Mazzucchelli S, D'Urzo A, Nardini M, Konarev PV, Invernizzi G, et al. Interactions of ataxin-3 with its molecular partners in the protein machinery that sorts protein aggregates to the aggresome. Int J Biochem Cell Biol. 2014 Jun;51:58–64.

51. Ouyang H, Ali YO, Ravichandran M, Dong A, Qiu W, MacKenzie F, et al. Protein aggregates are recruited to aggresome by histone deacetylase 6 via unanchored ubiquitin C termini. J Biol Chem. 2012 Jan 20;287(4):2317–27.

52. Rodrigues A-J, Coppola G, Santos C, Costa M do C, Ailion M, Sequeiros J, et al. Functional genomics and biochemical characterization of the C. elegans orthologue of the Machado-Joseph disease protein ataxin-3. FASEB J Off Publ Fed Am Soc Exp Biol. 2007 Apr;21(4):1126–36.

53. Evert BO, Araujo J, Vieira-Saecker AM, de Vos RAI, Harendza S, Klockgether T, et al. Ataxin-3 represses transcription via chromatin binding, interaction with histone deacetylase 3, and histone deacetylation. J Neurosci Off J Soc Neurosci. 2006 Nov 1;26(44):11474–86.

54. Li F, Macfarlan T, Pittman RN, Chakravarti D. Ataxin-3 is a histone-binding protein with two independent transcriptional corepressor activities. J Biol Chem. 2002 Nov 22;277(47):45004–12.

55. Paulson HL, Perez MK, Trottier Y, Trojanowski JQ, Subramony SH, Das SS, et al. Intranuclear inclusions of expanded polyglutamine protein in spinocerebellar ataxia type 3. Neuron. 1997 Aug;19(2):333–44.

56. Seidel K, den Dunnen WFA, Schultz C, Paulson H, Frank S, de Vos RA, et al. Axonal inclusions in spinocerebellar ataxia type 3. Acta Neuropathol (Berl). 2010 Oct;120(4):449–60.

57. Uversky VN. Mysterious oligomerization of the amyloidogenic proteins. FEBS J. 2010 Jul;277(14):2940–53.

58. Gales L, Cortes L, Almeida C, Melo CV, Costa M do C, Maciel P, et al. Towards a structural understanding of the fibrillization pathway in Machado-Joseph's disease: trapping early oligomers of non-expanded ataxin-3. J Mol Biol. 2005 Oct 28;353(3):642–54.

59. Ellisdon AM, Thomas B, Bottomley SP. The two-stage pathway of ataxin-3 fibrillogenesis involves a polyglutamine-independent step. J Biol Chem. 2006 Jun 23;281(25):16888–96.

60. Ellisdon AM, Pearce MC, Bottomley SP. Mechanisms of ataxin-3 misfolding and fibril formation: kinetic analysis of a disease-associated polyglutamine protein. J Mol Biol. 2007 Apr 27;368(2):595–605.

61. Natalello A, Frana AM, Relini A, Apicella A, Invernizzi G, Casari C, et al. A major role for side-chain polyglutamine hydrogen bonding in irreversible ataxin-3 aggregation. PloS One. 2011;6(4):e18789.

62. Lupton CJ, Steer DL, Wintrode PL, Bottomley SP, Hughes VA, Ellisdon AM. Enhanced Molecular Mobility of Ordinarily Structured Regions Drives Polyglutamine Disease. J Biol Chem. 2015 Oct 2;290(40):24190–200.

63. Scarff CA, Almeida B, Fraga J, Macedo-Ribeiro S, Radford SE, Ashcroft AE. Examination of Ataxin-3 (atx-3) Aggregation by Structural Mass Spectrometry Techniques: A Rationale for Expedited Aggregation upon Polyglutamine (polyQ) Expansion. Mol Cell Proteomics MCP. 2015 May;14(5):1241–53.

64. Nicastro G, Masino L, Esposito V, Menon RP, De Simone A, Fraternali F, et al. Josephin domain of ataxin-3 contains two distinct ubiquitin-binding sites.

Biopolymers. 2009 Dec;91(12):1203–14.

65. Masino L, Nicastro G, Calder L, Vendruscolo M, Pastore A. Functional interactions as a survival strategy against abnormal aggregation. FASEB J Off Publ Fed Am Soc Exp Biol. 2011 Jan;25(1):45–54.

CHAPTER 2

How epigallocatechin-3-gallate and tetracycline interact with the Josephin domain of ataxin-3 and alter its aggregation mode

2.1 INTRODUCTION

At present Spinocerebellar ataxia type 3 (SCA3/MJD), like others amyloidoses, is incurable and invariably fatal even though several effective compounds have been tested (1,2). The common feature of these pathologies is the conversion of soluble peptides and proteins into amyloid aggregates, through the formation of soluble oligomers that are responsible for cytotoxicity. Many therapeutic strategies developed are aim at reducing amyloid production, inhibit amyloid aggregation, destabilize the aggregated species and enhance their clearance (3). Numerous compounds have been found to inhibit specific amyloid fibril formation *in vitro* (4–6), particularly Aβ, PrP, and huntingtin (5,7,8). The interest in SCA3/MJD therapeutic treatments is relatively recent. Several approaches have been tested but only few compounds have been reported to be effective and even fewer obtained the approval for clinical trials. At the moment (January 2017) only three clinical trials regarding SCA3/MJD are ongoing and none of them have a therapeutic approach (9). Damfalpridine, varenicline, cabaletta, sodium phenylbutyrate and lithium carbonate have been already tested on patients, but the results are not available and/or they are not active anymore (9). Riluzole, an antiglutaminergic drug, promotes a decrease in soluble ATX3 levels paralleled by the increase of aggregates, but when tested in a mouse model it was not able to ameliorate the SCA3/MJD phenotype and also it displayed Purkinje cells toxicity (10).

Alternative approaches might be targeted to internal cell machinery to decrease the levels of pathological ATX3 by RNA interference. Many studies reported this approach as effective, but the main problem is to reach the brain and, possibly, the neuronal population affected in SCA3/MJD without altering the general levels of ATX3. The most promising delivery might be the use of stable nucleic acid lipid particles (11), but this kind of therapy needs an accurate safety study before being available for patients treatment.

Nevertheless, some promising approaches have been identified. Neuropeptide Y overexpression ameliorates the pathological phenotype of two different murine models improving motor coordination and other neuropathological parameters and decreasing inflammation levels through up-regulation of some neurotrophic factors (12). Aripiprazole, an atypical antypsichotic, modulates the general levels of ATX3 of two disease models (murine and *Drosophila melanogaster*) through the activation of a general cellular response instead of acting directly on ATX3 (13).

Our group has previously demonstrated that tetracyclines and (−)-epigallocatechin-3-gallate (EGCG) are able to interfere with ATX3 fibrillation (14). Tetracyclines are a group of structurally related antibiotics discovered in the late 1940s (15) and, like aripiprazole, they are already being used in clinical and their pharmacological properties and toxicological profile are well characterized (16–18). They are pluripotent drugs that affect many mammalian cell functions including proliferation, migration, apoptosis and matrix remodeling. In the recent years there was a growing interest in reassessing these molecules as antiamyloidogenic compounds (19). The use of tetracyclines in treating amyloidoses could affect the main pathological target, but they may also contribute to improve other pathological events concurrent with amyloid deposit formation, *e.g.*, inflammation, ROS generation with resulting oxidative stress, apoptosis and uncoupling of metal homeostasis (20). It has been reported that tetracyclines are able to inhibit the aggregation of prion protein fragments and amyloid β (Aß), destabilizing their aggregates and promoting their degradation by proteases (21,22). In particular, tetracyclines are able to sequester Aβ oligomers and prevent further progression of the amyloid fibril growth, resulting in significant reduction of peptide toxicity (21). They bind to amyloid fibrils of PrP, hinder their assembly, and revert the protease resistance of PrP aggregates extracted from brain tissue of patients with Creutzfeldt- Jacob disease (17,22). In addition, these drugs have been described to behave as fibril disrupters (23). There are few works regarding the effect of these drugs on HD as a polyQ model and the results are conflicting. Recently, we have demonstrated that they are able to interfere with ATX3 aggregation *in vitro* and ameliorating the SCA3/MJD phenotype of a *Caenorhabditis elegans* model (14,24,25). In particular, we tested the effect of tetracycline hydrochloride (structure reported in Fig. 1) and observed that it is able to increase the solubility of an expanded variant of ATX3 carrying 55 glutamine repeats. The aggregates formed in the presence of this drug are structurally very similar to the untreated ones, but morphological analyses revealed some differences. Furthermore, these aggregates are less toxic to mammalian cells.

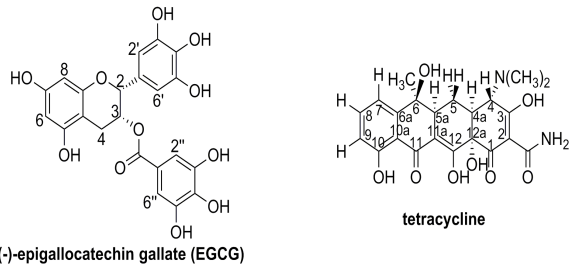

Fig. 1. Structure and numbering of EGCG and tetracycline.

In parallel, we have demonstrated that EGCG (structure reported in Fig. 1) is able to interfere with ATX3 deposition too, albeit in a completely different manner (14). The

advantage of using this molecule is that it is a natural compound, being the most abundant green tea catechin (50 to 80% of total catechins) (26–28). This family of molecules has been used since hundreds of years for their potent antioxidant action: they act via direct scavenging of reactive oxygen and nitrogen species, induction of defense enzymes and binding and chelation of divalent metals, such as copper and iron (29). In particular, EGCG is a potent inhibitor of Fe^{2+} and iron ascorbate toxicity and *in vivo* it increases expression and activity of antioxidant enzymes (30). Furthermore, EGCG crosses the blood–brain barrier in mammals and is reported to be safe for humans when tested in clinical studies (30,31). Recently it has been demonstrated to be able to modulate the early steps in the aggregation process of huntingtin *in vitro* and to prevent α-synuclein amyloid deposition (32,33). Thus, EGCG interferes with a very early step of amyloid formation pathway and suppresses the assembly of on-pathway amyloidogenic oligomers and protofibrils (34). EGCG seems to inhibit amyloid fibrillogenesis by stabilizing the unstructured state of the natively unfolded α-synuclein protein and reinforces the inhibitory intramolecular interactions in the protein (35). Instead of amyloid fibrils, highly stable spherical oligomers are formed in EGCG-treated aggregation reactions, indicating that the compound redirects aggregation-prone molecules into an assembly pathway distinct from the amyloid formation cascade (33). Likewise, EGCG also redirects $Aß_{42}$ aggregation and thus prevents the formation of toxic, β-sheet–rich aggregation products such as amyloid oligomers or protofibrils (33). Moreover, EGCG is capable of converting large, mature α-synuclein and amyloid-β fibrils into smaller, amorphous protein aggregates that are non-toxic to mammalian cells through direct binding to β-sheet aggregates. It mediates this conformational change without their disassembly into monomers or small diffusible oligomers (36). We confirmed a similar effect on an expanded ATX3 aggregation, albeit we did not observe a disaggregating ability of preformed ATX3 fibers. The *in vitro* treatment with EGCG leads to a rapid decrease in monomer content in favor of large and soluble off-pathway SDS-resistant aggregates. As observed with other amyloid proteins, these aggregates do not have a defined structure and are safe for the cells. We also observed an improvement in the pathologic phenotype of a SCA3 *C. elegans* model (14).

Both tetracycline and EGCG are capable to interfere with amyloid deposition of many proteins, suggesting a non-specific interaction. Probably they recognize a structural pattern common to all this amyloid oligomers/protein instead of a specific domain in the target protein.

This work is amied at improving our understanding of the mechanism of interaction of tetracycline and EGCG with the JD. We performed spectroscopic analyses, *i.e.*, NMR, FT-IR, as well as protein solubility assays, thus showing that both compounds are able to interfere with JD aggregation in a way similar to that observed in the case of expanded ATX3.

2.2 RESULTS AND DISCUSSION

EGCG and tetracycline differently affect JD aggregation

In a previous work, we demonstrated that EGCG and tetracycline differently modulate the aggregation pathway of an expanded AT3 variant (14), the former generating SDS-resistant, ß-sheet-poor, soluble aggregates, the latter giving rise to aggregated species resembling those arising in the absence of any compound, but substantially more soluble. To further elucidate the mechanism of action of the two compounds, we have examined whether they exert the same effect on JD aggregation, that is, aggregation of the structured N-terminal protein domain. The rationale of our approach relies upon the well-established notion that the aggregation process of full-length AT3, irrespective of the polyQ size, starts with JD misfolding and aggregation, which triggers the earliest steps of expanded AT3 fibrillation (41,42). Thus, quite plausibly, any treatment affecting or preventing JD aggregation would also affect or prevent the process at the level of full-length AT3.

A His-tagged JD was purified by affinity chromatography and the monomeric form was isolated by size-exclusion chromatography (Fig. S1 in the Supporting Information). The protein was then incubated at 37 °C in the presence or the absence of either compound at molar ratios of protein/drug of 1:5. Aliquots were taken at different incubation times and the soluble fraction was isolated as the supernatant from a centrifugation at 14000 *g*. The SDS-soluble protein fraction was quantified by sodium dodecyl sulfate polyacrylamide gel electrophoresis (SDS-PAGE) of the supernatants and subsequent densitometric analyses.

Starting from the earliest incubation time (i.e., 1 h), EGCG treatment resulted in a significant reduction in the SDS-soluble amount of the protein (Fig 2 A, C and D). Based on previous work, EGCG may undergo structural changes such as epimerization and dimerization (44). This prompted us to check its stability. Under our working conditions, the molecule proved to be completely stable, as assessed by ^{1}H NMR spectroscopy, over a time span of 72 h (Fig. S2 in the Supporting Information).

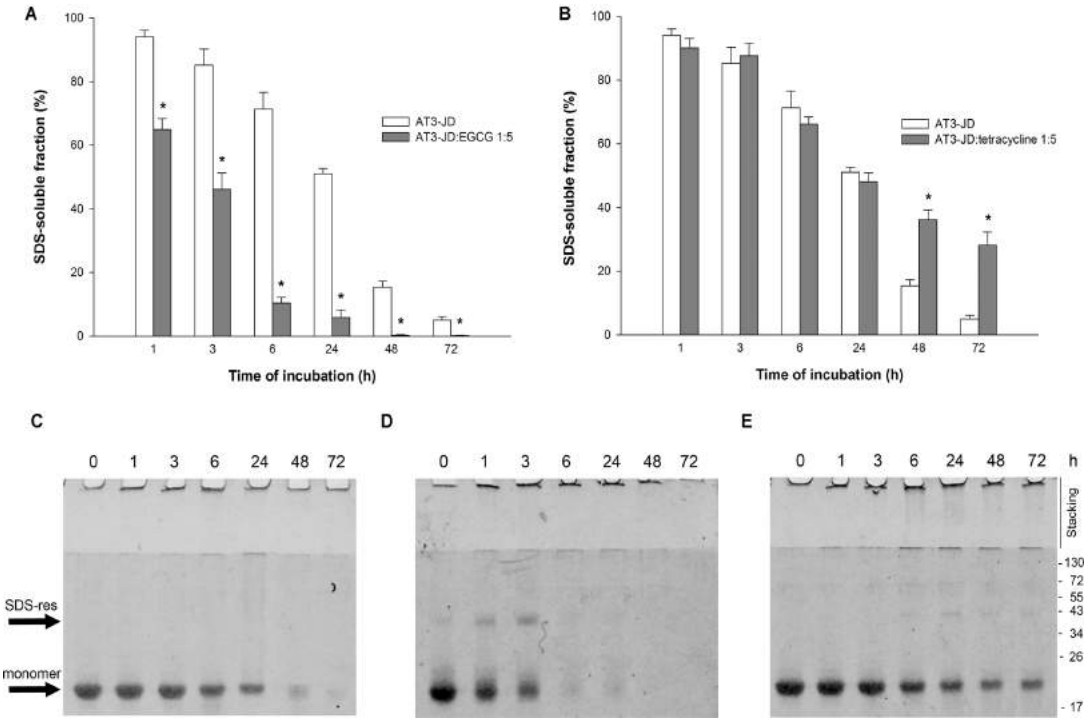

Fig. 2. SDS-soluble protein fraction analysis of the JD incubated with EGCG or tetracycline. A 150 μM solution of JD was incubated at 37 °C in the presence or absence of: A) EGCG, or B) tetracycline. The amount of SDS-soluble protein was quantified by centrifuging the incubation mixtures, subjecting the supernatants to SDS-PAGE, and to subsequent densitometric analysis. Signals were normalized at zero-time protein content. Error bars represent standard errors and are derived from at least three independent experiments. * = $P < 0.01$. SDS-PAGE (16 %) of the soluble protein fraction of: C) JD, D) JD/EGCG 1:5, and E) JD/tetracycline 1:5. The gels were stained with IRDye blue protein stain (LiCor). The monomeric and the soluble, aggregated, SDS-resistant species are indicated by arrows.

In contrast, tetracycline significantly retarded SDS-soluble species disappearance, in particular at the longest incubation times (Fig.s 2B, C, and E). Size exclusion chromatography (SEC) analyses of the incubation mixtures showed that in the control sample (i.e., JD alone, Fig.3A), higher molecular weight species appeared in the void volume starting from 6 h of incubation. Their estimated molecular mass is 300 kDa or higher. Scanty, if any, accumulation of intermediate forms between the void volume and the monomeric protein was observed. EGCG treatment (Fig. 3 B) resulted in a much faster disappearance of the monomeric form and accumulation of aggregates. This fits well with the aggregation pattern determined by using SDS-PAGE (Fig.s 2 A and D). In contrast, tetracycline treatment (Fig. 3 C) did not appreciably alter the JD aggregation pattern as detected by using SEC, which apparently contrasts with our SDS-PAGE results, whereby a much larger accumulation of SDS-soluble species was detected at later times.

One possible explanation might be that there are SDS-soluble aggregated species, which can only be detected by SEC analysis, as already observed in the case of full-length,

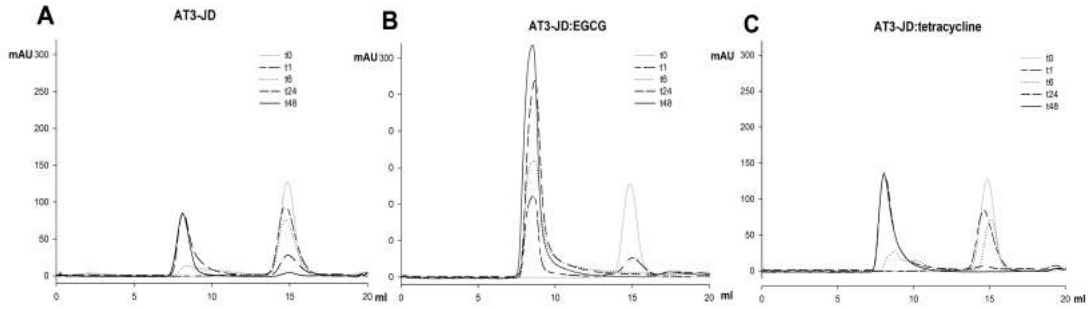

Fig. 3. SEC profiles of JD incubated with EGCG or tetracycline. An amount of 500 µg of: A) JD, B) JD/EGCG 1:5, and C) JD/tetracycline 1:5 was loaded onto a Superose 12 10:300 GL column equilibrated in phosphate buffered saline solution after the indicated incubation times. *Adapted from (43)*

expanded AT3 (14).The much higher intensity of the void-volume peak detected in the presence of either compounds, as compared to the control sample, quite likely results from a tight protein-drug interaction, as supported by our observations (data not shown).

EGCG, but not tetracycline, strongly affects the structural features of the aggregation intermediates, as shown by FTIR spectroscopy

The effects of EGCG and tetracycline on the JD misfolding and aggregation were also studied by FTIR spectroscopy in the attenuated total reflection (ATR) mode. The ATR/FTIR absorption spectrum of freshly purified JD is reported in Fig. 4 A in the amide I band, mainly due to the C=O stretching vibrations of the peptide bond, which is particularly sensitive to protein secondary structures (45). To disclose the different amide I components, we calculated the second derivative spectrum, whose minima correspond to the absorption maxima (46).

In agreement with previous FTIR characterization of the JD (38,39), the second derivative spectrum of the native protein (Fig. 4 B) displayed a major component at approximately ~1635 cm^{-1} that, along with the component at around ~1690 cm^{-1}, can be assigned to the native intramolecular ß-sheet structures. The component at about ~1657 cm^{-1} occurs in the spectral region of α-helical and random coil structures. During incubation at 37 °C in PBS solution, the amide I peaks of the native protein decreased in intensity and two new components appeared in the spectra at approximately ~1693 and 1623 cm^{-1} (Fig. 4 B), which were assigned to the formation of intermolecular ß-sheet structures in the protein aggregates (38). A different behavior was observed in the presence of EGCG (JD/compound 1:5) in comparison with JD alone. Indeed, the second derivative components of the native protein decreased in intensity immediately after EGCG addition, and the peak at about ~1635 cm^{-1} appeared to be down-

shifted to approximately ~1630 cm^{-1}, in the typical spectral region of intermolecular ß-sheet structures of protein aggregates (Fig. 4 C). Very similar spectral changes were previously observed for the full-length expanded AT3 in the presence of EGCG (14). The presence of an almost constant peak at about ~630 cm^{-1} suggests that EGCG is able to redirect JD aggregation from the fibril-formation process to off-pathway aggregates. JD second derivative spectra

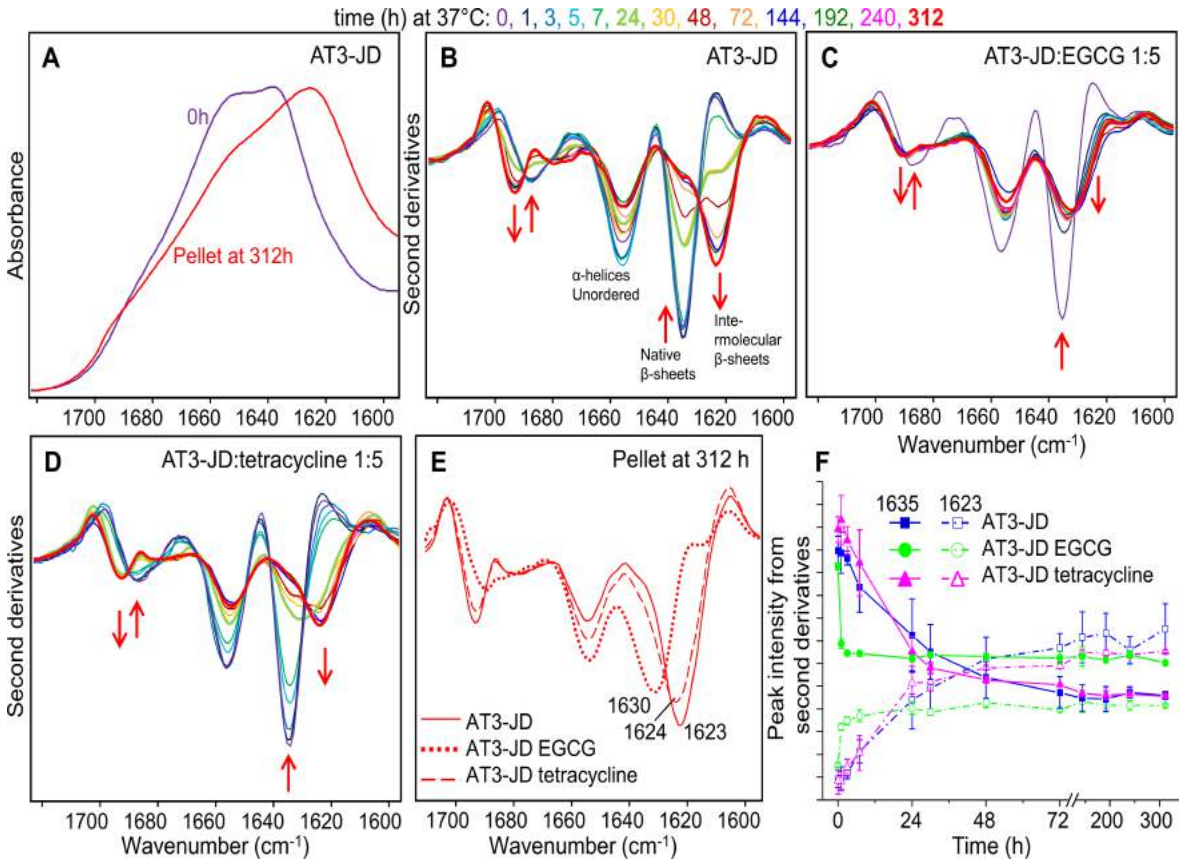

Fig. 4. JD misfolding and aggregation studied by using FTIR spectroscopy. A) ATR/FTIR absorption spectra of freshly purified JD and of the pellet collected after incubation of the protein at 37 °C for 312 h. Spectra are reported in the amide I spectral region. B) Second derivatives of the absorption spectra of the JD (150 µM) collected at different incubation times at 37 °C. The assignment of the main components to protein secondary structures are reported. Arrows point to the spectral changes occurring at increasing incubation time. C) Second derivatives of the absorption spectra of 150 µM JD incubated in the presence of 750 µM EGCG (i.e., JD/EGCG 1:5) and otherwise under the conditions reported for panel B. D) Second derivatives of the absorption spectra of 150 µM JD incubated in the presence of 750 µM tetracycline (i.e., JD/tetracycline 1:5) and otherwise under the conditions reported for panel B. E) Second derivative spectra of the pellet collected from a solution of JD incubated in isolation for 312 h at 37 °C, or JD in the presence of EGCG, or of tetracycline. The positions of the main peak, due to ß-sheet structures, is indicated. Spectra are shown after normalization at the peak around ~1515 cm^{-1} of tyrosines to compensate for possible differences in the protein content. F) Time course of the components at ~1635 and 1623 cm^{-1} (assigned to native JD ß-sheets and to intermolecular ß-sheet structures of the protein aggregates, respectively) reported for either the JD alone, or incubated in the presence of EGCG or tetracycline. The intensities are taken from the second derivative spectra after normalization of the tyrosine peak approximately appearing at ~1515 cm^{-1}.

collected at different incubation times in the presence of tetracycline at a JD/compound molar ratio of 1:5 (Fig. 4D) indicate that tetracycline does not prevent JD misfolding and aggregation.

However, the final aggregates obtained in the presence of this compound displayed a minor reduction in intensity of the intermolecular ß-sheet component, which also occurred at slightly higher wavenumbers compared with the JD alone as shown in Fig. 4 E, where the second derivative spectra of the pellets obtained after 312 h of protein incubation at 37 °C are reported. In contrast, pellets obtained after incubation with EGCG confirmed the aforementioned downshift to approximately ~1630 cm^{-1}, which is indicative of an off-pathway aggregation mode. The time courses of the intensities of native and intermolecular ß-sheet structures in the JD aggregates are reported in Fig. 4 F. Noteworthy, under our conditions, JD misfolding and aggregation at 37 °C in the presence of EGCG was almost completed after an incubation period of 1–2 h, whereas it took about 48 h in the presence of tetracycline, the latter being a pattern essentially indistinguishable from that of the control sample. These results suggest that, unlike tetracycline, EGCG binds to the native JD, leading to the formation of misfolded, aggregation-prone intermediates that are off-path- way of fibrillogenesis.

NMR spectroscopy highlights different interaction modes of EGCG and tetracycline with the JD

Recently, we have extensively exploited STD NMR spectroscopy (47–54) to characterize the binding of several natural (55–58) and synthetic ligands (59–63) to amyloid oligomers, thus demonstrating the reliability and versatility of this technique. Moreover, Melacini and co-workers validated STD NMR methods in characterizing the amyloid oligomer interaction with soluble proteins (in particular Aß peptide oligomers) (64,65) and in also mapping peptide early self-association events (66). In general, when an STD NMR experiment is acquired on a mixture containing the target protein and a potential ligand, the detection of NMR signals of the test molecule in the STD spectra is a clear-cut evidence of an interaction. Here, we have employed STD NMR experiments to investigate the nature of the interactions of EGCG and tetracycline with both JD monomers and oligomers at the atomic level.

To a solution containing 1.5 mM EGCG or tetracycline in PBS solution, pH 7.2 at 5 °C, an aliquot of monomeric JD was added to a final concentration of 7 µM. Under these conditions, the monomeric state is preserved for at least one day. This is a time suitable for the acquisition of several STD spectra at different saturation times. The same experiments were performed after a pre-incubation period of 5 d at 37 °C of the sole JD. This treatment promotes protein aggregation, with resulting enrichment in JD soluble oligomers, as supported by SEC

analysis (Fig. S3 in the Supporting Information). STD spectra (Fig. 5) unambiguously highlighted a different binding mode by the two compounds. In fact, EGCG resonances appear in both STD spectra depicted in Fig. 5 A (spectra 2 and 4, recorded in the presence of the JD monomer or the oligomer, respectively), whereas the tetracycline signals are only detected in the STD spectrum recorded in the presence of protein oligomers (Fig. 5 B, spectrum 4). Thus, the sole EGCG is capable of interacting with the monomeric form, which might, at least in part, account for the different effects of the two compounds in affecting oligomerization.

The binding epitopes identified on either compounds (Fig. 6; Fig.s S4 and S5 in the Supporting Information for the corresponding STD build-up curves) indicate that the whole ligand structure is involved in the receptor recognition process, which is in agreement with previous findings concerning EGCG interaction with AT3Q55 oligomers (55) and tetracycline binding to Aß oligomers (56).

In this latter case, we reported in particular the formation of supramolecular colloidal particles presenting a disordered and non-homogeneous internal structure that justifies the absence of a specific ligand binding epitope. We hypothesize the formation of similar supramolecular complexes also in the presence of JD oligomers.

T o provide a complementary insight into the nature of the EGCG interaction with the JD monomers, titration of the ^{15}N-labelled protein with increasing ligand concentrations was performed, and the changes in the protein NMR fingerprint were monitored by acquisition of ^{15}N-SOFAST-HMQC spectra (Fig. 7) (67).

First, a SOFAST-HMQC spectrum was acquired on a sample containing 0.3 mm ^{15}N-labelled JD dissolved in PBS solution, pH 6.5 at 25 °C, to verify the match with the backbone amide assignments previously published (68). Then, the protein was titrated with EGCG (JD/compounds ratios 1:0.5, 1:1, 1:2, 1:3, and 1:4) and the corresponding SOFAST-HMQC spectra were collected (Fig. 7). The most significant variation observed is the intensity of the protein cross- peaks, which decreased at each step of titration. This decay correlated with the appearance of a white pellet at the bottom of the NMR tube, occurring after each addition of the ligand, di- agnostic of the precipitation of a certain amount of sample. This suggests that the main effect induced by EGCG probably consists in a conformational change of the JD, as already observed by FTIR spectroscopy (Fig. 4), which, in turn, promotes fast protein aggregation and precipitation.

The protein sample stability over time in the absence of EGCG was assessed by

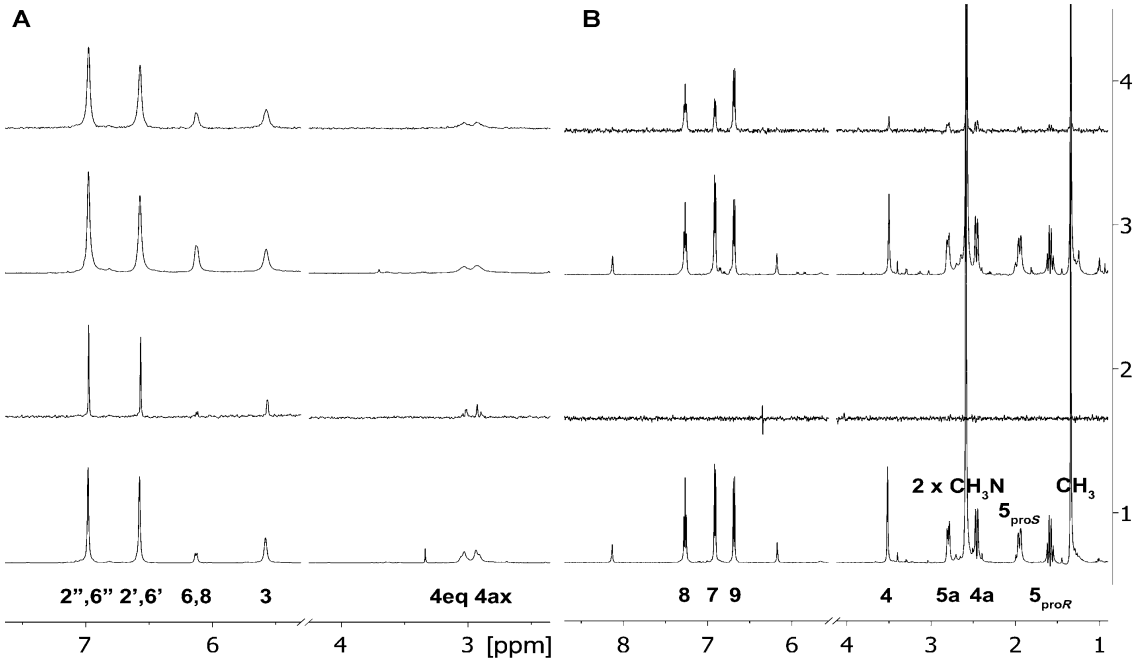

Fig. 5. STD NMR characterization of EGCG and tetracycline binding to the JD monomer and oligomers. A) 1) ^{1}H NMR spectrum of a mixture containing JD (7 μM) immediately after purification and 1.5 mM EGCG. 2) STD NMR spectrum of the same mixture investigated in spectrum 1 at a saturation time of 3 s. 3) ^{1}H NMR spectrum of a mixture containing JD (7 μM) five days after purification and 1.5 mM EGCG. 4) STD NMR spectrum of the same mixture investigated in spectrum 3 at a saturation time of 3 s. **B)** 1) ^{1}H NMR spectrum of a mixture containing JD (7 μM) immediately after purification and 1.5 mM tetracycline. 2) STD NMR spectrum of the same mixture investigated in spectrum 1 at a saturation time of 3 s. 3) ^{1}H NMR spectrum of a mixture containing JD (7 μM) five days after purification and 1.5 mM tetracycline. 4) STD NMR spectrum of the same mixture investigated in spectrum 3 at a saturation time of 3 s. All samples were dissolved in PBS solution, pH 7.2, 5 °C. The spectrometer frequency was 600 MHz. The EGCG H2 signal is overlapped by water resonance. Ligand proton assignment is reported under spectra A1 for EGCG and B1 for tetracycline. All the spectra were recorded at 600 MHz.

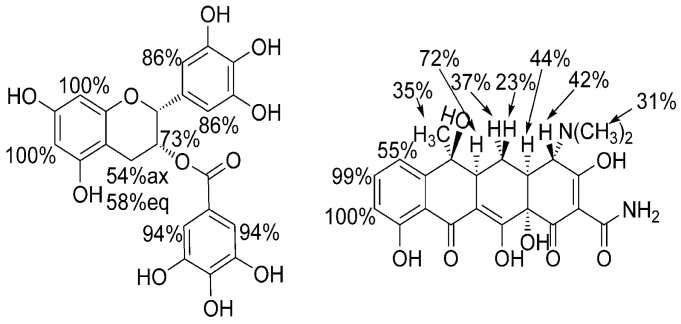

Fig. 6. Binding epitopes of EGCG and tetracycline calculated for the inter- action with the JD oligomers. In each case, the largest absolute STD effect has been scaled to 100%. The EGCG H2 signal is overlapped by water resonance and thus its STD effect was not calculated.

comparing the SOFAST-HMQC spectra of the JD recorded immediately after purification (Fig. 7 A)and after an incubation period of 20 h (which is longer than a full titration experiment) at 25 °C (Fig. 7 F). In particular, the protein sample was split into two aliquots, one being employed for the titration experiments (Fig.s 7 A–E), the other being incubated at 25 °C in the absence of EGCG (Fig. 7 F). The spectra given in Fig.s 7 A and F are identical, supporting the stability of the protein under these experimental conditions.

Thus, protein precipitation is a direct consequence of EGCG addition to the JD sample. From the comparison of spectra A and C in Fig. 7 we derived that, for a protein/ligand molar ratio of 1:1, the amino acid residues most affected by signal broadening are those colored blue in Fig. 7 G. They map to the six-stranded antiparallel ß-sheet constituting the "core" of the C-terminal subdomain of the JD. Thus, we can infer that the EGCG-induced processes of misfolding and self-aggregation of the JD start in this structural region. Also, small chemical shift deviations (CSDs) were observed, mainly assigned to residues belonging to the α-helical hairpin moiety (Fig. 7 H, pink color). This is a structural motif endowed with high conformational flexibility, likely playing a key role in molecular-recognition and interaction/aggregation processes (69,70).

Notably, even at high JD/compound ratios and after significant protein precipitation, the ligand resonances were not visible in the ^{1}H NMR spectra of the mixture (Fig. S6 in the Supporting Information). This suggests that the stoichiometry of the JD/compound complex should be higher than 1:1 and that at least a part of the ligand precipitates together with the protein aggregates. This is also supported by the dramatic reduction in the diffusion coefficient of EGCG when co-incubated with JD in large stoichiometric excess to JD (JD/EGCG 1:30), as measured by NMR diffusion-ordered spectroscopy (DOSY). The diffusion co-efficient of EGCG in the free state (1.5 mM, PBS solution, pH 7.4, 25 °C) was 4.98 $m^2 s^{-1}$, whereas after addition of 50 μM JD, it dropped to 1.96 $m^2 s^{-1}$ (reduction of 61%), which supports the existence of an equilibrium free/bound state of the ligand molecules. In the ^{1}H NMR spectra recorded on the same sample prepared for the DOSY acquisition, the EGCG resonances were visible only because of the large ligand stoichiometric excess.

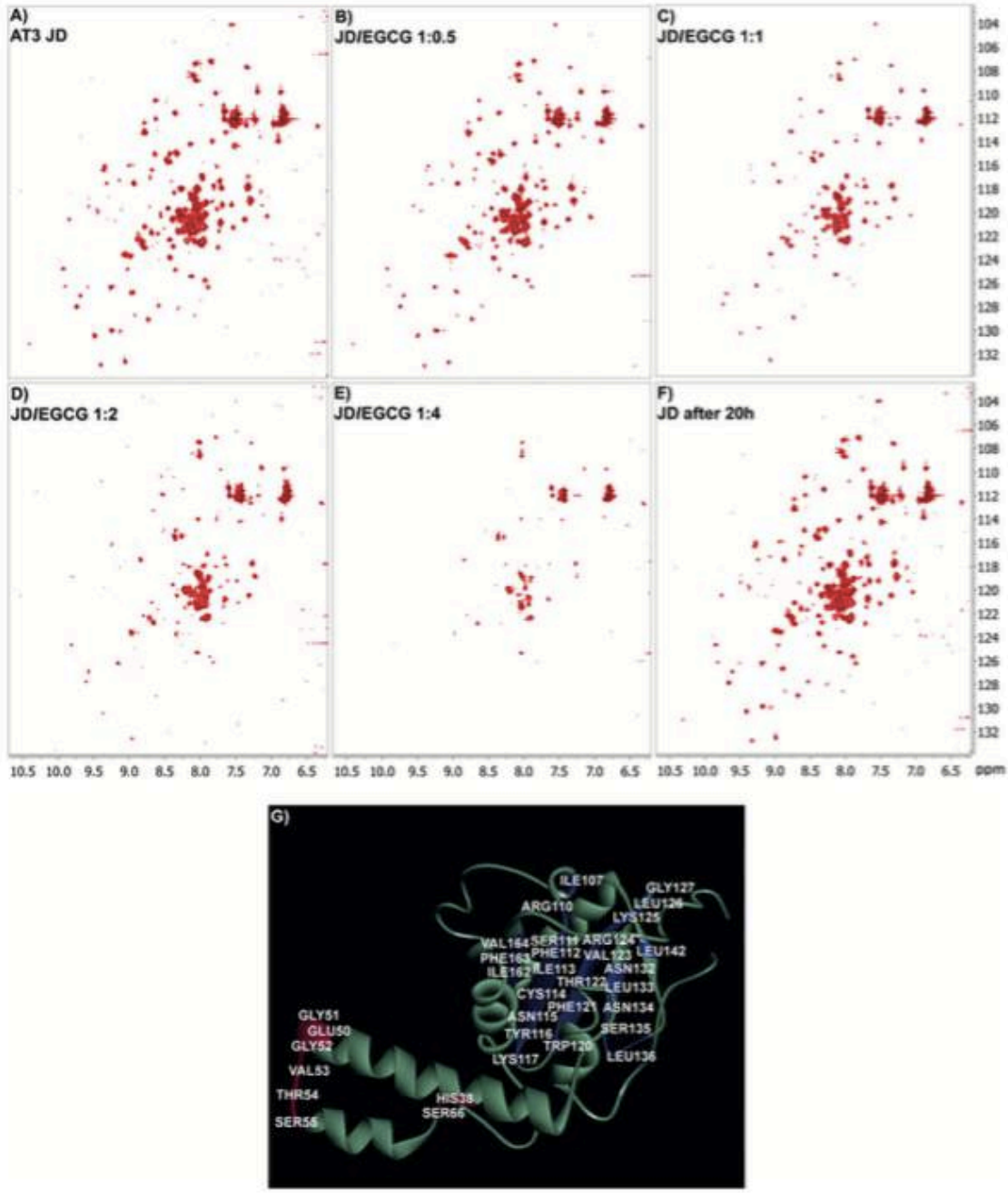

Fig. 7. ^{15}N-SOFAST-HMQC titration experiments for the characterization of the EGCG interaction with the JD monomer. The ^{15}N -SOFAST-HMQC spectra were recorded in a solution containing: A) 0.3 mM ^{15}N -JD in PBS solution, pH 6.5 at 25 °C; B) 0.3 mM ^{15}N-JD and 0.15 mM EGCG in PBS solution, pH 6.5 at 25 °C; C) 0.3 mM ^{15}N-JD and 0.3 mM EGCG in PBS solution, pH 6.5 at 25 °C; D) 0.3 mM ^{15}N -JD and 0.6 mM EGCG in PBS solution, pH 6.5 at 25 °C; E) 0.3 mM ^{15}N -JD and 1.2 mM EGCG in PBS solution, pH 6.5 at 25 °C, F) 0.3 mM ^{15}N -JD in PBS solution, pH 6.5, after an incubation period of 20 h at 25 °C. All the spectra were recorded at 600 MHz. G) Residues affected by either signal broadening (blue) or chemical shift perturbation (pink) mapped on the structure of the monomeric JD (PDB ID: 1ZYB).

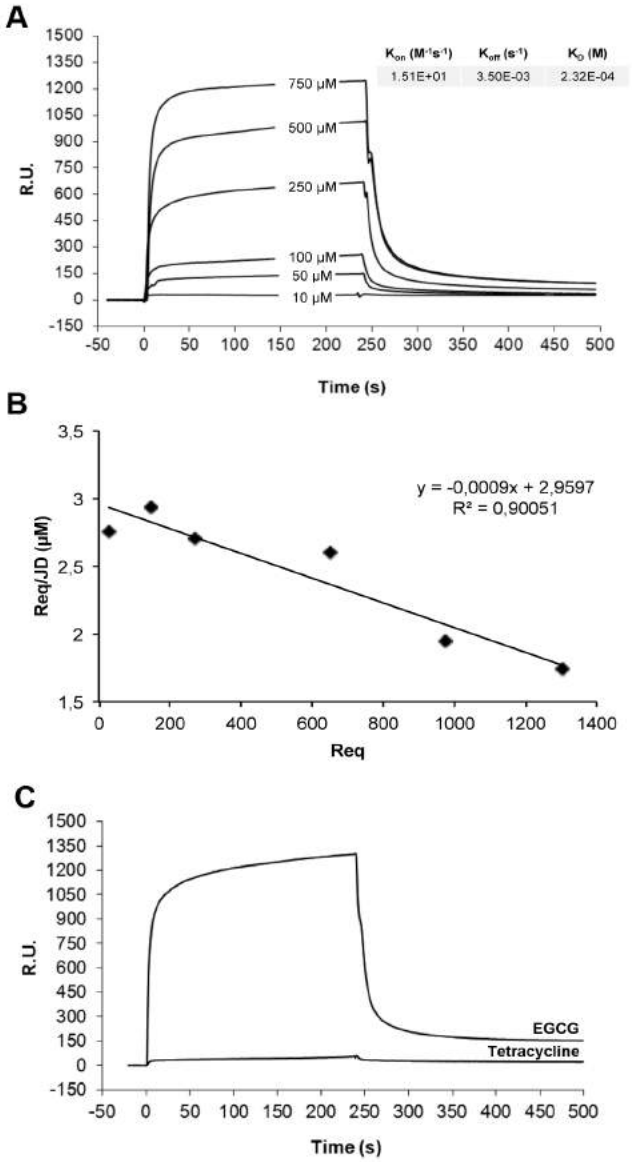

Fig. 8. Association/dissociation kinetics for the binding between JD and EGCG. A) JD was imobilized on the sensor chip and the indicated concentrations of EGCG were flowed onto the chip surface. B) The R_{eq} values obtained for each given EGCG concentration were used to generate the Scatchard plot. C) Overlay of the BIAcore sensograms showing the different binding capacity of EGCG and tetracycline (injected at a concentration of 750 mm) for the JD, immobilized on the surface of the sensor chip.

SPR provides evidence of weak JD–EGCG interaction

We performed SPR analyses to determine the binding affinity of the JD–EGCG and JD–tetracycline complexes. In particular, we studied the real time association and dissociation of EGCG or tetracycline to/from JD (Fig.s 8 A and B) coupled directly to the sensor chip CM5 by monitoring the binding and release of EGCG or tetracycline to and from the chip.

In the case of EGCG, the experiments provided evidence of compound binding to the JD. A good fitting was obtained by using the Langmuir 1:1 and BIA evaluation 4.1 software (BIA-core). As the presence of multiple binding sites for EGCG would yield an undistinguishable curve, the K_D value reported in the caption of Fig. 8 should be regarded as an apparent one.

No interaction was determined by using tetracycline as an analyte (Fig. 8 C), which is suggestive of a much lower affinity toward the monomer compared to EGCG, which is in accordance with the NMR data (Fig. 5).

2.3 CONCLUSION

In a previous work, we investigated the capability of EGCG and tetracycline to contrast amyloid aggregation and toxicity of full-length expanded variants of AT3 (14). We observed a

significant protective effect by both compounds, but also demonstrated substantially different mechanisms of action. Actually, in the presence of EGCG, off-pathway, SDS-resistant soluble aggregates arose, whereas tetracycline did not produce major alterations in the structural features of the aggregates compared with the control, but substantially increased their solubility.

We have thus undertaken the present work to provide in- sight into how either compound precisely interact with AT3. To this end, we have taken advantage of NMR spectroscopy to identify the individual moieties of the protein and compounds involved in the interaction. However, we have examined their effects on the aggregation of the sole N-terminal JD, as the C-terminal disordered domain would severely hinder NMR measurements.

Our results show that both EGCG and tetracycline affect JD aggregation in a fashion qualitatively similar to that they exert on the full-length, expanded AT3. Most notably, NMR experiments have enabled us to also identify the individual binding epitopes on either compound, which show that the whole ligand structure participates in the protein binding. This points to a nonspecific interaction mode, as also supported by the K_D values assessed by SPR analysis. Not less important, we have also shown that EGCG is able to bind both the monomeric and the oligomeric form of the JD, whereas tetracycline only inter- acts with the oligomeric one. A possible concern regarding the effects of the two compounds assayed is that they might sequester functional AT3 with a resulting loss of function. However, this should not result in any detrimental effect, as previous work showed that knock-out mice were viable and fertile and did not present a reduced life span (71). In conclusion, our results suggest that the JD in isolation is a suitable model for assessing the effect of potential antiamyloid agents on AT3, which should significantly speed up re- search designed for this purpose. This work also provides a more in-depth understanding of the interaction mode between AT3 and the compounds under investigation, which might provide hints to rationally design more effective variants thereof.

2.4 MATERIAL AND METHODS

JD purification. The JD-encoding gene was cloned in a pET21-a vector and the protein was expressed in *Escherichia coli* BL21 Tuner (DE3) pLacI (*E. coli* B F ompT hsdSB (rB mB) gal dcm lacY1(DE3) pLacI (CamR); Novagen, Germany) as a His-tagged protein. Cells were

grown at 37 °C in LB low salt-ampicillin medium, induced with 0.2mM isopropylthio-ß-d-galactoside (IPTG) at OD_{600} 0.8 for 2 h at 30 °C. Protein purification was performed as previously described for the expanded form (14). To express the ^{15}N-labeled JD, cells were grown at 37 °C in 2 L of LB low salt-ampicillin in ^{15}N-free medium. At OD_{600} 0.7, the cells were centrifuged for 30 min at 5000 *g*. The pelleted cells were resuspended in isotopically labeled minimal medium (3 g L^{-1} KH_2PO_4, 6 g L^{-1} $Na_2HPO_4 \cdot 7\ H_2O$, 0.12 g L^{-1} $MgSO_4$, 0.2 g L^{-1} NaCl, 1 g L^{-1} $^{15}NH_4Cl$, 0.4% glucose), then incubated to allow the recovery of growth and clearance of unlabeled metabolites. After 1 h, protein expression was induced with 1 mM IPTG for 2 h at 30 °C (37). Purification of the labeled protein was performed according to the same protocol as for the unlabeled protein.

SDS-PAGE and densitometry analysis of the soluble protein fraction. The purified JD (150 μM) was incubated at 37 °C in PBS solution in the presence or absence of EGCG or tetracycline (Sigma–Aldrich, USA) at a protein/compound molar ratio of 1:5. JD aliquots at different times of incubation (0, 1, 3, 6, 24, 48, and 72 h) were centrifuged at 14000 *g* for 15min and 3 μl of the supernatants were subjected to SDS-PAGE. The gels were stained with IRDye Blue Protein Stain (LiCor, USA), scanned at 700 nm with the Odyssey Fc System (LiCor) and analyzed with the Image Studio software (LiCor).

SEC analysis. The purified JD (150 μM) was incubated at 37 °C in PBS solution in the presence or absence of EGCG or tetracycline at a protein/com- pound molar ratio of 1:5. Aliquots of the protein samples (500 μg) were withdrawn at different times of incubation (0, 1, 6, 24, and 48 h) and loaded onto a Superose 12 10:300 GL gel filtration column (GE Healthcare, Life Sciences, UK), pre-equilibrated with PBS solution (25 mM potassium phosphate, pH 7.2, 150 mM NaCl), and eluted at a flow rate of 0.5 mL min^{-1}.

Fourier transform infrared (FTIR) spectroscopy. FTIR analyses were performed following the experimental procedures already optimized and described in previous FTIR characterizations of JD (38,39) and of expanded AT3 (14,38). In particular, a sample (600 μL) of the purified JD (150 μM in PBS solution) was incubated in the test tube at 37 °C in the presence or absence of EGCG or tetracycline at a protein/compound molar ratio of 1:5. An aliquot (3 μL) was taken at different times of incubation and deposited on the diamond

element of the device for measurements in the attenuated total reflection (ATR) mode. The Golden Gate (Specac, USA) device with a single reflection diamond crystal was employed. The FTIR spectrum was collected after solvent evaporation, which took place in about 1 min. The formation of a semi-dry film was expected following this procedure (40). ATR/FTIR spectra were collected by using a Varian 670-IR spectrometer (Varian Australia Pty Ltd, Mulgrave VIC, Australia) equipped with a nitrogen-cooled mercury cadmium telluride detector under the following conditions: 2 cm^{-1} spectral resolution, 25 kHz scan speed, 1000 scans co-addition, and triangular apodization. The ATR/FTIR spectra of a PBS solution and of the two compounds at a concentration of 600 μM in PBS solution were also collected at each incubation time at 37 °C and were subtracted from the protein spectra (38). Second derivatives of the spectra were obtained, after the smoothing of the measured spectra by the Savitzky–Golay algorithm, by using the software Resolutions Pro (Varian Australia Pty Ltd, Mulgrave VIC, Australia).

NMR spectroscopy. NMR experiments were recorded on a Varian 400 MHz Mercury or a Bruker 600 MHz Avance III spectrometer equipped with a QCI cryo-probe, with a z-axis gradient coil. EGCG and tetracycline were dissolved in PBS solution, pH 7.2 and, for ligand–receptor interaction experiments based on ligand observation, an aliquot of the protein solution, dissolved in the same buffer, was added to reach the final concentration required. Conversely, for experiments based on protein observation, small aliquots of a 12 mM EGCG solution in PBS solution, pH 6.5, were added to a sample containing the ^{15}N-la- belled JD, with a final maximum dilution of the initial protein concentration of 10%. Sodium azide (0.05%; w/v) was added to the sample to prevent protein degradation by bacteria. Basic sequences were employed for ^{1}H NMR, STD NMR, ^{15}N-SOFAST-HMQC spectroscopic and diffusion experiments.

Solvent suppression was performed by excitation sculpting. ^{1}H NMR spectra were acquired with a number of transients ranging from 8 and 256 and 2 s recycle delay. For the STD NMR experiments, a train of Gaussian-shaped pulses each of 50 ms was employed to saturate selectively the protein envelope; the total saturation time of the protein envelope was varied between 3 and 0.15 s, 1024 scans; acquisitions were performed at 5 °C. ^{15}N- SOFAST-HMQC experiments were acquired with a number of transients ranging from 8 and 32, and 640 increments; acquisitions were performed at 25 °C. Diffusion experiments were acquired

employing an array of 30 spectra for each experiment (128 scans, with 2 s recycle delay) varying the gradient strength from 3.33 to 19.4 G cm^{-2}. The lengths of and delays between the gradient pulses were optimized depending on the experimental conditions and ranged between 0.002 and 0.005 s and 0.2–0.7 s, respectively; acquisitions were performed at 25 °C. Data fitting and diffusion coefficient determinations were performed by using the software Dosytoolbox (http ://personalpages.manchester.ac.uk/staff/mathias. nilsson/software.htm)

Surface plasmon resonance (SPR). Surface plasmon resonance experiments were carried out with a BIAcore X system (GE Healthcare). JD and AT3Q55 proteins were coupled to a carboxymethylated dextran surface of two different CM5 sensor chips by using amine coupling chemistry at surface densities of 5000 and 4000 resonance units, respectively, by injecting 60 µL of each protein at the concentration of 50 µg mL^{-1} resuspended in 10 mM sodium acetate buffer, pH 4 (flow rate of 5 µL min^{-1}). A reference cell was saturated with 1 M ethanolamine, pH 8.5. Different concentrations of EGCG, diluted in the running buffer (10mM 4-(2-hydroxyethyl)-1-piperazineethanesulfonic acid (HEPES), pH 7.4, 150mM NaCl, 3mM ethylenediaminetetraacetic acid (EDTA), 0.005% v/v Surfactant P20), were tested twice over the surface of sensor chip CM5 for 4 min (40 µL injections at flow rate of 10 mL min^{-1}). Surface regeneration was accomplished by injecting 50 mM NaOH (30 s contact) two or three times. The interaction rate constants were calculated by simultaneous fitting of the binding curves obtained with different concentrations of analyte, by using the BIAevaluation 4.1 software (BIAcore).

2.5 CANDIDATE'S CONTRIBUTION

The candidate contributed to the aggregation assays and the relevant SDS-PAGE and SEC analyses and Biacore experimentations. She also prepared the protein for FT-IR and NMR analyses, which were performed in collaboration with Drs. Antonino Natalello and Cristina Airoldi, respectively. The candidate contributed to perform the statistical analysis.

2.6 REFERENCES

1. Bauer PO, Nukina N. The pathogenic mechanisms of polyglutamine diseases and current therapeutic strategies. J Neurochem. 2009 Sep;110(6):1737–65.

2. Paulson HL, Bonini NM, Roth KA. Polyglutamine disease and neuronal cell death. Proc Natl Acad Sci U S A. 2000 Nov 21;97(24):12957–8.

3. Aguzzi A, O'Connor T. Protein aggregation diseases: pathogenicity and therapeutic perspectives. Nat Rev Drug Discov. 2010 Mar;9(3):237–48.

4. Merlini G, Ascari E, Amboldi N, Bellotti V, Arbustini E, Perfetti V, et al. Interaction of the anthracycline 4'-iodo-4'-deoxydoxorubicin with amyloid fibrils: inhibition of amyloidogenesis. Proc Natl Acad Sci U S A. 1995 Mar 28;92(7):2959–63.

5. Heiser V, Scherzinger E, Boeddrich A, Nordhoff E, Lurz R, Schugardt N, et al. Inhibition of huntingtin fibrillogenesis by specific antibodies and small molecules: implications for Huntington's disease therapy. Proc Natl Acad Sci U S A. 2000 Jun 6;97(12):6739–44.

6. Howlett DR, George AR, Owen DE, Ward RV, Markwell RE. Common structural features determine the effectiveness of carvedilol, daunomycin and rolitetracycline as inhibitors of Alzheimer beta-amyloid fibril formation. Biochem J. 1999 Oct 15;343 Pt 2:419–23.

7. Findeis MA. Approaches to discovery and characterization of inhibitors of amyloid beta-peptide polymerization. Biochim Biophys Acta. 2000 Jul 26;1502(1):76–84.

8. Cashman NR, Caughey B. Prion diseases--close to effective therapy? Nat Rev Drug Discov. 2004 Oct;3(10):874–84.

9. https://clinicaltrials.gov/ct2/results?term=Machado+joseph+disease&Search=Search.

10. Schmidt J, Schmidt T, Golla M, Lehmann L, Weber JJ, Hübener-Schmid J, et al. In vivo assessment of riluzole as a potential therapeutic drug for spinocerebellar ataxia type 3. J Neurochem. 2016 Jul;138(1):150–62.

11. Conceição M, Mendonça L, Nóbrega C, Gomes C, Costa P, Hirai H, et al. Intravenous administration of brain-targeted stable nucleic acid lipid particles alleviates Machado-Joseph disease neurological phenotype. Biomaterials. 2016 Mar;82:124–37.

12. Duarte-Neves J, Gonçalves N, Cunha-Santos J, Simões AT, den Dunnen WFA, Hirai H, et al. Neuropeptide Y mitigates neuropathology and motor deficits in mouse models of Machado-Joseph disease. Hum Mol Genet. 2015 Oct 1;24(19):5451–63.

13. Costa M do C, Ashraf NS, Fischer S, Yang Y, Schapka E, Joshi G, et al. Unbiased screen identifies aripiprazole as a modulator of abundance of the polyglutamine disease protein, ataxin-3. Brain J Neurol. 2016 Sep 19;

14. Bonanomi M, Natalello A, Visentin C, Pastori V, Penco A, Cornelli G, et al. Epigallocatechin-3-gallate and tetracycline differently affect ataxin-3 fibrillogenesis and reduce toxicity in spinocerebellar ataxia type 3 model. Hum Mol Genet. 2014 Dec 15;23(24):6542–52.

15. Chopra I, Roberts M. Tetracycline antibiotics: mode of action, applications, molecular

biology, and epidemiology of bacterial resistance. Microbiol Mol Biol Rev MMBR. 2001 Jun;65(2):232–260 ; second page, table of contents.

16. Choi Y, Kim H-S, Shin KY, Kim E-M, Kim M, Kim H-S, et al. Minocycline attenuates neuronal cell death and improves cognitive impairment in Alzheimer's disease models. Neuropsychopharmacol Off Publ Am Coll Neuropsychopharmacol. 2007 Nov;32(11):2393–404.

17. Forloni G, Salmona M, Marcon G, Tagliavini F. Tetracyclines and prion infectivity. Infect Disord Drug Targets. 2009 Feb;9(1):23–30.

18. Noble W, Garwood C, Stephenson J, Kinsey AM, Hanger DP, Anderton BH. Minocycline reduces the development of abnormal tau species in models of Alzheimer's disease. FASEB J Off Publ Fed Am Soc Exp Biol. 2009 Mar;23(3):739–50.

19. Bendeck MP, Conte M, Zhang M, Nili N, Strauss BH, Farwell SM. Doxycycline modulates smooth muscle cell growth, migration, and matrix remodeling after arterial injury. Am J Pathol. 2002 Mar;160(3):1089–95.

20. Stoilova T, Colombo L, Forloni G, Tagliavini F, Salmona M. A new face for old antibiotics: tetracyclines in treatment of amyloidoses. J Med Chem. 2013 Aug 8;56(15):5987–6006.

21. Forloni G, Colombo L, Girola L, Tagliavini F, Salmona M. Anti-amyloidogenic activity of tetracyclines: studies in vitro. FEBS Lett. 2001 Jan 5;487(3):404–7.

22. Tagliavini F, Forloni G, Colombo L, Rossi G, Girola L, Canciani B, et al. Tetracycline affects abnormal properties of synthetic PrP peptides and PrP(Sc) in vitro. J Mol Biol. 2000 Jul 28;300(5):1309–22.

23. Ono K, Yamada M. Antioxidant compounds have potent anti-fibrillogenic and fibril-destabilizing effects for alpha-synuclein fibrils in vitro. J Neurochem. 2006 Apr;97(1):105–15.

24. Chen M, Ona VO, Li M, Ferrante RJ, Fink KB, Zhu S, et al. Minocycline inhibits caspase-1 and caspase-3 expression and delays mortality in a transgenic mouse model of Huntington disease. Nat Med. 2000 Jul;6(7):797–801.

25. Smith DL, Woodman B, Mahal A, Sathasivam K, Ghazi-Noori S, Lowden PAS, et al. Minocycline and doxycycline are not beneficial in a model of Huntington's disease. Ann Neurol. 2003 Aug;54(2):186–96.

26. Graham HN. Green tea composition, consumption, and polyphenol chemistry. Prev Med. 1992 May;21(3):334–50.

27. Sang S, Lambert JD, Ho C-T, Yang CS. The chemistry and biotransformation of tea constituents. Pharmacol Res. 2011 Aug;64(2):87–99.

28. Balentine DA, Wiseman SA, Bouwens LC. The chemistry of tea flavonoids. Crit Rev

Food Sci Nutr. 1997 Dec;37(8):693–704.

29. Mandel SA, Youdim MBH. In the rush for green gold: Can green tea delay age-progressive brain neurodegeneration? Recent Patents CNS Drug Discov. 2012 Dec;7(3):205–17.

30. Mandel SA, Amit T, Weinreb O, Youdim MBH. Understanding the broad-spectrum neuroprotective action profile of green tea polyphenols in aging and neurodegenerative diseases. J Alzheimers Dis JAD. 2011;25(2):187–208.

31. Suganuma M, Okabe S, Oniyama M, Tada Y, Ito H, Fujiki H. Wide distribution of [3H](-)-epigallocatechin gallate, a cancer preventive tea polyphenol, in mouse tissue. Carcinogenesis. 1998 Oct;19(10):1771–6.

32. Ehrnhoefer DE, Duennwald M, Markovic P, Wacker JL, Engemann S, Roark M, et al. Green tea (-)-epigallocatechin-gallate modulates early events in huntingtin misfolding and reduces toxicity in Huntington's disease models. Hum Mol Genet. 2006 Sep 15;15(18):2743–51.

33. Ehrnhoefer DE, Bieschke J, Boeddrich A, Herbst M, Masino L, Lurz R, et al. EGCG redirects amyloidogenic polypeptides into unstructured, off-pathway oligomers. Nat Struct Mol Biol. 2008 Jun;15(6):558–66.

34. Rochet JC, Lansbury PT. Amyloid fibrillogenesis: themes and variations. Curr Opin Struct Biol. 2000 Feb;10(1):60–8.

35. Bertoncini CW, Fernandez CO, Griesinger C, Jovin TM, Zweckstetter M. Familial mutants of alpha-synuclein with increased neurotoxicity have a destabilized conformation. J Biol Chem. 2005 Sep 2;280(35):30649–52.

36. Bieschke J, Russ J, Friedrich RP, Ehrnhoefer DE, Wobst H, Neugebauer K, et al. EGCG remodels mature alpha-synuclein and amyloid-beta fibrils and reduces cellular toxicity. Proc Natl Acad Sci U S A. 2010 Apr 27;107(17):7710–5.

37. Marley J, Lu M, Bracken C. A method for efficient isotopic labeling of recombinant proteins. J Biomol NMR. 2001 May;20(1):71–5.

38. Natalello A, Frana AM, Relini A, Apicella A, Invernizzi G, Casari C, et al. A major role for side-chain polyglutamine hydrogen bonding in irreversible ataxin-3 aggregation. PloS One. 2011;6(4):e18789.

39. Apicella A, Natalello A, Frana AM, Baserga A, Casari CS, Bottani CE, et al. Temperature profoundly affects ataxin-3 fibrillogenesis. Biochimie. 2012 Apr;94(4):1026–31.

40. Goormaghtigh E, Raussens V, Ruysschaert JM. Attenuated total reflection infrared spectroscopy of proteins and lipids in biological membranes. Biochim Biophys Acta. 1999 Jul 6;1422(2):105–85.

41. Robertson AL, Headey SJ, Saunders HM, Ecroyd H, Scanlon MJ, Carver JA, et al. Small heat-shock proteins interact with a flanking domain to suppress polyglutamine aggregation. Proc Natl Acad Sci U S A. 2010 Jun 8;107(23):10424–9.

42. Masino L, Nicastro G, De Simone A, Calder L, Molloy J, Pastore A. The Josephin domain determines the morphological and mechanical properties of ataxin-3 fibrils. Biophys J. 2011 Apr 20;100(8):2033–42.

43. Bonanomi M, Visentin C, Natalello A, Spinelli M, Vanoni M, Airoldi C, et al. How Epigallocatechin-3-gallate and Tetracycline Interact with the Josephin Domain of Ataxin-3 and Alter Its Aggregation Mode. Chem Weinh Bergstr Ger. 2015 Dec 7;21(50):18383–93.

44. Sang S, Lee M-J, Hou Z, Ho C-T, Yang CS. Stability of tea polyphenol (-)-epigallocatechin-3-gallate and formation of dimers and epimers under common experimental conditions. J Agric Food Chem. 2005 Nov 30;53(24):9478–84.

45. Barth A. Infrared spectroscopy of proteins. Biochim Biophys Acta. 2007 Sep;1767(9):1073–101.

46. Susi H, Byler DM. Resolution-enhanced Fourier transform infrared spectroscopy of enzymes. Methods Enzymol. 1986;130:290–311.

47. Mayer M, Meyer B. Characterization of Ligand Binding by Saturation Transfer Difference NMR Spectroscopy. Angew Chem Int Ed. 1999 Jun 14;38(12):1784–8.

48. Mayer M, Meyer B. Charakterisierung von Ligandenbindung durch Sättigungstransfer-Differenz-NMR-Spektroskopie. Angew Chem. 1999 Jun 14;111(12):1902–6.

49. Caraballo R, Dong H, Ribeiro JP, Jiménez-Barbero J, Ramström O. Direct STD NMR identification of beta-galactosidase inhibitors from a virtual dynamic hemithioacetal system. Angew Chem Int Ed Engl. 2010;49(3):589–93.

50. Caraballo R, Dong H, Ribeiro JP, Jiménez-Barbero J, Ramström O. Direct STD NMR Identification of β-Galactosidase Inhibitors from a Virtual Dynamic Hemithioacetal System. Angew Chem. 2010 Jan 12;122(3):599–603.

51. Palmioli A, Sacco E, Airoldi C, Di Nicolantonio F, D'Urzo A, Shirasawa S, et al. Selective cytotoxicity of a bicyclic Ras inhibitor in cancer cells expressing K-Ras(G13D). Biochem Biophys Res Commun. 2009 Sep 4;386(4):593–7.

52. Airoldi C, Sommaruga S, Merlo S, Sperandeo P, Cipolla L, Polissi A, et al. Targeting bacterial membranes: NMR spectroscopy characterization of substrate recognition and binding requirements of D-arabinose-5-phosphate isomerase. Chem Weinh Bergstr Ger. 2010 Feb 8;16(6):1897–902.

53. Airoldi C, Sommaruga S, Merlo S, Sperandeo P, Cipolla L, Polissi A, et al. Targeting bacterial membranes: identification of Pseudomonas aeruginosa D-arabinose-5P isomerase and NMR characterisation of its substrate recognition and binding properties.

Chembiochem Eur J Chem Biol. 2011 Mar 21;12(5):719–27.

54. Airoldi C, Giovannardi S, La Ferla B, Jiménez-Barbero J, Nicotra F. Saturation Transfer Difference NMR Experiments of Membrane Proteins in Living Cells under HR-MAS Conditions: The Interaction of the SGLT1 Co-transporter with Its Ligands. Chem – Eur J. 2011 Nov 25;17(48):13395–9.

55. Sironi E, Colombo L, Lompo A, Messa M, Bonanomi M, Regonesi ME, et al. Natural Compounds against Neurodegenerative Diseases: Molecular Characterization of the Interaction of Catechins from Green Tea with Aβ1–42, PrP106–126, and Ataxin-3 Oligomers. Chem – Eur J. 2014 Oct 13;20(42):13793–800.

56. Airoldi C, Colombo L, Manzoni C, Sironi E, Natalello A, Doglia SM, et al. Tetracycline prevents Aβ oligomer toxicity through an atypical supramolecular interaction. Org Biomol Chem. 2011 Jan 21;9(2):463–72.

57. Airoldi C, Sironi E, Dias C, Marcelo F, Martins A, Rauter AP, et al. Natural compounds against Alzheimer's disease: molecular recognition of Aβ1-42 peptide by Salvia sclareoides extract and its major component, rosmarinic acid, as investigated by NMR. Chem Asian J. 2013 Mar;8(3):596–602.

58. Jesus AR, Dias C, Matos AM, de Almeida RFM, Viana AS, Marcelo F, et al. Exploiting the therapeutic potential of 8-β-d-glucopyranosylgenistein: synthesis, antidiabetic activity, and molecular interaction with islet amyloid polypeptide and amyloid β-peptide (1-42). J Med Chem. 2014 Nov 26;57(22):9463–72.

59. Airoldi C, Zona C, Sironi E, Colombo L, Messa M, Aurilia D, et al. Curcumin derivatives as new ligands of Aβ peptides. J Biotechnol. 2011 Dec 20;156(4):317–24.

60. Airoldi C, Cardona F, Sironi E, Colombo L, Salmona M, Silva A, et al. cis-Glyco-fused benzopyran compounds as new amyloid-β peptide ligands. Chem Commun Camb Engl. 2011 Oct 7;47(37):10266–8.

61. Airoldi C, Cardona F, Sironi E, Salmona M, Ornaghi F, Sancini G, et al. Fluorescent amyloid β-peptide ligand derivatives as potential diagnostic tools for Alzheimer's disease. Pure Appl Chem. 2013 Jun 6;85(9):1813–23.

62. Merlo S, Sironi E, Colombo L, Cardona F, Martorana AM, Salmona M, et al. Cis-Glyco-Fused Benzopyran Derivatives as Hit Compounds for the Development of Therapeutic and Diagnostic Tools against Neurodegenerative Diseases. ChemPlusChem. 2014 Jun 1;79(6):835–43.

63. Airoldi C, Mourtas S, Cardona F, Zona C, Sironi E, D'Orazio G, et al. Nanoliposomes presenting on surface a cis-glycofused benzopyran compound display binding affinity and aggregation inhibition ability towards Amyloid β1-42 peptide. Eur J Med Chem. 2014 Oct 6;85:43–50.

64. Milojevic J, Raditsis A, Melacini G. Human Serum Albumin Inhibits Aβ Fibrillization through a "Monomer-Competitor" Mechanism. Biophys J. 2009 Nov 4;97(9):2585–94.

65. Milojevic J, Melacini G. Stoichiometry and Affinity of the Human Serum Albumin-Alzheimer's Aβ Peptide Interactions. Biophys J. 2011 Jan 5;100(1):183–92.

66. Huang H, Milojevic J, Melacini G. Analysis and Optimization of Saturation Transfer Difference NMR Experiments Designed to Map Early Self-Association Events in Amyloidogenic Peptides. J Phys Chem B. 2008 May 1;112(18):5795–802.

67. Schanda P, Kupče Ē, Brutscher B. SOFAST-HMQC Experiments for Recording Two-dimensional Deteronuclear Correlation Spectra of Proteins within a Few Seconds. J Biomol NMR. 2005 Dec 1;33(4):199–211.

68. Nicastro G, Masino L, Frenkiel TA, Kelly G, McCormick J, Menon RP, et al. Letter to the Editor: Assignment of the 1H, 13C, and 15N resonances of the Josephin domain of human ataxin-3. J Biomol NMR. 2004 Dec 1;30(4):457–8.

69. Nicastro G, Menon RP, Masino L, Knowles PP, McDonald NQ, Pastore A. The solution structure of the Josephin domain of ataxin-3: structural determinants for molecular recognition. Proc Natl Acad Sci U S A. 2005 Jul 26;102(30):10493–8.

70. Sanfelice D, De Simone A, Cavalli A, Faggiano S, Vendruscolo M, Pastore A. Characterization of the conformational fluctuations in the Josephin domain of ataxin-3. Biophys J. 2014 Dec 16;107(12):2932–40.

71. Switonski PM, Fiszer A, Kazmierska K, Kurpisz M, Krzyzosiak WJ, Figiel M. Mouse ataxin-3 functional knock-out model. Neuromolecular Med. 2011 Mar;13(1):54–65.

2.7 SUPPORTING INFORMATION

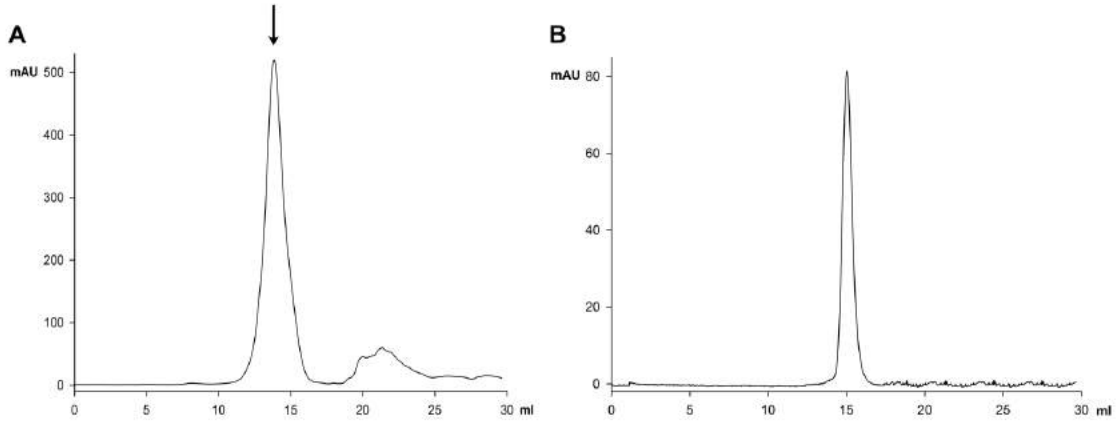

Fig. S1. SEC profiles of JD (A) 6 mg His-tagged JD were loaded onto a Superose 12 10/300 GL column equilibrated in PBS buffer. The arrow indicates the peak corresponding to JD monomeric form. (B) 300 µg monomeric JD were reloaded onto the same column.

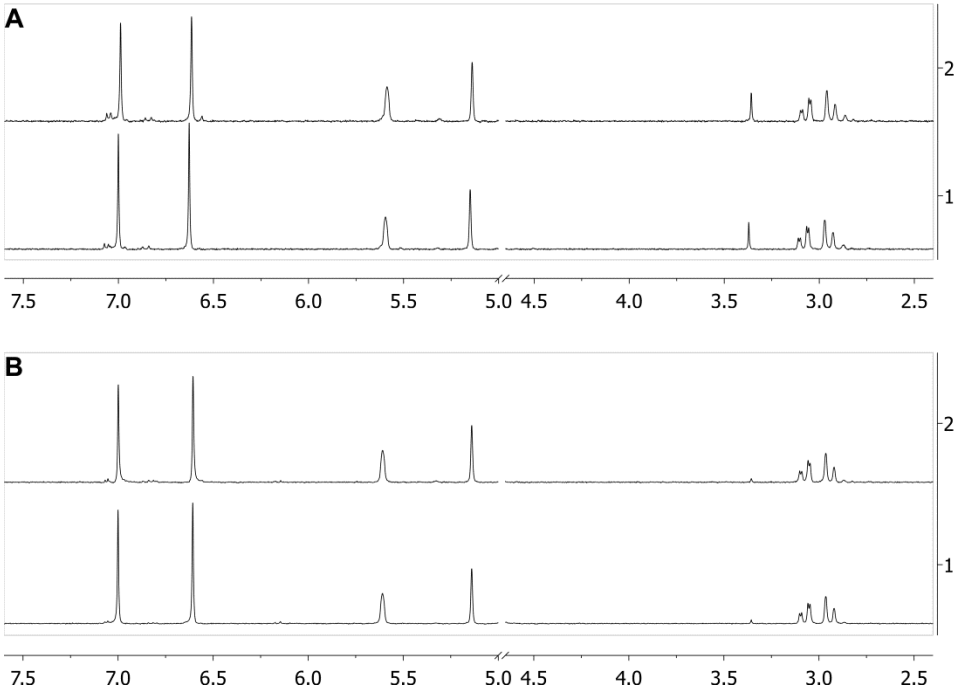

Fig. S2. ^{1}H NMR monitoring of EGCG stability at 37 °C, pH 7.4 or 6.5. ^{1}H NMR spectra were recorded on a solution containing 2 mM EGCG dissolved in PBS, pH 7.4 (A) or 6.5 (B) immediately after dissolving the compound (1) or after 72 h (2) of incubation at 37 °C. No significant changes of compound resonances were observed.

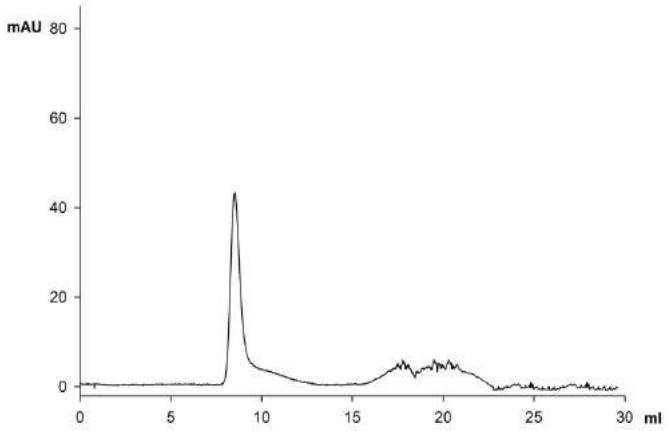

Fig. S3. SEC profiles of aggregated JD. 300 µg JD were loaded onto a Superose 12 10/300 GL column equilibrated in PBS buffer after a 6-d incubation.

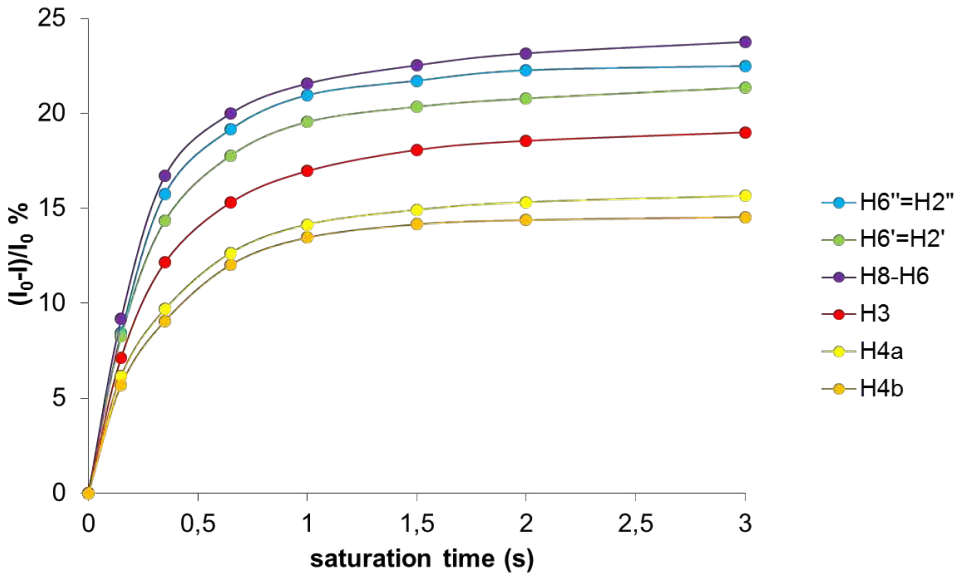

Fig. S4. STD NMR characterization of EGCG/JD oligomer interaction. Fractional STD effect for each non-overlapping signal of EGCG was calculated by $(I_0\text{-}I)/ I_0$, in which $(I_0\text{-}I)$ is the peak intensity in the STD NMR spectrum and I_0 is the peak intensity in the off-resonance spectrum.

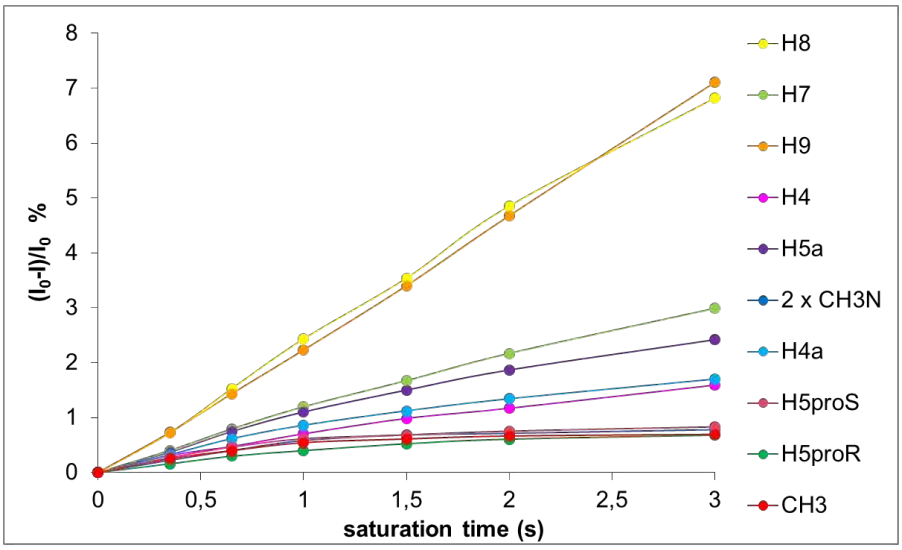

Fig. S5. STD NMR characterization of tetracycline/JD oligomer interaction. Fractional STD effect for each signal of tetracycline was calculated by $(I_0\text{-}I)/ I_0$, in which $(I_0\text{-}I)$ is the peak intensity in the STD NMR spectrum and I_0 is the peak intensity in the off-resonance spectrum.

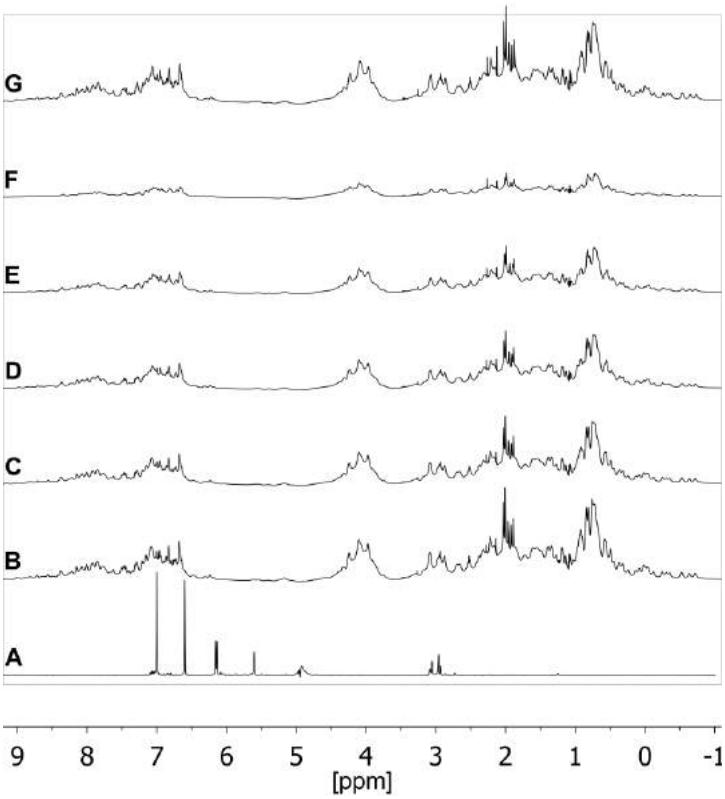

Fig. S6. ^{1}H NMR titration experiments for the characterization of EGCG interaction with JD monomer. ^{1}H NMR spectra recorded in a solution containing (A) 1 mM EGCG, in PBS, pH 6.5 at 25 °C; (B) 0.3 mM ^{15}N-JD in PBS, pH 6.5 at 25 °C; (C) 0.3 mM ^{15}N -JD and 0.15 mM EGCG in PBS, pH 6.5 at 25 °C; (D) 0.3 mM ^{15}N -JD and 0.3 mM EGCG in PBS, pH 6.5 at 25 °C; (E) 0.3 mM ^{15}N -JD and 0.6 mM EGCG in PBS, pH 6.5 at 25 °C; (F) 0.3 mM ^{15}N -JD and 1.2 mM EGCG in PBS, pH 6.5 at 25 °C; (G) 0.3 mM ^{15}N -JD in PBS, pH 6.5, after a 20-h incubation at 25 °C. All the spectra were acquired with 128 transients.

CHAPTER 3

EGCG and related phenol compounds redirect the amyloidogenic aggregation pathway of ataxin-3 towards non-toxic aggregates and prevent toxicity in neural cells and *Caenorhabditis elegans* animal model

3.1 INTRODUCTION

In recent years, plenty of investigations have highlighted the beneficial effects of polyphenols in preventing and/or mitigating several disorders such as cancer, stroke and neurodegenerative diseases (1–3). Polyphenols are a large and diverse class of chemical compounds present in beverages obtained from fruits, vegetables, teas, cocoa and other plants. They are divided into several subclasses, the largest being represented by flavonoids. The latter share a basic structure consisting of two aromatic rings bound together by three carbon atoms that form an oxygenated heterocycle. Catechins, quercetin, myricetin are among the most common flavonoids (4). Fresh tea leaves contain a high amount of catechins, known to constitute 25-35% of the solid green tea extract and consisting of eight related compounds, namely (+)-catechin (C), (−)-epicatechin (EC), (+)-gallocatechin (GC), (−)-epigallocatechin (EGC), (+)-catechingallate (CG), (−)-epicatechin gallate (ECG), (+)-gallocatechin gallate (GCG) and (−)-epigallocatechin-3-gallate (EGCG). EGCG is the most abundant catechin, with an estimated content of about 90 mg per cup of green tea (2.5 g of green tea leaves/200 ml of water), and is thought to make a substantial contribution to the beneficial effects ascribed to this beverage, in particular to its neuroprotective properties (5).

It was formerly believed that EGCG protection against neurotoxicity could be essentially accounted for by its antioxidant activity, with resulting reduction of the harmful effects of oxygen-derived free radicals (6). Actually, oxidative damage and increased accumulation of iron in specific brain areas are considered major pathological features of Parkinson's disease (7), Alzheimer's disease (8) and amyotrophic lateral sclerosis (9), so special interest has been given to the therapeutic potential of nutritional antioxidants in neurodegenerative diseases. More recently, however, EGCG was also shown to directly interfere with amyloid fibril formation from several peptides and proteins and to remodel preformed fibrils, thus generating non-toxic species (10–13). In keeping with this idea, we previously observed that EGCG affects the aggregation pathway of ataxin-3 (ATX3), the protein responsible for spinocerebellar ataxia type 3 (SCA3), by a mechanism similar to that reported for the other mentioned amyloidogenic proteins. Specifically, EGCG interferes with the early steps of ATX3 aggregation, thus leading to the formation of off-pathway, non-toxic, SDS-stable final aggregates (14).

Unfortunately, one major constraint in the employment of EGCG as a pharmaceutical tool is its limited bioavailability, mainly due to poor systemic absorption, especially when administered orally (15). Several factors contribute to this outcome: its

chemical instability at the intestinal pH of 8.5; the time required to cross the mucolytic layer and to be absorbed by the small intestinal epithelial cells; the transporters involved in its transport and the efflux transporters that recycle EGCG back into the lumen of the intestine; finally, the phase II enzymes involved in its transformation (16). EGCG also causes cytotoxicity at high concentrations (17). No less important, it displays a scanty capability to cross the blood-brain barrier (BBB) (18).

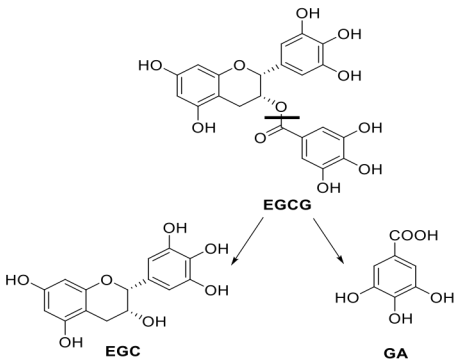

Figure 1. Structure of EGCG, EGC and GA.

Searching for more effective treatments based on the administration of cathechins, we report here a study aimed at assessing the action mechanisms and the neuroprotective effects of also EGC and gallic acid (GA) (Fig.1). This approach is justified by two reasons. First, EGC and GA have simpler structures compared with EGCG, hence they might be less subject to chemical and enzymatic degradation after administration; second, a controlled conjugation of GA to nanodevices is an attainable goal, due to its structural simplicity and the presence of an unesterified carboxyl group, unlike the case of EGC and EGCG. Conjugation of therapeutic compounds to nanodevices offers a considerable advantage, as it makes it possible, in principle, their targeted delivery to the CNS (19,20). Furthermore, the therapeutic potential of GA has been already reported, in that it is capable of inhibiting fibril formation by amyloid β (Aβ) peptide (10), α-synuclein (21) and insulin (22). Additionally, a comparative analysis of the effects of the three mentioned catechins might provide a deeper insight into their action mechanism, particularly at the molecular level.

As already commented for tetracycline and EGCG (Chapter 1, introduction), EGC and GA probably recognize a common structural feature between several proteins undergoing aggregation, instead of a specific pattern in the target protein.

We therefore characterized in parallel the effects of EGCG, EGC and GA on the aggregation mode of both a pathogenic variant of ATX3 carrying 55 consecutive glutamines (ATX3-Q55), and its N-terminal globular domain (Josephin domain, JD). Although the polyglutamine stretch is close at the C-terminus, it has been clearly established that the aggregation process starts at the level of the JD (23,24), which prompted us to analyze the effects of the catechins on also this protein moiety in isolation. We also assessed the neuroprotective effect of EGCG and GA in a transgenic *Caenorhabditis elegans* SCA3 model.

The molecular mechanisms of the interaction between the catechins and ATX3 were mainly investigated by molecular docking simulations, Fourier transform infrared (FTIR) spectroscopy, atomic force microscopy (AFM) and saturation transfer difference (STD) NMR experiments. Our results strongly support the idea that the GA moiety of EGCG is the minimal functional unit, although somewhat less neuroprotective than EGCG itself. Thus, thanks to its substantial stability and structural simplicity, it could be employed in the future development of pharmaceutical nanodevices.

3.2 RESULTS

EGC and GA affect JD and ATX3-Q55 aggregation kinetics and structural features in the same way as EGCG

To evaluate the effect of epigallocatechin (EGC) and gallic acid (GA) on ataxin-3 (ATX3) aggregation, freshly prepared His-tagged JD and ATX3-Q55 (an expanded form carrying 55 consecutive glutamines) were incubated at 37°C in PBS at a final concentration of 100 μM and 25 μM, respectively, in the presence or the absence of EGCG, ECG or GA at a 1:5 molar ratio protein:compound (Fig. 2). Besides a full-length expanded form of the protein, we also analyzed the JD as plenty of data show that the amyloid aggregation process starts from this domain (23-25). Aliquots were taken at different times of incubation and the soluble fraction obtained by centrifugation and pellet removal was analyzed by SDS-PAGE (Fig. 2A and B) and densitometric quantification of the SDS-soluble fraction (Fig. 2C and D). The latter is identified as the protein migrating in monomeric form in the SDS-gel. We confirmed that, for both proteins, EGCG treatment induced a rapid decrease in the SDS-soluble fraction starting from the earliest time of incubation compared with untreated samples (Fig. 2A-D). It also induced the formation of SDS-resistant species that are large and do not enter the separating gel, as previously reported (14,26) (Fig. 2A and B). In the case of JD, the much scantier amount of such species can be only justified by the formation of large aggregates, which are therefore discarded by centrifugation (Fig. 2A).

Furthermore, both EGC and GA promoted a faster decrease in the JD SDS-soluble fraction in comparison with the untreated sample, like in the case of EGCG (Fig. 2A and C), although the latter exerted a much more pronounced effect. At the earliest times (1-6 h of incubation), the decrease in soluble fraction was also paralleled by the appearance of soluble, SDS-resistant species (Fig. 2A).

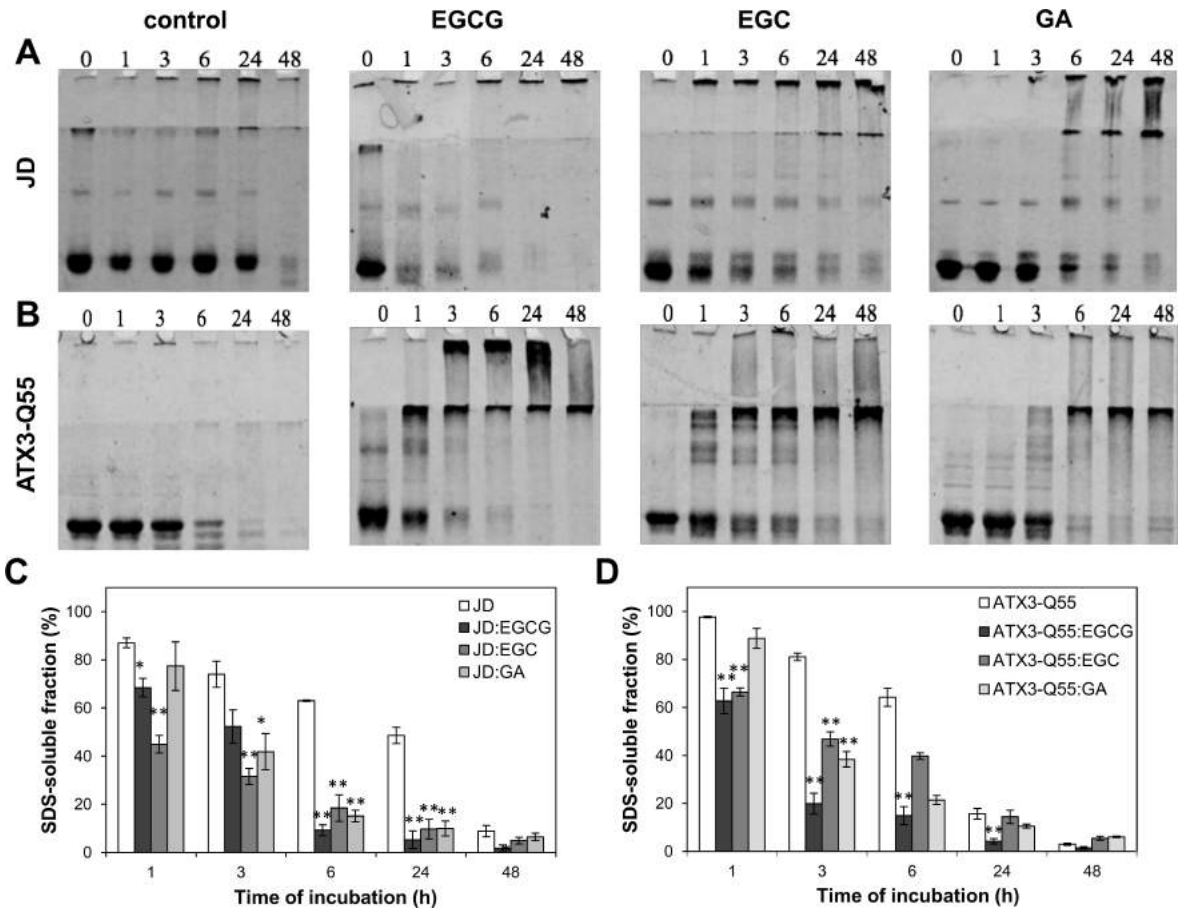

Figure 2. SDS-PAGE analysis of JD and ATX3-Q55 soluble fraction. (A) SDS-PAGE (16%) of the soluble protein fraction obtained by centrifugation of aliquots of 125 μM JD incubated at 37°C in the absence or the presence of EGCG, EGC or GA at a molar ratio protein:compound 1:5. (B) SDS-PAGE (12%) of the soluble protein fraction obtained by centrifugation of aliquots of 25 μM ATX3-Q55 incubated at 37°C in the absence or the presence of EGCG, EGC or GA at a molar ratio protein:compound 1:5. The gels were stained with IRDye Blue Protein Stain (LiCor, USA). (C-D) SDS-soluble protein amounts of JD (C) and ATX3-Q55 (D) were quantified by densitometry. Signals were normalized at t_0 protein content. Error bars represent standard errors and are derived from at least three independent experiments. * $P < 0.05$; ** $P < 0.01$.

Likewise, also in the case of ATX3-Q55, the addition of EGC or GA induced a rapid decrease in the SDS-soluble fraction and the appearance of large, soluble SDS-resistant species but to a lesser extent with respect to EGCG (Fig. 2B and D).

EGCG, EGC and GA drastically affect the structural features of JD and ATX3-Q55 aggregation intermediates

The effects of GA and EGC on JD secondary structure and aggregation were also investigated by Fourier transform infrared (FTIR) spectroscopy and were compared with those of EGCG (Fig. 3). In the Amide I spectral region (1600-1700 cm^{-1}), the second derivative spectrum of the freshly purified JD displayed minima, corresponding to maxima of the absorption spectrum, at ~1635 cm^{-1} and ~1690 cm^{-1}, both assigned to intramolecular β-sheets, and at ~1657 cm^{-1} due to α-helical and random coil structures of the native protein (27). During incubation at 37°C in PBS, the component assigned to the protein native secondary structures decreased in intensity and two new peaks appeared in the

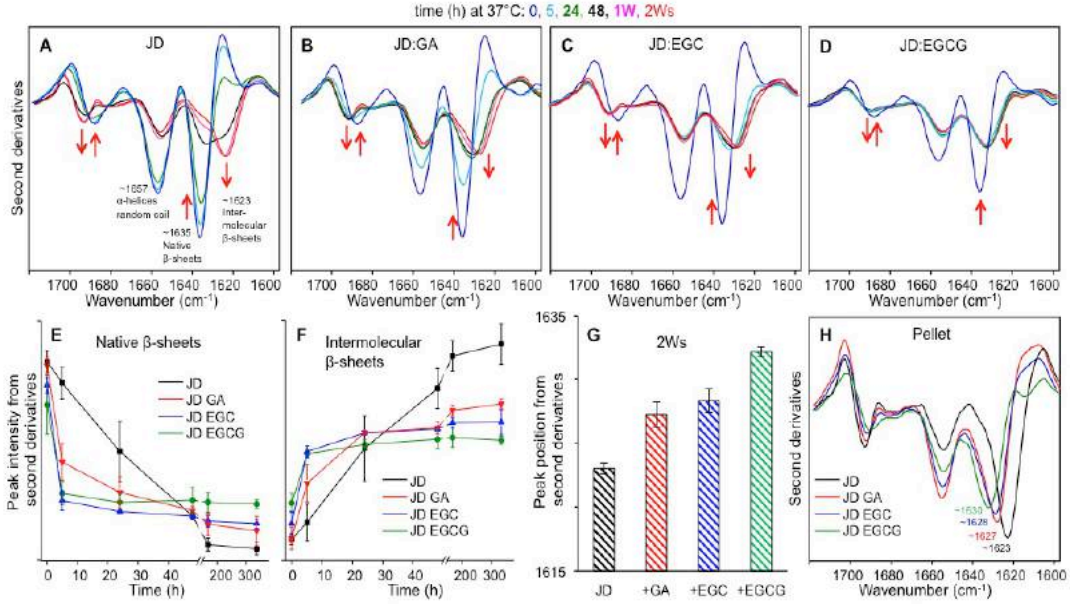

Figure 3. FTIR analyses of the effects of EGCG, EGC and GA on JD misfolding and aggregation. (A-D) Second derivatives of absorption spectra of JD (150 μM) in the presence or the absence of compounds (750 μM), collected at different incubation times in PBS at 37 °C. Peak positions of the main components and their assignment to the protein secondary structures are reported in (A). The arrows point to increasing incubation times. (E) Time course of the component assigned to native β-sheets. (F) Time course of the component assigned to intermolecular β-sheets. (G) Peak position of the component assigned to intermolecular β-sheets taken from second derivatives of spectra collected from JD samples incubated for two weeks (2 ws) at 37 °C in the presence or the absence of compounds. (H) Second derivative spectra of the pellet collected from JD samples incubated for two weeks at 37 °C in the presence or the absence of compounds. Second derivative spectra were normalized at the tyrosine peak at ~1515 cm^{-1}.

spectra at ~1693 cm^{-1} and ~1623 cm^{-1}, in the typical spectral region of intermolecular β-sheets in protein aggregates (Fig. 3A). These results indicate the loss in native secondary structures and the formation of protein aggregates, in agreement with previous reports (26,27). FTIR analysis was also performed in the presence of GA at 1:5 of protein:ligand molar ratio (Fig. 3B). Compared with JD alone, GA induced an earlier intensity decrease of the native β-sheet peak (Fig. 3B and E) and an increase in the intermolecular β-sheet component (Fig. 3B and F), which at the end of the incubation reached a lower intensity compared with the control. Moreover, the peak position of the intermolecular β-sheets was upshifted to ~1627 cm^{-1} in the sample incubated with GA (Fig. 3G and H), suggesting the formation of slightly loosely packed aggregates in the presence of this compound. Similar effects on JD misfolding and aggregation were also observed in the presence of EGC (Fig. 3C and E-H) and, more markedly, in the presence of EGCG (Fig. 3D-H). In a previous work (26), we showed that EGCG is able to induce JD and full-length ATX3 misfolding, leading to the formation of aggregates that are off-pathway with respect to fibrillogenesis. The FTIR analyses here reported indicate that both GA and EGC are able to exert effects similar to those of EGCG on the structural properties of JD aggregation intermediates,

albeit to a reduced extent, with the following order of decreasing efficacy: EGCG>EGC>GA (Fig. 3E-H).

FTIR analyses were also performed on full-length, expanded ATX3-Q55. During incubation at 37°C in the absence of any compound added, the IR peak at ~1635 cm^{-1}, due

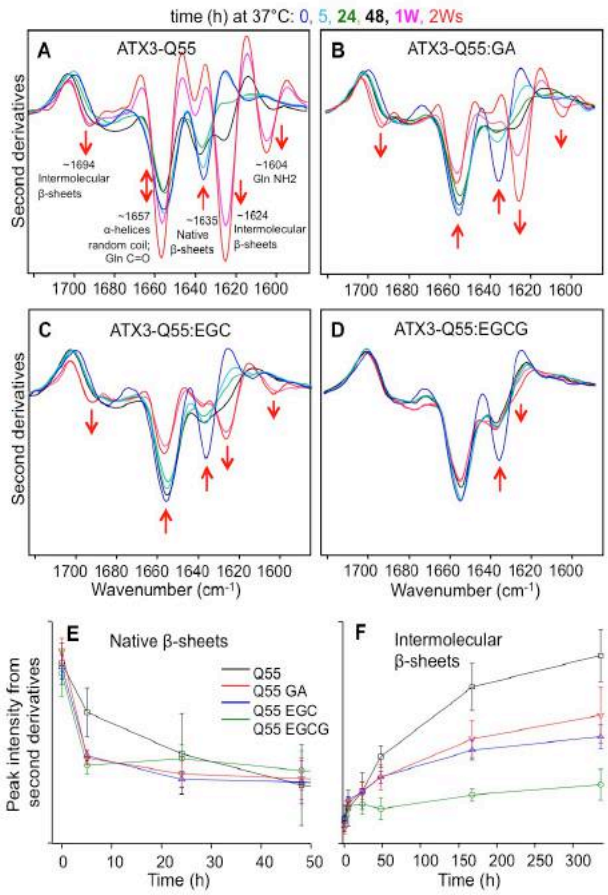

Figure 4. FTIR analyses of the effects of EGCG, EGC and GA on ATX3-Q55 aggregation. **(**A-D) Second derivatives of absorption spectra of ATX3-Q55 (25 µM) in the presence or the absence of compounds (125 µM), collected at different incubation times in PBS at 37°C. The assignment of the main components is reported in (A). The arrows point to increasing incubation times. (E) Time course of the component assigned to native β-sheets. (F) Time course of the component assigned to intermolecular β-sheets. Second derivative spectra were normalized at the tyrosine peak at ~1515 cm^{-1}.

to native β-sheets, decreased in intensity and a new peak appeared at ~1624 cm^{-1} (Fig. 4A). This new component, along with that detected at ~1694 cm^{-1}, has been assigned to the formation of intermolecular β-sheet structures in the protein aggregates (26,27). The ~1657 cm^{-1} component (due to α-helical and random coil structures in the freshly purified protein) decreased in intensity at the beginning of the incubation, then increased again at later times, with a parallel appearance of a new component at ~1604 cm^{-1}. In a previous work (27) we unambiguously assigned the ~1657 cm^{-1} and ~1604 cm^{-1} bands to glutamines involved in strong side chain-side chain (and possibly side chain-backbone) hydrogen bonding in the ATX3-Q55 mature amyloid aggregates. In the presence of GA at a 1:5

protein:compound molar ratio, a faster intensity decrease of the native β-sheet peak at ~1635 cm^{-1} (Fig. 4B and E) was observed in comparison with ATX3-Q55 alone. Moreover, the components assigned to intermolecular β-sheets and side-chain H-bonded glutamines, respectively at ~1624 cm^{-1} and at ~1604 cm^{-1}, in the presence of the compound reached a lower intensity compared with the control (Fig. 4B and F). These results suggest that GA is able to induce a partial unfolding of ATX3-Q55 and to decrease the fraction of the protein forming mature amyloid aggregates. Similar effects on ATX3-Q55 aggregation were observed for EGC at 1:5 of protein:compound molar ratio (Fig. 4C, E, and F). Interestingly, these effects were more evident in the case of EGC compared with GA. In the presence of EGCG at a 1:5 ATX3-Q55:compound molar ratio, the 1635 cm^{-1} component immediately decreased in intensity with a simultaneous appearance of a shoulder at lower wavenumbers, which slightly increased with times (Fig. 4D-F). These results are in agreement with a previous study, whereby it was shown that EGCG induces the formation of ATX3-Q55soluble, SDS-resistant aggregates of ATX3-Q55, with low β-sheet content and without ordered side-chain hydrogen bonding (14). Overall, the FTIR data indicate that GA, EGC, and EGCG are able to induce ATX3-Q55 misfolding, redirecting its fibrillogenic process toward off-pathway aggregates. As in the case of JD, the efficacy of these compounds is in the following order: EGCG>EGC>GA (Fig. 4). Under all conditions, a fraction of the protein formed mature amyloid aggregates with an ordered array of H-bonded glutamine side chains, as indicated by the FTIR spectra of the pellet collected after two weeks incubation at 37 °C of ATX3-Q55 with and without the different compounds (Supplementary information Fig. S1).

EGCG, EGC and GA inhibit ATX33-Q55 fibrillogenesis

Tapping mode atomic force microscopy was employed to obtain information on the effects of EGCG, EGC and GA on ATX3-Q55 aggregate morphology. Figure 6 compares representative images obtained after 48 h aggregation of 25 μM ATX3-Q55 in the absence and in the presence of EGCG, EGC and GA at a molar ratio protein:compound of 1:5. ATX3-Q55 alone formed fibrils arranged into bundles of height between 20 and 60 nm (Fig. 6A), in agreement with previous obervations (14,27). The mean bundle length was 1100 ± 200 nm and the mean bundle height, measured at the middle of the bundle, was 43 ± 8 nm. In the presence of EGCG (Fig. 6B), fibrillation was completely suppressed and clusters of non fibrillar material were observed, with cluster height between 20 and 80 nm

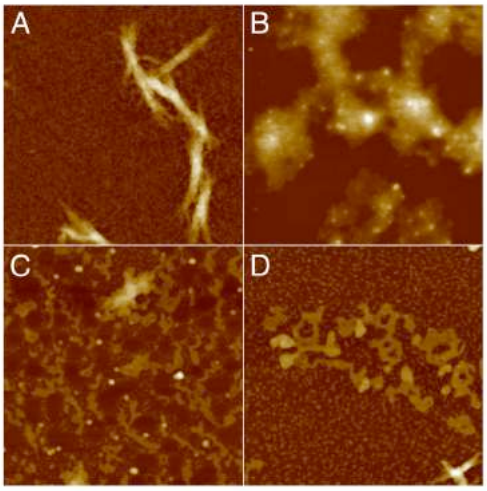

Figure 5. AFM analysis of AT3XQ55 aggregates obtained in absence and in the presence of EGCG, EGC and GA. Tapping mode AFM images (height data) of ATX3Q55 aggregates obtained after 48 h incubation of 25 μM ATX3Q55 in the absence (A) and in the presence of EGCG (B), EGC (C), GA (D) at a molar ratio protein:compound 1:5. Scan size 3.0 μm, Z range 120 nm (A), 50 nm (B), 80 nm (B, C, D).

and typical cluster size in the scan plane of 0.5 – 1 μm, in agreement with previous findings (14).

In the presence of EGC and GA, fibrillation was not completely suppressed. The fibril bundle lengths were 900 ± 100 nm for EGC and 800±200 nm for GA, and the bundle heights were 40±10 nm and 44 ± 10 nm respectively. These results indicate that these compounds were less effective than EGCG. However, in the presence of EGC bundles of modified morphology were often observed (Fig. 6C) and for both EGC and GA, non-fibrillar and relatively flat aggregates of height between 10 and 12 nm were also found (Fig. 6C and D). These results suggest the formation of off-pathway species.

Molecular docking investigations show that EGCG, EGC and GA bind the JD in the same regions

In order to get insight into the binding mode of the ligands EGCG, EGC and GA to the JD, molecular docking investigations were carried out for all ten conformations presented in the 1YZB pdb file (28,29). Our results reveal that the interaction of GA, EGC and EGCG with the protein is non-specific, as supported by the fact that different binding sites were found over the whole surface of JD for all ligands (Fig. 6; Supplementary Material, Fig. S2). We focused our attention on the best pose of each ligand in all JD NMR structures (Table 1).

This analysis highlights for all compounds three binding sites located at the top, middle and bottom regions of the protein, respectively. In the case of GA and EGCG, the best binding site is located in the middle region around the amino acids 120-166 (Fig. 6A and C). This region is involved in the binding event in seven NMR structures, in the case of GA, and in eight NMR structures in the case of EGCG. In contrast, EGC showed a higher affinity for the top and bottom region, around the amino acids 37-78 and 74-118, respectively (Fig. 6B). In such case, EGC binding to the central region was observed in two NMR structures only.

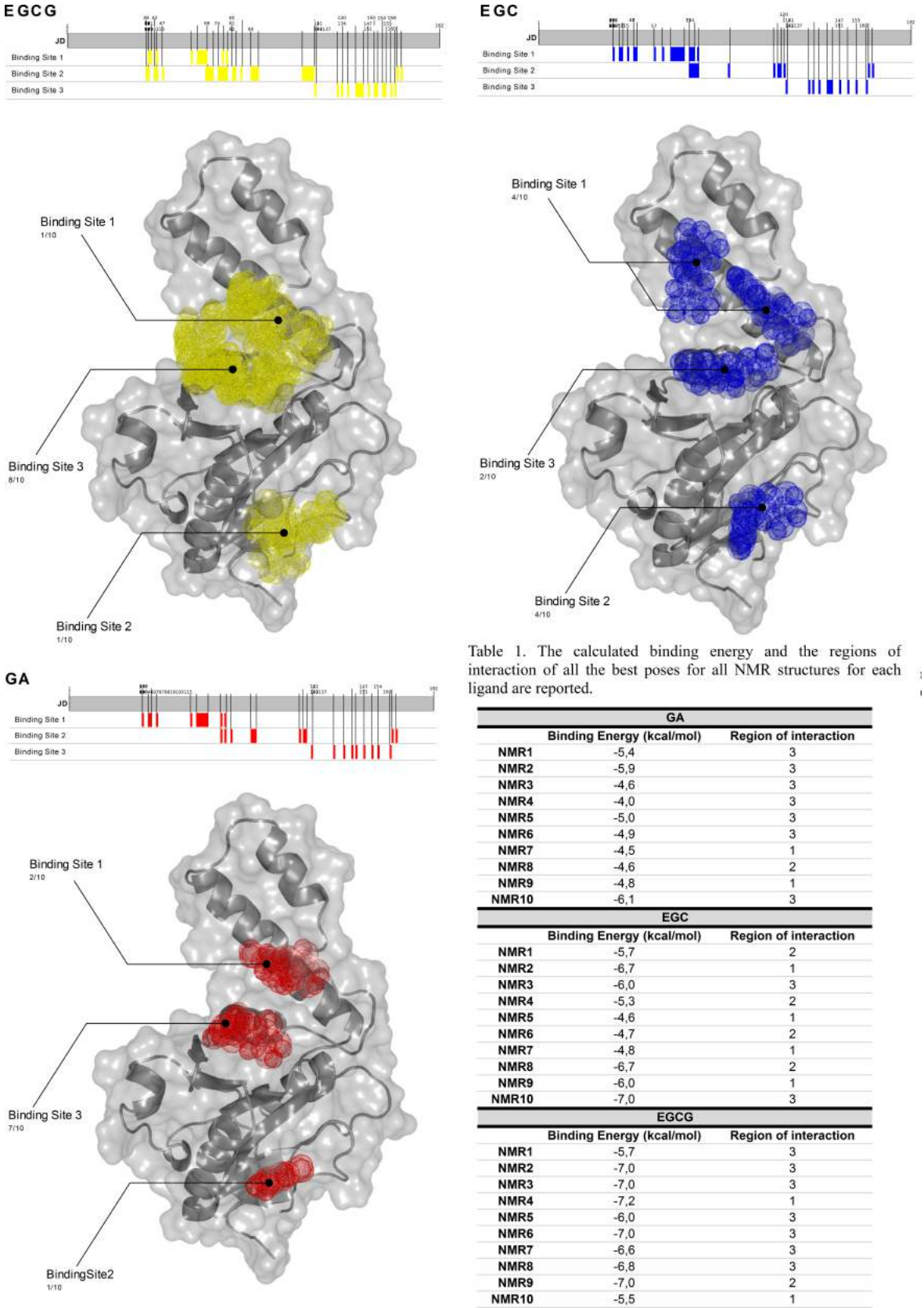

Table 1. The calculated binding energy and the regions of interaction of all the best poses for all NMR structures for each ligand are reported.

	GA	
	Binding Energy (kcal/mol)	**Region of interaction**
NMR1	-5,4	3
NMR2	-5,9	3
NMR3	-4,6	3
NMR4	-4,0	3
NMR5	-5,0	3
NMR6	-4,9	3
NMR7	-4,5	1
NMR8	-4,6	2
NMR9	-4,8	1
NMR10	-6,1	3
	EGC	
	Binding Energy (kcal/mol)	**Region of interaction**
NMR1	-5,7	2
NMR2	-6,7	1
NMR3	-6,0	3
NMR4	-5,3	2
NMR5	-4,6	1
NMR6	-4,7	2
NMR7	-4,8	1
NMR8	-6,7	2
NMR9	-6,0	1
NMR10	-7,0	3
	EGCG	
	Binding Energy (kcal/mol)	**Region of interaction**
NMR1	-5,7	3
NMR2	-7,0	3
NMR3	-7,0	3
NMR4	-7,2	1
NMR5	-6,0	3
NMR6	-7,0	3
NMR7	-6,6	3
NMR8	-6,8	3
NMR9	-7,0	2
NMR10	-5,5	1

Figure 6. Best scoring poses for EGCG (A), EGC (B) and GA (C) docked on JD structure derived from 1YZB-PDB code. Molecular docking was performed with Glide software.

STD NMR analysis provides evidence of EGCG and EGC binding to monomeric JD

To provide experimental evidence of the binding mode of EGCG, EGC and GA to JD, we performed Saturation Transfer Difference (STD) NMR experiments (28,29). STD NMR is a robust method allowing to detect and characterize receptor-ligand interactions in solution, based on the observation of the signals of the small molecule (ligand). In previous works, we have exploited it to characterize the molecular interaction of different natural (30–32) and synthetic ligands (33–35) with amyloid peptide and proteins, including ATX3-Q55 (36) and JD (26).

Here, we have carried out experiments on ligand/protein mixtures dissolved in deuterated phosphate buffer, pH 7.2, 5 °C. The selective saturation of some aliphatic resonances of JD was achieved by irradiating at -1.00 ppm (on-resonance frequency). In fact, when the experimental conditions are chosen properly to assure the absence of direct irradiation of the test compound (verified through blank experiments on a sample containing the potential ligand only), the presence of its NMR signals in the STD spectrum unequivocally indicates its interaction with the receptor. On the other hands, any signal coming from non-binding compounds is erased in the STD spectrum, thus demonstrating that the molecule is not a ligand (Fig. 7).

STD NMR spectra recorded on samples containing 7 μM JD and each of the three potential ligands EGCG, EGC and GA, are depicted in Figures 7B, D and F respectively. In agreement with data reported on the interaction of these compounds with ATX3-Q55 (36), EGCG and EGC are ligands of JD monomers, as demonstrated by the presence of some their resonances in STD spectra B and D, while no evidence of binding to the protein was obtained for GA, whose STD spectrum (Fig. 7F) shows no resonances from this molecule. As GA also has an effect comparable to, although somewhat weaker than that of EGCG and EGC in redirecting amyloid aggregation, we suggest that the failure to detect binding may be accounted for by a weaker interaction by the former.

EGCG, EGC and GA inhibit ATX3-Q55 aggregate toxicity in neural cells

It has been previously reported that the interaction of ATX3-Q55 amyloid aggregates with neural cell membranes induces an increase in membrane permeability, resulting in the disruption of calcium homeostasis and subsequent cytotoxicity (37). To test the ability of EGCG, EGC and GA to inhibit such cytotoxic effectsATX3-Q55, rat cerebellar granule cells were loaded with the calcium-sensitive fluorescent dye Oregon Green, to monitor

calcium influx induced by protein aggregates. Cells were incubated for 24 h with 48 h-aged ATX3-Q55 aggregates formed in the absence or the presence of EGCG, EGC and GA. Figure 8 reports the corresponding fluorescence increase, resulting from calcium influx, measured with respect to control cells incubated without protein aggregates. In the presence of EGC or EGC, the increase in intracellular calcium levels elicited by protein aggregates was completely suppressed. However, even GA reduced calcium influx by as much as 75%.

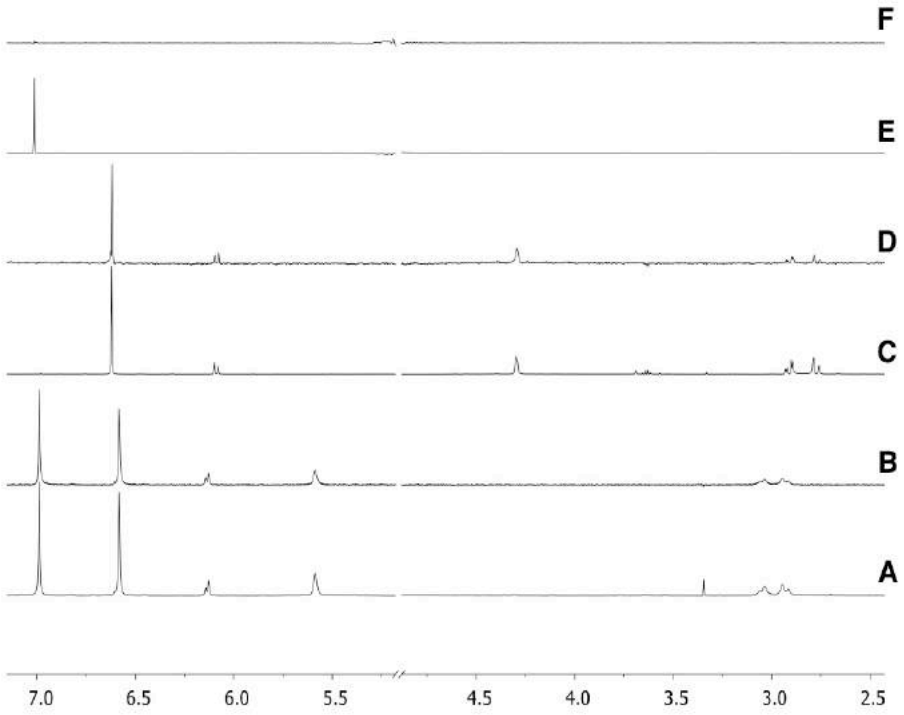

Figure 7. STD NMR characterization of EGCG, EGC and GA to JD. (A) ^{1}H NMR spectrum of a mixture containing JD (7 μM) and 1.5 mM EGCG. (B) STD NMR spectrum of the same mixture of spectrum A at a saturation time of 3 s. (C) ^{1}H NMR spectrum of a mixture containing JD (7 μM) and 1.5 mM EGC. (D) STD NMR spectrum of the same mixture of spectrum C at a saturation time of 3 s. (E) ^{1}H NMR spectrum of a mixture containing JD (7 μM) and 1.5 mM GA. (F) STD NMR spectrum of the same mixture of spectrum E at a saturation time of 3 s. All the samples were dissolved in PBS solution, pH 7.2, 5 °C. The spectrometer frequency was 600 MHz. The EGCG H_2 signal is overlapped by water resonance.

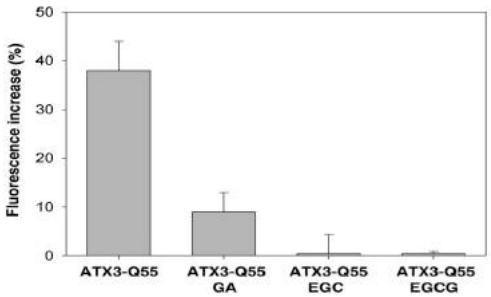

I

Figure 8. Fluorescence analysis of the effect of EGCG, ECG and GA on ATX3-Q55 aggregate toxicity in primary neuronal cells. Oregon Green fluorescence increase, indicating Ca^{2+} influx, recorded in rat cerebellar granule neurons after 24 h incubation with 48 h aged ATX3-Q55 aggregates obtained in the absence or the presence of EGCG, EGC, GA. Fluorescence changes were measured with respect to control cells incubated without protein aggregates.

EGCG, EGC and GA ameliorate the pathological phenotype of a SCA3 *C. elegans* model

A SCA3 *C. elegans* model was used to evaluate the effects of EGCG, EGC and GA on worm pathological phenotype. A wild type variant (ATX3Q17-GFP) and a pathological one (ATX3Q130-GFP) were expressed in the nervous system in fusion with GFP and under the control of the *unc-119* promoter. Wild type Bristol N2 strain was used as a control. The compounds were directly added to *E. coli* OP50 suspension used to feed worms. Their effect was evaluated by monitoring life span and quantifying body bends frequency after 24 h (Fig. 9A) and 48 h (Fig. 9B) of incubation. None of these compounds was able to increase in a statistically significant manner worms' survival (data not shown).

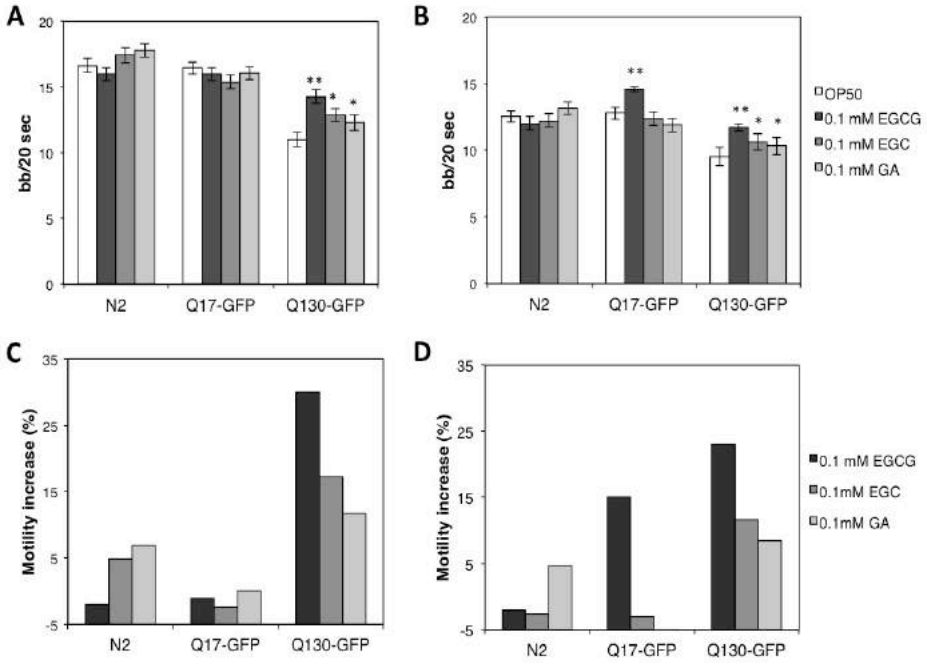

Figure 9. Pharmacological assay on ATX3 transgenic worms. One-day synchronized adult worms were placed on a plate seeded with *E. coli* in the presence or the absence of 0.1 mM EGCG, EGC or GA, and cultured at 25 °C. Number of body bends/20 sec were scored after 24 h (A) and 48 h (B) of treatment. Data were also expressed as percentage of motility increase with respect to the untreated animals after 24 h (C) and 48 h (D) of treatment. Error bars represent standard errors. Plots are representative of at least three independent experiments. * $P < 0.05$; ** $P < 0.001$

However, after 24 h of treatment, all compounds promoted a statistically significant increase in worm mobility in the Q130-GFP strain with respect to untreated worms. This increment was 30, 17 and 12 % in the presence of EGCG, EGC and GA, respectively (Fig. 9C). A statistically significant increase in mobility was also observed after 48 h of treatment in Q130-GFP strain (25, 12, 8 % in the presence of EGCG, EGC and GA respectively, Fig. 9D).

3.3 DISCUSSION

In a previous report we demonstrated EGCG capability to redirect ATX3 aggregation pathway towards non-amyloid, non-toxic aggregates and to ameliorate the ataxic phenotype of *C. elegans* (14). However, in view of its employment as a drug for the treatment of the relevant disease, its major flaw is that it can undergo chemical modifications with resulting loss of antiamyloid efficacy and scanty bioavailability (15,16). This prompted us to assay the efficacy of simpler compounds, yet structurally related to EGCG, *i.e.*, EGC and GA. Furthermore, simpler structures should make possible, in principle, to easily accomplish their derivatization to specific vectors, such as nanoparticles, with enhanced brain delivery (35,38). This prompted us to perform an extensive characterization of their action at the molecular and cellular level, as well as on the *C. elegans* animal model.

In particular, we analyzed the effects of the three compounds on expanded ATX3-Q55 and JD aggregation, the latter being assayed because of its well-known involvement in the earliest events of aggregation (23–25). On the whole, our SDS-PAGE and FTIR analyses have clearly shown that the effects exerted by the three compounds on ATX3 amyloidogenesis are qualitatively similar, as all of them redirect the aggregation process towards soluble, SDS-resistant and non-amyloid off-pathway aggregates. In particular, FTIR spectra collected during the progress of ATX3-Q55 aggregation showed the absence of the 1604 cm^{-1} peak, assigned to glutamine side-chain hydrogen bond network, which is the hallmark of amyloid aggregation of proteins carrying expanded polyglutamine stretches (14). AFM data also support this hypothesis in that clear morphological differences were observed between aggregates generated by ATX3-Q55 in the presence or the absence of the compounds. Indeed, all treatments resulted in formation of clusters of non-fibrillar material. Nevertheless, the data show a different efficacy among the treatments with the following order: EGCG>EGC>GA.

To better understand the mode by which the three compounds prevent amyloidogenesis, we also performed molecular docking and NMR analyses on the JD. Molecular docking analyses on the JD highlighted three interacting regions which point to a non-specific binding mode. All three compounds bound to each of them, although with different patterns. Noteworthy, all three compounds bound to the previously identified aggregation-prone regions (APR) (23,24).

STD NMR confirmed that EGCG and EGC are capable to bind to the monomeric form of the protein, whereas the failure of detecting GA binding is quite likely due to a

weaker and/or transient interaction by this compound. A previous work reports a similar failure to detect in NMR spectroscopy the interaction of this compound with monomeric α-synuclein (39). Overall, these results provide a possible interpretation of the mechanism by which these compounds prevent ATX3 fibrillogenesis, given their capability of directly binding to the APR, which suggests that the interaction occurs at the very beginning of the aggregation process.

Provided that the compounds antiamyloid action relies upon their capability of preventing intermolecular interactions among APR, a still unanswered issue is how this initial effect give rises to non-amyloid aggregates. Wobst and coworkers recently reported that EGCG can prevent the tau protein aggregation into toxic oligomers (40), whereby they also observed that such capability interferes with the formation of β-sheet-rich oligomeric tau species. Thus, it might be that EGCG's primary effect on the APR, and/or subsequent as yet unidentified interactions, results in an altered pattern of β-sheet formation, as actually showed by our FTIR data. It should be also mentioned, however, that, according to a recent analysis on fourteen disease-related proteins and peptides, EGCG would bind to cross-ß sheet aggregation intermediates (41). Thus, the case of ATX3 does not conform to this generally observed pattern, given the capability of the compound to first bind to monomeric protein, as actually also reported for other proteins (42).

Noteworthy, tetracycline, another well-known antiamyloid agent, was proven to interfere with ATX3 fibrillogenesis and prevent toxicity by a substantially different mechanism compared with that displayed by EGCG, EGC and GA. In fact, tetracycline did not change the structural features of the aggregated species, but drastically increased their solubility (14). This effect is mediated by its capability to only bind oligomers (26), in keeping with our docking results that did not detect any possible binding mode between the antibiotic and JD in monomeric form (unpublished results).

The protective effect of the three compounds was demonstrated *in vivo* using both neural cells and the *C. elegans* animal model. In the first approach, we preincubated ATX3-Q55 with EGCG, EGC and GA, which resulted in the formation of aggregates displaying a substantially lower calcium-mediated cytotoxicity, compared with those formed by the untreated protein. Furthermore, all three compounds ameliorated the pathological phenotype of diseased worms, as shown by their improvement in locomotion. Both experimentations also confirmed the aforementioned order of efficacy, *i.e.*, EGCG>EGC>GA. It should be stressed, nevertheless, that even GA displayed a significant capability of preventing cytotoxicity.

As regards the mechanisms underlying the effects detected, the protective action on neural cells must be only fulfilled via prevention of toxic amyloid aggregates formation. In contrast, the outcome detected in *C. elegans* quite likely results from a combination of effects exerted at the cellular level, along with those specifically acting on aggregate formation. This hypothesis is in agreement with other literature reports, wherein the cytoprotective role of phenolic compounds mainly occurs via protection against oxidative stress and/or autophagy stimulation (43–45).

In conclusion, we have demonstrated that EGC and GA display a mechanism of action similar to that observed for EGCG, irrespective of whether they act at the molecular, cellular, or whole animal level. However, we observed a different efficacy by the three compounds, as above outlined. It is worthwhile to mention that GA represents the minimal functional unit of EGCG and, in general, of related phenolic compounds. This finding stimulates our interest in GA-mediated effects because, due to its relatively simple structure, it is suitable for conjugation to nanovectors, which may be bound to molecules enabling them to cross the blood brain barrier.

3.4 MATERIALS AND METHODS

ATX3 purification. ATX3-Q55 cDNA was previously subcloned in the pQE30 vector and the protein expressed in the *Escherichia coli* strain SG13009 (*E. coli* K12 Nals, StrS, RifS, Thi2, Lac2, Ara+, Gal+, Mtl2, F2, RecA+, Uvr+, Lon+; Qiagen Hamburg GmbH, Hamburg, Germany) as His-tagged protein (Natalello et al. 2011). JD cDNA was previously subcloned in pET21a vector and the protein expressed in the *E. coli* strain BL21 Tuner (DE3) pLacI (*E. coli* B F^- ompT hsdSB (rB^- mB^-) gal dcm lacY1(DE3) pLacI (CamR); Novagen, Germany) as His-tagged protein. Proteins were purified as previously described (14,26).

SDS-PAGE and densitometry analysis of soluble protein fraction. Freshly purified ATX3-Q55 (25 μM) or JD (150 μM) was incubated at 37°C in PBS solution (25 mM potassium phosphate, pH 7.2, 150 mM NaCl) in the presence or the absence of EGCG, EGC or GA (Sigma-Aldrich Inc., St Louis, MO, USA) at a protein:compound molar ratio of 1:5. Protein aliquots at different times of incubation (0, 1, 3, 6, 24, 48, and 72 h) were centrifuged 15 min at 14000 *x g* and 10 μL for the expanded form or 3 μL for the JD of the supernatants were subjected to SDS-PAGE. The gels were stained with IRDye Blue Protein Stain (LiCor Biosciences, Lincoln, NE, USA), scanned at 700 nm with the

Odyssey Fc System and analyzed with the Image Studio software (LiCor Biosciences, Lincoln, NE, USA).

FTIR spectroscopy. FTIR analyses were performed using a previously optimized approach (14,26,27,46). Briefly, 2 µL of the sample solution, taken at different times of incubation at 37 °C in PBS, were deposited on the diamond surface of the single reflection device (Quest, Specac, UK) for measurements in Attenuated Total Reflection (ATR). After solvent evaporation, in order to obtain a protein hydrated film, the ATR/FTIR spectra were collected using a Varian 670-IR spectrometer (Varian Australia Pty Ltd, Mulgrave, VIC, Australia) equipped with a nitrogen-cooled mercury cadmium telluride detector under the following conditions: 2 cm^{-1} spectral resolution, 25 kHz scan speed, 1000 scans co-addition and triangular apodization. The protein spectra were obtained by subtraction of the proper reference spectra (14,27). Second derivatives of the spectra were obtained after Savitzky-Golay smoothing. Spectra collection and analyses were performed using the ResolutionsPro software (Varian Australia Pty Ltd, Mulgrave, VIC, Australia).

Atomic Force Microscopy (AFM). ATX3-Q55 was incubated at 37 °C in PBS buffer at a concentration of 25 µM in the presence or the absence of EGCG, ECG or GA at a molar ratio protein:compound of 1:5. At fixed aggregation times, a 10 µl aliquot was withdrawn, incubated on a freshly cleaved mica substrate for 5 min, then rinsed with Milli-Q water and dried under mild vacuum. AFM images were acquired in tapping mode in air using a Multimode Scanning Probe Microscope equipped with ‘‘E’’ scanning head (maximum scan size 10 µm) and driven by a Nanoscope V controller (Bruker). Single beam uncoated silicon cantilevers (type OMCL-AC160TS, Olympus) were used. The drive frequency was between 270 and 320 kHz, the scan rate between 0.25 and 0.5 Hz. Aggregate size was measured from the cross-sections of topographic AFM images. Errors were calculated according to Student’s statistics assuming a confidence level of 95%.

Docking analysis. The NMR resolved three-dimensional structure of JD protein was retrieved from the protein data bank (PDB ID: 1YZB) (47,48). Docking analysis were performed using Glide software from Schrödinger suite (49). All 10 NMR conformations of the PDB file were used in the docking procedure. The ligands EGCG, EGC and GA were prepared with the specific tool LigPrep, generating any possible protonated states at

pH 7.2± 0.2. The XP Scoring function was used to score and rank of the compounds poses (49).

NMR analysis. NMR experiments were recorded on a Bruker 600 MHz Avance III equipped with a QCI cryo-probe, with a z-axis gradient coil. EGCG EGC and GA were dissolved in PBS, pH 7.2 and an aliquot of protein solution, dissolved in the same buffer, was added to reach the final concentration required. Basic sequences were employed for ^{1}H and STD-NMR experiments.
Solvent suppression was performed by excitation sculpting. ^{1}H spectra were acquired with 128 scans and 2 s recycle delay. For STD-NMR experiments, a train of Gaussian-shaped pulses each of 50 ms was employed to saturate selectively the protein envelope; the total saturation time of the protein envelope was varied between 3 s and 0.15 s, 1024 scans; acquisitions were performed at 5 °C.

Granule cell preparation. Sprague-Dawley rats were housed in the animal facility of the Department of Pharmacy, Section of Pharmacology and Toxicology of Genoa University. Experimental procedures and animal care complied with the EU Parliament and Council Directive of 22 September 2010 (2010/63/EU) and were approved by the Italian Ministry of Health (protocol number 2207) in accordance with D.M. 116/1992. All efforts were made to minimize animal suffering and to use the minimum number of animals necessary to produce reliable results. Granule cells were prepared from cerebella of 7-8 day old rats as previously described (50). The cells were plated at a density of $1x10^{6}$ per dish on 20 mm poly-L-lysine-coated glass coverslips and maintained in Basal Eagle's culture medium, containing 10% fetal calf serum, 100 μg/ml gentamicin and 25 mM KCl, at 37 °C in a humidified 95% air, 5% CO_2 atmosphere. Cultures were treated with 10 μM cytosine arabinoside from day 1 in order to minimize proliferation of non-neuronal cells. Experiments were performed in cultures between days 6 and 10 after plating.

Intracellular Ca^{2+} concentration measurements in rat cerebellar granule cells. Granule cells were incubated at 37 °C for 40 min in a 6 μM solution of the cell-permeant AM ester of Oregon Green (Molecular Probes, Eugene, OR) and then washed several times with washing solution (135 mM NaCl, 5.4 mM KCl, 1.8 mM $CaCl_2$, 1.0 mM $MgCl_2$, 5.0 mM Hepes, 10 mM glucose, pH 7.4). Then they were transferred to a recording chamber mounted onto a Nikon Eclipse TE300 inverted microscope. Cells were visualized using a

×100 objective in oil (N.A. 1.3) as previously described (51). The fluorescence signal was detected using a Hamamatsu digital CCD camera with a 450–490 nm excitation filter, a 505 nm dichroic mirror, and a 520 nm emission filter (Nikon Italia, Florence, Italy). Images were acquired with the Simple PCI software (Hamamatsu, Sewickley, PA). Fluorescence intensity was calculated in arbitrary units by building a scale of the pixel intensity located in the region of interest. Fluorescence intensity changes were calculated as

$(F - F_0) \times 100/F_0$

where F is the fluorescence intensity measured with protein aggregated for 24 h after treatment and F_0 the basal fluorescence level (Fig. S3).

C. elegans strains and maintenance. ATX3Q17 and ATX3Q130 cDNAs were previously cloned in pPDP 95.77 vector as GFP fusion protein under control of pan neural *unc-119* promoter as reported in (14). Bristol N2 wild type was used as control. Worms were cultured at 25 °C on solid nematode growth medium (NGM: 50 mM NaCl, 2.5 g/L peptone, 17 g/L agar; 1 mM $CaCl_2$, 1 mM $MgSO_4$, 5 μg/ml cholesterol in ethanol) and seeded with *E. coli* as food source, according to the standard procedure (52).

Worms age synchronization. To generate an age-synchronized population, a small plate (3 ml) of nematodes was transferred onto a new large plate (25 ml) to obtain many eggs. After 2 d, the population was collected in 2.5 ml of M9 buffer (42 mM Na_2HPO_4, 22 mM KH_2PO_4, 86 mM NaCl, 1 mM $MgSO_4$) and an equal volume of 4% glutaraldehyde was added. After 4 h of incubation at 4 °C, the suspension was centrifuged 5 min at 1500 *g*. The eggs were washed twice in M9 buffer and plated in the half uninoculated sector of a moon large plate (plate seeded with *E. coli* OP50 only in half section of plate) (52). Fluorescent ATX3Q17 and ATX3Q130 worms were selected using SteREO Discovery.V12 (Zeiss, Oberkochen, Germany).

Pharmacological assay. One day-synchronized adult worms were placed onto a new plate in the presence or in the absence of 0.1 mM EGCG, EGC or GA. All compounds were added on the *E. coli* OP50 suspension before seeding the plates. Body bends were recorded for 20 sec after 24 and 48 h of treatment. For each treatment, at least 20 worms were used.

3.5 CANDIDATE'S CONTRIBUTION

The candidate performed the aggregation assays and the relevant SDS-PAGE and compound validation on *C. elegans* model. She also prepared the protein for FT-IR[*], AFM[$], Calcium influx[$] and NMR analyses[§] (performed in collaboration with: Dr. Antonino Natalello[*]; Prof. Annalisa Relini[$]; Dr. Cristina Airoldi[§]). Docking analyses were performed in collaboration with Prof. Luca De Gioia and coworkers. The candidate contributed to statistical analyses.

3.6 REFERENCES

1. Butterfield D, Castegna A, Pocernich C, Drake J, Scapagnini G, Calabrese V. Nutritional approaches to combat oxidative stress in Alzheimer's disease. J Nutr Biochem. 2002 Aug;13(8):444.

2. Götz ME, Künig G, Riederer P, Youdim MB. Oxidative stress: free radical production in neural degeneration. Pharmacol Ther. 1994;63(1):37–122.

3. Halliwell B. Role of free radicals in the neurodegenerative diseases: therapeutic implications for antioxidant treatment. Drugs Aging. 2001;18(9):685–716.

4. Pandey KB, Rizvi SI. Plant Polyphenols as Dietary Antioxidants in Human Health and Disease. Oxid Med Cell Longev. 2009;2(5):270–8.

5. Higdon JV, Frei B. Tea catechins and polyphenols: health effects, metabolism, and antioxidant functions. Crit Rev Food Sci Nutr. 2003;43(1):89–143.

6. Choi YT, Jung CH, Lee SR, Bae JH, Baek WK, Suh MH, et al. The green tea polyphenol (-)-epigallocatechin gallate attenuates beta-amyloid-induced neurotoxicity in cultured hippocampal neurons. Life Sci. 2001 Dec 21;70(5):603–14.

7. Götz ME, Freyberger A, Riederer P. Oxidative stress: a role in the pathogenesis of Parkinson's disease. J Neural Transm Suppl. 1990;29:241–9.

8. Weinreb O, Mandel S, Amit T, Youdim MBH. Neurological mechanisms of green tea polyphenols in Alzheimer's and Parkinson's diseases. J Nutr Biochem. 2004 Sep;15(9):506–16.

9. Xu Z, Chen S, Li X, Luo G, Li L, Le W. Neuroprotective effects of (-)-epigallocatechin-3-gallate in a transgenic mouse model of amyotrophic lateral sclerosis. Neurochem Res. 2006 Oct;31(10):1263–9.

10. Bastianetto S, Yao Z-X, Papadopoulos V, Quirion R. Neuroprotective effects of green and black teas and their catechin gallate esters against beta-amyloid-induced toxicity. Eur J Neurosci. 2006 Jan;23(1):55–64.

11. Masuda M, Suzuki N, Taniguchi S, Oikawa T, Nonaka T, Iwatsubo T, et al. Small molecule inhibitors of alpha-synuclein filament assembly. Biochemistry (Mosc). 2006 May 16;45(19):6085–94.

12. Ehrnhoefer DE, Duennwald M, Markovic P, Wacker JL, Engemann S, Roark M, et al. Green tea (-)-epigallocatechin-gallate modulates early events in huntingtin misfolding and reduces toxicity in Huntington's disease models. Hum Mol Genet. 2006 Sep 15;15(18):2743–51.

13. Ferreira N, Cardoso I, Domingues MR, Vitorino R, Bastos M, Bai G, et al. Binding of epigallocatechin-3-gallate to transthyretin modulates its amyloidogenicity. FEBS Lett. 2009 Nov 19;583(22):3569–76.

14. Bonanomi M, Natalello A, Visentin C, Pastori V, Penco A, Cornelli G, et al. Epigallocatechin-3-gallate and tetracycline differently affect ataxin-3 fibrillogenesis and reduce toxicity in spinocerebellar ataxia type 3 model. Hum Mol Genet. 2014 Dec 15;23(24):6542–52.

15. Cabrera C, Artacho R, Giménez R. Beneficial effects of green tea--a review. J Am Coll Nutr. 2006 Apr;25(2):79–99.

16. Gawande S, Kale A, Kotwal S. Effect of nutrient mixture and black grapes on the pharmacokinetics of orally administered (-)epigallocatechin-3-gallate from green tea extract: a human study. Phytother Res PTR. 2008 Jun;22(6):802–8.

17. Siddiqui IA, Adhami VM, Bharali DJ, Hafeez BB, Asim M, Khwaja SI, et al. Introducing nanochemoprevention as a novel approach for cancer control: proof of principle with green tea polyphenol epigallocatechin-3-gallate. Cancer Res. 2009 Mar 1;69(5):1712–6.

18. Ferri P, Angelino D, Gennari L, Benedetti S, Ambrogini P, Del Grande P, et al. Enhancement of flavonoid ability to cross the blood-brain barrier of rats by co-administration with α-tocopherol. Food Funct. 2015 Feb;6(2):394–400.

19. Kreuter J. Nanoparticulate systems for brain delivery of drugs. Adv Drug Deliv Rev. 2001 Mar 23;47(1):65–81.

20. Masserini M. Nanoparticles for Brain Drug Delivery. Int Sch Res Not. 2013 May 21;2013:e238428.

21. Liu Y, Carver JA, Calabrese AN, Pukala TL. Gallic acid interacts with α-synuclein to prevent the structural collapse necessary for its aggregation. Biochim Biophys Acta. 2014 Sep;1844(9):1481–5.

22. Jayamani J, Shanmugam G. Gallic acid, one of the components in many plant tissues, is a potential inhibitor for insulin amyloid fibril formation. Eur J Med Chem. 2014 Oct 6;85:352–8.

23. Scarff CA, Almeida B, Fraga J, Macedo-Ribeiro S, Radford SE, Ashcroft AE. Examination of Ataxin-3 (atx-3) Aggregation by Structural Mass Spectrometry Techniques: A Rationale for Expedited Aggregation upon Polyglutamine (polyQ) Expansion. Mol Cell Proteomics MCP. 2015 May;14(5):1241–53.

24. Lupton CJ, Steer DL, Wintrode PL, Bottomley SP, Hughes VA, Ellisdon AM. Enhanced Molecular Mobility of Ordinarily Structured Regions Drives Polyglutamine Disease. J Biol Chem. 2015 Oct 2;290(40):24190–200.

25. Masino L, Nicastro G, Calder L, Vendruscolo M, Pastore A. Functional interactions as a survival strategy against abnormal aggregation. FASEB J Off Publ Fed Am Soc Exp Biol. 2011 Jan;25(1):45–54.

26. Bonanomi M, Visentin C, Natalello A, Spinelli M, Vanoni M, Airoldi C, et al. How Epigallocatechin-3-gallate and Tetracycline Interact with the Josephin Domain of Ataxin-3 and Alter Its Aggregation Mode. Chem Weinh Bergstr Ger. 2015 Dec 7;21(50):18383–93.

27. Natalello A, Frana AM, Relini A, Apicella A, Invernizzi G, Casari C, et al. A major role for side-chain polyglutamine hydrogen bonding in irreversible ataxin-3 aggregation. PloS One. 2011;6(4):e18789.

28. Nicastro G, Menon RP, Masino L, Knowles PP, McDonald NQ, Pastore A. The solution structure of the Josephin domain of ataxin-3: structural determinants for molecular recognition. Proc Natl Acad Sci U S A. 2005 Jul 26;102(30):10493–8.

29. Nicastro G, Habeck M, Masino L, Svergun DI, Pastore A. Structure validation of the Josephin domain of ataxin-3: conclusive evidence for an open conformation. J Biomol NMR. 2006 Dec;36(4):267–77.

30. Mayer M, Meyer B. Charakterisierung von Ligandenbindung durch Sättigungstransfer-Differenz-NMR-Spektroskopie. Angew Chem. 1999 Jun 14;111(12):1902–6.

31. Mayer M, Meyer B. Characterization of Ligand Binding by Saturation Transfer Difference NMR Spectroscopy. Angew Chem Int Ed. 1999 Jun 14;38(12):1784–8.

32. Airoldi C, Colombo L, Manzoni C, Sironi E, Natalello A, Doglia SM, et al. Tetracycline prevents Aβ oligomer toxicity through an atypical supramolecular interaction. Org Biomol Chem. 2011 Jan 21;9(2):463–72.

33. Airoldi C, Sironi E, Dias C, Marcelo F, Martins A, Rauter AP, et al. Natural compounds against Alzheimer's disease: molecular recognition of Aβ1-42 peptide by Salvia sclareoides extract and its major component, rosmarinic acid, as investigated by NMR. Chem Asian J. 2013 Mar;8(3):596–602.

34. Guzzi C, Colombo L, Luigi AD, Salmona M, Nicotra F, Airoldi C. Flavonoids and Their Glycosides as Anti-amyloidogenic Compounds: Aβ1-42 Interaction Studies to Gain New Insights into Their Potential for Alzheimer's Disease Prevention and Therapy. Chem Asian J. 2017 Jan 3;12(1):67–75.

35. Airoldi C, D'Orazio G, Richichi B, Guzzi C, Baldoneschi V, Colombo L, et al. Structural Modifications of cis-Glycofused Benzopyran Compounds and Their Influence on the Binding to Amyloid-β Peptide. Chem Asian J. 2016 Jan;11(2):299–309.

36. Airoldi C, Cardona F, Sironi E, Colombo L, Salmona M, Silva A, et al. cis-Glyco-fused benzopyran compounds as new amyloid-β peptide ligands. Chem Commun Camb Engl. 2011 Oct 7;47(37):10266–8.

37. Airoldi C, Zona C, Sironi E, Colombo L, Messa M, Aurilia D, et al. Curcumin derivatives as new ligands of Aβ peptides. J Biotechnol. 2011 Dec 20;156(4):317–24.

38. Sironi E, Colombo L, Lompo A, Messa M, Bonanomi M, Regonesi ME, et al. Natural Compounds against Neurodegenerative Diseases: Molecular Characterization of the Interaction of Catechins from Green Tea with Aβ1–42, PrP106–126, and Ataxin-3 Oligomers. Chem – Eur J. 2014 Oct 13;20(42):13793–800.

39. Pellistri F, Bucciantini M, Invernizzi G, Gatta E, Penco A, Frana AM, et al. Different ataxin-3 amyloid aggregates induce intracellular Ca(2+) deregulation by different mechanisms in cerebellar granule cells. Biochim Biophys Acta. 2013 Dec;1833(12):3155–65.

40. Cupaioli FA, Zucca FA, Boraschi D, Zecca L. Engineered nanoparticles. How brain friendly is this new guest? Prog Neurobiol. 2014 Sep;119-120:20–38.

41. Ardah MT, Paleologou KE, Lv G, Abul Khair SB, Kazim AS, Minhas ST, et al. Structure activity relationship of phenolic acid inhibitors of α-synuclein fibril formation and toxicity. Front Aging Neurosci. 2014;6:197.

42. Wobst HJ, Sharma A, Diamond MI, Wanker EE, Bieschke J. The green tea polyphenol (-)-epigallocatechin gallate prevents the aggregation of tau protein into toxic oligomers at substoichiometric ratios. FEBS Lett. 2015 Jan 2;589(1):77–83.

43. Andrich K, Bieschke J. The Effect of (-)-Epigallo-catechin-(3)-gallate on Amyloidogenic Proteins Suggests a Common Mechanism. Adv Exp Med Biol. 2015;863:139–61.

44. Kim H-S, Quon MJ, Kim J-A. New insights into the mechanisms of polyphenols beyond antioxidant properties; lessons from the green tea polyphenol, epigallocatechin 3-gallate. Redox Biol. 2014;2:187–95.

45. Daglia M, Di Lorenzo A, Nabavi SF, Talas ZS, Nabavi SM. Polyphenols: well beyond the antioxidant capacity: gallic acid and related compounds as neuroprotective agents: you are what you eat! Curr Pharm Biotechnol. 2014;15(4):362–72.

46. Zhou J, Farah BL, Sinha RA, Wu Y, Singh BK, Bay B-H, et al. Epigallocatechin-3-gallate (EGCG), a green tea polyphenol, stimulates hepatic autophagy and lipid clearance. PloS One. 2014;9(1):e87161.

47. Apicella A, Natalello A, Frana AM, Baserga A, Casari CS, Bottani CE, et al. Temperature profoundly affects ataxin-3 fibrillogenesis. Biochimie. 2012 Apr;94(4):1026–31.

48. Friesner RA, Murphy RB, Repasky MP, Frye LL, Greenwood JR, Halgren TA, et al. Extra precision glide: docking and scoring incorporating a model of hydrophobic enclosure for protein-ligand complexes. J Med Chem. 2006 Oct 19;49(21):6177–96.

49. Robello M, Amico C, Cupello A. Regulation of GABAA receptor in cerebellar granule cells in culture: differential involvement of kinase activities. Neuroscience. 1993 Mar;53(1):131–8.

50. Pellistri F, Bucciantini M, Relini A, Nosi D, Gliozzi A, Robello M, et al. Nonspecific interaction of prefibrillar amyloid aggregates with glutamatergic receptors results in

Ca2+ increase in primary neuronal cells. J Biol Chem. 2008 Oct 31;283(44):29950–60.

51. Brenner S. The genetics of Caenorhabditis elegans. Genetics. 1974 May;77(1):71–94.

3.7 SUPPORTING INFORMATION

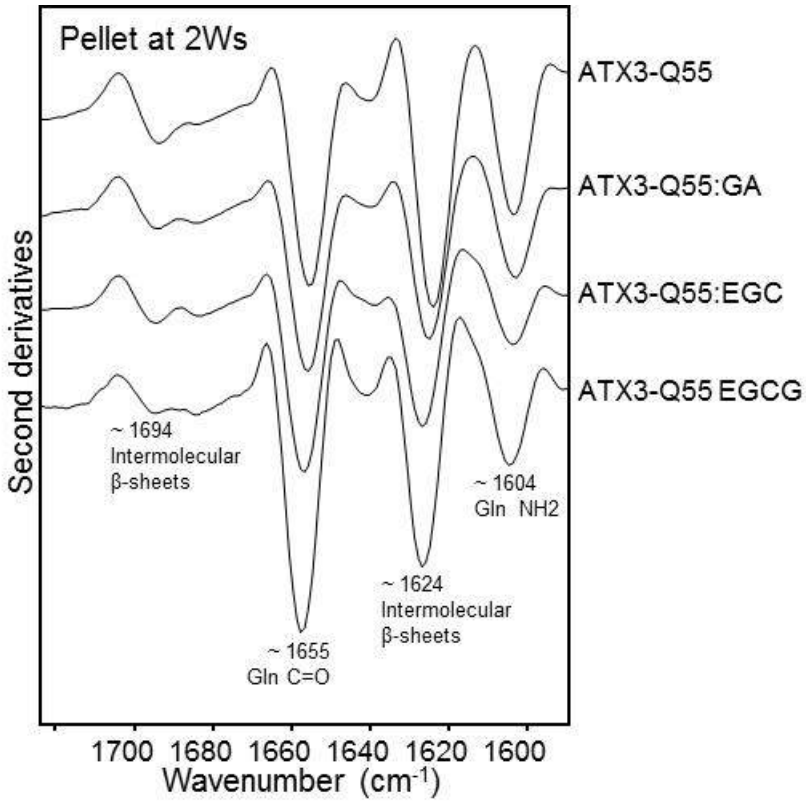

Figure S1. Second derivative spectra of the pellet collected from ATX3-Q55 samples incubated for two weeks at 37°C in the presence or the absence of compounds.

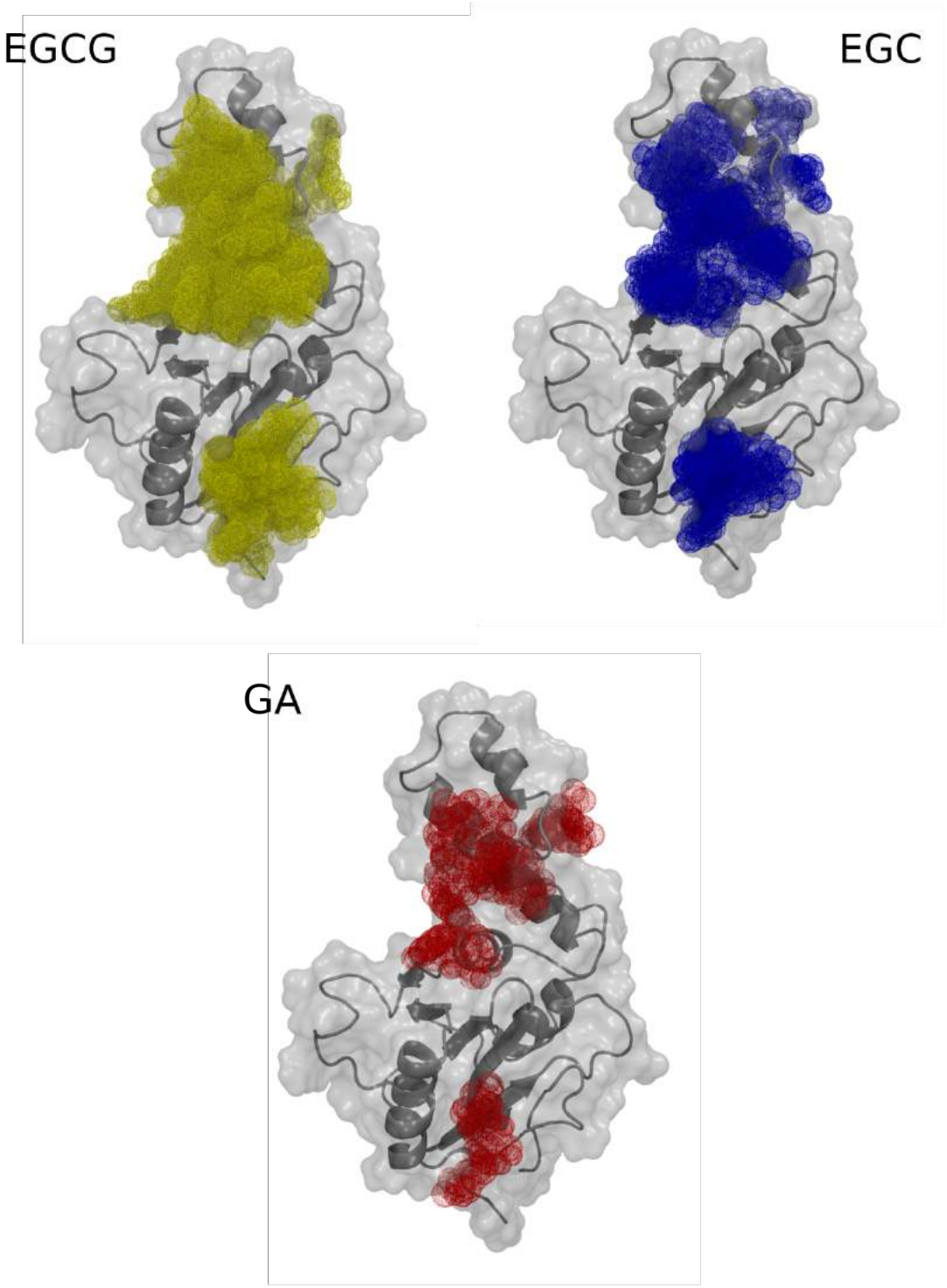

Figure S2. Binding sites of EGCG (yellow), EGC (blue) and GA (red) to the JD, as detected during the docking simulations in the 10 NMR structures of the protein.

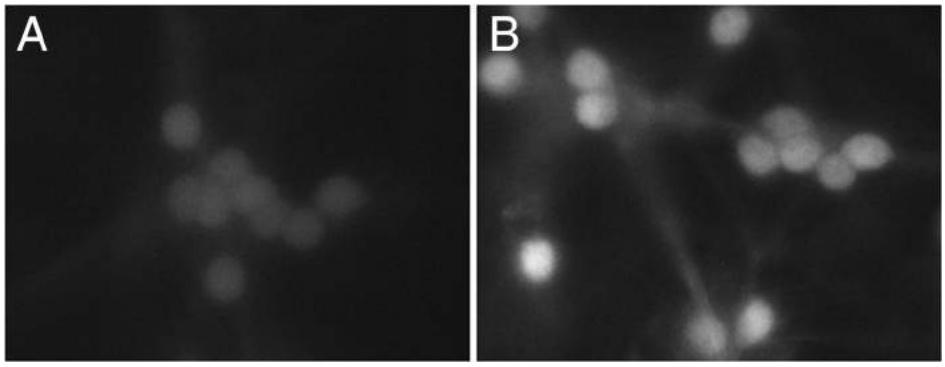

Figure S3. Rat cerebellar granule cells loaded with Oregon Green. Representative images of: A) control cells exhibiting basal fluorescence; B) cells incubated for 24 h with 48h-aged ATX3-Q55 aggregates, showing an increase in fluorescence intensity due to calcium influx induced by protein aggregates. The fluorescence increases reported in Fig 7 were obtained as $(F - F_0) \times 100/F_0$, where F is the fluorescence intensity measured in cells exposed to ATX3-Q55 aggregates formed in the absence and the presence of GA, EGC, EGCG, and F_0 the basal fluorescence level measured in untreated cells.

CHAPTER 4

The effects of epigallocatechin-3-gallete and gallic acid on ataxin-3 aggregation: an *in situ* study

4.1 INTRODUCTION

Plenty of molecules have been tested as inhibitors of ataxin-3 (ATX3) aggregation and only few succeed in doing so; (-)-epigallocatechin-3-gallate (EGCG) is one among these. However, instead of preventing, this molecule promotes an even accelerated, but off-pathway, aggregation. Moreover, aggregates formed in its presence are safe for cells (1,2). Epigallocatechin (EGC) and gallic acid (GA) are two molecules structurally related to EGCG and their effect is very similar to the one exerted by the whole molecule, although with a different extent (Visentin *et al.*, submitted). Protein co-incubation with EGCG, EGC or GA results in formation of large, soluble and SDS-resistant aggregates, morphologically and structurally different from the "classical" fibrillar aggregates formed by untreated protein (1, Visentin *et al.*, submitted). Safety and effectiveness of all of them was assayed in a *Caenorhabditis elegans* model of spinocerebellar ataxia type 3, in which they were shown to be effective in ataxic phenotype mitigation (1, Visentin *et al.,* submitted). None of our previously analyses provide information on their effect on intracellular aggregation.

Escherichia coli is a prokaryotic organism, which reacts to stress conditions (*e.g.*, aging, rate of protein synthesis, environment changes or expression of recombinant protein) by forming inclusion bodies (IBs) at one extremity of the cell. IBs formed by amyloidogenic proteins display amyloidogenic features as well. Even being a simple prokaryotic system, it has a protein quality control. Taking in account all this characteristics, it has been recently re-evaluated as model to study protein aggregation (3–5), also in living cells (6–8).

Several approaches are exploited to study IBs and their formation *in situ*. One of the most common is to express the target protein in fusion with another fluorescent protein, *i.e.*, green fluorescent protein and its variants. These chimera proteins permit not only to visualize where the aggregates are located in the cells (9), but also to investigate a protein deposition process at the single cells level (10). Another strategy to study IBs and follow aggregation *in vivo* using fluorescence is to label a target protein with a tetra-cysteine sequence. Bis-arsenical fluorescein-based dye specifically recognise this tag. The resulting aggregates will be visualised as hyperfluorescent spot inside the cell (11).

Conformational dyes are based on fluorescence changes too. In fact, these compounds change their spectroscopic features upon interaction with amyloid aggregates. One of the most common is thioflavin-S but it presents several limitations: many cellular components interfere with the reported signal and, moreover, it cannot be used to study the effect of compounds carrying aromatic groups. In the last years, a new dye has been

developed: ProteoStat® (12). This is a rotor molecule with a strong red shift relative to other dyes commonly used and with an absorption and emission maxima at 500 nm and 600 nm, respectively. Its fluorescence *in vivo* is less influenced by intracellular components and *in vitro* promotes an higher enhancement in the presence of aggregated protein (12). This dye also allows a better discrimination between amyloid-like deposits and non-ordered aggregates (5,13).

Spectroscopic techniques can also be applied to study aggregates *in vivo*. For instance, nuclear magnetic resonance gives information about structural properties and heterogeneity of protein embedded within IBs. However, to acquire these data, backbone carbonyl and nitrogen labelling is required (14). Fourier transform infrared (FTIR) is instead a label-free technique. Protein aggregates are characterized by the presence of intermolecular ß-sheet that can be assigned to a specific marker band (15,16), which is also detectable in IBs (17). Moreover, IR spectra highlight possible structural alterations of cell membranes promoted by protein aggregation and IBs formation (18).

In this work, we characterized the effect of EGCG and GA on *E. coli* cells expressing two ATX3 variants carrying 24 and 55 glutamine repeats, respectively, which represent a normal and an expanded, pathogenic variant, respectively. We investigated the effect of the two compounds by analyzing ProteoStat® binding to IBs on intact cells and recording FT-IR spectra of whole cells.

4.2 RESULTS

ATX3-Q55 and ATX3-Q24 strains characterization

EGCG and GA are two flavonoids active against ATX3 aggregation. We have previously characterised their action *in vitro* and in a *C. elegans* model of spinocerebellar ataxia type 3. In order to better understand the effects of the two flavonoids *in vivo*, we analysed their effect on IBs formed by *E. coli* cells expressing a wild type variant (ATX3-Q24), as a control, and an expanded one carrying 55 glutamine repeats (ATX3-Q55).

We first verified protein expression levels of the two strains after 4 h of induction at 37 °C, using uninduced strains as a control. As reported in Figure 1 A, upon 4 h of induction both ATX3-Q55 and ATX3-Q24 were mainly located in the insoluble fraction, whereas in the uninduced control no protein was detected. Insoluble fraction was obtained by centrifugation of crude extract: supernatant was referred to as soluble fraction and pellet as insoluble. We proceeded with ProteoStat® staining, a new dye recently developed for protein aggregates detection (12). Upon protein expression, we recorded an increased

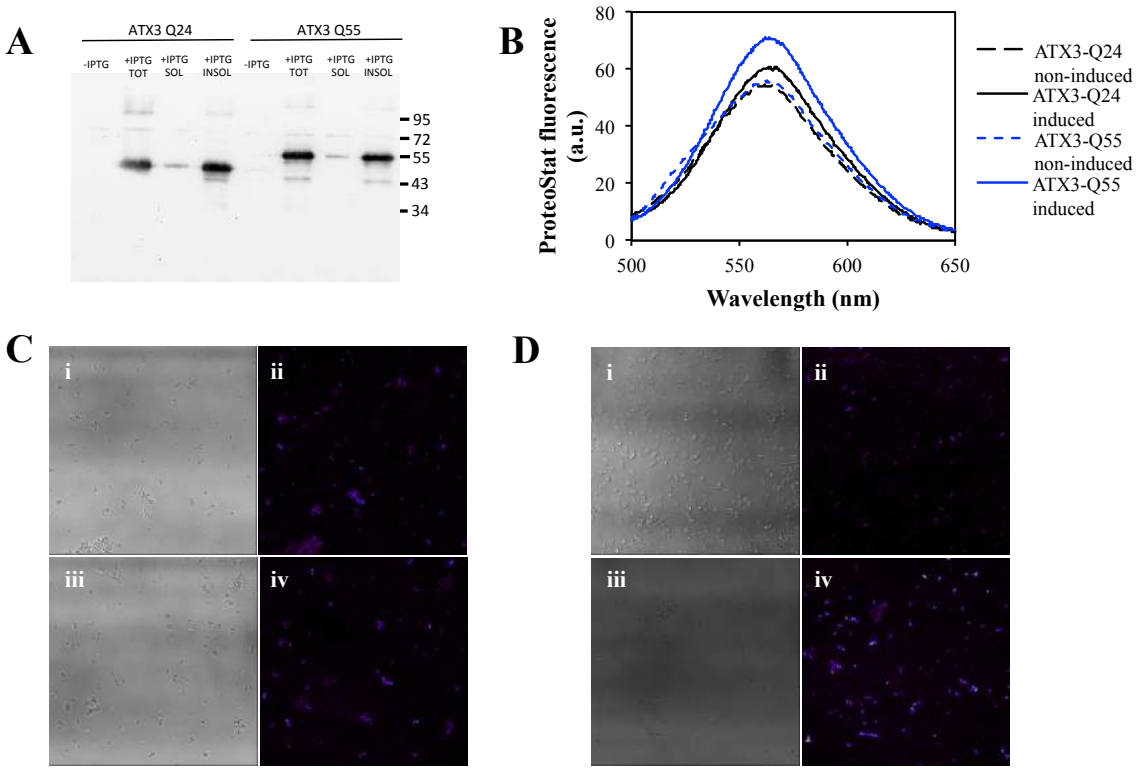

Figure 1. ATX3-Q24 and ATX3-Q55 strains characterization (A) Western blot analysis. Cell extract of ATX3-Q24 and ATX3-Q55 strain in the presence or the absence of induction was analysed by western blot. In the induced samples soluble and insoluble fraction were separated by centrifugation and individually analysed. (B) ProteoStat fluorescence spectra of ATX3-Q24 and ATX3-Q55 cells. ProteoStat emission spectra of induced and non-induced ATX3-Q24 and ATX3-Q55 cells. (C) Confocal microscopy of ATX3-Q24 cells. Control cells without IPTG (i, ii) and expressing ATX3-Q24 (iii, iv) after ProteoStat staining were analysed by confocal microscopy. Images acquired in transmission mode are reported on the left, fluorescence images on the right. (D) Confocal microscopy of ATX3-Q55 cells. Control cells without IPTG (i, ii) and expressing ATX3-Q24 (iii, iv) after ProteoStat staining were analysed by confocal microscopy. Images acquired in transmission mode are reported on the left, fluorescence images on the right. In fluorescence images colours are represented as spectrum palette. Scale bar correspond to 10 µm.

signal compared to uninduced cells; moreover, ATX3-Q55 promoted a stronger fluorescence increment compared with ATX-Q24 (Fig. 1B). In Figures 1C and D we report images obtained by confocal microscopy analysis of ATX3-Q24 and ATX3-Q55 cells, respectively. After induction, in both strains we observed inclusion bodies (IBs), which were positive to ProteoStat® staining. However, those formed by ATX3-Q55 were more fluorescent compared with those detected in ATX3-Q24 cells (Fig. 1B and C).

EGCG and GA effects studied by protein distribution analyses and ProteoStat® fluorescence

The same analyses were performed on the two strains upon treatment with 10 µM (-)-epigallocatechine-3-gallate (EGCG) or gallic acid (GA). To allow compounds to enter the cells, they were added in the medium 40 min before inducing protein expression.

We observed that EGCG treatment promoted an increase in the insoluble fraction in both ATX3-Q24 and ATX3-Q55 strains (Fig. 2) compared to untreated samples. Indeed, in the soluble fraction of protein-expressing cells in the absence of compounds in the

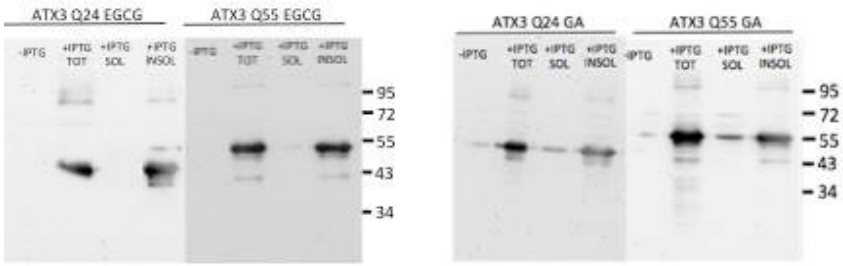

Figure 2. Western blot analysis of ATX3-Q24 and ATX3-Q55 expression in the presence of EGCG and GA. On the left panel is reported western blot analysis of ATX3-Q24 expression in the presence of 10 µM EGCG or 10 µM GA; on the right panel ATX3-Q55 expression in the same conditions. In the induced sample, soluble and insoluble fraction were separated and analysed individually. Immunodecoration was performed using an anti-ATX3 antibody and anti-rabbit as secondary antibody.

medium, a small amount of protein was still detectable in the soluble fraction (Fig. 1A). On the contrary, GA treatment promoted an increase in soluble fraction (Fig. 2) compared to untreated cells (Fig. 1A). A similar effect was observed in both strains.

Initially, we recorded ProteoStat® fluorescence spectra of stained cells; then, an aliquot of the same cells was analysed by confocal microscopy. As reported in Figure 3A and B, compared to untreated cells EGCG treatment promoted a 20% and an almost 40% increase in ProteoStat® fluorescence, in cells expressing wild type ATX3 and expanded ATX3, respectively. This analysis confirms an opposite effect by GA compared that exerted by EGCG. In fact, fluorescence of cells treated with this small compound was even lower than that of the untreated cells. In agreement with this results, the aggregation propensity factor (APF; see Materials and Methods) values calculated for cells treated with EGCG were 18,5 and 21,9 for ATX3-Q24 and ATX3-Q55 cells respectively, while in the GA treatment APF values were negative (-6,9 for ATX3-Q24 and -7,9 ATX3-Q55, Fig. 3C).

Confocal microscopy images reported in Figure 3D (panels i and iii) highlighted in both strains the formation of very large IBs positive to ProteoStat® staining upon EGCG treatment. Actually, the IBs observed were more fluorescent and even bigger compared to the ones of untreated cells. IBs formed by ATX3-Q55 were more fluorescent than the ATX3-Q24 ones. Cells treated with GA, on the contrary, showed very low fluorescence for both ATX3-Q24 and ATX3-Q55 cells (Fig. 3D ii and iv), suggesting low dye binding.

In keeping with confocal microscopy and fluorescence observations, flow cytometry analysis highlighted an increase in fluorescence after EGCG treatment, whereas in the presence of GA a decrease was recorded (Table 1). Both compounds were more efficient towards ATX3-Q55 cells: EGCG promoted a 18% increase with respect to the untreated sample, while in ATX3-Q24 the increase was almost 10%. Instead, GA decreased fluorescence by 18% and 9% in the expanded and wild type strain, respectively.

Flow cytometry assays were also performed, whereby cells were plotted on SSC-H *vs* FSC-H dot plots. Populations (P1) were then gated as reported in figure S1 and analyzed for ProteoStat® fluorescence in FL-3.

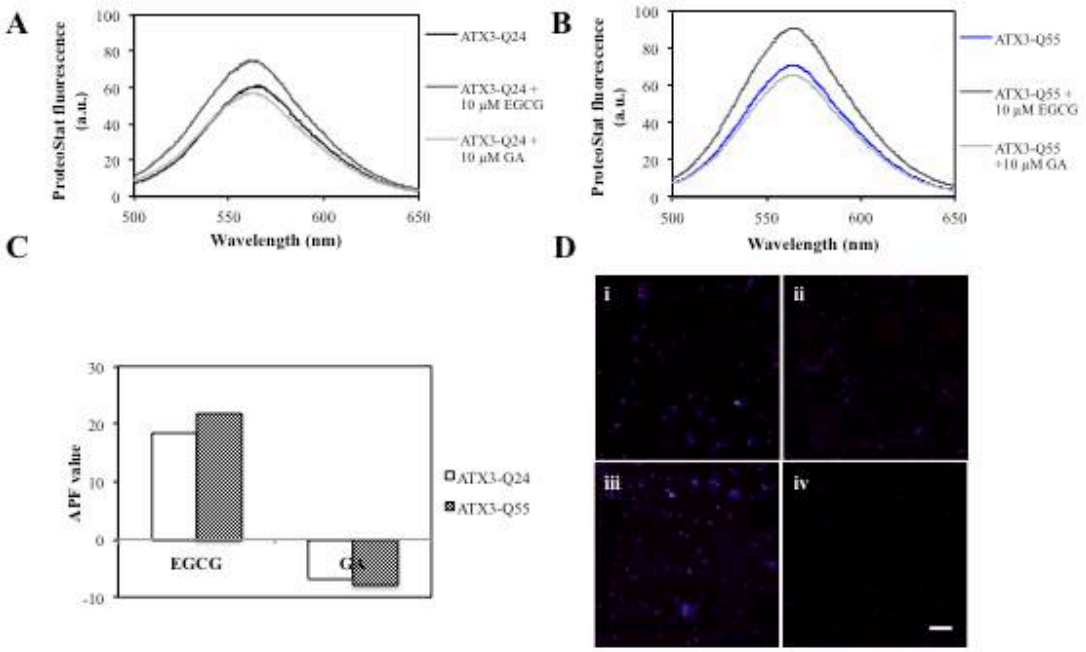

Figure 3. ATX3-Q24 and ATX3-Q55 expressing cells in the presence or the absence of EGCG and GA. (A-B) ProteoStat fluorescence spectra. ProteoStat emission spectra of induced ATX3-Q24 (A) and ATX3-Q55 (B) cells in the presence of 10 μM EGCG or GA. (C) APF value. APF value calculated for ATX3-Q24 and ATX3-Q55 cells treated with EGCG or GA. (D) Confocal analysis (i-ii) ATX3-Q24 expressing cells. Cells expressing ATX3-Q24 in the presence of EGCG (i) and GA (ii) were analysed by confocal microscopy after ProteoStat staining. (iii-iv) ATX3-Q55 expressing cells. Cells expressing ATX3-Q55 in the presence of EGCG (iii) and GA (iv) were analysed by confocal microscopy after ProteoStat staining. Fluorescence images are reported using spectrum colours palette. Scale bar correspond to 10 μm.

Table 1. Fluorescent values derived from flow cytometry analysis. Fluorescence maximum, median and relative standard deviation are reported for ATX3-Q24 and ATX3-Q55 expressing cells in the presence of vehicle, EGGC and GA an, as control, non-induced cells.

		Uninduced	Induced (vehicle)	+ EGCG	+ GA
Q24	Median	1070 ± 95	1730 ± 225	1852 ± 250	1513 ± 90
	Max fluorescence	62306	179085	26214	49769
Q55	Median	1240 ± 250	2162 ± 237	2548 ± 320	1351 ± 132
	Max fluorescence	119087	201536	248986	117395

ATX3-Q24 and ATX3-Q55 expressing cells analysed by FTIR microspectroscopy.

E. coli viable cells expressing ATX3-Q24 and ATX3-Q55, as well as their negative uninduced controls, were analyzed by FTIR microspectroscopy. In addition, the effects on *E. coli* cells of the two anti-amyloidogenic compounds, *i.e.,* EGCG and GA, were investigated *in situ*. In particular, cells were washed with 0.9% NaCl and resuspended in

this physiological solution. Few microliters of cell suspension were deposited on BaF_2 windows and dried at room temperature in a laminar flow hood, in order to remove the excess water.

FTIR spectra were acquired in transmission mode, between 4000-800 cm^{-1}, at 2 cm^{-1} spectral resolution and by the coaddition of 512 scans. At least five spectra for each sample were measured to evaluate possible heterogeneity and three independent experiments were performed to verify data reproducibility.

As an example, in Figure S2 the IR absorption spectrum of uninduced *E. coli* intact cells is shown and the absorption of the main biomolecules is indicated. To assign the IR absorptions to specific biomolecules, we analyzed the second derivatives of the absorption spectra that allow to better resolve the overlapped components of the IR complex bands. Second derivative spectra have been first analyzed in the Amide I band region, due to the C=O stretching of the peptide bond, that gives information on protein secondary structures and aggregation. For comparison, second derivatives have been obtained after normalization of the absorption spectra at the Amide I band area.

In Figure 4A, are reported the second derivative of the spectrum of *E. coli* cells expressing ATX3-Q24, that of uninduced control cells, as well as of induced cells treated with EGCG and GA. The second derivative spectra of the uninduced cells are characterized by two main components at ~1657 cm^{-1}, due to α-helix and random coils structures of the whole cell proteins, and at ~1639 cm^{-1}, assigned to intramolecular native ß-sheets. In addition, two absorptions at ~1692 cm^{-1} and at ~1680 cm^{-1}, respectively due to ß-sheets and ß-turns, were detected. These spectral features were found to change in part in cells expressing ATX3-Q24. In particular, compared to uninduced cell spectra, we detected an increase in the intensity of the α-helix/random coil band, accompanied by an intensity reduction of the intramolecular ß-sheet component and the appearance of a shoulder below 1632 cm^{-1}, indicating the appearance of a new ß-sheet structure, likely due to protein aggregates. Interestingly, the treatment with EGCG and GA led in particular to a decrease in the α-helix/random coil absorption and to a broadening of the ß-sheet shoulder, more evident in the case of EGCG.

To investigate whether the expression of the recombinant protein and the subsequent treatment with EGCG and GA affected someway the IR cell response, the absorption of other biomolecules was studied. In particular, we analyzed the spectral range 3050-2800 cm^{-1} (Fig 4B), dominated by the absorption of lipid hydrocarbon tails, which can give information mainly on membrane lipids. In this spectral range, the second

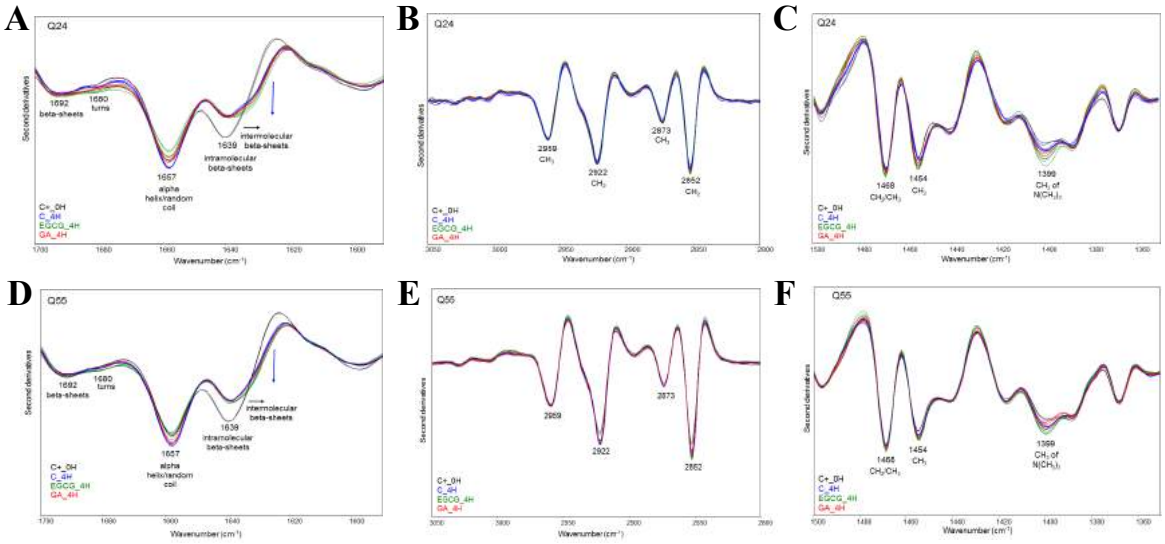

Figure 4. Amide I band, lipid hydrocarbon tail stretching region and lipid hydrocarbon tail and head group absorption of analyses after 4 h of induction of ATX3Q24 and ATX3Q55 expressing cells. (A) Second derivative spectra of ATX3-Q24 expressing cells, of uninduced control and of induced cells treated with EGCG and GA, have been reported in the Amide I region. (B) Second derivative spectra of ATX3-Q24 expressing cells, of the uninduced control and of cells treated with EGCG and GA, have been reported in the lipid hydrocarbon tail absorption region. (C) Second derivative spectra of ATX3-Q24 expressing cells, of the uninduced control and of cells treated with EGCG and GA, have been reported in the lipid hydrocarbon tail and head groups absorption region. (D) Second derivative spectra of ATX3-Q55 expressing cells, of uninduced control and of induced cells treated with EGCG and GA, have been reported in the Amide I region. (E) Second derivative spectra of ATX3-Q55 expressing cells, of the uninduced control and of cells treated with EGCG and GA, have been reported in the lipid hydrocarbon tail absorption region. (F) Second derivative spectra of ATX3-Q55 expressing cells, of the uninduced control and of cells treated with EGCG and GA, have been reported in the lipid hydrocarbon tail and head groups absorption region. (A, C, D, F) Second derivative spectra have been obtained after normalization of the absorption spectra at the Amide I band area. (B and E) Second derivative spectra have been normalized at the 2960 cm^{-1} CH_3 band.

derivative spectra of uninduced cells are characterized by four main components: at ~2959 cm^{-1} and ~2873 cm^{-1}, due to CH_3 stretching vibrations, and at ~2922 cm^{-1} and ~2852 cm^{-1} due to CH_2 stretching vibrations. Notably, these spectral features were found to be almost identical in cells expressing ATX3-Q24, as well as in EGCG and GA treated cells, with the exception of the CH_2 2852 cm^{-1} that showed higher intensity in cells treated with GA and even more with EGCG. In Figure 4C, we report the analysis in the spectral range 1500-1350 cm^{-1}, due to the bending vibrations of the CH_2/CH_3 groups from hydrocarbon tails and head groups, sensitive to hydrocarbon chain packing and conformational variations. In particular, the second derivative spectra of uninduced cells are characterized by a peak at ~ 1468 cm^{-1}, due to the overlapping absorption of CH_2 and CH_3, and at ~1454 cm^{-1}, due to CH_3; furthermore, the component at ~1399 cm^{-1} can be mainly assigned to the CH_3 of the $N(CH_3)_3$ group, typical of choline. Interestingly, we found very similar spectral features in cells expressing the protein, while these bands were found to slightly increase in intensity in cells treated with the two anti-amyloidogenic compounds, being more pronounced in the case of EGCG.

We also analyzed the effects of EGCG and GA in intact *E. coli* cells expressing ATX3 Q55. In Figure 4D, the second derivatives of *E. coli* cells expressing ATX3 Q55, of

uninduced cells, as well as of induced cells treated with EGCG and GA are shown. Compared to control cells, the second derivative spectra of cells expressing the ATX3-Q55 variant displayed an increase in the intensity of the α-helix/random coil band at ~1657 cm^{-1}, and a reduction of the intramolecular ß-sheet component at 1639 cm^{-1}. In addition, a shoulder below 1632 cm^{-1}, mainly due to intermolecular beta sheets, appeared. As found for cells expressing the ATX3-Q24 variant, the treatment with EGCG and GA led to a decrease in the α-helix/random coil absorption and to a broadening of the ß-sheet shoulder, more evident for EGCG.

Concerning lipid absorption between 3050-2800 cm^{-1} (Fig. 4E), we detected an increase in the intensity of the CH_2 bands at ~2922 cm^{-1} and ~2852 cm^{-1} in induced cells expressing the ATX3-Q55 variant and in GA and EGCG treated cells, compared to the uninduced control. This suggests that the expression of the protein led to a rearrangement of the hydrocarbon tail length and that, in particular the treatment with EGCG, caused a further increase in acyl chain length. This was confirmed by the spectral analysis between 1500-1350 cm^{-1} (Fig. 4F). Indeed, the same spectral behavior was detected for the ~1468 cm^{-1} (CH_2 and CH_3) and the ~1454 cm-^{1} (CH_3) bands, as well as for the phosphat marker at ~1399 cm^{-1}.

4.3 DISCUSSION

We previously reported the capability of (-)-epigallocatechin-3-gallate (3) and of two structurally related molecules, *i.e.*, epigallocatechin (EGC) and gallic acid (GA), to interfere with ataxin-3 (ATX3) aggregation. All these molecules mediate the anti-amyloidogenic effect by the same mechanism (1, Visentin *et al*., submitted): they redirect the aggregation pathway toward the formation of large SDS-resistant aggregates, and also mitigate the ataxic phenotype of a *C. elegans* model. In particular, our data pinpoint GA as the minimal functional unit of EGCG.

In the present work, we studied the effect of EGCG and GA on entire *E. coli* cells expressing ATX3-Q24 and ATX3-Q55. Our attention was especially focused on the effect on IBs and on cell membrane.

A preliminary analysis on protein expression revealed that after 4 h of induction, both variants were mainly localised in the insoluble fraction, even if a small amount of protein was still detectable in the soluble fraction, according to a previous report by Invernizzi and coworkers (8). The same analysis on cells treated with EGCG and GA

showed a different protein distribution. In fact, EGCG promoted an increment in insoluble fraction; on the contrary, in the presence of GA the soluble fraction was comparable to that of untreated cells or slightly more populated. In keeping with these data, confocal analyses highlighted the presence of IBs in expressing cells, not detectable in uninduced ones. These IBs increased in size in the presence of EGGC, whereas in the presence of GA their size was comparable to that observed in untreated cells.

In ProteoStat® fluorescence analysis, we observed a signal enhancement upon EGCG treatment compared to induced untreated samples, whereas GA promoted a drastic signal decrease. This effect was detected in both strains and, remarkably, the fluorescence recorded in ATX3-Q55-expressing cells attained higher fluorescence values, consistent with its amyloid behaviour. These data suggest that EGCG is capable to interfere with ATX3 aggregation also in living cells, which confirms its pro-aggregational action already observed *in vitro* (1,2). GA action is also in keeping with previous *in vitro* data, as we reported that this small compound exerts an effect similar to EGCG, but with a different time course (Visentin *et al.*, submitted) and a smaller increment in protein solubility compared to the treatment with the whole molecule.

Amide I region of IR spectra of intact *E. coli* cells expressing ATX3 highlighted the presence of protein aggregates after 4 h of protein expression (~1632 cm^{-1} shoulder) (15), paralleled by the decrease in α-helix/random coil signal. The signal of the aggregates was remarkably more pronounced in the presence of EGCG, in agreement with protein distribution analyses. This shift of the intermolecular ß-sheet peak can be explained by the bigger size of IBs formed in the presence of this compounds, but it can also be attributed to the formation of structurally different aggregates, as observed *in vitro* (1,2). Probably, under this particular condition, the broadening of the signal is accounted for by the contribution of both effects, justifying also the increased ProteoStat® signal. In the presence of GA, as expected because of increased protein solubility, the amount and the shape of intermolecular ß-sheet peak was similar to that of the untreated sample.

IR spectra analysis provides also information on membrane composition and fluidity. In particular, ATX3-Q24 expression mediated the only detected increment in phosphatidylcoline signal (PC, ~1399), especially in the presence of EGCG, and no significant lipid modification. This suggests a reorganization of membrane packing, resulting in increased membrane fluidity, without major lipid changes. In ATX3-Q55 expressing cells, we observed the same effect on PC, but in this case it was paralleled by a significant increase in the CH_2 band intensity, usually associated with increased acyl chain

length. Therefore, in this case we observed a membrane rearrangement towards a fluidity increment, but also general lipid structural changes. This suggests that ATX3-Q55 itself exerts an effect on cell membrane, not detectable in ATX3-Q24 expressing cells.

Plasma membrane can be regarded not only as a barrier between extra- and intra-cellular environments, but also as stress sensor. Due to this capability, its composition and fluidity can be modulated in response to stressing stimulations. Protein aggregation represents one of these stress conditions, resulting in significant reorganization of cell membrane (18). In keeping with these reports, increased PC levels could be due to increased membrane fluidity as a reaction to IBs formation to avoid cell lysis. Finally, plasma membrane has a critical role in signal transduction and PC represents an important source of lipid signalling molecules. The observed increment in the level of this lipid could reflect an increased cellular trafficking, especially after EGCG treatment and, to a minor extent, after GA treatment.

Overall, our data confirm that EGCG and GA can interfere with ATX3 amyloid deposition and highlight their capability to exert these effects in living cells. We also observed differences in their mechanism of action, which can be explained based on previous *in vitro* results but that need further studies to be fully understood.

4.4 MATERIALS AND METHODS

Ataxin-3 expression. ATX3-Q24 and ATX3-Q55 cDNA were cloned in pET21a plasmid (8) and expressed in *E. coli* BL21 (DE3) Competent Cells. Cells were grown at 37 °C in LB-ampicillin medium in the presence of 5% glucose until they reach OD_{600} 0.2. Cells were divided in two tubes and collected 10 min at 4000 rpm; in one tube the pellet was resuspended in LB-ampicillin medium in the presence of 5% glucose (not induced), the pellet in the second tube in LB-ampicillin medium (induced). In all the samples the compound (epigallocatechin-3-gallate or gallic acid), or an equal buffer volume, was added at a final concentration of 1 mM. After 40 min of incubation at 37 °C in agitation, protein expression was induced in the tubes without glucose adding 1 mM isopropil b-D-1-tiogalattopiranoside. Cells were collected after 4 h of induction, resuspended in 2% paraformaldehyde and stored at 4 °C.

SDS-PAGE and western blot analyses. Protein expression was monitored by western blot. Two OD_{600} of cells were collected 5 min at 6000 rpm at the end of induction and the corresponding pellet was stored at -20°C. After thawing, the pellet was resuspended in 1

mL of PBS (25 mM potassium phosphate, pH 7.2, 150 mM NaCl) and sonicated 40 sec with 0.1 s on and 0.1 pulse off at 30% amplitude. 500 µl of induced samples were transferred into a new eppendorf and centrifuged 30 min at 16000 *g*; supernatant represented the soluble fraction, whereas the pellet resuspended into equal volume was the insoluble fraction. Cellular extracts were subjected to SDS-PAGE and transferred into Immobilon PVD-F, previously activated with methanol. The membrane was saturated 1 h at room temperature and then Z46 antibody (Paolo Tortora, Milano) was added at 1:5000 dilution in 5% milk in TTBS. After 1h at room temperature and 3 washings of 10 min in TTBS (0.1% Tween 20, 50 mM TrisHCl, pH 7.5, 150 mM NaCl), Goat Anti-Rabbit IgG H&L (HRP, Abcam) was added at 1:10000 dilution in 5% milk in TTBS and incubated 1 h at room temperature. Membrane was washed 3 times for 10 min in TTBS and reviled with ECL Chemiluminescent HRP Substrate (Millipore) according to the manufacturer's protocols in a Biorad Versadoc.

ProteoStat® staining. Fixed cells were washed in PBS to remove paraformaldehyde residues and resuspended in ProteoStat® dye (Enzo Life Sciences) diluted 1:5000 in PBS for FACS analysis and 1:3000 for fluorescence analysis and confocal microscopy. Before proceeding with the assay cells were incubated 30 min at room temperature in the dark.

Fluorescence analysis. Fluorescence spectra of cells stained as reported above were recorded on a JASCO FP-8200 fluorescence spectrophotometer at OD_{600} 0.2 at 25 °C recording emission between 500 and 650 nm after exiting the samples at 484 nm. Aggregation propensity factor (APF) for cells treated with EGCG or GA was calculated as:

$$APF = 100\ (MFI_{compound} - MFI_{control})/\ MFI_{compound.}$$

Where $MFI_{compound}$ corresponds to ProteoStat® maximum fluorescence intensity in the presence of compound and $MFI_{control}$ to ProteoStat® maximum fluorescence intensity in the absence of this compound (induced cells).

Confocal microscopy analisys. Ten µL of ProteoStat® stained cells were deposited on the top of a glass slides and analyzed with a laser scanning confocal microscope (Leica SP5 AOBS equipped with a HCX PL APO 63 1.4 oil immersion objective, Germany) using a 488-nm argon laser and a 500/600 nm emission filter. Images were digitally captured and analysed with LAS AF 579 Lite Software (Leica Microsystems, Germany).

Flow cytometry. ProteoStat® stained cells were analyzed using a BD FACSCanto flow cytometer (BD Biosciences, San Jose, California, USA) using the protocol previously described in (5). Briefly, P1 population was gated by forward scatter (FSC) and side scatter (SCC). Cells in P1 were then analysed in the fluorescence channel FL-3 (530/30 nm band pass filter) using a 488 nm laser source (PE-A). A total of 50,000 events were acquired. Data analysis was performed with the FACSDiva Sofware (BD Bio-sciences).

Fourier transform infrared spectroscopy. After 4 h of induction in the presence or the absence of 10 µM EGCG or GA, 1 OD_{600} of cells were collected by centrifugation and resuspended in 0.9% NaCl, after three washes in the same buffer. Five µl of the suspension were deposited onto a BaF_2 window and dried at room temperature for about 30 min. FT-IR absorption spectra from 4000 to 600 cm^{-1} were acquired in the transmission mode by coupling the UMA 500 infrared microscope equipped with a nitrogen cooled MCT detector (narrow band, 250 µl) – to a FTS 40A spectrometer (Digilab-USA) at 2 cm^{-1} resolution, 20 kHz speed, 256 scan co-additions, and triangular apodization. Absorption spectra with a low noise level were obtained by setting the microscope aperture at about 100 µm x 100 µm (19). The background spectrum was collected before each measurement and no baseline correction was required on the spectra. Spectra were only corrected for possible residual water vapour. A second derivative analysis of the spectra in the Amide I and Amide II region was performed after a 15 point smoothing by the Savitzky–Golay method (3rd polynomial, 13 smoothing points), using the GRAMS/32 software (Galactic Industries, USA). To compare data from different growing cultures, the second derivative spectra were always normalized at the tyrosine band around 1515 cm^{-1}, in order to account for possible differences in the total protein content.

4.5 CANDIDATE'S CONTRIBUTION

The candidate prepared all cellular samples and personally performed protein expression analysis and fluorescence measurements. Under the supervision of Dr. Susanna Navarro, the candidate performed FACS and confocal analyses. FT-IR measurements were acquired by Dr. Diletta Metelli.

4.6 REFERENCES

1. Bonanomi M, Natalello A, Visentin C, Pastori V, Penco A, Cornelli G, et al. Epigallocatechin-3-gallate and tetracycline differently affect ataxin-3 fibrillogenesis and reduce toxicity in spinocerebellar ataxia type 3 model. Hum Mol Genet. 2014 Dec 15;23(24):6542–52.

2. Bonanomi M, Visentin C, Natalello A, Spinelli M, Vanoni M, Airoldi C, et al. How Epigallocatechin-3-gallate and Tetracycline Interact with the Josephin Domain of Ataxin-3 and Alter Its Aggregation Mode. Chem Weinh Bergstr Ger. 2015 Dec 7;21(50):18383–93.

3. Villar-Piqué A, Ventura S. Modeling amyloids in bacteria. Microb Cell Factories. 2012 Dec 28;11:166.

4. De Groot NS, Sabate R, Ventura S. Amyloids in bacterial inclusion bodies. Trends Biochem Sci. 2009 Aug;34(8):408–16.

5. Navarro S, Carija A, Muñoz-Torrero D, Ventura S. A fast and specific method to screen for intracellular amyloid inhibitors using bacterial model systems. Eur J Med Chem. 2016 Oct 4;121:785–92.

6. Espargaró A, Sabate R, Ventura S. Thioflavin-S staining coupled to flow cytometry. A screening tool to detect in vivo protein aggregation. Mol Biosyst. 2012 Nov;8(11):2839–44.

7. Pouplana S, Espargaro A, Galdeano C, Viayna E, Sola I, Ventura S, et al. Thioflavin-S staining of bacterial inclusion bodies for the fast, simple, and inexpensive screening of amyloid aggregation inhibitors. Curr Med Chem. 2014;21(9):1152–9.

8. Invernizzi G, Aprile FA, Natalello A, Ghisleni A, Penco A, Relini A, et al. The relationship between aggregation and toxicity of polyglutamine-containing ataxin-3 in the intracellular environment of Escherichia coli. PloS One. 2012;7(12):e51890.

9. Garcia-Mata R, Gao Y-S, Sztul E. Hassles with taking out the garbage: aggravating aggresomes. Traffic Cph Den. 2002 Jun;3(6):388–96.

10. Zhao Y, He W, Liu W-F, Liu C-C, Feng L-K, Sun L, et al. Two distinct states of Escherichia coli cells that overexpress recombinant heterogeneous β-galactosidase. J Biol Chem. 2012 Mar 16;287(12):9259–68.

11. Ignatova Z, Gierasch LM. Monitoring protein stability and aggregation in vivo by real-time fluorescent labeling. Proc Natl Acad Sci U S A. 2004 Jan 13;101(2):523–8.

12. Shen D, Coleman J, Chan E, Nicholson TP, Dai L, Sheppard PW, et al. Novel cell- and tissue-based assays for detecting misfolded and aggregated protein accumulation within aggresomes and inclusion bodies. Cell Biochem Biophys. 2011 Jul;60(3):173–85.

13. Regitz C, Fitzenberger E, Mahn FL, Dußling LM, Wenzel U. Resveratrol reduces amyloid-beta ($A\beta_{1-42}$)-induced paralysis through targeting proteostasis in an Alzheimer model of Caenorhabditis elegans. Eur J Nutr. 2016 Mar;55(2):741–7.

14. Curtis-Fisk J, Spencer RM, Weliky DP. Native conformation at specific residues in recombinant inclusion body protein in whole cells determined with solid-state NMR spectroscopy. J Am Chem Soc. 2008 Sep 24;130(38):12568–9.

15. Ami D, Bonecchi L, Calì S, Orsini G, Tonon G, Doglia SM. FT-IR study of heterologous protein expression in recombinant Escherichia coli strains. Biochim Biophys Acta. 2003 Dec 5;1624(1-3):6–10.

16. Ami D, Natalello A, Taylor G, Tonon G, Maria Doglia S. Structural analysis of protein inclusion bodies by Fourier transform infrared microspectroscopy. Biochim Biophys Acta. 2006 Apr;1764(4):793–9.

17. Ami D, Natalello A, Gatti-Lafranconi P, Lotti M, Doglia SM. Kinetics of inclusion body formation studied in intact cells by FT-IR spectroscopy. FEBS Lett. 2005 Jun 20;579(16):3433–6.

18. Ami D, Natalello A, Schultz T, Gatti-Lafranconi P, Lotti M, Doglia SM, et al. Effects of recombinant protein misfolding and aggregation on bacterial membranes. Biochim Biophys Acta. 2009 Feb;1794(2):263–9.

19. Orsini F, Ami D, Villa AM, Sala G, Bellotti MG, Doglia SM. FT-IR microspectroscopy for microbiological studies. J Microbiol Methods. 2000 Sep;42(1):17–27.

4.7 SUPPORTING INFORMATION

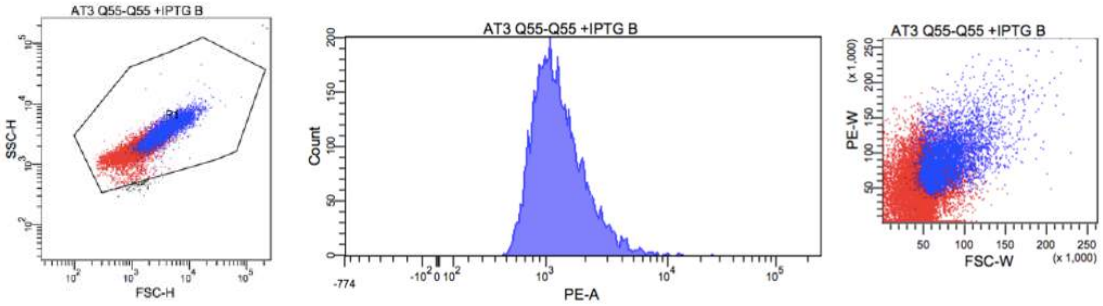

Figure S1. Representative population gating. Left image shows SSC-H *vs* FSC-H dot plot from 50,000 total events. P1 population was gated and represented in a fluorescence histogram (central panel). Right panel shows PE-W *vs* FSC-W dot plot.

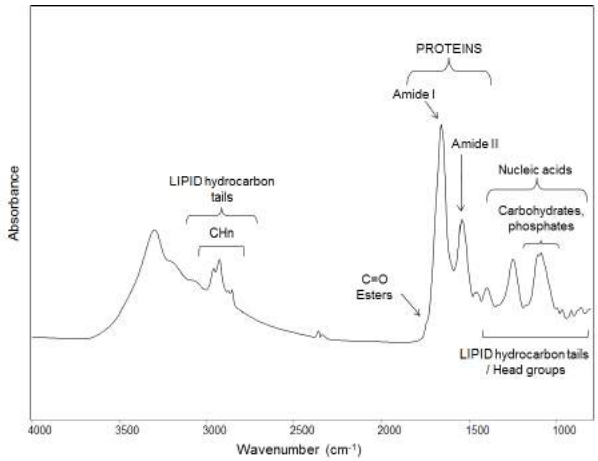

Figure S2. FTIR absorption spectrum of uninduced *E. coli* intact cells. The absorption of the main biomolecules is indicated.

CHAPTER 5

Protein environment: a crucial triggering factor in Josephin domain aggregation. The role of trifluorethanol.

5.1 INTRODUCTION

Spinocerebellar ataxia type 3 (SCA3) is one of the nine known polyglutamine (polyQ) disease (1). Those disorders are caused by the repetition of CAG triplet over the critical threshold (30-40 repeats) in the coding sequence of the respective gene. The only common feature of this disease-related protein is the presence of polyQ tract that trigger protein aggregation in the presence of the expansion (2,3). The resulting intra-neuronal amyloid aggregates are considered hallmark of the pathology.

Ataxin 3 (ATX3), the causative protein of SCA3, is a deubiquitinating enzyme with nuclear and cytoplamatic localization (4). It consists of a globular N terminal domain (Josephin domain, JD) and a disordered C-terminal tail in which the polyQ tract and one or two ubiquitin-interacting motif are present (5). SCA3 onset is triggered by protein carrying more than 55 glutamines. The aggregation process consists of two stages: the first one is polyQ independent and occurs in all ATX3 variants, whereas the second one starts only in the presence of an expanded polyQ and results in final amyloid-like fibrils generation (6–8). However, the expanded polyQ tract does not significantly affect protein stability but enhances local structural fluctuation of the flanking region, in particular of two critical α-helices of the JD. The aggregation-prone regions (APR) are located in these α-helices. APR exposure is prolonged in the presence of expanded polyQ, enhancing the probability of aberrant interactions with other ATX3 monomers and leading to the critical transition α-helix to ß-sheet, which initiates the aggregation. Moreover, the expanded polyQ tract stabilizes the final fibrils, generating glutamine side-chain hydrogen bonds but without remodelling the fibrils core (9,10).

The fluorinated alcohol 2,2,2-trifluoroethanol (TFE) is an osmolyte extensively used to study protein dynamics, stability and aggregation. The action of this compound can be accounted for two major effects: (i) tertiary structure disruption and (ii) stabilization of the secondary structure, especially α-helix but also ß-hairpin. The stabilized secondary structure is sequence dependent (11) and reflects the native composition (12). TFE addition creates a highly hydrophobic local environment with reduced polarity. Under these conditions, hydrogen bonds among side chains are promoted and the secondary structure stabilized. At high concentration, the formation of partially folded states occurs because the hydrophobic contacts in the protein core are disrupted and the protein loses its tertiary structure. This conformation is aggregation prone, and for this reason TFE is often used to promote and study protein aggregation. The action of this alcohol on all α-helical (13–15) or all ß-sheet (14) proteins is well characterized, whereas little is known about protein

composed of both.

In this study, we characterized the effect of TFE on JD aggregation using a biophysical approach. By circular dichroism we evaluated its impact on secondary structure, then, by spectroscopic analysis, we studied its effects at time 0 and after 24 h of co-incubation. By electron microscopy and Fourier transform infrared spectroscopy we provided a morphological and structural characterization of the final aggregates. Chemical and thermal stabilities were also studied. Finally, we also performed some *in silico* predictions.

5.2 RESULTS

TFE increases α helix content of JD

Trifluoroethanol is an alcohol known for its capability to stabilize secondary structures, preferentially α-helices. Recently, it has been demonstrated that the aggregation of expanded ATX3 starts from the conversion of a critical α-helix located in the JD (structure reported in Fig. 1) into a ß-sheet after an aberrant interaction with other ATX3 monomers. For this reason, we decided to assess whether TFE is capable to prevent ATX3 aggregation via α-helix stabilization.

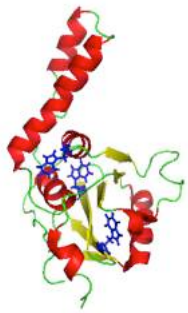

Figure 1. Ribbon representation of the JD structure. The Protein Data Bank accession code for the structure is 1ZYB with tryptophan residues highlighted in blue. The figure was prepared with PyMOL.

To monitor the effect of TFE on JD structure, we recorded CD spectra in far and near UV (Fig. 2A-B) in the presence of 0, 1, 2, 5, 10, 20% TFE *(v/v)*. As reported in Figure 2A, the untreated JD structure is mainly α-helical but is also displays a high contribution of ß-sheet. After TFE addition, we observed an increase in the α-helix signal, which was directly related to the amount of TFE added (Fig. 2C). In contrast, in the near UV, we observed a decrease of the signal in the presence of increasing amount of TFE and, in the presence of the highest concentration tested (10 and 20%), the signal was almost completely lost. The disappearance of signal in the near UV in the presence of the highest TFE concentration points to tertiary structure loss, so we decided to perform all other experiments using TFE *(v/v)* in the range 0-5%. Overall, these results indicate that TFE disrupts tertiary structure, whereas the secondary is even strengthened.

Low TFE concentrations do not significantly alter JD structure

To better understand the effect of TFE on the protein structure, we analysed tryptophan fluorescence after the addition of 0, 1, 2, 5% *(v/v)* of the compound to a solution of 80 µM freshly purified JD. As reported in the Figure 3A, there was some decrease of the signal at all concentrations tested relative to the untreated protein. This decrease was related to the amount of TFE added. 1H-NMR analysis confirmed that in the

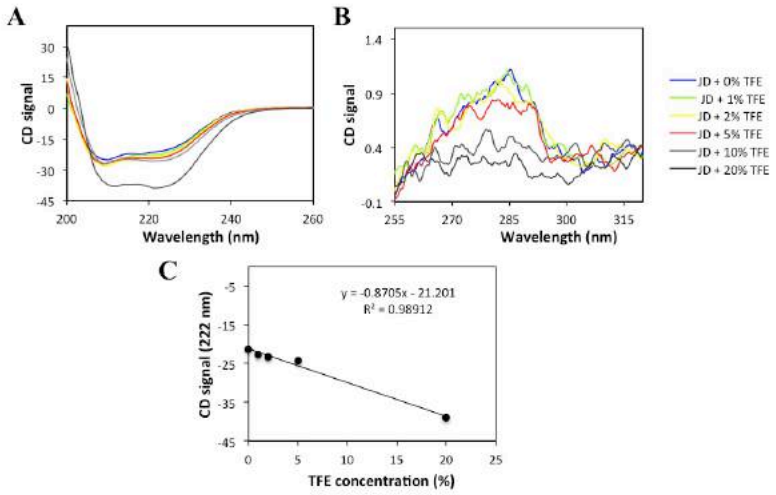

Figure 2. CD spectra of JD in the presence of different TFE concentrations. (A) Far UV spectra. Far UV CD spectra of JD in the presence of 0. 1. 2. 5. 10. 20 % of TFE *(v/v)*. (B) Near UV spectra. Near UV CD spectra of JD in the presence of 0. 1. 2. 5. 10. 20 % of TFE *(v/v)*. All the measurements were performed at 25 °C. (C) Correlation between TFE concentration and CD signal at 222nm. Plot of correlation between TFE amount added to 15 µM JD and CD signal at 222 nm.

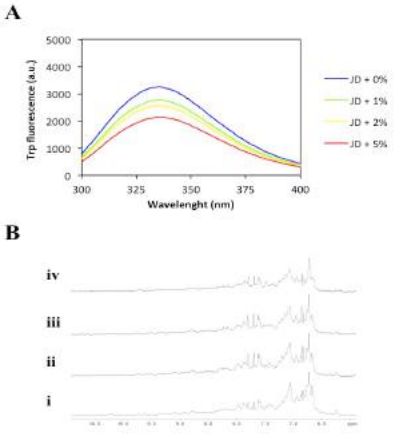

Figure 3. JD structural properties after TFE addition at time 0. (A) Tryptophan fluorescence. Tryptophan intrinsic fluorescence of freshly purified JD in the presence of 0, 1, 2 and 5% of TFE *(v/v)* (B) bisANS binding assay. bisANS binding of freshly purified JD in the presence 0, 1, 2 and 5% of TFE *(v/v)* (C) 1H-NMR titration. 1H-NMR spectra recorded in solution containing 0% (i), 1 (ii), 2 (iii) and 5 (iv)% of TFE *(v/v)*. All the measurements were performed at 25 °C.

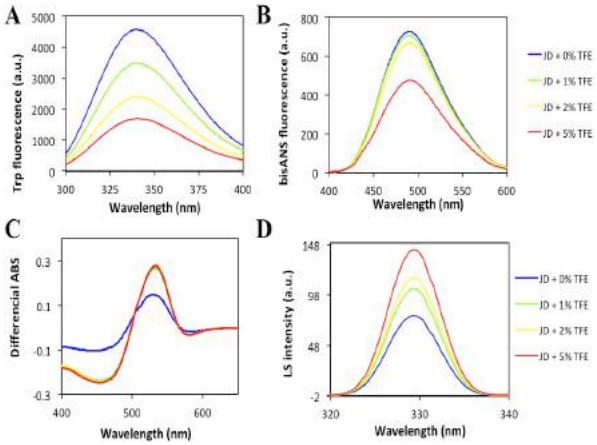

Figure 4. Aggregation properties of JD in the presence of different TFE concentrations after 24h of incubation at 37 °C. (A) Tryptophan fluorescence. Tryptophan intrinsic fluorescence of aggregated JD in the presence of 0, 1, 2 and 5% of TFE *(v/v)*. (B) bisANS binding assay. bisANS binding of aggregated JD in the presence of 0, 1, 2 and 5% of TFE *(v/v)*. (C) Congo red binding assay. Congo red binding of aggregated JD in the presence of 0, 1, 2 and 5% of TFE *(v/v)*. Data are represented as differential absorbance spectra. (D) Light scattering. Light scattering of aggregated JD in the presence of 0, 1, 2 and 5% of TFE *(v/v)*. All the measurements were performed at 25 °C.

presence of TFE there were small changes in protein structure. Although they w ere more evident at 5% (Fig. 3B iv), at 0, 1 and 2% (Fig. 3C i, ii and iii respectively) such changes were minimal. Further characterization using other chemical-physical methods (bisANS, Congo red spectra and light scattering), reinforced even more the hypothesis that TFE negligibly affects JD structure (Supplementary information Fig. S1).

TFE promotes aggregation of purified JD

Solutions of 80 µM freshly purified JD in the presence of 0, 1, 2 and 5% TFE *(v/v)* were incubated for 24 h at 37 °C in static condition. Tryptophan fluorescence measurements performed after the incubation showed that TFE-induced signal decrease was much stronger than that observed at 0 time (Fig. 4A and 3A), consistent with a higher extent of aggregation, as outlined below. BisANS measurements performed on the aggregated JD displayed an essentially unchanged signal up to 2% TFE, whereas at 5% concentration the signal was appreciably lower (Fig. 4B). In the Congo red assay, all samples displayed the typical signal shift at 540 nm, which however was much stronger in the presence of TFE, no appreciable difference being detected among the different concentrations (Fig. 4C). We then proceeded with light scattering assays that revealed a TFE-dependent increase in the signal recorded: the maximum value was detected in the presence of 5% TFE *(v/v)* (142 a.u.) and the minimum in its absence (77 a.u.), whereas 1 and 2% TFE *(v/v)* samples had intermediate values (Fig. 4C).

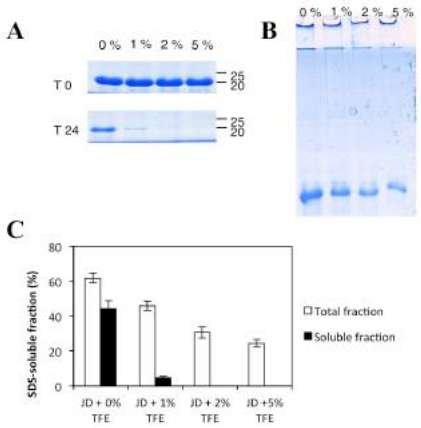

Figure 5. Aggregation kinetics of JD in the presence of different TFE concentrations. (A - B) Aggregation assay. SDS-PAGE of total (B) and soluble (A) fraction of JD incubated in the presence of 0, 1, 2 and 5 % of TFE *(v/v)*. Gels were stained using BluSafe Reagent. (C) Densitometric analysis. Densitometric analysis of SDS-soluble band of total and soluble fraction is reported.

An aliquot of each sample was centrifuged for 30 min at 14000 *g* to separate the soluble fraction, which was then subjected to SDS-PAGE and densitometric analysis. This revealed that after 24 h about 44% of protein of the untreated sample was still soluble, but only 5% at 1% TFE *(v/v)* and none at 2 and 5% TFE *(v/v)* (Fig. 5A and C). An aliquot of these samples was subjected to SDS-PAGE before centrifugation. SDS-soluble protein was detected in all samples corresponding to 62, 46, 30 and 24% of the initial protein in the

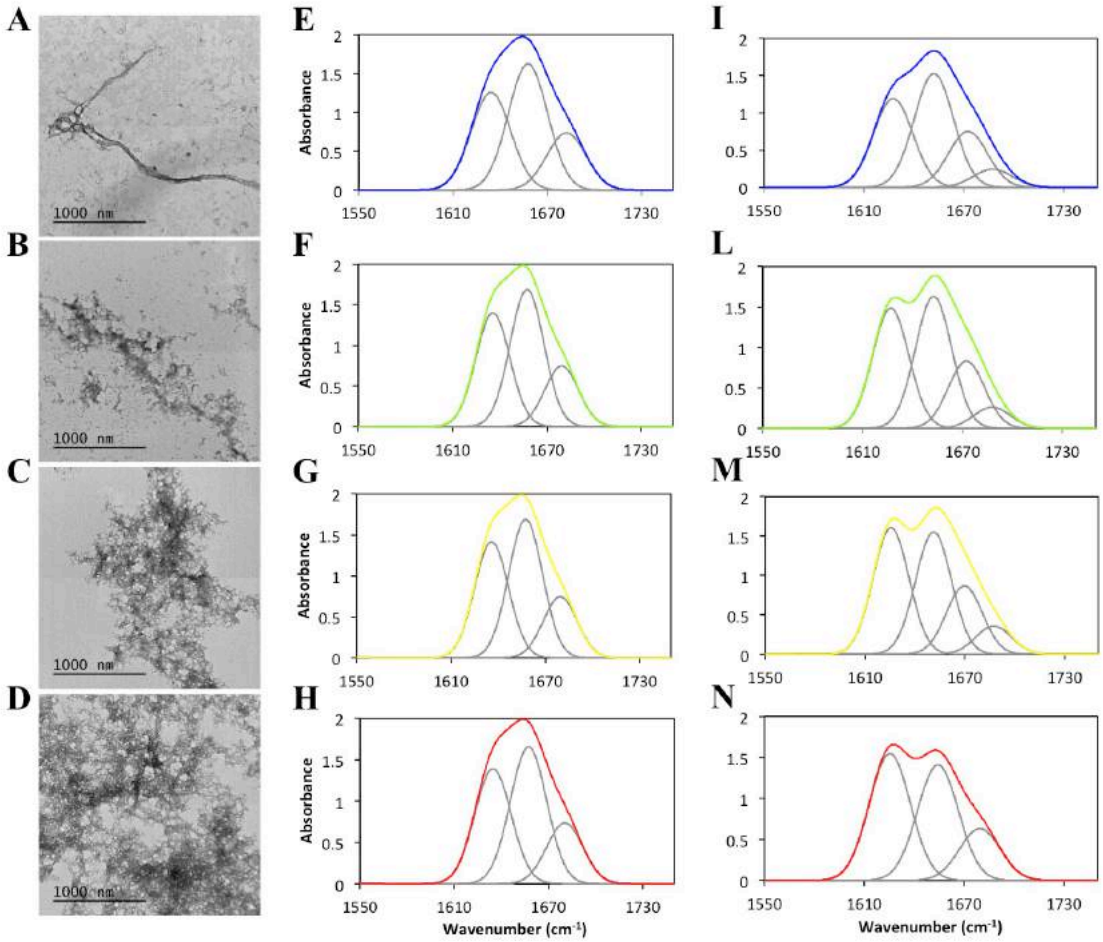

Figure 6. TEM and FTIR analyses of the JD aggregates in the presence of of different TFE concentrations. (A – D) TEM images of JD after 24 h of incubation in the presence of TFE. TEM images of negatively stained aggregates formed in the presence of 0 (A), 1 (B), 2 (C) and 5 % (D) of TFE *(v/v)* after 24 h of incubation at 37 °C. (E - N) FTIR spectra of JD in the presence of TFE. ATR/FTIR spectra of JD after 0 h (E - H) and 24 h (I – N) in the presence of 0, 1, 2 and 5% of TFE *(v/v)*. All the spectra were acquired in the amide I region and the fitted individual bands after Gaussian deconvolution are shown (grey lines).

presence of 0, 1, 2 and 5% TFE *(v/v)*, respectively. In the stacking gel, it was also possible to detect SDS-resistant aggregates that did not to enter the separating gel (Fig. 5B and C).

We then proceeded with the morphological analysis of the aggregates formed after 24 h of incubation by transmission electron microscopy. In Figure 6A-D it is apparent that the aggregates formed under all conditions were ordered, but TFE promoted an increase in size. Furthermore, in the absence and in presence of 1% TFE *(v/v)* small oligomers were observed.

We next analysed the structural features of these aggregates by recording the amide I region of the Fourier transform infrared spectroscopy, corresponding to the absorption of the carbonyl peptide bond. After spectra deconvolution, it was possible to assign each peak to the corresponding secondary structure and calculate the relative contribution to the main absorbance signal. At 0 time, the main difference was the peak at 1657 cm^{-1} corresponding to α-helix. In fact, this signal increased in parallel with the amount of TFE added. After 24 h there was a general decrease in native peaks (native ß sheet: 1635 and 1687 cm^{-1}; α helix:

Table 1. Secondary structure of fresh and aggregated JD in the presence of different TFE concentrations. Assignment of secondary structures of ATR/FTIR spectra acquired after 0 and 24 h of incubation at 37 °C in the presence of 0, 1, 2 and 5% TFE *(v/v)*. All the deconvolutions were performed using PickFit software.

		JD + 0% TFE		JD + 2% TFE		JD + 2% TFE		JD + 5% TFE	
		t 0	t 24	t 0	t 24	t 0	t 24	t 0	t 24
		Area (%)	Area (%)	Area (%)	Area (%)	Area (%)	Area (%)	Area (%)	Area (%)
1628	ß-sheet (inter)	-	32.1	-	35.3	-	36.6	-	41.1
1635/1687	ß-sheet (intra)	35.3	6.5	34.3	6.2	35.7	8.3	33.6	39.3
1657	α-helix	44.0	41.1	45.3	38.7	45.7	35.4	45.9	17.6
1672/1681	turns	20.7	20.2	20.5	19.7	18.9	19.8	20.4	-

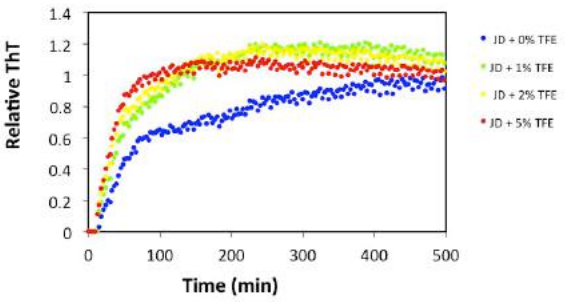

Figure 7. Aggregation kinetics of JD in the presence of different TFE concentrations**.** Aggregation kinetics of 40 µM JD in the presence of 0, 1, 2 and 5% TFE *(v/v)* was monitored following the ThT fluorescence signal at 37 °C for 500 min.

1657 cm^{-1}; turns: 1672 and 1681 cm^{-1}) paralleled by the appearance of a new peak at 1628 cm^{-1} assigned to intermolecular ß sheet. The extent of these changes was related to the amount of TFE added: indeed, in the presence of 1, 2 and 5% osmolyte the peak corresponding to the intermolecular ß sheet was 10% 14% and 28%, respectively, relative to the unt reated control (Fig. 6E-N and table 2). Next, we assessed the aggregation kinetics of 40 µM JD in the presence of 0, 1, 2 and 5% TFE at 37 °C by monitoring ThT fluorescence. As reported in Figure 7, TFE accelerated the process and lead to an increase in the final fluorescence values.

TFE impacts on thermal but not on chemical stability of TFE

To assess whether TFE impacts on protein stability, we performed thermal unfolding monitoring CD signal at 222 nm and tryptophan fluorescence at 350 nm (Fig. 8A-B). These two techniques provide information on changes in secondary and tertiary structure, respectively. We followed the unfolding in the temperature range 20-80 °C, with a heating rate of 1 °C/min. When monitoring far UV signal of JD in PBS, we observed a conformational transition between 45 and 65 °C with a melting temperature (T_m) of approximately 60 °C. TFE promoted a shift of T_m to a temperature lower by about 4 °C in the presence of 1% TFE *(v/v)*, 6° C in the presence of 2% and 12 °C in the presence of 5% (Fig. 8 A). When monitoring tryptophan fluorescence, the main transition in the absence of TFE occurred between 45 and 55 °C, with a T_m of approximately 50 °C; in the presence of 1, 2, or 5% TFE *(v/v)* it was at about 47 °C, 45 °C and 42 °C, respectively. Under the latter condition, the transition was still detectable but was scanty (Fig. 8B). To assess chemical

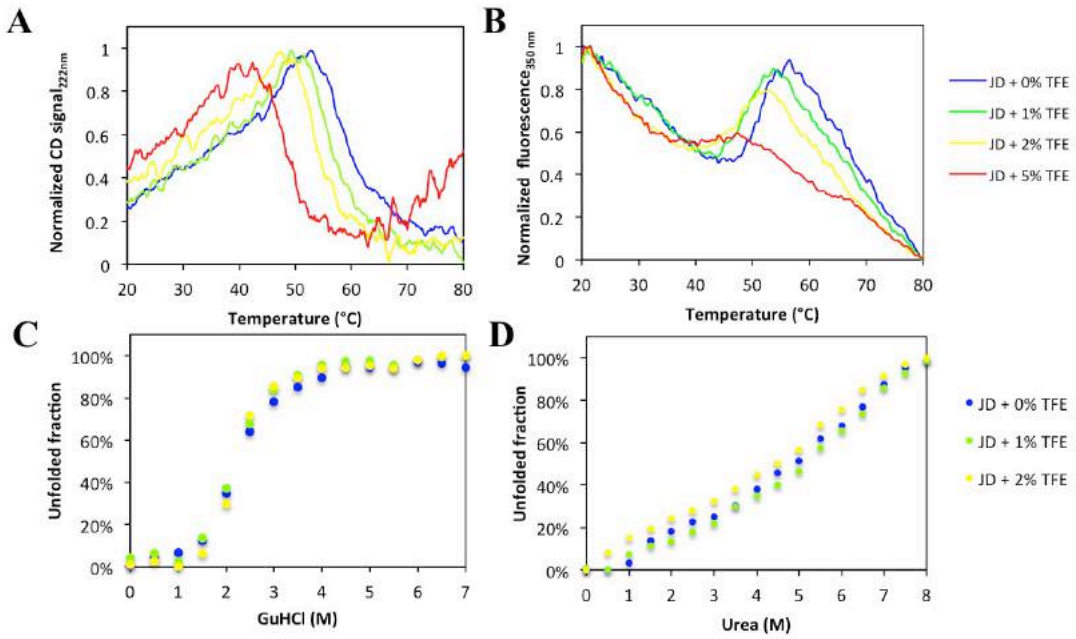

Figure 8. Thermal and chemical stability of JD in the presence of different TFE concentrations. (A) Thermal unfolding monitored at 222 nm. Unfolding profile monitored by CD recording the far-UV signal with a rate of 1 °C/ min in the presence of 0, 1, 2 and 5% of TFE (*v/v*). (B) Thermal unfolding monitored at 350 nm. Unfolding profile monitored by fluorescence recording the tryptophan signal at 350 nm with a rate of 1 °C/ min in the presence of 0, 1, 2 and 5% of TFE (*v/v*). (C) JD unfolding induced by guanidinium chloride. Equilibrium unfolding curves induced by GuHCl in the presence of 0%. 1% and 2% of TFE (*v/v*). (D) JD unfolding induced by urea. Equilibrium unfolding curves induced by urea in the presence of 0%. 1% and 2% of TFE *(v/v)*. Fluorescence emission were recorded at 25 °C and emission signal at 360 nm were plotted as function of denaturant concentration.

stability we monitored unfolding curve in the presence of guanidinium hydrocloride (GuHCl) and urea. The reactions were left overnight at room temperature to reach equilibrium and then we measured tryptophan fluorescence. In the presence of both denaturants there was no difference between protein with and without TFE *(v/v)*. In the presence of GuHCl we obtained a complete protein unfolding whereas in the presence of urea the unfolding process was not complete even at the highest concentration, in keeping with previous reports (Fig. 8C-D). Next, we tested the dynamic unfolding using stopped flow technique and urea as denaturant. According to the unfolding curve, we did not observe significant differences between the sample in the presence or the absence of TFE (Supporting information Fig. S2).

TFE has several binding sites in JD

In Figure 9 and table 2 we report results of Aggrescan3D predictions of the aggregation-prone region on protein surface. The simulation in static condition identified residues 31, 86-87, 136-137, 146-147 and 150-151 as aggregation-prone residues (A3D score > 0.5). Simulation in dynamic conditions that take in account possible structural fluctuations identified the same residues, albeit with higher scores, and some other additional residues, i.e., 27, 149-151 and 163.

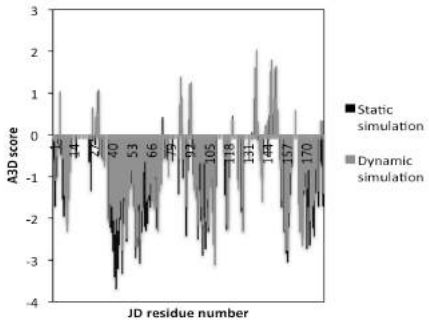

Figure 9. Aggrescan 3D prediction. A3D prediction of aggregation prone regions of JD. Predictions were performed using static (black) and dynamic (grey) condition.

Table 2. Aggrescan 3D results. Residues with A3D score > 0.5 are reported.

		A3D score	
		static	dynamic
5	F		1.0307
27	Y		0.6525
30	P		0.529
31	V	1.0259	1.0731
86	V	0.7132	1.3891
87	W	0.1934	0.913
136	L	0.873	1.6143
137	L	0.1736	2.0413
146	T	0.4577	0.9447
147	Y	1.5224	1.7954
149	A		0.8808
150	L	1.5889	1.6524
151	F	0.5956	0.6121
163	F		0.5957

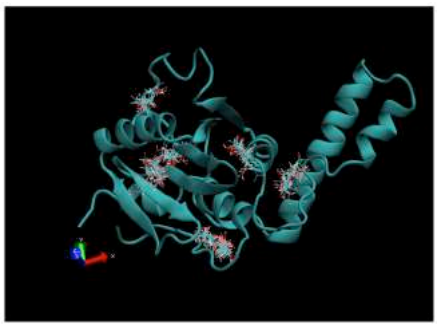

Figure 10. Molecular docking. Distribution of sampled poses in docking sites on 1YZB. All ligand configurations for each mainly populated cluster are shown.

We also performed molecular docking between JD and TFE as reported in Figure 10 and table S1. Ensemble docking calculations resulted in 200 docking modes, 20 per each 1YZB initial conformation. We predicted 14 clusters and 90% of sampled ligand poses were contained in six of them. These six mainly populated clusters are shown in Fig. 9. For each ligand configuration cluster we showed the identified protein residues involved in the interaction. In a greater detail, the residue contact probability is shown. This quantity has been calculated as previously reported (25) using the following procedure: for each snapshot (i.e., each mode pertaining to a certain cluster), the distance between the ligand and all residues of 1YZB was calculated. If, at least one distance value among the computed ligand-residue distances was equal or less than a chosen threshold (0.5 nm), the residue was considered as in contact with the ligand. The number of "contact snapshots" divided by the number of total snapshots is defined as the contact probability associated with the residue (25).

5.3 DISCUSSION

In the treatment of amyloid-related neurodegenerative diseases, the prevention of protein aggregation represents one feasible strategy. ATX3 is a polyQ-containing, aggregation-prone protein that triggers spinocerelbellar ataxia type 3 (SCA3) when its polyQ stretch exceeds a critical threshold (1). Its aggregation process consists of two different stages: the first one is polyQ independent and leads to proto-fibrillar aggregates, whereas in the second the polyQ tract drives the formation of final amyloid aggregates (9,10). Recently, a major role in this process has been assigned to a specific α-helix of the JD (α4) that is converted into ß-sheet after aberrant interactions with other JD monomers (9). To confirm the mentioned role of this α-helix, we assessed the effect of TFE on the JD in isolation for its well-known capability to stabilize secondary structure. We used isolated JD because this is the ATX3 domain the aggregation pathway starts from and also determines shape and structure of the final fibrils (7). For this purpose, we used very low TFE concentrations: maximum values is 5% *(v/v)*, which is no greater than half the value generally adopted in other studies (13,26–28). These working concentrations were chosen taking into account that at 10 and 20% TFE *(v/v)* CD spectra not only revealed an increase in α-helix signal but also a loss of tertiary structure, in keeping with a well-known mechanism of action of TFE. All the subsequent analyses were therefore performed at 1, 2 and 5% TFE *(v/v)*, so as to select conditions whereby it stabilizes α-helices while preserving tertiary structure, as supported by scanty changes observed in tryptophan and bisANS fluorescence, near and far CD and ^{1}H-NMR spectra. These data suggest that TFE promotes the formation of a native-like state largely indistinguishable from the fully native one. Similar effect were previously observed also in the case of acylphosphatase (26, 27). Surprisingly, in the presence TFE, the aggregation was faster and the resulting aggregates larger compared to those generated by untreated protein, although our spectroscopic data point to a tighter structure in terms of α-helix content, exposure of tryptophan and plausibly of aggregation-prone regions (APR). Concurrently, in the presence of TFE the JD also displayed a lower binding to bisANS and a higher one to Congo red. Thus, our results suggest that these aggregates are very similar, if not identical, to those formed by the protein in aqueous solution, although this native-like state is more aggregation prone compared to the fully native protein.

Although TFE affected JD thermal stability, it did not perturb chemical on, either at equilibrium or in dynamic conditions.

Simulation experiments presented in previous reports (9,10) lead to identify APR, mainly located in the pocket between the two JD subdomains. We also performed simulations using Aggrescan3D, which lead us to find new ones located on the protein surface. However, in the previous works the authors used different predictors, mainly focused on primary sequence, while A3D takes in account the three-dimensional structure of the protein. Thus, our predictions are not at odds with the previously identified ones.

We also performed molecular docking using JD and TFE, whereby we identified several binding sites, most of which overlapped with APR identified by A3D. The presence of several TFE-binding sites on JD surface might justify the compound's capability to affect JD behaviour even at low concentrations, as outlined above.

Our results also highlight the role of the environment in affecting the mode of ATX3 aggregation. In fact, TFE is known to generate a hydrophobic environment very similar to that present in membranes (30). This in turn, would be sufficient to induce the formation of a native-like state, which is more aggregation-prone than the fully-native protein. Our data are in agreement with those by Ruggeri and coworkers *(31)*, who report that ATX3 aggregation conforms to a novel, recently described pathway of amyloid aggregation, whereby aggregation precedes misfolding (29). Thus, according to the model, globular protein aggregation starts from a native-like state without the need of crossing the high-energy barrier associated with misfolding events.

5.4 MATERIAL AND METHODS

Josephin domain purification. The JD-encoding gene was previously cloned in a pET21-a vector and the protein was expressed in *Escherichia coli* BL21 Tuner (DE3) pLacI *(E. coli* B F ompT hsdSB (rB mB) gal dcm lacY1(DE3) pLacI (CamR); Novagen, Germany) as a His-tagged protein (16). Cells were grown at 37 °C in Luria Bertani - ampicillin medium and protein expression was induced adding 0.1mM isopropil-β-D-1-tiogalattopiranoside at OD_{600} 0.8 for 3 h at 30 °C. Cells were resuspended in 5ml/g wet weight of lysis buffer (25 mM potassium phosphate, pH 7.2, 150 mM NaCl, 0.5 mM phenylmethanesulfonyl fluoride, 10 mM imidazole, 10% glycerol, 1 mM 2-mercaptoethanol, 2 µg/ml aprotinin, 5 mM benzamidine, 1µg/ml pepstatine A), incubated for 30 min at 4 °C in agitation and further sonicated. After DNase I (0.2 mg/g of cells, wet weight) addition, cell suspension was incubated 30 min at room temperature and then centrifuged 45 min at 20000 *g*. His-tagged JD was purified with a HisTrap FF Column (GE Healthcare) previously equilibrated in washing buffer (25 mM potassium phosphate, pH 7.2, 150 mM NaCl, 2

mM phenylmethanesulfonyl fluoride, 10 mM imidazole, 10% glycerol, 1 mM 2-mercaptoethanol); before injection, the sample was filtered through a 0.45 µM pore membrane. Protein was eluted with elution buffer (25 mM potassium phosphate, pH 7.2, 150 mM NaCl, 2 mM phenylmethanesulfonyl fluoride, 150 mM imidazole, 10% glycerol, 1 mM 2-mercaptoethanol) and then subjected to Sephadex G-25 PD10 desalting column equilibrated with PBS (25 mM potassium phosphate, pH 7.2, 150 mM NaCl). Protein concentration was determined by UV absorption, with extinction coefficient at 280 nm of 24,750 M^{-1} cm^{-1}.

Josephin domain aggregation and soluble fraction analysis. Freshly purified JD was diluted to a final concentration of 80 µM in PBS in the presence of 0, 1, 2, 5% TFE and incubated 24 h at 37 °C in static condition. For soluble fraction analysis, 15 µl of fresh and incubated protein were centrifuged 15 min at 14000 *g* and 3 µl of the supernatant were subjected to SDS-PAGE. For total fraction analysis, 3 µl of protein mixtures were subjected to SDS-PAGE before centrifugation. The gels were stained with BluSafe® for 30 min at room temperature.

Spectroscopic methods. Circular dichroism (CD) measurements were performed in PBS at 25 °C using quarz cuvette with 1 mm pathlengths on a Jasco-810 spectropolarimeter equipped with PTC-348 Peltier temperature-control system. Protein concentration was 15 µM for far UV and 60 µM for near UV. Thermal unfolding was performed monitoring the CD signal at 222 nm and increasing temperature from 20 °C to 80 °C at 1 °C/min. Fluorescence measurement were performed in PBS at 25 °C using a 1 cm path length quartz cuvette on a Jasco FP-8200 spectrofluorometer equipped with PTC-348 Peltier temperature-control system. Protein spectra were recorded by exciting the sample at 280 nm and detecting the emission in the range 300 to 400 nm. Each trace was the average of 3 accumulated spectra. Thermal unfolding was performed monitoring the signal at 350 nm and increasing temperature from 20 °C to 80 °C at 1 °C/min. JD concentration was 20 µM. Light scattering of fresh and preincubated JD was performed by exciting the sample at 330 nm and recording the emission 320 to 340 nm. Each trace was the average of 3 accumulated spectra at 25 °C.

Congo red binding. JD incubated 24 h at 37 °C in the presence of 0, 1, 2, 5% TFE *(v/v)* was diluted at 20 µM in PBS in the presence of 20 µM Congo red. Optical absorption

spectra were recorded from 400 to 700 nm at room temperature on a Analytik Jena Specord®200 plus. Spectra of protein and CR alone were recorded to subtract protein scattering and dye contribution.

bis-ANS binding. Fresh and incubated JD was prepared at a final concentration of 80 µM in PBS in the presence of 0, 1, 2, 5% TFE *(v/v)* and 25 µM 4,4′-Dianilino-1,1′-binaphthyl-5,5′-disulfonic acid dipotassium salt (bis-ANS) was added. The samples were excited at 370 nm and spectra recorded following the emission from 400 to 600 nm at 25 °C in a Jasco FP-8200 spectrofluorometer equipped with PTC-348 Peltier temperature-control system. A 1-cm path length quartz cuvette was used. Each trace was the average of 3 spectra.

Aggregation kinetics. Freshly purified JD was prepared at 80 µM in PBS in the presence of 0, 1, 2, 5% TFE *(v/v)* and thioflavin T (ThT) was added at final concentration of 25 µM; 200 µl of reaction were loaded in 96-well plate and followed for 500 min at 37 °C in a Perkin Elmer - Victor TM3 multilabel plate reader. Each reaction was prepared in triplicate. The signal at 535 nm, after excitation at 445 nm, was recorded every 3 min.

Fourier transform infrared (FTIR) spectroscopy. Five µl of fresh and aggregated JD at 80 µM in PBS in the presence of 0, 1, 2, 5% TFE *(v/v)* were deposited on the diamond element of a Bruker Tensor 27 FTIR spectrometer. Measurements were performed in attenuated total reflection (ATR) mode after solvent evaporation. Data are reported as absorbance profile and fitted with a Gaussian distribution.

Electron microscopy. For electron microscopy analysis, aggregated JD in the presence of 0, 1, 2, 5% TFE *(v/v)* was diluted to a final concentration of 10 µM in PBS. Ten µl of sample was deposited on a carbon-coated copper grid and incubated 5 min at room temperature. The grid was than washed with distilled water, stained 1 min with 2% uranyl acetate *(v/v)* and analyzed with a HITACHI H-7000 transmission electron microscope operating at an accelerating voltage of 75 kV.

Chemical denaturation. Two stock solution containing 0 M and 8 M guanidinium chloride or urea were prepared with freshly purified JD at a final concentration of 5 µM and in the presence of 0, 1, 2 % TFE *(v/v)*. The two solutions were combined to obtain proper

denaturant concentration in a range between 0 M and 7 M (GuHCl) or 8 M (urea). The samples were kept at room temperature overnight to allow equilibrium attainment and protein spectra were analysed as described in the Spectroscopy section. Signal at 360 were plotted.

Stopped-flow fluorescence. Unfolding reactions were followed recording changes in fluorescence in a Bio-Logic SFM-3 stopped-flow instrument at 25 °C using excitation at 280 and 350 nm fluorescence cut-off filter. Unfolding reaction was promoted by dilution of 25 μM protein stock in PBS in the presence of 0, 1, 2 % TFE *(v/v)* with appropriate volumes of the same buffer containing 10 M urea.

Protein System and Compound. The 1YZB PDB code (17,18) was considered for Aggrescan3D simulations an docking analyses. The TFE chemical formula CF_3CH_2OH has been considered as compound to be docked on the 1YZB model.

Aggrescan3D simulation. We performed Aggrescan3D (19) simulations using 1YZB PBD code. The simulations were run in both static or dynamic mode without introducing mutation and setting 10 Å as distance of aggregation.

Molecular Docking. Molecular docking was performed using Autodock-Vina (20). The protein and ligand structures were prepared by removing nonpolar hydrogen atoms and rebuilding polar hydrogen atoms with AutoDock tools (21), followed by the assignment of partial charges based on Gasteiger-Marsili method (22). Ensemble docking procedure was employed by considering all steps contained in the 1YZB file (10 different configurations). The exhaustiveness parameter was set to 200, and the number of generated poses was 20 for each docking run. The docking was blind. At the end of the docking procedure, all obtained modes, each characterized by an affinity value, were clusterized on the basis of their position in the sample domain. In a greater detail, the distribution of docking ligand poses on 1YZB has been clusterized by using a RMSD clustering method (GROMACS-linkage (23,24)) with a cut-off of 0.5 nm.

5.5 CANDIDATE'S CONTRIBUTION

The candidate performed the aggregation assays and the relevant SDS-PAGE, dye-binding, spectroscopic analyses and A3D simulations. TEM was performed under the supervision of Dr. Susanna Navarro. Docking simulations were performed by Dr. Gianvito Grasso and

coworkers; NMR analyses were performed by the spectroscopic service of the Universitat Autonoma de Barcelona.

5.6 REFERENCES

1. Cummings CJ, Zoghbi HY. Trinucleotide repeats: mechanisms and pathophysiology. Annu Rev Genomics Hum Genet. 2000;1:281–328.

2. Ross CA, Poirier MA. Opinion: What is the role of protein aggregation in neurodegeneration? Nat Rev Mol Cell Biol. 2005 Nov;6(11):891–8.

3. Todd TW, Lim J. Aggregation formation in the polyglutamine diseases: protection at a cost? Mol Cells. 2013 Sep;36(3):185–94.

4. Kawaguchi Y, Okamoto T, Taniwaki M, Aizawa M, Inoue M, Katayama S, et al. CAG expansions in a novel gene for Machado-Joseph disease at chromosome 14q32.1. Nat Genet. 1994 Nov;8(3):221–8.

5. Masino L, Musi V, Menon RP, Fusi P, Kelly G, Frenkiel TA, et al. Domain architecture of the polyglutamine protein ataxin-3: a globular domain followed by a flexible tail. FEBS Lett. 2003 Aug 14;549(1-3):21–5.

6. Ellisdon AM, Thomas B, Bottomley SP. The two-stage pathway of ataxin-3 fibrillogenesis involves a polyglutamine-independent step. J Biol Chem. 2006 Jun 23;281(25):16888–96.

7. Masino L, Nicastro G, De Simone A, Calder L, Molloy J, Pastore A. The Josephin domain determines the morphological and mechanical properties of ataxin-3 fibrils. Biophys J. 2011 Apr 20;100(8):2033–42.

8. Robertson AL, Headey SJ, Saunders HM, Ecroyd H, Scanlon MJ, Carver JA, et al. Small heat-shock proteins interact with a flanking domain to suppress polyglutamine aggregation. Proc Natl Acad Sci U S A. 2010 Jun 8;107(23):10424–9.

9. Lupton CJ, Steer DL, Wintrode PL, Bottomley SP, Hughes VA, Ellisdon AM. Enhanced Molecular Mobility of Ordinarily Structured Regions Drives Polyglutamine Disease. J Biol Chem. 2015 Oct 2;290(40):24190–200.

10. Scarff CA, Almeida B, Fraga J, Macedo-Ribeiro S, Radford SE, Ashcroft AE. Examination of Ataxin-3 (atx-3) Aggregation by Structural Mass Spectrometry Techniques: A Rationale for Expedited Aggregation upon Polyglutamine (polyQ) Expansion. Mol Cell Proteomics MCP. 2015 May;14(5):1241–53.

11. Schönbrunner N, Wey J, Engels J, Georg H, Kiefhaber T. Native-like β-structure in a Trifluoroethanol-induced Partially Folded State of the All-β-sheet Protein Tendamistat. J Mol Biol [Internet]. 1996 Jan 1 [cited 2016 Nov 15];260(3). Available from: https://www.mysciencework.com/publication/show/5e723d552852bb63ecb0e12bb696e5ba

12. Buck M. Trifluoroethanol and colleagues: cosolvents come of age. Recent studies with peptides and proteins. Q Rev Biophys. 1998 Aug;31(3):297–355.

13. Marinelli P, Castillo V, Ventura S. Trifluoroethanol Modulates Amyloid Formation by the All α-Helical URN1 FF Domain. Int J Mol Sci. 2013 Aug 30;14(9):17830–44.

14. Perham M, Liao J, Wittung-Stafshede P. Differential Effects of Alcohols on Conformational Switchovers in α-Helical and β-Sheet Protein Models. Biochemistry (Mosc). 2006 Jun 1;45(25):7740–9.

15. Povey JF, Smales CM, Hassard SJ, Howard MJ. Comparison of the effects of 2,2,2-trifluoroethanol on peptide and protein structure and function. J Struct Biol. 2007 Feb;157(2):329–38.

16. Bonanomi M, Visentin C, Natalello A, Spinelli M, Vanoni M, Airoldi C, et al. How Epigallocatechin-3-gallate and Tetracycline Interact with the Josephin Domain of Ataxin-3 and Alter Its Aggregation Mode. Chem Weinh Bergstr Ger. 2015 Dec 7;21(50):18383–93.

17. Nicastro G, Menon RP, Masino L, Knowles PP, McDonald NQ, Pastore A. The solution structure of the Josephin domain of ataxin-3: structural determinants for molecular recognition. Proc Natl Acad Sci U S A. 2005 Jul 26;102(30):10493–8.

18. Nicastro G, Habeck M, Masino L, Svergun DI, Pastore A. Structure validation of the Josephin domain of ataxin-3: conclusive evidence for an open conformation. J Biomol NMR. 2006 Dec;36(4):267–77.

19. Zambrano R, Jamroz M, Szczasiuk A, Pujols J, Kmiecik S, Ventura S. AGGRESCAN3D (A3D): server for prediction of aggregation properties of protein structures. Nucleic Acids Res. 2015 Jul 1;43(W1):W306–313.

20. Trott O, Olson AJ. AutoDock Vina: improving the speed and accuracy of docking with a new scoring function, efficient optimization, and multithreading. J Comput Chem. 2010 Jan;31(2):455–61.

21. Morris GM, Huey R, Lindstrom W, Sanner MF, Belew RK, Goodsell DS, et al. AutoDock4 and AutoDockTools4: Automated docking with selective receptor flexibility. J Comput Chem. 2009 Dec;30(16):2785–91.

22. Gasteiger J, Marsili M. Iterative partial equalization of orbital electronegativity—a rapid access to atomic charges. Tetrahedron. 1980 Jan;36(22):3219–28.

23. Paissoni C, Spiliotopoulos D, Musco G, Spitaleri A. GMXPBSA 2.1: A GROMACS tool to perform MM/PBSA and computational alanine scanning. Comput Phys Commun. 2015 Jan;186:105–7.

24. Shao J, Tanner SW, Thompson N, Cheatham TE. Clustering molecular dynamics trajectories: 1. Characterizing the performance of different clustering algorithms. J Chem Theory Comput. 2007;3(6):2312–34.

25. Deriu MA, Grasso G, Licandro G, Danani A, Gallo D, Tuszynski JA, et al. Investigation of the Josephin Domain Protein-Protein Interaction by Molecular Dynamics. Salahub D, editor. PLoS ONE. 2014 Sep 30;9(9):e108677.

26. Curto LM, Angelani CR, Caramelo JJ, Delfino JM. Truncation of a β-barrel scaffold dissociates intrinsic stability from its propensity to aggregation. Biophys J. 2012 Nov 7;103(9):1929–39.

27. Bemporad F, Chiti F. "Native-like aggregation" of the acylphosphatase from Sulfolobus solfataricus and its biological implications. FEBS Lett. 2009 Aug 20;583(16):2630–8.

28. Rezaei-Ghaleh N, Ebrahim-Habibi A, Moosavi-Movahedi AA, Nemat-Gorgani M. Effect of polyamines on the structure, thermal stability and 2,2,2-trifluoroethanol-induced aggregation of alpha-chymotrypsin. Int J Biol Macromol. 2007 Dec 1;41(5):597–604.

29. Chiti F, Dobson CM. Amyloid formation by globular proteins under native conditions. Nat Chem Biol. 2009 Jan;5(1):15–22.

30. Khan MS, Tabrez S, Bhat SA, Rabbani N, Al-Senaidy AM, Bano B. Effect of trifluoroethanol on α-crystallin: folding, aggregation, amyloid, and cytotoxicity analysis. J Mol Recognit JMR. 2016 Jan;29(1):33–40.

31. Ruggeri FS, Longo G, Faggiano S, Lipiec E, Pastore A, Dietler G. Infrared nanospectroscopy characterization of oligomeric and fibrillar aggregates during amyloid formation. Nat Commun. 2015 Jul 28;6:7831.

5.7 SUPPORTING INFORMATION

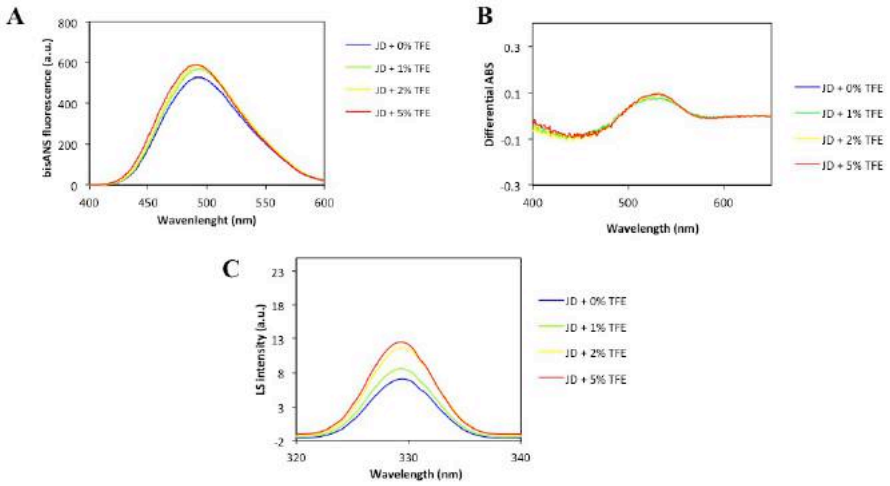

Figure S1. Aggregation properties of JD in the presence of different TFE concentrations at 0 time. BisANS (A), Congo red (B) binding assays and light scattering of 80 μM fresh JD after the addition of 0, 1, 2 and 5% TFE *(v/v)*. All the measurements were performed at 25 °C.

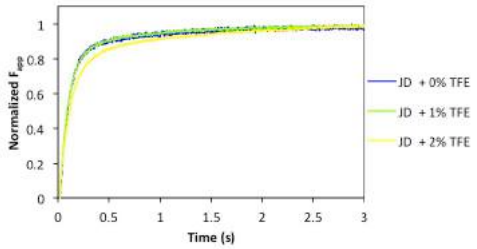

Figure S2. Stopped-flow unfolding of JD in the presence of different TFE concentrations. Representative stopped-flow traces for JD in the presence of 0, 1 and 2% TFE *(v/v)* at 7.8 M urea.

Table S1. Mainly populated clusters together with the percentage over the whole number of obtained modes, average of interaction energies and best configuration energy for each cluster.

Ligand cluster	% over the all modes	Average Interaction Energy (kcal/mol)	Mode with the best Interaction Energy (kcal/mol)
Cluster 01	10%	-3.25±0.09	-3.4
Cluster 02	17%	-3.50±0.21	-3.3
Cluster 03	14%	-3.25±0.12	-3.2
Cluster 05	13.5%	-3.28±0.19	-3.1
Cluster 08	23.5%	-3.70±0.38	-4.3
Cluster 09	12%	-3.39±0.11	-3.5

APPENDIX

HMG Advance Access published July 30, 2014

Human Molecular Genetics, 2014 **1–11**
doi:10.1093/hmg/ddu373

Epigallocatechin-3-gallate and tetracycline differently affect ataxin-3 fibrillogenesis and reduce toxicity in spinocerebellar ataxia type 3 model

Marcella Bonanomi[1,†], Antonino Natalello[1,2,†], Cristina Visentin[1], Valentina Pastori[1], Amanda Penco[4], Giuseppina Cornelli[1], Giorgio Colombo[1], Maria G. Malabarba[5,6], Silvia M. Doglia[1,2], Annalisa Relini[4,7], Maria E. Regonesi[1,3,*] and Paolo Tortora[1]

[1]Department of Biotechnologies and Biosciences, [2]Department of Physics G. Occhialini, [3]Department of Statistics and Quantitative Methods, University of Milano-Bicocca, 20126 Milan, Italy, [4]Department of Physics, University of Genoa, 16146 Genoa, Italy, [5]IFOM, The FIRC Institute of Molecular Oncology Foundation, 20139 Milan, Italy, [6]Department of Health Sciences, University of Milan, 20122 Milan, Italy and [7]National Institute of Biostructures and Biosystems (INBB), 00136 Rome, Italy

Received May 13, 2014; Revised July 2, 2014; Accepted July 11, 2014

The polyglutamine (polyQ)-containing protein ataxin-3 (AT3) triggers the neurodegenerative disease spinocerebellar ataxia type 3 (SCA3) when its polyQ tract is expanded beyond a critical length. This results in protein aggregation and generation of toxic oligomers and fibrils. Currently, no effective treatment is available for such and other polyQ diseases. Therefore, plenty of investigations are being carried on to assess the mechanism of action and the therapeutic potential of anti-amyloid agents. The polyphenol compound epigallocatechin-3-gallate (EGCG) and tetracycline have been shown to exert some effect in preventing fibrillogenesis of amyloidogenic proteins. Here, we have incubated an expanded AT3 variant with either compound to assess their effects on the aggregation pattern. The process was monitored by atomic force microscopy and Fourier transform infrared spectroscopy. Whereas in the absence of any treatment, AT3 gives rise to amyloid β-rich fibrils, whose hallmark is the typical glutamine side-chain hydrogen bonding, when incubated in the presence of EGCG it generated soluble, SDS-resistant aggregates, much poorer in β-sheets and devoid of any ordered side-chain hydrogen bonding. These are off-pathway species that persist until the latest incubation time and are virtually absent in the control sample. In contrast, tetracycline did not produce major alterations in the structural features of the aggregated species compared with the control, but substantially increased their solubility. Both compounds significantly reduced toxicity, as shown by the MTT assay in COS-7 cell line and in a transgenic *Caenorhabditis elegans* strain expressing in the nervous system an AT3 expanded variant in fusion with GFP.

INTRODUCTION

Amyloidoses are clinical disorders caused by deposition of proteins that abnormally self-assemble into insoluble fibrils and impair tissue–organ function. More than 20 unrelated precursor proteins can undergo misfolding, which is followed by protein aggregation into β-sheet rich, amyloid fibrils (1,2). Increasing evidence suggests that the most toxic species in cells are not the mature amyloid fibrils, but the pre-fibrillar oligomeric structures (3,4). In line with this idea, some evidence also suggests that formation of mature fibrillar aggregates may even be a defense mechanism for the cell (5). The discovery of molecules that inhibit protein deposition or reverse fibril formation could certainly disclose new avenues for developing therapeutic strategies aimed at preventing or controlling the corresponding amyloid-related diseases. Different classes of structurally unrelated compounds have been investigated for their ability to interfere with protein self-aggregation and stability of amyloid fibers (6). Among these, the flavonoids

*To whom correspondence should be addressed at: Piazza della Scienza 2, Milan, Italy. Tel: +39 0264483437; Fax: +39 0264483565; Email: mariaelena.regonesi@unimib.it
†These authors contributed equally to this work.

represent a large group of naturally occurring polyphenolic substances, well tolerated and abundant in some foods (7). Epigallocatechin-3-gallate (EGCG) is the most represented tea catechin (50–80% of total catechins) and it is known as a potent antioxidant via direct scavenging of reactive oxygen species (ROS) and reactive nitrogen species, induction of defense enzymes and binding of divalent metals, such as copper and iron (8,9). Furthermore, EGCG was reported to cross the blood–brain barrier in mammals (10) and to be safe for humans when tested in clinical studies (11). Current data also show that EGCG interacts with a large variety of amyloid-forming proteins such as amyloid beta (Aβ) (12), α-synuclein (13), transthyretin (14) and huntingtin (15), producing unstructured, off-pathway oligomers and reducing toxicity.

Another well-studied group of inhibitors are tetracyclines, a class of drugs capable of crossing the blood–brain barrier and already used in clinical practice, offering the advantage of a safe toxicological profile and well-characterized pharmacological properties (16–18). It has been shown that such compounds, to different extents, prevent fibrillogenesis of prion protein (PrP) (17), transthyretin (19), α-synuclein (20), β2-microglobulin (21) and Aβ (22,23). In most of these cases, tetracyclines are also able to redissolve mature fibrils. Although the exact mechanism of anti-amyloidogenic activity of tetracyclines is largely unknown, it is likely related to their ability to interfere with the formation of fibrillar aggregates (17,24). They may also contribute to improving other pathological events associated with amyloid deposit formation, including inflammation, ROS generation causing oxidative stress, apoptosis and uncoupling of metal homeostasis (25).

In this study, we sought to evaluate the effect of EGCG and tetracycline on the aggregation process and toxicity of the expanded ataxin-3 (AT3), the polyglutamine (polyQ)-containing protein responsible for spinocerebellar ataxia type 3 (SCA3). To date, no effective treatment has been developed for such disease and no compounds have been tested for their effect on AT3 aggregation process. We therefore studied the *in vitro* effects of EGCG and tetracycline on expanded AT3 aggregation by taking advantage of different analytical methods, in particular Fourier transform infrared (FTIR) spectroscopy and atomic force microscopy (AFM). We demonstrated that the two compounds differently modulate the protein aggregation. EGCG interferes within the early steps of aggregation, accelerating the misfolding of the Josephin domain (JD) and preventing the formation of mature fibrils; in contrast, tetracycline modulates the process by increasing the solubility of aggregated species, with no major alterations in their structural features. In both cases, co-incubation of AT3 with these compounds reduces the toxicity of protein aggregates in COS-7 cells. We also confirmed the effects of the two inhibitors *in vivo*, using transgenic *Caenorhabditis elegans* as a simplified SCA3 model, which provides a clear evidence of the beneficial effect of the two compounds on the disease, although neither EGCG nor tetracycline were able to disassemble preformed AT3-amyloid fibrils *in vitro*.

RESULTS

EGCG and tetracycline differently affect AT3 aggregation kinetics and solubility

In recent years, plenty of evidence has highlighted a critical role for soluble oligomeric amyloid species in triggering cellular toxicity (26,27). Here, we have examined whether and how EGCG or tetracycline affect the amyloid aggregation pattern of an expanded variant of AT3, thus preventing its toxic effects. We produced His-tagged, monomeric AT3Q55 to a degree of purity of at least 93%, as assessed by densitometric analysis of SDS-gels (Supplementary Material, Figs S1 and S2A). Also, no cross-reactive degradation products were detected by western blotting in preparations of freshly purified AT3Q55 (Supplementary Material, Fig. S2B). The protein (25 μM) was then incubated at 37°C in the presence or the absence of either compound at 1 : 1 or 1 : 5 protein–drug molar ratios. Aliquots were taken at different incubation times and the soluble fraction isolated as the supernatant from a centrifugation at 14 000*g*. The protein content was determined using Bradford assay. Compared with the control, both treatments resulted in a substantially slower decline in soluble protein content starting from 24 h of incubation (Fig. 1A and B). SDS-soluble protein fraction was also quantified by SDS–PAGE of the supernatants and subsequent densitometric analyses. Starting from the earliest incubation time (3 h), EGCG treatment resulted in a significant reduction in SDS-soluble amount of the protein (Fig. 1C, E and F; Supplementary Material, Fig. S3). In contrast, tetracycline somewhat retarded its disappearance (Fig. 1D, E and G; Supplementary Material, Fig. S3). The effects were best detected at the highest protein–drug molar ratios.

Surprisingly, the reduced solubility of EGCG-treated protein was paralleled by the appearance of large SDS-resistant aggregates in the soluble fraction (Fig. 1F). These soluble aggregates are large in size and do not enter the separating gel (>250 kDa). In contrast, in time course experiments without EGCG, large SDS-resistant complexes were hardly detected in the soluble fraction (Fig. 1E). Tetracycline treatment yielded a pattern qualitatively similar to that of untreated protein, as regards SDS-resistant species accumulation (Fig. 1G). Further characterization of the aggregation products was performed by SEC (Supplementary Material, Fig. S4). In the control sample (Supplementary Material, Fig. S4A), higher molecular-weight products appeared in the void-volume starting from 3 h of incubation, which correspond to a molecular mass of 300 kDa or higher. Scanty, if any, accumulation of intermediate forms between void-volume and monomeric protein was observed. Tetracycline treatment (Supplementary Material, Fig. S4C) did not appreciably altered this pattern, the only significant difference being a somewhat faster formation of higher molecular-weight forms compared with the control sample. In contrast, EGCG treatment (Supplementary Material, Fig. S4B) resulted in a much faster disappearance of the monomeric form and accumulation of aggregates, with also appreciable accumulation of intermediate forms. This fits well with the aggregation pattern determined in SDS–PAGE (Fig. 1E–G). The much higher void-volume-peak detected in the case of EGCG treatment quite likely results from tight protein–drug interaction, as substantiated by our observations (data not shown).

EGCG, but not tetracycline, drastically affects the structural features of the aggregation intermediates

By FTIR spectroscopy, we investigated the structural features of AT3Q55 aggregation products arising in the presence of either compound. This technique provides insights into protein secondary structures through the analysis of the amide I band

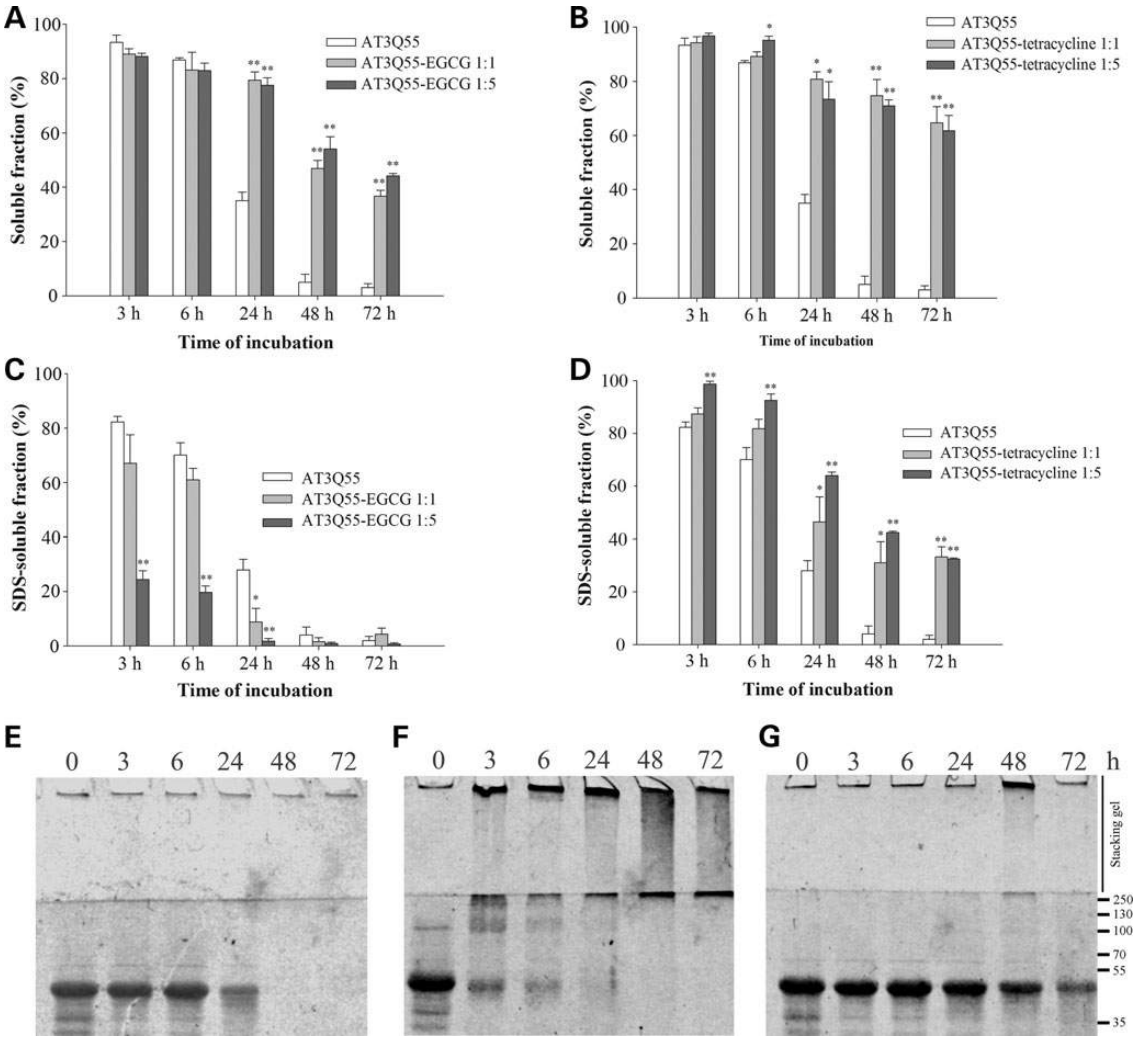

Figure 1. Soluble protein fraction analysis of AT3Q55 incubated in the presence or the absence of EGCG or tetracycline. (**A** and **B**) Protein quantification of the soluble fraction obtained by centrifugation of aliquots of 25 μM AT3Q55 incubated at 37°C in the presence or the absence of EGCG (A) or tetracycline (B) at a molar ratio protein–compound of 1 : 1 or 1 : 5. The data were expressed as percentage of protein amount with respect to $t = 0$. Error bars represent standard errors and are derived from at least three independent experiments. $^{*}P < 0.05$, $^{**}P < 0.01$. (**C** and **D**) SDS-soluble protein amounts of AT3Q55 incubated in the presence or the absence of EGCG (C) or tetracycline (D) were quantified by densitometry. Signals were normalized at $t = 0$ protein content. Error bars represent standard errors and are derived from at least three independent experiments. $^{*}P < 0.05$, $^{**}P < 0.01$. (**E**–**G**) SDS–PAGE (12%) of the soluble protein fraction of AT3Q55 (E), AT3Q55-EGCG 1 : 5 (F) and AT3Q55-tetracycline 1 : 5 (G). The gels were stained with Imperial Protein Stain (Thermo Fisher Scientific).

(1700–1600 cm^{-1} spectral region), due to the C=O stretching vibration of the peptide bond. Noteworthy, it also makes it possible to detect intermolecular β-sheets in protein aggregates (28,29). The second derivative spectrum of freshly purified AT3Q55 (25 μM) in the amide I region is reported in Figure 2A. This mathematical procedure allows disclosing the different absorption components, which in the derivative spectrum appear as negative peaks (30). The spectrum of the native protein (Fig. 2A) is dominated by the component at ≈1657 cm^{-1}, assigned to α-helices and random coils, while the band at ≈1635 cm^{-1}, along with the shoulder at ≈1690 cm^{-1}, is due to intramolecular β-sheets, as previously discussed (31). We then collected spectra of AT3 incubated at 37°C in the presence of either drug. The complete incubation mixture was analyzed, i.e. without prior centrifugation. During the incubation of untreated protein, the component at ≈1635 cm^{-1} decreased in intensity, almost disappearing after 24 h. Instead, the component at ≈1657 cm^{-1} first slightly decreased and subsequently increased again. Moreover, after 6 h two new components at ≈1624 and ≈1694 cm^{-1} were seen in the spectra. Finally, at longer incubation times, a new component appeared at ≈1604 cm^{-1} (Fig. 2B). These spectral changes are in agreement with our previous FTIR study (31), whereby we demonstrated that the disappearance of the 1635 cm^{-1} component is representative of native intramolecular β-sheets disruption, while the appearance of the ≈1624 and ≈1694 cm^{-1} peaks is due to the formation of intermolecular β-sheets. We also could unambiguously assign the components at 1604 and at 1657 cm^{-1} in the final aggregates to ordered side-chain hydrogen bonding of expanded polyQ tracts, a hallmark of AT3 mature and SDS-insoluble amyloid fibrils (31).

Spectral changes observed upon incubation of AT3Q55 in the presence of EGCG at a 1 : 5 molar ratio were substantially different from those of the control sample (Fig. 2C). In particular, the

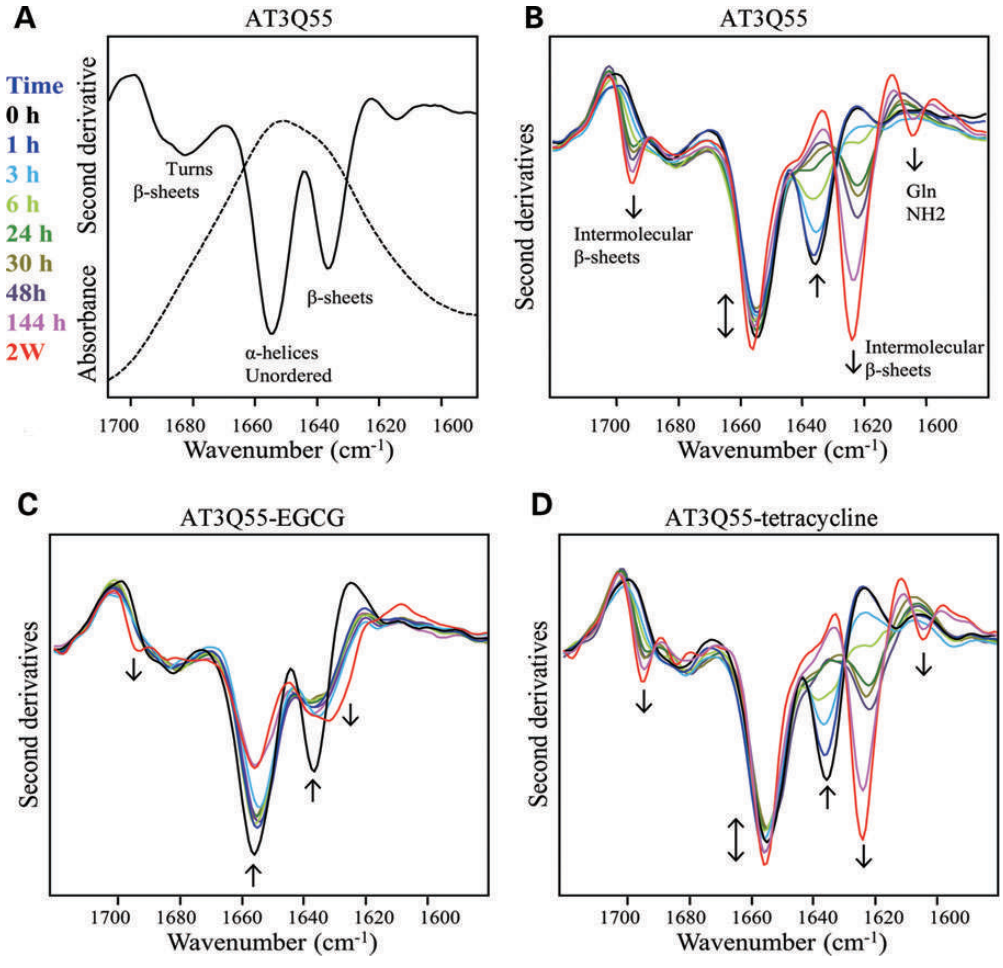

Figure 2. FTIR spectra of freshly purified AT3Q55 and kinetics of aggregation of AT3Q55 incubated in the presence or the absence of EGCG or tetracycline. (**A**) Absorption spectrum in the amide I region (dotted line), and its second derivative (continuous line), of freshly purified AT3Q55. (**B**–**D**) Second derivative spectra of AT3Q55 (25 μM) in the presence or the absence of compounds (125 μM) collected at different times of incubation in PBS at 37°C. Arrows point to increasing time. Band assignment of the main components is indicated.

≈1635 cm^{-1} component, assigned to native β-sheets, strongly decreased immediately after EGCG addition, indicating that this compound induces unfolding/misfolding of the protein. Two shoulders at ≈1628 and ≈1691 cm^{-1} appeared in the spectra and increased in intensity only at longer times of incubation (Fig. 2C). The comparison of the spectra in Figure 2C and B demonstrates that EGCG induces the formation of intermolecular β-sheet structures to a much lesser extent compared with those observed in its absence. Noteworthy, the 1604 cm^{-1} peak, assigned to the glutamine side-chain hydrogen bond network, was not detected in the spectra of the AT3Q55-EGCG solution, although most protein in solution was found to be SDS-resistant (Fig. 1F). Under these conditions, only a very small protein pellet was obtained by centrifugation at 14 000*g* after 2 weeks of incubation, whose FTIR spectrum was very similar to that of SDS-insoluble fibrils (data not shown). It displayed, in particular, the peaks assigned to glutamine side-chain hydrogen bonding (31).

The spectral changes observed upon incubation of AT3Q55 in the presence of tetracycline at a 1 : 5 molar ratio (Fig. 2D) were, instead, very similar to those found for the untreated protein (Fig. 2B).

Incubation of AT3 in the presence of EGCG or tetracycline gives rise to aggregates displaying different morphologies

AT3Q55 solutions incubated in the presence or the absence of either compound were analyzed by tapping mode AFM to get insight into the morphology of the resulting aggregates. Representative images are reported in Figure 3. Bundles of fibrils were observed for AT3Q55 alone after 24 and 48 h. The height of these bundles was between 20 and 60 nm, in keeping with previous observations (31). Instead, in the presence of EGCG, no such bundles were detected. Actually, after 24 h the sample mainly consisted of globular particles of height between 2.0 and 3.5 nm, isolated or associated in small clusters. After 48 h, large clusters of non-fibrillar material were found. The cluster height was between 20 and 80 nm and the typical cluster size in the scan plane was 0.5–1 μm.

In contrast, tetracycline did not significantly affect the aggregation pattern. Indeed, fibrils morphologically indistinguishable from those observed in the control sample were found at both incubation times, although many irregular, compact and relatively flat aggregates with height of 26 ± 2 nm and irregular edges also appeared along with mature fibrils.

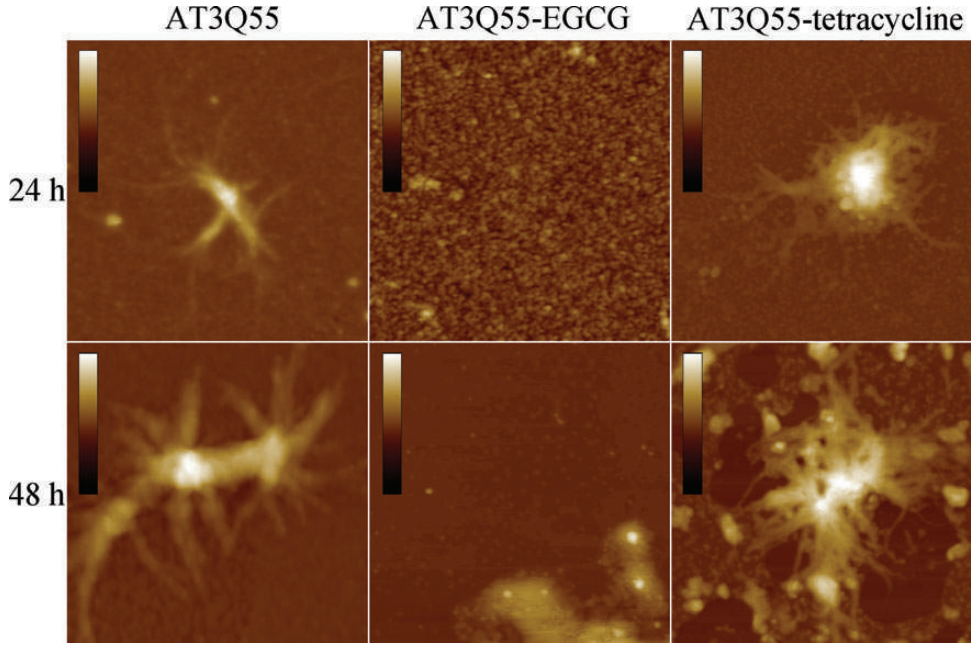

Figure 3. Tapping mode AFM images (height data) of AT3Q55 aggregates obtained after 24 h (top) or 48 h (bottom) incubation in the absence of inhibitors (left), in the presence of EGCG (middle) or tetracycline (right). Scan size 1.9 μm. The scale bars correspond to a *Z* range of (from top to bottom): AT3Q55, 110, 150 nm; AT3Q55-EGCG, 20, 80 nm; AT3Q55-tetracycline, 200, 100 nm.

EGCG and tetracycline do not disrupt AT3Q55 preformed fibrils

To assess the effect of EGCG or tetracycline on preformed amyloid aggregates, we first produced AT3Q55 fibrils by incubating the protein at 37°C for 2 weeks in PBS buffer. The FTIR spectrum of the pellet of the resulting sample (Supplementary Material, Fig. S5A) displayed four main components: 1695 and 1624 cm^{-1} due to intermolecular β-sheets, 1657 and 1604 cm^{-1} assigned, respectively, to the C=O stretching and NH_2 deformation modes of glutamine side chains involved in strong hydrogen bonding (31). The fibrils were resuspended in PBS alone (Supplementary Material, Fig. S5B), in PBS in the presence of EGCG (Supplementary Material, Fig. S5C) or tetracycline (Supplementary Material, Fig. S5D) at a molar ratio of 1 : 5 (protein compound). No significant spectral changes were observed in the three samples during a 1-week incubation at 37°C, indicating that EGCG and tetracycline are not able to redissolve mature AT3Q55 fibrils.

Both EGCG and tetracycline treatments reduce AT3Q55 cytotoxicity

We also examined the toxicity of AT3Q55 species formed in the presence or the absence of EGCG (Fig. 4A) or tetracycline (Fig. 4B) on the COS-7 cell line. AT3Q55 aliquots were added to the cellular medium and toxicity was assessed using the MTT assay (Fig. 4). When 3- or 6 h-preincubated AT3Q55 preparations were added to the cell cultures, MTT reduction dropped to ∼60% of the untreated cells. However, a statistically significant lower toxicity was determined when administering AT3Q55 aggregates generated in the presence of either EGCG (Fig. 4A) or tetracycline (Fig. 4B). The lack of any statistically significant differences between treated and not treated cells after a 24-h preincubation can be quite plausibly justified by the fact that oligomeric, toxic forms of amyloidogenic proteins, including AT3, evolve into non-toxic fibrils at later incubation times (31,32).

Transgenic worms expressing AT3 variants display a SCA3 phenotype

To evaluate the effect of the two compounds on AT3 toxicity *in vivo*, we used a SCA3 *C. elegans* model. A wild type (Q17) and an expanded form (Q130) of AT3 were expressed in the nervous system in fusion with GFP under the control of the pan neuronal promoter *unc-119*. The expression of the two proteins was monitored by confocal analysis using GFP fluorescence (Supplementary Material, Fig. S6). We observed that the fluorescence of both proteins was diffuse in the young animals (1 day; Supplementary Material, Fig. S6A) but in the older animals (4 days) a focal fluorescence distribution was detected in both nematode strains, although to a lesser extent in the AT3Q17-GFP-expressing worms (Supplementary Material, Fig. S6B). The amyloid nature of the aggregates formed only by the expanded protein was confirmed by X-34 staining (Supplementary Material, Fig. S6C).

We then evaluated the effect of AT3 expression on worm survival, which highlighted a significant reduction in lifespan compared with the wild-type strain (Fig. 5A; median survival: 6 days for N2, 4 days for AT3Q17-GFP and 3 days for AT3Q130-GFP strains). Since the lack of movement coordination is a hallmark of SCA3, we monitored the changes in mobility of the transgenic worms and determined the locomotion activity using the body bends assay (Fig. 5B). AT3Q130-GFP-expressing worms displayed an age-dependent uncoordinated movement, whereas older transgenic AT3Q17-GFP expressing worms showed a behavior similar to that of the N2 worms (data not shown). The

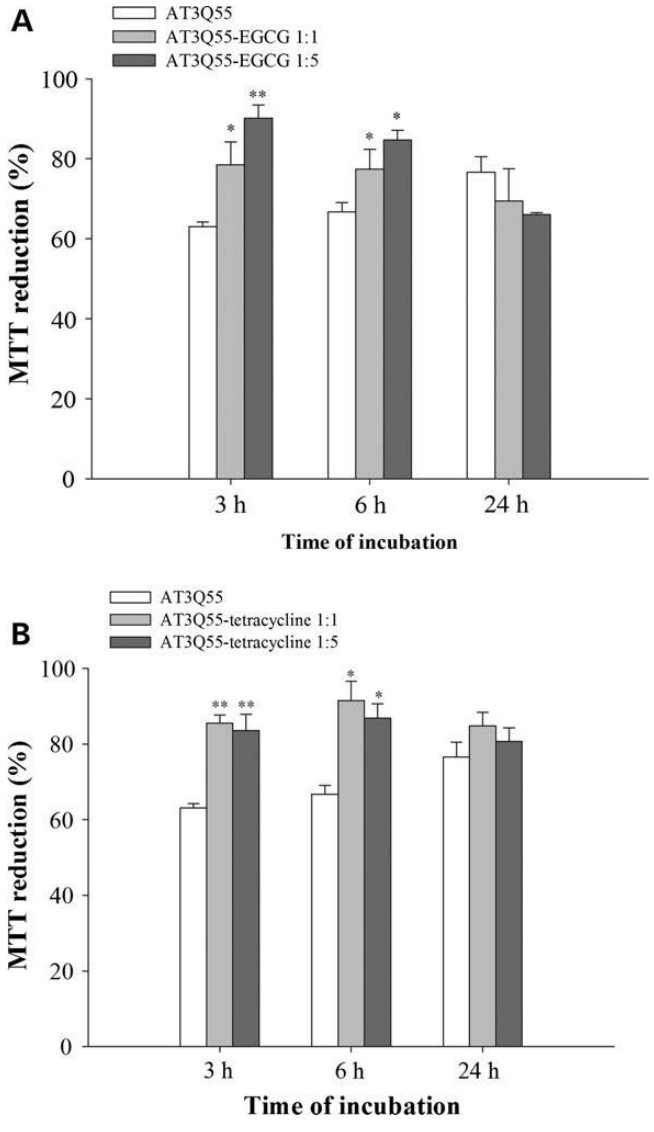

Figure 4. AT3Q55 toxicity assay. 25 μM AT3Q55 was incubated alone, with EGCG (**A**) or tetracycline (**B**) (molar ratio 1 : 1 and 1 : 5) for the indicated times, and aliquots were diluted in cell culture medium to a protein final concentration of 2.5 μM. Metabolic activity was monitored by MTT reduction. Bars represent standard errors and are derived from at least three independent experiments. Values are normalized to untreated cells; $^{*}P < 0.05$, $^{**}P < 0.01$.

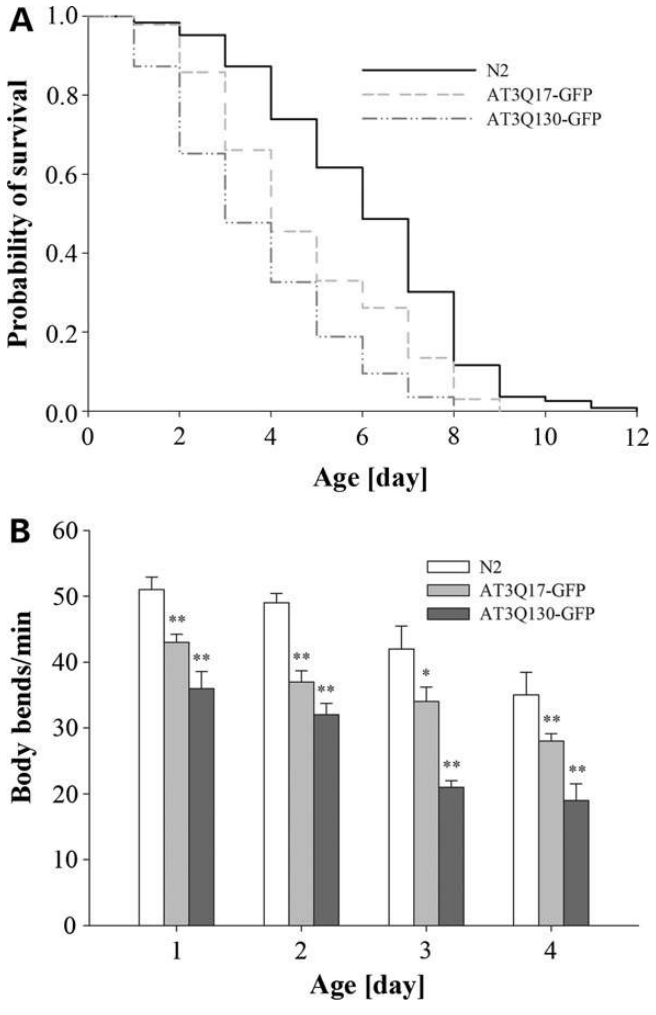

Figure 5. Phenotype of AT3 transgenic worms. (**A**) Kaplan–Meier survival curves of N2, AT3Q17-GFP and AT3Q130-GFP animals. One day-synchronized adult worms were placed in plates seeded with *E. coli*, cultured at 25°C and transferred to fresh plates for the following days. Survival rate was scored every day and expressed as probability of survival. Plots are representative of at least three independent experiments (40 animals for each strain). (**B**) Body bends on plate of N2, AT3Q17-GFP and AT3Q130-GFP worms. Worms were transferred daily on a new plate and body bends were counted for 20 s. Data are expressed as body bends/min and error bars represent standard errors. Plots are representative of at least three independent experiments (20 animals for each strain). $^{*}P < 0.05$, $^{**}P < 0.01$.

quantification of locomotion revealed a significant reduction in the number of body bends per min in AT3Q130-GFP worms in all days tested. A lesser reduction was also observed in AT3Q17-GFP transgenic worms (Fig. 5B). This characterization confirms the robustness of the model and supports the goodness of the body bends assay to test the pharmacological effect of drugs.

EGCG and tetracycline protect against AT3 toxicity in *C. elegans* model

We performed the body bends assay on worms treated with 0.1 mM EGCG (Fig. 6A) or 0.1 mM tetracycline (Fig. 6B). After 24 and 48 h of EGCG treatment, AT3Q130-GFP-expressing worms displayed a statistically significant increase in the number of body bends, i.e. 30 and 25%, respectively, compared with untreated worms (Fig. 6A). In the presence of tetracycline, we also observed a statistically significant increase, by 48 and 23%, respectively (Fig. 6B). Both compounds did not elicit any effect in AT3Q17-GFP-expressing worms, except for the treatment with EGCG for 48 h (15%; Fig. 6A). N2 motility was not affected at any times. For both compounds, no significant differences in motility were detected at earlier and later times of treatment (data not shown).

DISCUSSION

The green tea polyphenol EGCG and the antibiotic tetracycline are attractive candidates for the treatment of neurodegenerative

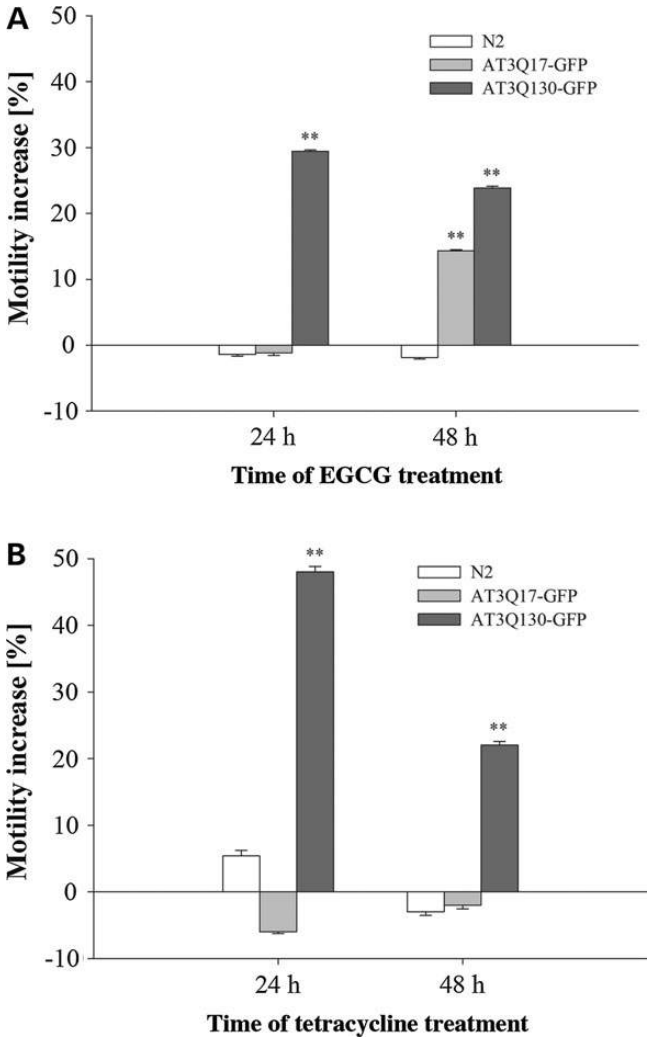

Figure 6. Pharmacological assay on AT3 transgenic worms. One day-synchronized adult worms were placed on a plate seeded with *E. coli* in the presence or absence of 0.1 mM EGCG (**A**) or 0.1 mM tetracycline (**B**) and cultured at 25°C. Body bends/min were scored after 24 or 48 h of treatment. Data are expressed as percentage of motility with respect to the untreated strain and error bars represent standard errors. Plots are representative of at least three independent experiments (15 animals for each strain). $^{*}P < 0.05$, $^{**}P < 0.01$.

diseases for their well-established anti-amyloidogenic effect (33–35), proven safety record in humans and blood–brain barrier permeability (16,36). As no cure or suitable therapeutic compound is available to date for SCA3 treatment, this study was undertaken to verify possible anti-amyloidogenic activity of EGCG and tetracycline on AT3 aggregation.

As regards the effects that the polyphenol EGCG exerts on AT3Q55 aggregation kinetics, we observed that, starting from 24 h, it substantially retarded the disappearance of soluble matter from supernatants of protein solutions incubated under aggregative conditions. Although this observation points to the compound capability to contrast amyloidogenesis, we observed that it also induced a significantly faster decline in the SDS-soluble fraction of the supernatants, especially at the molar ratio 1 : 5 protein-EGCG (Fig. 1A and C). This, in turn, was paralleled by a substantial accumulation of soluble, SDS-resistant species, which were unable to enter the separating gel (Fig. 1E and F). This pattern can be represented quantitatively (Supplementary Material, Fig. S7A and B) as time courses of SDS-soluble, SDS-resistant soluble and insoluble (pelleted) species. This makes it apparent that the massive appearance of soluble, SDS-resistant species is a hallmark of EGCG treatment, as in its absence they are scanty, if any, at any time.

Our findings raise the question as to whether soluble, SDS-resistant species are on- or off-pathway intermediates. Aggregation kinetics support the latter hypothesis, as they do not evolve into insoluble material, either after 72 h or even after a 2-week incubation, as outlined below. This idea was even more reinforced by FTIR analyses that highlighted dramatic structural differences between soluble, SDS-resistant species appearing in the presence of EGCG, and pelleted final aggregation products that accumulate in its absence. In particular, the former differ from final insoluble aggregates in that they do not display the 1604 cm^{-1} peak, assigned to glutamine side-chain hydrogen bond network, and also are much poorer in intermolecular β-sheets (peaks at ≈1635 and 1690 cm^{-1}). Thus, EGCG quite likely interferes at a very early step of the amyloid pathway, accelerating misfolding of the JD and redirecting the protein toward off-pathway aggregates, whose precise structural features have still to be defined in detail. Albeit not conclusively, our data support the idea that the drug is capable of binding monomeric rather than oligomeric AT3, as substantiated by the appearance of peculiar structural changes from the very beginning of the incubation (1 h), when the untreated protein has not yet undergone any appreciable structural modification. This plausibly suggests that EGCG directs AT3 towards the off-pathway by primarily acting on the monomeric protein. In keeping with this assumption, a previous report shows interaction of the drug with monomeric human serum albumin (37). Interestingly, another report shows that EGCG binds transthyretin tetramer, thus preventing its dissociation into monomers, which is the rate-limiting step for amyloid fibril formation (38). This finding also supports the view that the drug can interact with proteins before they undergo amyloid aggregation.

Consistent with the proposed aggregation pattern, AFM analysis confirmed substantial structural differences between the aggregates arisen in the presence and those in the absence of EGCG. In its presence, no mature fibrils were generated, but only larger spherical amorphous species, possibly resulting from oligomer clustering. Our results fit with the common hypothesis that EGCG prevents on-pathways, which lead to toxic amyloid oligomers and protofibrils (15). Actually, highly stable, off-pathway aggregates were assembled. This substantial change in the aggregation pattern quite likely underlies the protective effect of the drug we have detected on COS-7 cells by the MTT assay. The beneficial effect of the compound was also confirmed in the SCA3 *C. elegans* model, in which the EGCG treatment resulted in a significant increase in motility and improvement in locomotion in the diseased worms only.

Unlike EGCG, tetracycline did not apparently impact on the structural features of the aggregation intermediates, but drastically reduced the formation of insoluble (pelleted) aggregates, with scanty accumulation of soluble, SDS-resistant species (Supplementary Material, Fig. S7C). This was substantiated by both FTIR spectroscopy (Fig. 2D) and AFM analyses (Fig. 3).

FTIR did not demonstrate substantial modifications in aggregation kinetics and secondary structure compared with the untreated protein; in addition, AFM confirmed the formation of mature amyloid fibrils along with irregular and compact aggregates. Thus, although tetracycline treatment also results in some accumulation, at the latest incubation times, of soluble, SDS-resistant species (Fig. 1G; Supplementary Material, Fig. S7C), these are quite likely on-pathway intermediates committed to evolve into final insoluble fibrils, with which they share internal structure, as assessed by FTIR.

Unlike the present study, previous reports show that tetracycline dramatically inhibits fibrillogenesis of a set of other amyloidogenic proteins, notably PrP and α-synuclein (21). In spite of the lack of such an effect, our treatment also leads to a significant reduction in toxicity, as shown in the COS-7 cell line and the SCA3 *C. elegans* model. We suggest that the drug might bind to the surface of the growing oligomers and fibrils, with resulting substantial increase in their solubility (Fig. 1B, D and G; Supplementary Material, Fig. S5C), but with no major changes in their structural features (Figs 2D and 3). This, in turn, might also explain how the drug can substantially prevent the toxic effects of the oligomeric species, i.e. by masking the exposed hydrophobic patches. This does not rule out, of course, that subtle structural changes in the AT3 aggregates, undetectable by our analytical methods, may also occur.

Although previous reports show that EGCG and tetracycline are capable of remodeling and redissolving mature amyloid fibrils of different proteins (13,25), our FTIR results clearly demonstrate that these drugs do not affect the secondary structures of the AT3 mature fibrils (Supplementary Material, Fig. S5). This might be plausibly accounted for by the presence of glutamine side-chain hydrogen bonding that cooperatively contributes to the stability and irreversible aggregation of the SDS-insoluble polyQ mature fibers (31). Based on these observations, we conclude that the remodeling action does not represent an essential prerequisite for the protective effect to be exerted.

Our findings might also help better clarify previous results showing the drug protective effect towards a set of amyloid-generating proteins (39), considering in particular another polyQ-containing peptide, i.e. huntingtin exon-1 (15).

We are currently carrying on further structural analyses by NMR spectroscopy to precisely elucidate the mode of interaction between AT3 and either compound, including the functional groups involved, thus clarifying their different mechanisms of action. Finally, our work also confirms that our SCA3 *C. elegans* model proves to be a suitable tool for assessing a drug's capability of counteracting AT3 toxicity in living organisms.

MATERIALS AND METHODS

AT3Q55 purification

AT3Q55 gene was previously cloned in pQE30 vector and the protein was expressed in SG13009 (*Escherichia coli* K12 Nals, StrS, RifS, Thi−, Lac−, Ara+, Gal+, Mtl−, F−, RecA+, Uvr+, Lon+; Qiagen Hamburg GmbH, Hamburg, Germany) as His-tagged protein (31). Cells were grown at 37°C in 2TY–ampicillin–kanamycin medium, induced with 1 mM IPTG at OD_{600} 0.8 for 45 min at 30°C. To obtain crude extract, pelleted cells were resuspended in lysis buffer (5 ml/g wet weight; 25 mM potassium phosphate, pH 7.2, 150 mM NaCl, 0.5 mM phenylmethanesulfonyl fluoride, 10 mM imidazole, 10% glycerol, 1 mM 2-mercaptoethanol, 1 mg/ml lysozyme plus protease inhibitors cocktail) and incubated for 30 min at 4°C. The cell suspension was then sonicated in three pulses of 30 s each. DNase I (0.2 mg/g of cells, wet weight) was added, and the sample further incubated for 30 min at room temperature. Finally, it was centrifuged for 45 min at 20 000*g*. The supernatant was filtered through a 0.45-μm pore size SFCA membrane (Corning), loaded onto HisPur™ Cobalt Resin (Thermo Fisher Scientific, Rockford, IL, USA) and washed with 20 bed volumes of wash buffer (25 mM potassium phosphate, pH 7.2, 150 mM NaCl, 2 mM phenylmethanesulfonyl fluoride, 10 mM imidazole, 10% glycerol, 1 mM 2-mercaptoethanol). The bound protein was then eluted with elution buffer (25 mM potassium phosphate, pH 7.2, 150 mM NaCl, 2 mM phenylmethanesulfonyl fluoride, 150 mM imidazole, 10% glycerol, 1 mM 2-mercaptoethanol). Protein was stored at −80°C. Before each experiment, protein fractions were thawed and loaded onto a Superose 12 10/300 GL gel filtration column (GE Healthcare, Life Sciences, Little Chalfont, UK), pre-equilibrated with PBS buffer (25 mM potassium phosphate, pH 7.2, 150 mM NaCl). Elution was performed at a flow rate of 0.5 ml/min in the same buffer. Fractions were collected and protein content determined using Coomassie brilliant blue G-250 (Thermo Fisher Scientific) and bovine serum albumin as a standard protein.

SDS–PAGE and densitometry analysis of soluble protein fraction

Purified AT3Q55 (25 μM) was incubated at 37°C in PBS buffer in the presence or the absence of EGCG or tetracycline (Sigma-Aldrich, St. Louis, MO, USA) at a protein–compound molar ratio of 1 : 1 or 1 : 5. AT3 aliquots at different times of incubation (0, 3, 6, 24, 48 and 72 h) were centrifuged at 14 000*g* for 15 min and 10 μl of the supernatants were subjected to SDS–PAGE. The gels were stained with Imperial Protein Stain (Thermo Fisher Scientific), scanned at 700 nm with Odyssey® Fc System (LiCor, Lincoln, NE, USA) and analyzed with Image Studio software (LiCor).

FTIR spectroscopy

For FTIR analyses, purified AT3Q55 (25 μM, corresponding to ≈1 mg/ml) was incubated at 37°C in PBS buffer (25 mM potassium phosphate, pH 7.2, 150 mM NaCl) in the presence or the absence of EGCG or tetracycline at a protein–compound molar ratio 1 : 5. FTIR measurements of the protein semi-dry films were performed in attenuated total reflection (ATR) (40) as previously described (31,41,42). Briefly, a 3-μl aliquot of the samples at different times of incubation (0, 1, 3, 6, 24, 30, 48, 144 h and 2 weeks) was deposited on the single reflection diamond ATR plate (Golden Gate, CA, USA) and dried at room temperature so as to obtain a semi-dry protein film. ATR/FTIR spectra were measured using a Varian 670-IR spectrometer (Varian Australia Pty Ltd, Mulgrave, VIC, Australia) equipped with a nitrogen-cooled mercury cadmium telluride detector under the following conditions: 2 cm^{-1} spectral resolution, 25 kHz scan speed and 1000 scans co-addition and triangular apodization. The ATR–FTIR spectra of PBS and of the two compounds at 125 μM in PBS

were also collected at each incubation time at 37°C. The AT3Q55 spectra were obtained by subtraction of the proper reference spectra (Supplementary Material, Fig. S8). Second derivatives of the spectra were obtained by the Savitzky-Golay algorithm (5 points), after an 11-point binomial smoothing of the measured spectra, using the software Grams/AI (Thermogalactic, MA, USA). In a control experiment, the FTIR spectrum of freshly purified AT3Q55 in form of a semi-dry film was also measured in the transmission mode by an infrared microscope. In particular, a 3-μl aliquot of AT3Q55 in PBS was deposited on a BaF_2 window and dried at room temperature. The microFTIR absorption spectrum was acquired in the transmission mode using the Varian 610-IR infrared microscope coupled to a Varian 670-IR spectrometer (43,44). The second derivative of the absorption spectrum collected in the transmission mode (data not shown) displayed the same spectral features of that collected in the ATR mode, indicating that the ATR spectra are not affected by the interaction of the protein with the diamond surface of the ATR device.

Atomic force microscopy

AT3Q55 was purified by gel filtration, frozen at −80°C and thawed before the AFM experiments. AT3Q55 (25 μM) was incubated at 37°C in PBS buffer in the presence or absence of EGCG and tetracycline at a molar ratio protein–compound of 1 : 5. At fixed aggregation times, a 10-μl aliquot was withdrawn, incubated on a freshly cleaved mica substrate for 5 min, then rinsed with Milli-Q water and dried under mild vacuum. AFM images were acquired in tapping mode in air using a Dimension 3100 Scanning Probe Microscope equipped with a 'G' scanning head (maximum scan size 100 μm) and driven by a Nanoscope IIIa controller, and a Multimode Scanning Probe Microscope equipped with 'E' scanning head (maximum scan size 10 μm) and driven by a Nanoscope IVcontroller (Digital Instruments—Bruker). Single beam uncoated silicon cantilevers (type OMCL-AC160TS, Olympus) were used. The drive frequency was between 270 and 330 kHz, the scan rate between 0.5 and 0.8 Hz.

MTT assay

COS-7 cells were cultured in DMEM supplemented with 10% (v/v) fetal bovine serum, 100 U/ml penicillin, 100 μg/ml streptomycin and 4 mM L-glutamine, maintained at 37°C in a humidified 5% CO_2 incubator. For MTT assays, cells were trypsinized and plated at a density of 10 000 cells per well on 96-well plates in 100 μl fresh medium without phenol red. After 24 h, 25 μM AT3Q55 alone or co-incubated with the two compounds (1 : 1 and 1 : 5 molar ratio) at different times (3, 6 and 24 h) was added to the cell medium at a final concentration of 2.5 μM and cells were further incubated for 1 h at 37°C. Then MTT was added to the cells at a final concentration of 0.5 mg/ml. Absorbance values of formazan were determined at 570 nm with an automatic plate reader after 2 h.

Caenorhabditis elegans strains

AT3Q17 (wild type) and AT3Q130 (pathological form) cDNAs, cloned in pPD95.77 plasmid in frame with GFP, under control of pan neural promoter *unc-119*, were kindly provided by Dr Nobuyuki Nukina (45). The recombinant DNAs were injected at concentration of 5–20 ng/ml into the *lin-15(n765ts)* strain together with the LIN-15 rescuing plasmid. A wild-type Bristol N2 strain was used as control. All strains were grown at 25°C on solid nematode growth medium (NGM) seeded with *E. coli* (OP50) for food according to standard procedures (46). At least three independent lines for each construct were tested for the phenotype.

Worms age synchronization

To prepare age-synchronized animals, a small plate (3 ml) of nematodes was transferred onto a new large plate (25 ml) with fresh NGM agar seeded with *E. coli* (OP50) to obtain many eggs. After 2 or 3 days of incubation at 25°C, the population was collected in 2.5 ml of M9 buffer (42 mM Na_2HPO_4, 22 mM KH_2PO_4, 86 mM NaCl and 1 mM $MgSO_4$) and an equal volume of 4% glutaraldehyde was added. The suspension was incubated for 4 h at 4°C and, after a brief centrifugation, washed twice in M9 buffer. Half sector of a 25 ml plate was seeded with *E. coli*. Collected worms were put down to uninoculated sector of plate and incubated at 25°C (46).

Life-span assay

One day-synchronized adult worms were isolated and placed daily onto a fresh plate seeded with *E. coli* at 25°C. Surviving and dead animals were counted daily until all worms had died. The test was performed on 40 animals for each strain.

Body bends frequency test

One day-synchronized adult worms were placed onto a new plate and body bends per minute were counted under a microscope (Leica MZ FLIII, Leica Microsystem). The test was performed on 20 animals.

Pharmacological test

One day-synchronized adult worms were isolated and placed onto a fresh plate in the presence or the absence of 0.1 mM EGCG or tetracycline. The body bends test was performed after 24 and 48 h. For each treatment, 15 animals were used.

Statistical analysis

All experiments were done at least in triplicate. Data are presented as means ± SE. *P*-values were calculated using the Student's *t*-test. ($^{*}P < 0.05$, $^{**}P < 0.01$). For the life-span assay, animal survival was plotted using Kaplan–Meier survival curves. Significant differences at the $P < 0.05$ level were calculated by one-way ANOVA.

SUPPLEMENTARY MATERIAL

Supplementary Material is available at *HMG* online.

ACKNOWLEDGEMENTS

We thank Dr Nobuyuki Nukina for the gift of pPD95.77 plasmids and the *Caenorhabditis elegans* Genetics Centre for providing the N2 Bristol strain. We also thank Dr Anna Maria Villa for technical support in confocal microscopy analysis and Dr Diletta Ami for preliminary characterization of transgenic nematodes.

FUNDING

This work was supported by grants from Regione Lombardia, Italy (Network-Enabled Drug Design), Fondazione Cariplo, Italy (progetto Nobel: Network Operativo per la Biomedicina di Eccellenza in Lombardia), University of Milano-Bicocca (Fondo di Ateneo per la Ricerca) and University of Genoa (Fondi di Ateneo per la Ricerca).

Conflict of Interest statement. None declared.

REFERENCES

1. Gillmore, J.D. and Hawkins, P.N. (2006) Drug insight: emerging therapies for amyloidosis. *Nat. Clin. Pract. Nephrol.*, **2**, 263–270.
2. Sipe, J.D., Benson, M.D., Buxbaum, J.N., Ikeda, S.-I., Merlini, G., Saraiva, M.J.M. and Westermark, P. (2010) Amyloid fibril protein nomenclature: 2010 recommendations from the nomenclature committee of the International Society of Amyloidosis. *Amyloid*, **17**, 101–104.
3. Bucciantini, M., Calloni, G., Chiti, F., Formigli, L., Nosi, D., Dobson, C.M. and Stefani, M. (2004) Prefibrillar amyloid protein aggregates share common features of cytotoxicity. *J. Biol. Chem.*, **279**, 31374–31382.
4. Glabe, C.G. (2008) Structural classification of toxic amyloid oligomers. *J. Biol. Chem.*, **283**, 29639–29643.
5. Wickner, S., Maurizi, M.R. and Gottesman, S. (1999) Posttranslational quality control: folding, refolding, and degrading proteins. *Science*, **286**, 1888–1893.
6. De Lorenzi, E., Giorgetti, S., Grossi, S., Merlini, G., Caccialanza, G. and Bellotti, V. (2004) Pharmaceutical strategies against amyloidosis: old and new drugs in targeting a 'protein misfolding disease'. *Curr. Med. Chem.*, **11**, 1065–1084.
7. Commenges, D., Scotet, V., Renaud, S., Jacqmin-Gadda, H., Barberger-Gateau, P. and Dartigues, J.F. (2000) Intake of flavonoids and risk of dementia. *Eur. J. Epidemiol.*, **16**, 357–363.
8. Balentine, D.A., Wiseman, S.A. and Bouwens, L.C. (1997) The chemistry of tea flavonoids. *Crit. Rev. Food Sci. Nutr.*, **37**, 693–704.
9. Mandel, S.A. and Youdim, M.B.H. (2012) In the rush for green gold: can green tea delay age-progressive brain neurodegeneration?. *Recent Patents CNS Drug Discov.*, **7**, 205–217.
10. Suganuma, M., Okabe, S., Oniyama, M., Tada, Y., Ito, H. and Fujiki, H. (1998) Wide distribution of [3H](−)-epigallocatechin gallate, a cancer preventive tea polyphenol, in mouse tissue. *Carcinogenesis*, **19**, 1771–1776.
11. Henning, S.M., Niu, Y., Lee, N.H., Thames, G.D., Minutti, R.R., Wang, H., Go, V.L.W. and Heber, D. (2004) Bioavailability and antioxidant activity of tea flavanols after consumption of green tea, black tea, or a green tea extract supplement. *Am. J. Clin. Nutr.*, **80**, 1558–1564.
12. Rezai-Zadeh, K., Arendash, G.W., Hou, H., Fernandez, F., Jensen, M., Runfeldt, M., Shytle, R.D. and Tan, J. (2008) Green tea epigallocatechin-3-gallate (EGCG) reduces beta-amyloid mediated cognitive impairment and modulates tau pathology in Alzheimer transgenic mice. *Brain Res.*, **1214**, 177–187.
13. Bieschke, J., Russ, J., Friedrich, R.P., Ehrnhoefer, D.E., Wobst, H., Neugebauer, K. and Wanker, E.E. (2010) EGCG remodels mature alpha-synuclein and amyloid-beta fibrils and reduces cellular toxicity. *Proc. Natl. Acad. Sci. USA*, **107**, 7710–7715.
14. Ferreira, N., Cardoso, I., Domingues, M.R., Vitorino, R., Bastos, M., Bai, G., Saraiva, M.J. and Almeida, M.R. (2009) Binding of epigallocatechin-3-gallate to transthyretin modulates its amyloidogenicity. *FEBS Lett.*, **583**, 3569–3576.
15. Ehrnhoefer, D.E., Duennwald, M., Markovic, P., Wacker, J.L., Engemann, S., Roark, M., Legleiter, J., Marsh, J.L., Thompson, L.M., Lindquist, S. *et al.* (2006) Green tea (-)-epigallocatechin-gallate modulates early events in huntingtin misfolding and reduces toxicity in Huntington's disease models. *Hum. Mol. Genet.*, **15**, 2743–2751.
16. Choi, Y., Kim, H.-S., Shin, K.Y., Kim, E.-M., Kim, M., Kim, H.-S., Park, C.H., Jeong, Y.H., Yoo, J., Lee, J.-P. *et al.* (2007) Minocycline attenuates neuronal cell death and improves cognitive impairment in Alzheimer's disease models. *Neuropsychopharmacology*, **32**, 2393–2404.
17. Forloni, G., Salmona, M., Marcon, G. and Tagliavini, F. (2009) Tetracyclines and prion infectivity. *Infect. Disord. Drug Targets*, **9**, 23–30.
18. Noble, W., Garwood, C., Stephenson, J., Kinsey, A.M., Hanger, D.P. and Anderton, B.H. (2009) Minocycline reduces the development of abnormal tau species in models of Alzheimer's disease. *FASEB J.*, **23**, 739–750.
19. Cardoso, I. and Saraiva, M.J. (2006) Doxycycline disrupts transthyretin amyloid: evidence from studies in a FAP transgenic mice model. *FASEB J.*, **20**, 234–239.
20. Ono, K. and Yamada, M. (2006) Antioxidant compounds have potent anti-fibrillogenic and fibril-destabilizing effects for alpha-synuclein fibrils in vitro. *J. Neurochem.*, **97**, 105–115.
21. Giorgetti, S., Raimondi, S., Pagano, K., Relini, A., Bucciantini, M., Corazza, A., Fogolari, F., Codutti, L., Salmona, M., Mangione, P. *et al.* (2011) Effect of tetracyclines on the dynamics of formation and destructuration of beta2-microglobulin amyloid fibrils. *J. Biol. Chem.*, **286**, 2121–2131.
22. Forloni, G., Colombo, L., Girola, L., Tagliavini, F. and Salmona, M. (2001) Anti-amyloidogenic activity of tetracyclines: studies in vitro. *FEBS Lett.*, **487**, 404–407.
23. Diomede, L., Cassata, G., Fiordaliso, F., Salio, M., Ami, D., Natalello, A., Doglia, S.M., De Luigi, A. and Salmona, M. (2010) Tetracycline and its analogues protect *Caenorhabditis elegans* from β amyloid-induced toxicity by targeting oligomers. *Neurobiol. Dis.*, **40**, 424–431.
24. Airoldi, C., Colombo, L., Manzoni, C., Sironi, E., Natalello, A., Doglia, S.M., Forloni, G., Tagliavini, F., Del Favero, E., Cantù, L. *et al.* (2011) Tetracycline prevents Aβ oligomer toxicity through an atypical supramolecular interaction. *Org. Biomol. Chem.*, **9**, 463–472.
25. Stoilova, T., Colombo, L., Forloni, G., Tagliavini, F. and Salmona, M. (2013) A new face for old antibiotics: tetracyclines in treatment of amyloidoses. *J. Med. Chem.*, **56**, 5987–6006.
26. Glabe, C.G. (2006) Common mechanisms of amyloid oligomer pathogenesis in degenerative disease. *Neurobiol. Aging*, **27**, 570–575.
27. Stefani, M. (2012) Structural features and cytotoxicity of amyloid oligomers: implications in Alzheimer's disease and other diseases with amyloid deposits. *Prog. Neurobiol.*, **99**, 226–245.
28. Barth, A. (2007) Infrared spectroscopy of proteins. *Biochim. Biophys. Acta*, **1767**, 1073–1101.
29. Seshadri, S., Khurana, R. and Fink, A.L. (1999) Fourier transform infrared spectroscopy in analysis of protein deposits. *Methods Enzymol.*, **309**, 559–576.
30. Susi, H. and Byler, D.M. (1986) Resolution-enhanced Fourier transform infrared spectroscopy of enzymes. *Methods Enzymol.*, **130**, 290–311.
31. Natalello, A., Frana, A.M., Relini, A., Apicella, A., Invernizzi, G., Casari, C., Gliozzi, A., Doglia, S.M., Tortora, P. and Regonesi, M.E. (2011) A major role for side-chain polyglutamine hydrogen bonding in irreversible ataxin-3 aggregation. *PLoS ONE*, **6**, e18789.
32. Bucciantini, M., Giannoni, E., Chiti, F., Baroni, F., Formigli, L., Zurdo, J., Taddei, N., Ramponi, G., Dobson, C.M. and Stefani, M. (2002) Inherent toxicity of aggregates implies a common mechanism for protein misfolding diseases. *Nature*, **416**, 507–511.
33. Kopito, R.R. (2000) Aggresomes, inclusion bodies and protein aggregation. *Trends Cell Biol.*, **10**, 524–530.
34. Garcia-Mata, R., Gao, Y.-S. and Sztul, E. (2002) Hassles with taking out the garbage: aggravating aggresomes. *Traffic Cph. Den.*, **3**, 388–396.
35. Gales, L., Cortes, L., Almeida, C., Melo, C.V., Costa, M. do C., Maciel, P., Clarke, D.T., Damas, A.M. and Macedo-Ribeiro, S. (2005) Towards a structural understanding of the fibrillization pathway in Machado-Joseph's disease: trapping early oligomers of non-expanded ataxin-3. *J. Mol. Biol.*, **353**, 642–654.
36. Wu, L., Zhang, Q.-L., Zhang, X.-Y., Lv, C., Li, J., Yuan, Y. and Yin, F.-X. (2012) Pharmacokinetics and blood-brain barrier penetration of (+)-catechin and (−)-epicatechin in rats by microdialysis sampling coupled to high-performance liquid chromatography with chemiluminescence detection. *J. Agric. Food Chem.*, **60**, 9377–9383.

37. Maiti, T.K., Ghosh, K.S. and Dasgupta, S. (2006) Interaction of (-)-epigallocatechin-3-gallate with human serum albumin: fluorescence, fourier transform infrared, circular dichroism, and docking studies. *Proteins*, **64**, 355–362.
38. Miyata, M., Sato, T., Kugimiya, M., Sho, M., Nakamura, T., Ikemizu, S., Chirifu, M., Mizuguchi, M., Nabeshima, Y., Suwa, Y. *et al.* (2010) The crystal structure of the green tea polyphenol (−)-epigallocatechin gallate-transthyretin complex reveals a novel binding site distinct from the thyroxine binding site. *Biochemistry*, **49**, 6104–6114.
39. Cheng, B., Gong, H., Xiao, H., Petersen, R.B., Zheng, L. and Huang, K. (2013) Inhibiting toxic aggregation of amyloidogenic proteins: a therapeutic strategy for protein misfolding diseases. *Biochim. Biophys. Acta*, **1830**, 4860–4871.
40. Goormaghtigh, E., Raussens, V. and Ruysschaert, J.-M. (1999) Attenuated total reflection infrared spectroscopy of proteins and lipids in biological membranes. *Biochim. Biophys. Acta*, **1422**, 105–185.
41. Apicella, A., Natalello, A., Frana, A.M., Baserga, A., Casari, C.S., Bottani, C.E., Doglia, S.M., Tortora, P. and Regonesi, M.E. (2012) Temperature profoundly affects ataxin-3 fibrillogenesis. *Biochimie*, **94**, 1026–1031.
42. Santambrogio, C., Frana, A.M., Natalello, A., Papaleo, E., Regonesi, M.E., Doglia, S.M., Tortora, P., Invernizzi, G. and Grandori, R. (2012) The role of the central flexible region on the aggregation and conformational properties of human ataxin-3. *FEBS J.*, **279**, 451–463.
43. Ami, D., Natalello, A., Taylor, G., Tonon, G. and Doglia, S.M. (2006) Structural analysis of protein inclusion bodies by Fourier transform infrared microspectroscopy. *Biochim. Biophys. Acta*, **1764**, 793–799.
44. Invernizzi, G., Aprile, F.A., Natalello, A., Ghisleni, A., Penco, A., Relini, A., Doglia, S.M., Tortora, P. and Regonesi, M.E. (2012) The relationship between aggregation and toxicity of polyglutamine-containing ataxin-3 in the intracellular environment of *Escherichia coli*. *PLoS ONE*, **7**, e51890.
45. Khan, L.A., Bauer, P.O., Miyazaki, H., Lindenberg, K.S., Landwehrmeyer, B.G. and Nukina, N. (2006) Expanded polyglutamines impair synaptic transmission and ubiquitin-proteasome system in *Caenorhabditis elegans*. *J. Neurochem.*, **98**, 576–587.
46. Brenner, S. (1974) The genetics of *Caenorhabditis elegans*. *Genetics*, **77**, 71–94.

SUPPORTING INFORMATION

Materials and Methods

Fluorescence microscopy and amyloid staining

1-day or 4-days transgenic worms were placed in PBS buffer drop with 5% glycerol and anesthetized with 1% sodium azide. GFP fluorescence was observed using a Leica Mod. TCS-SP2 (Leica Microsystem) and image processing was performed with Leica Confocal Software (LCS). For the X-34 staining, worms were incubated with 1 mM X-34 in 10 mM Tris/HCl pH 8.0 for 2 h, and then analyzed as above.

Fig. S1 SEC profiles of AT3Q55 on a Superose 12 10/300 GL in PBS buffer. (A) 10 mg His-tagged AT3Q55 was loaded onto a gel filtration column. The arrow indicates the peak corresponding to the AT3Q55 monomeric form. (B) 2 mg of monomeric AT3Q55 was reloaded onto the same column.

Fig. S2 SDS-PAGE (12%) of freshly purified AT3Q55. (A) SDS-gel (5 μg protein) stained with Imperial Protein Stain (Thermo Scientific Rockford, IL USA), along with molecular weight markers; (B) western blot (1 μg protein) performed using anti-AT3 Z46 polyclonal antibody, as previously reported (31).

Fig. S3 SDS-PAGE (12%) of the soluble protein fraction of AT3Q55-EGCG 1:1 and AT3Q55-tetracycline 1:1. The gels were stained with Imperial Protein Stain (Thermo Scientific Rockford, IL USA).

Fig. S4 SEC profiles of AT3Q55 on a Superose 12 10/300 GL in PBS buffer after incubation with either EGCG or tetracycline. 500 μg AT3Q55 was loaded onto a gel filtration column after the indicated incubation times with either drugs. Other details are reported in the Section Materials and Methods.

Fig. S5 FTIR spectra of AT3Q55 fibrils. (A) Absorption spectrum (bold line) and its second derivative in the amide I region of AT3Q55 fibrils obtained by centrifugation of the protein solution upon incubation at 37°C for two weeks. (B-C-D) Second derivative spectra of AT3Q55 fibrils resuspended in PBS (B), EGCG (C) and tetracycline (D) collected at different times of incubation at 37°C. Band assignment of the main components is reported in (B).

Fig. S6 Confocal microscopy analyses of AT3 expression. AT3Q17-GFP and AT3Q130-GFP expression in the 1-day animals (A) and in the 4-days animals (B) grown at 25°C was detected by GFP fluorescence. 4-days animals expressing the AT3 variants were stained for 2 h with 1 mM X-34 dye (C).

Fig. S7 Effect of EGCG and tetracycline on the time course of AT3Q55 aggregation. No drug added (A), EGCG (B), tetracycline (C). Protein-drug molar ratio was 1:5. Total soluble protein fraction was determined by the Bradford assay on supernatants after centrifuging the incubation mixtures at 14.000 x *g*. SDS-soluble fraction was quantified densitometrically in SDS-PAGE of the supernatants. Both were expressed as percentage of zero time. Soluble, SDS-resistant fraction was quantified by subtracting SDS-soluble from total soluble fraction. Insoluble fraction (expressed as percentage of total protein) was calculated as: 100 – total soluble fraction.

Fig. S8 Subtraction procedure in the ATR/FTIR analyses. A representative spectrum substraction procedure is shown, as accomplished in the case of AT3Q55 in the presence of tetracycline. The following absorption spectra (bottom panel) are shown: 25 μM freshly purified AT3Q55 in PBS and in the presence of 125 μM tetracycline (A); 125 μM tetracycline in PBS (B); AT3Q55 after reference spectrum subtraction (C=A-B). In the second derivative (top panel) of AT3Q55 subtracted spectrum (D) the ≈ 1595 cm^{-1} tetracycline peak (see spectra D and E) is not present, highlighting a successful subtraction procedure.

Fig S1

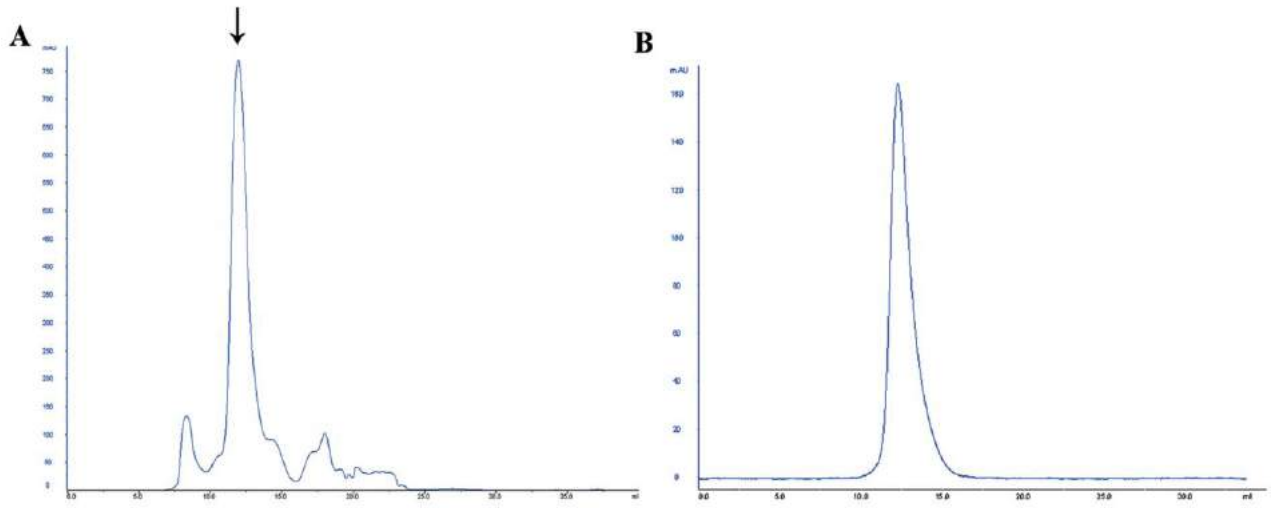

Fig S2

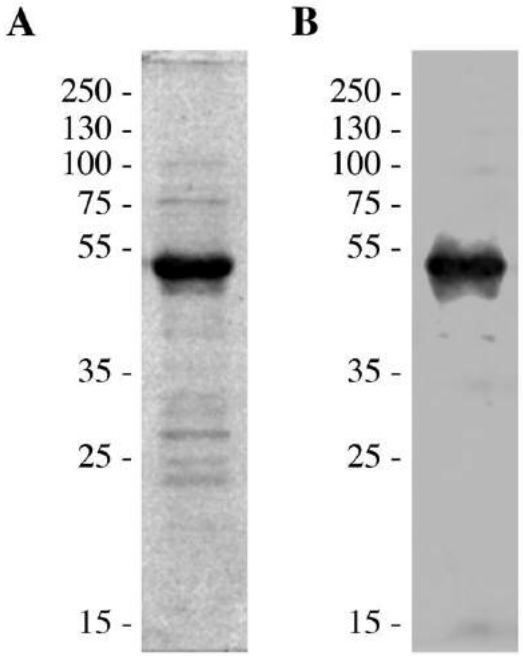
A
B
250 -
130 -
100 -
75 -
55 -
35 -
25 -
15 -
250 -
130 -
100 -
75 -
55 -
35 -
25 -
15 -

Fig S3

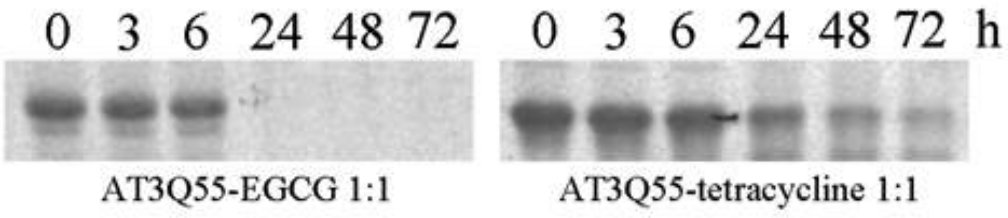
0 3 6 24 48 72
0 3 6 24 48 72 h
AT3Q55-EGCG 1:1
AT3Q55-tetracycline 1:1

Fig S4

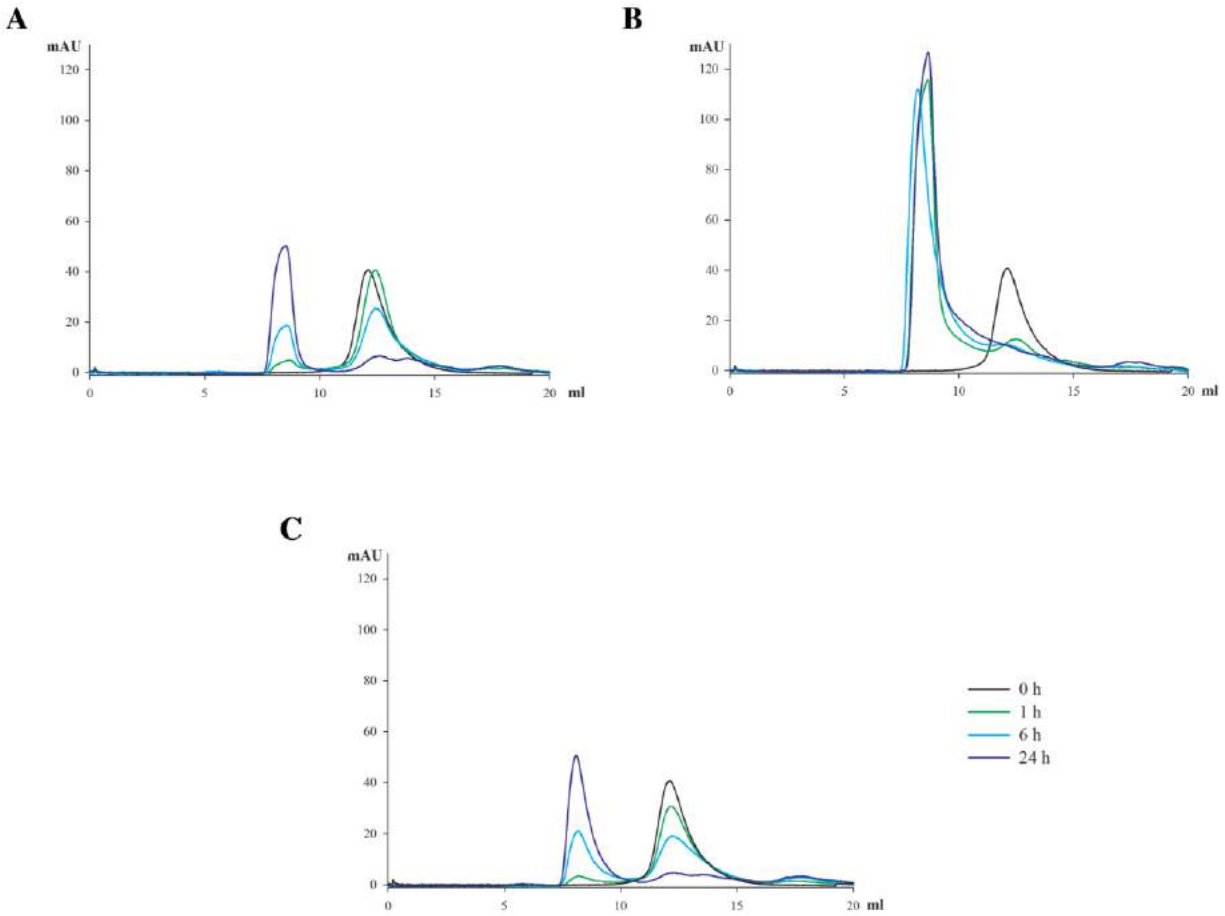

Fig S5

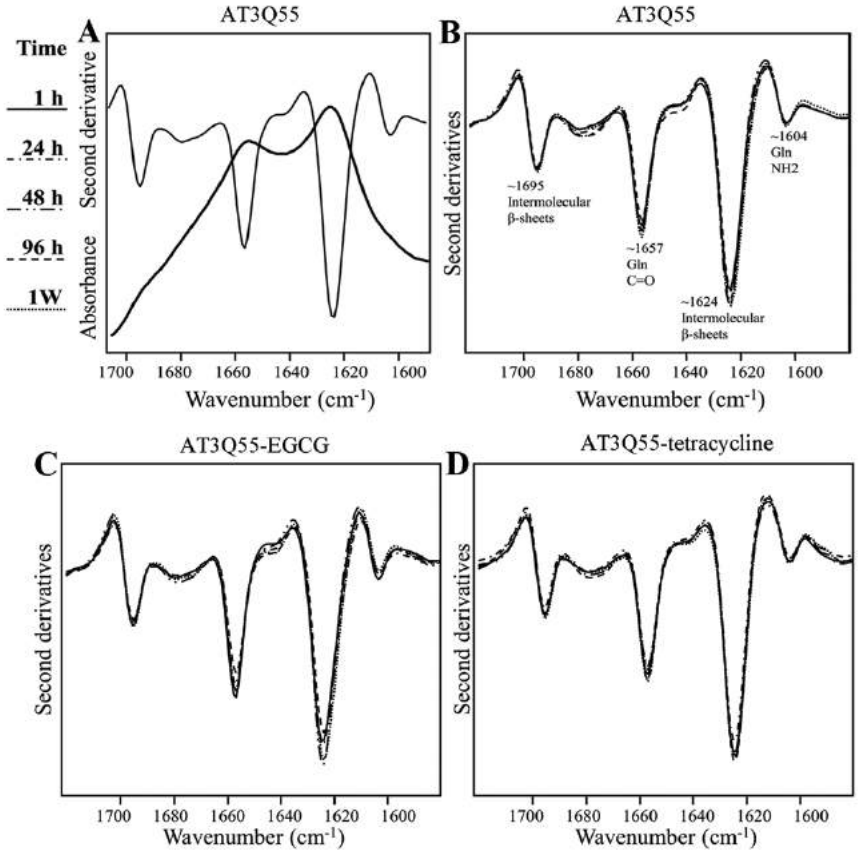
A
AT3Q55
Time
1 h
24 h
48 h
96 h
1W
Second derivative
Absorbance
1700 1680 1660 1640 1620 1600
Wavenumber (cm-1)
B
AT3Q55
Second derivatives
~1695
Intermolecular
β-sheets
~1657
Gln
C=O
~1624
Intermolecular
β-sheets
~1604
Gln
NH2
1700 1680 1660 1640 1620 1600
Wavenumber (cm-1)
C
AT3Q55-EGCG
Second derivatives
1700 1680 1660 1640 1620 1600
Wavenumber (cm-1)
D
AT3Q55-tetracycline
Second derivatives
1700 1680 1660 1640 1620 1600
Wavenumber (cm-1)

Fig S6

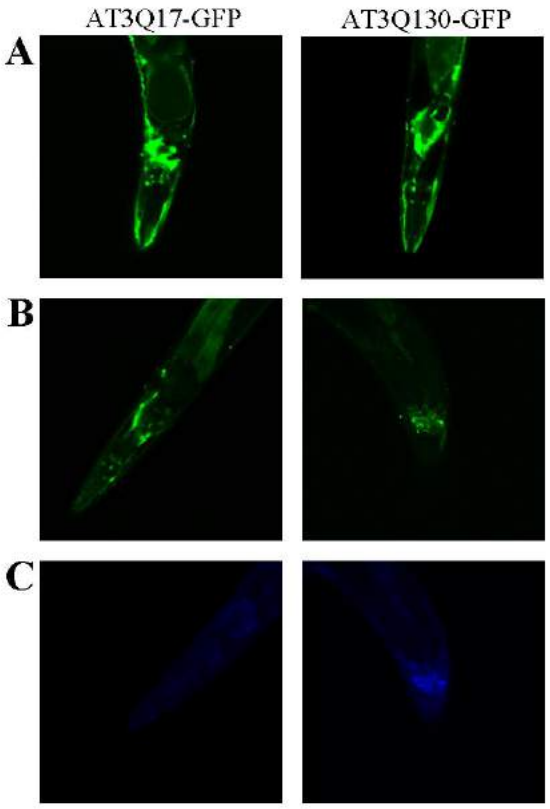

Fig S7

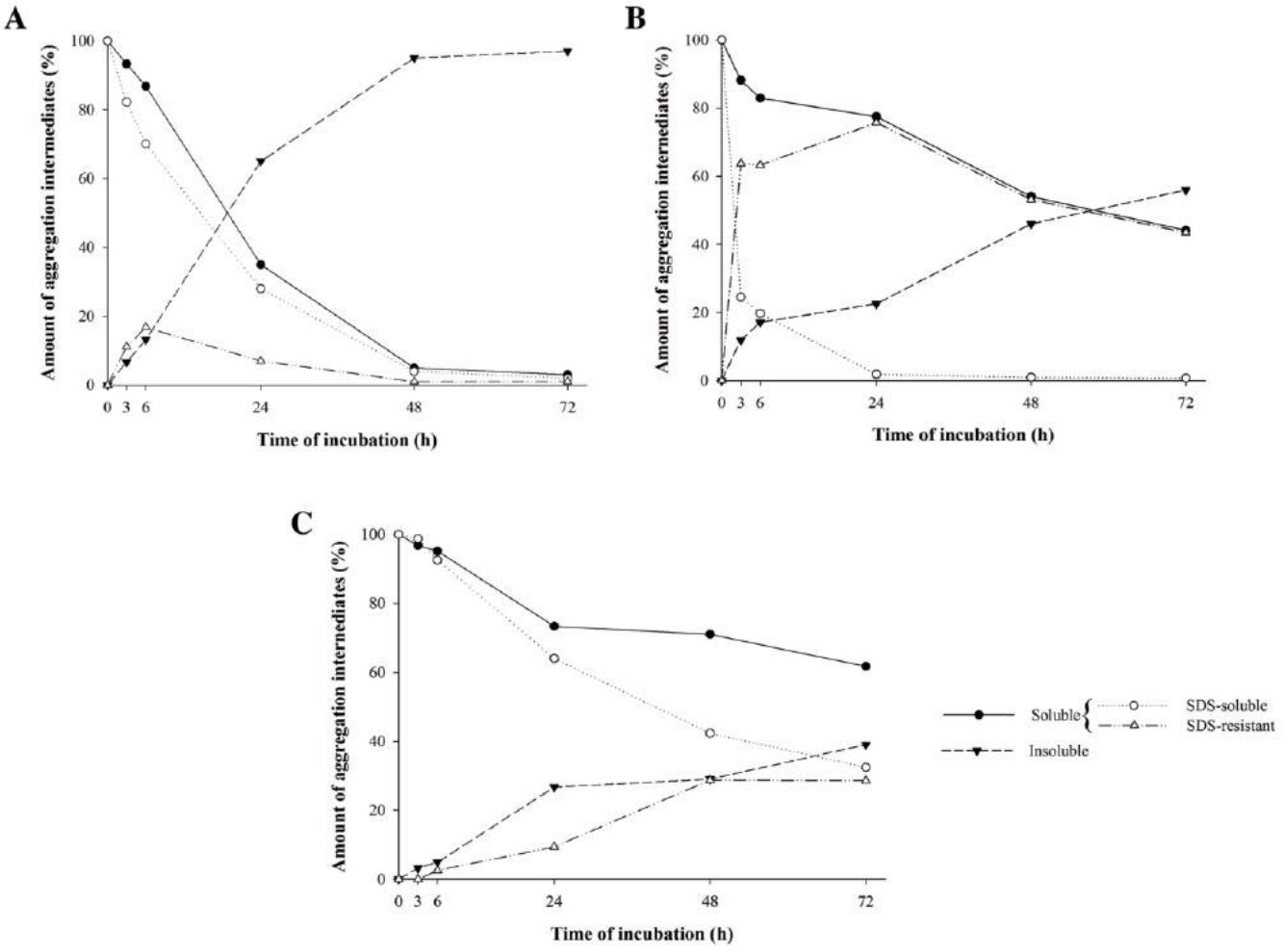
A
B
C
Amount of aggregation intermediates (%)
Time of incubation (h)
0 3 6 24 48 72
0 20 40 60 80 100
Soluble
SDS-soluble
SDS-resistant
Insoluble

Fig S8

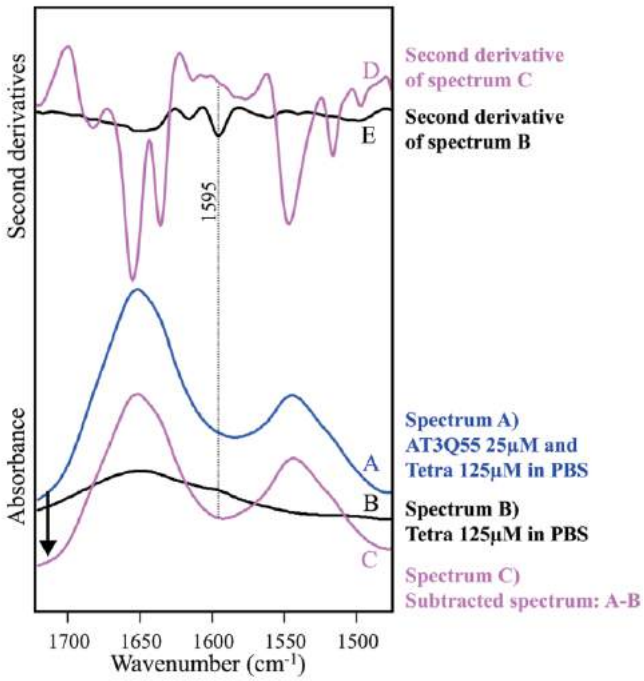
Second derivatives
Absorbance
1595
D
E
A
B
C
Second derivative of spectrum C
Second derivative of spectrum B
Spectrum A) AT3Q55 25µM and Tetra 125µM in PBS
Spectrum B) Tetra 125µM in PBS
Spectrum C) Subtracted spectrum: A-B
1700
1650
1600
1550
1500
Wavenumber (cm-1)

ChemPubSoc Europe

DOI: 10.1002/chem.201503086

CHEMISTRY A European Journal Full Paper

Molecular Recognition

How Epigallocatechin-3-gallate and Tetracycline Interact with the Josephin Domain of Ataxin-3 and Alter Its Aggregation Mode

Marcella Bonanomi,[a] Cristina Visentin,[a] Antonino Natalello,[a, b, c] Michela Spinelli,[a, d] Marco Vanoni,[a, c, d] Cristina Airoldi,*[a, c, d] Maria E. Regonesi,*[a, c] and Paolo Tortora[a, c]

Abstract: Epigallocatechin-3-gallate (EGCG) and tetracycline are two known inhibitors of amyloid aggregation able to counteract the fibrillation of most of the proteins involved in neurodegenerative diseases. We have recently investigated their effect on ataxin-3 (AT3), the polyglutamine-containing protein responsible for spinocerebellar ataxia type 3. We previously showed that EGCG and tetracycline can contrast the aggregation process and toxicity of expanded AT3, although by different mechanisms. Here, we have performed further experiments by using the sole Josephin domain (JD) to further elucidate the mechanism of action of the two compounds. By protein solubility assays and FTIR spectroscopy we have first observed that EGCG and tetracycline affect the JD aggregation essentially in the same way displayed when acting on the full-length expanded AT3. Then, by saturation transfer difference (STD) NMR experiments, we have shown that EGCG binds both the monomeric and the oligomeric JD form, whereas tetracycline can only interact with the oligomeric one. Surface plasmon resonance (SPR) analysis has confirmed the capability of the sole EGCG to bind monomeric JD, although with a K_D value suggestive for a non-specific interaction. Our investigations provide new details on the JD interaction with EGCG and tetracycline, which could explain the different mechanisms by which the two compounds reduce the toxicity of AT3.

Introduction

Spinocerebellar ataxia type 3 (SCA3), also known as Machado–Joseph disease, is one among several polyglutamine (polyQ) diseases, autosomal dominantly inherited neurodegenerative disorders that also include Huntington's disease. They are caused by unstable expansions of $(CAG)_n$ trinucleotide-repeated sequences at disease-specific gene loci that are translated into elongated polyQ tracts.[1–3] Ataxin-3 (AT3) is the protein that triggers SCA3 when its polyQ stretch exceeds a critical length of about 55 consecutive residues.[4,5] AT3 consists of a globular N-terminal domain, the so-called Josephin domain (JD), and a flexible tail containing the polyQ tract.[6] By comparing different polyQ proteins, it appears that the protein context surrounding the polyQ tract can differently affect aggregation pathways and kinetics. In the case of AT3, extensive studies have focused on the intrinsic amyloidogenic properties of the JD, as well as on the role of the polyQ expansion on protein stability and aggregation kinetics.[7,8] It is known that the expansion of the polyQ tract beyond a critical threshold triggers misfolding and protein aggregation into sodium dodecyl sulfate (SDS)-insoluble amyloid fibrils.[9] Nevertheless, it has been demonstrated that the first step of the fibrillation is reversible, polyQ-independent, and proceeds through aggregation of the JD.[10,11]

Recently, we further characterized the aggregation intermediates of an expanded AT3 variant.[12] This is a prerequisite to correlate the protein structure with the toxicity and to determine the capability of specific compounds to counteract one or both steps of AT3 aggregation. In fact, by biochemical and biophysical approaches, we have recently demonstrated that epigallocatechin-3-gallate (EGCG) and tetracycline (Figure 1) can contrast the aggregation and toxicity of expanded AT3, although by different mechanisms.[13] EGCG is a polyphenolic flavonoid widely considered to be the key bioactive ingredient of green tea. It has been extensively studied, primarily for its beneficial effects, ranging from antitumor and anti-inflammatory properties to neuroprotective behavior. In fact, EGCG has been reported to affect multiple biological pathways, such as gene expression, growth-factor-mediated signaling, and antioxidant pathways.[14–16] Also, it is endowed with well-established metal-chelating properties.[17] However,

[a] Dr. M. Bonanomi,[+] C. Visentin,[+] Dr. A. Natalello, Dr. M. Spinelli, Prof. M. Vanoni, Dr. C. Airoldi, Dr. M. E. Regonesi, Prof. P. Tortora
Department of Biotechnology and Biosciences, University of Milano-Bicocca
Piazza della Scienza 2, 20126 Milano (Italy)
E-mail: cristina.airoldi@unimib.it
mariaelena.regonesi@unimib.it

[b] Dr. A. Natalello
Consorzio Nazionale Interuniversitario per le Scienze Fisiche della Materia (CNISM), UdR Milano-Bicocca, Milano (Italy)

[c] Dr. A. Natalello, Prof. M. Vanoni, Dr. C. Airoldi, Dr. M. E. Regonesi, Prof. P. Tortora
Milan Center of Neuroscience (NeuroMI), 20126 Milano (Italy)

[d] Dr. M. Spinelli, Prof. M. Vanoni, Dr. C. Airoldi
SysBio Centre for Systems Biology, Milano and Rome (Italy)

[+] These authors contributed equally to this work.

Supporting information for this article is available on the WWW under http://dx.doi.org/10.1002/chem.201503086.

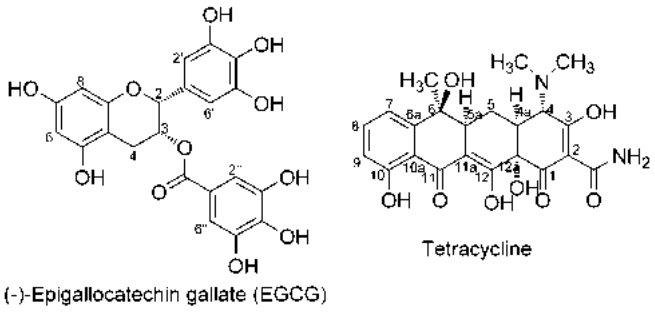

Figure 1. Structure and numbering of EGCG and tetracycline.

a wealth of data indicates that the antioxidant/metal-chelating capability of EGCG is unlikely to be the sole explanation for its neuro-rescue capacity. Plenty of works report on the capability of EGCG to interfere with the aggregation process of many amyloid proteins. It has been demonstrated that EGCG is able to inhibit the formation of toxic oligomers by steering misfolded Aβ,[18] α-synuclein,[19] transthyretin,[20] and mutant huntingtin[21] away from folding pathways that lead to amyloidogenic β-sheet-rich structures toward unstructured, non-toxic forms, either by binding the protein directly or possibly by acting as a protein chaperone. However, how EGCG works is not entirely clear. Its action seems to be largely independent of the primary sequence of the protein, given its capability to bind to unfolded bovine serum albumin[22] just as readily as to Aβ and α-synuclein.[23] A recent paper of ours also supports this view, as we characterized by saturation transfer difference (STD) NMR spectroscopy the binding of EGCG and other catechins to Aβ, PrP106-126, and AT3 oligomers.[24] All these data suggest that EGCG targets the only feature shared by the diverse proteins, that is, the polypeptide main chain.

Another well-studied class of natural compounds are tetracyclines, bacteriostatic agents with anti-inflammatory and remarkable neuroprotective properties. Major biological effects of tetracyclines are the inhibition of microglial activation, the attenuation of apoptosis, and the suppression of the production of reactive oxygen species.[25] These mechanisms are involved in the pathogenesis of several neurodegenerative diseases. Furthermore, numerous studies have demonstrated that such compounds are able to prevent fibrillogenesis of prion proteins (PrPs),[26] transthyretin,[27] α-synuclein,[28] β2-microglobulin,[29] and Aβ,[29,30] and, in most of these cases, to dissolve mature fibrils. In particular, it has been established that fibrillogenesis inhibition is a result of non-specific interactions with the different proteins. In this respect, by combining NMR spectroscopy, atomic force microscopy (AFM), FTIR spectroscopy and surface plasmon resonance (SPR) spectroscopy, we showed that co-incubation of tetracycline with Aβ oligomers leads to the formation of colloidal particles that specifically sequester oligomers, thus preventing the progression of the amyloid cascade.[31]

In a previous work, we have demonstrated that EGCG affects the AT3 aggregation pathway by a mechanism similar to that reported for the other mentioned amyloid proteins. In fact, EGCG is able to interfere with the early steps of AT3 aggregation and leads to the formation of off-pathway, non-amyloid, SDS-stable final aggregates. In contrast, tetracycline does not produce major alterations in the structural features of the aggregation intermediates but substantially increases their solubility. Nevertheless, both compounds reduce the toxicity of protein aggregates, as confirmed by their beneficial in vivo effects by using the transgenic *Caenorhabditis elegans* SCA3 model.[13]

Here, we report NMR investigations aimed at providing insight into the mode of interaction of these compounds with the JD, the sole structured part of AT3. For this purpose, we employed both ligand-based and receptor-based NMR methods.[32] We have demonstrated, by using protein solubility assays and FTIR spectroscopy, that the mechanism by which both compounds, EGCG and tetracycline, affect JD aggregation is essentially the same as that observed in the case of expanded AT3.[13] These results further demonstrate the direct involvement of the JD in full-length AT3 fibrillation. By STD NMR experiments we have clearly shown that EGCG is able to bind both the monomeric and the oligomeric JD form, whereas tetracycline can only interact with the oligomeric one. These results strongly support the hypothesis that the capability of EGCG of interfering with the early steps of AT3 aggregation and redirect the process towards a different pathway is due to its ability to bind the monomeric JD. This could account for the different action mechanisms of the two compounds.

Results and Discussion

EGCG and tetracycline differently affect JD aggregation

In a previous work, we demonstrated that EGCG and tetracycline differently modulate the aggregation pathway of an expanded AT3 variant,[13] the former generating SDS-resistant, β-sheet-poor, soluble aggregates, the latter giving rise to aggregated species resembling those arising in the absence of any compound, but substantially more soluble. To further elucidate the mechanism of action of the two compounds, we have examined whether they exert the same effect on JD aggregation, that is, aggregation of the structured N-terminal protein domain. The rationale of our approach relies upon the well-established notion that the aggregation process of full-length AT3, irrespective of the polyQ size, starts with JD misfolding and aggregation, which triggers the earliest steps of expanded AT3 fibrillation.[10,11] Thus, quite plausibly, any treatment affecting or preventing JD aggregation would also affect or prevent the process at the level of full-length AT3.

A His-tagged JD was purified by affinity chromatography and the monomeric form was isolated by size-exclusion chromatography (Figure S1 in the Supporting Information). The protein was then incubated at 37 °C in the presence or the absence of either compound at molar ratios of protein/drug of 1:5. Aliquots were taken at different incubation times and the soluble fraction was isolated as the supernatant from a centrifugation at 14000 *g*. The SDS-soluble protein fraction was quantified by sodium dodecyl sulfate polyacrylamide gel electrophoresis (SDS-PAGE) of the supernatants and subsequent densito-

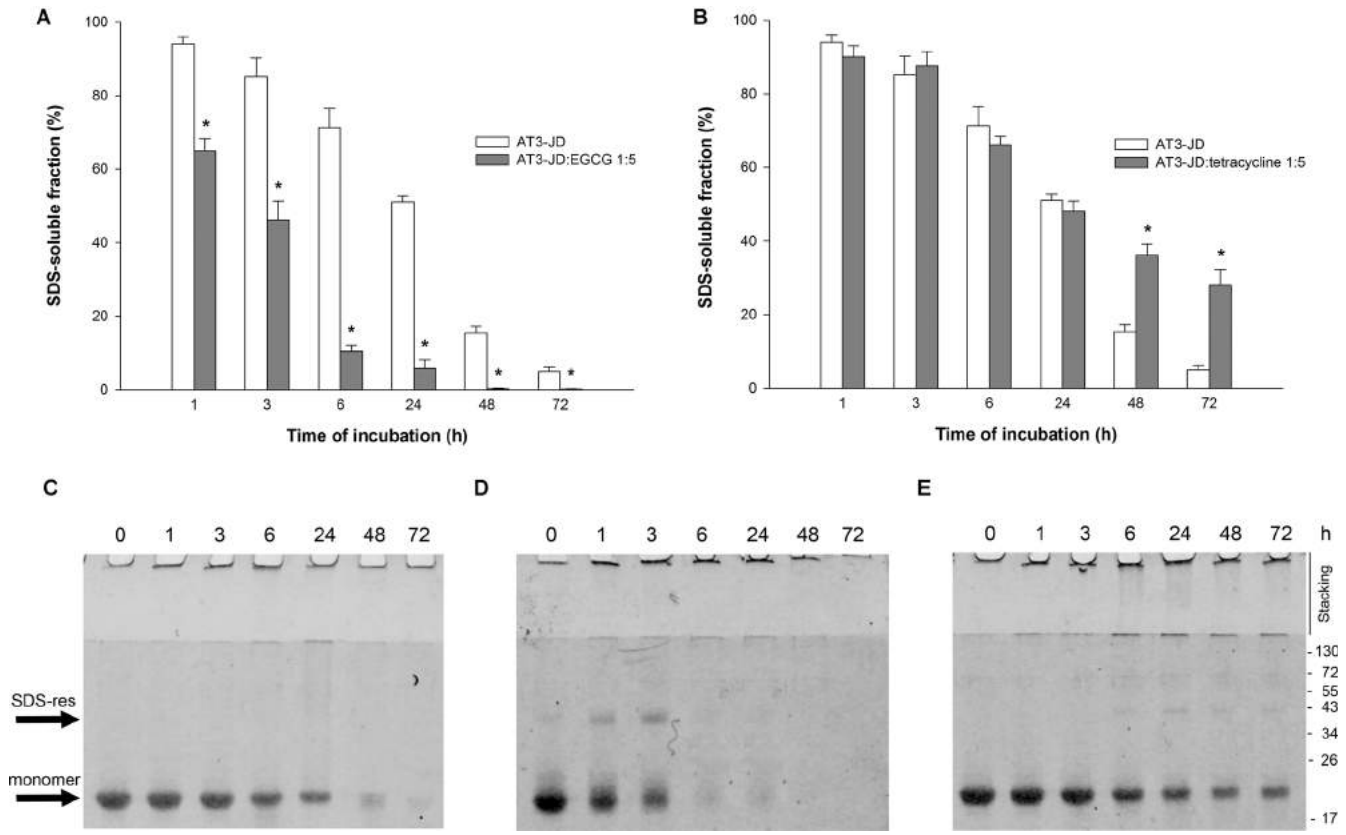

Figure 2. SDS-soluble protein fraction analysis of the JD incubated with EGCG or tetracycline. A 150 μM solution of JD was incubated at 37 °C in the presence or absence of: A) EGCG, or B) tetracycline. The amount of SDS-soluble protein was quantified by centrifuging the incubation mixtures, subjecting the supernatants to SDS-PAGE, and to subsequent densitometric analysis. Signals were normalized at zero-time protein content. Error bars represent standard errors and are derived from at least three independent experiments. *$=P<0.01$. SDS-PAGE (16%) of the soluble protein fraction of: C) JD, D) JD/EGCG 1:5, and E) JD/tetracycline 1:5. The gels were stained with IRDye blue protein stain (LiCor). The monomeric and the soluble, aggregated, SDS-resistant species are indicated by arrows.

metric analyses. Starting from the earliest incubation time (i.e., 1 h), EGCG treatment resulted in a significant reduction in the SDS-soluble amount of the protein (Figures 2A, C and D). Based on previous work, EGCG may undergo structural changes such as epimerization and dimerization.[33] This prompted us to check its stability. Under our working conditions, the molecule proved to be completely stable, as assessed by ^{1}H NMR spectroscopy, over a time span of 72 h (Figure S2 in the Supporting Information).

In contrast, tetracycline significantly retarded SDS-soluble species disappearance, in particular at the longest incubation times (Figures 2B, C, and E). Size exclusion chromatography (SEC) analyses of the incubation mixtures showed that in the control sample (i.e., JD alone, Figure 3A), higher molecular weight species appeared in the void volume starting from 6 h of incubation. Their estimated molecular mass is 300 kDa or higher. Scanty, if any, accumulation of intermediate forms between the void volume and the monomeric protein was observed. EGCG treatment (Figure 3B) resulted in a much faster disappearance of the monomeric form and accumulation of aggregates. This fits well with the aggregation pattern determined by using SDS-PAGE (Figures 2A and D). In contrast, tetracycline treatment (Figure 3C) did not appreciably alter the JD aggregation pattern as detected by using SEC, which apparently contrasts with our SDS-PAGE results, whereby a much larger accumulation of SDS-soluble species was detected at later times.

One possible explanation might be that there are SDS-soluble aggregated species, which can only be detected by SEC analysis, as already observed in the case of full-length, expanded AT3.[13] The much higher intensity of the void-volume peak detected in the presence of either compounds, as compared to the control sample, quite likely results from a tight protein–drug interaction, as supported by our observations (data not shown).

EGCG, but not tetracycline, strongly affects the structural features of the aggregation intermediates, as shown by FTIR spectroscopy

The effects of EGCG and tetracycline on the JD misfolding and aggregation were also studied by FTIR spectroscopy in the attenuated total reflection (ATR) mode. The ATR/FTIR absorption spectrum of freshly purified JD is reported in Figure 4A in the amide I band, mainly due to the C=O stretching vibrations of the peptide bond, which is particularly sensitive to protein secondary structures.[34] To disclose the different amide I components, we calculated the second derivative spectrum, whose

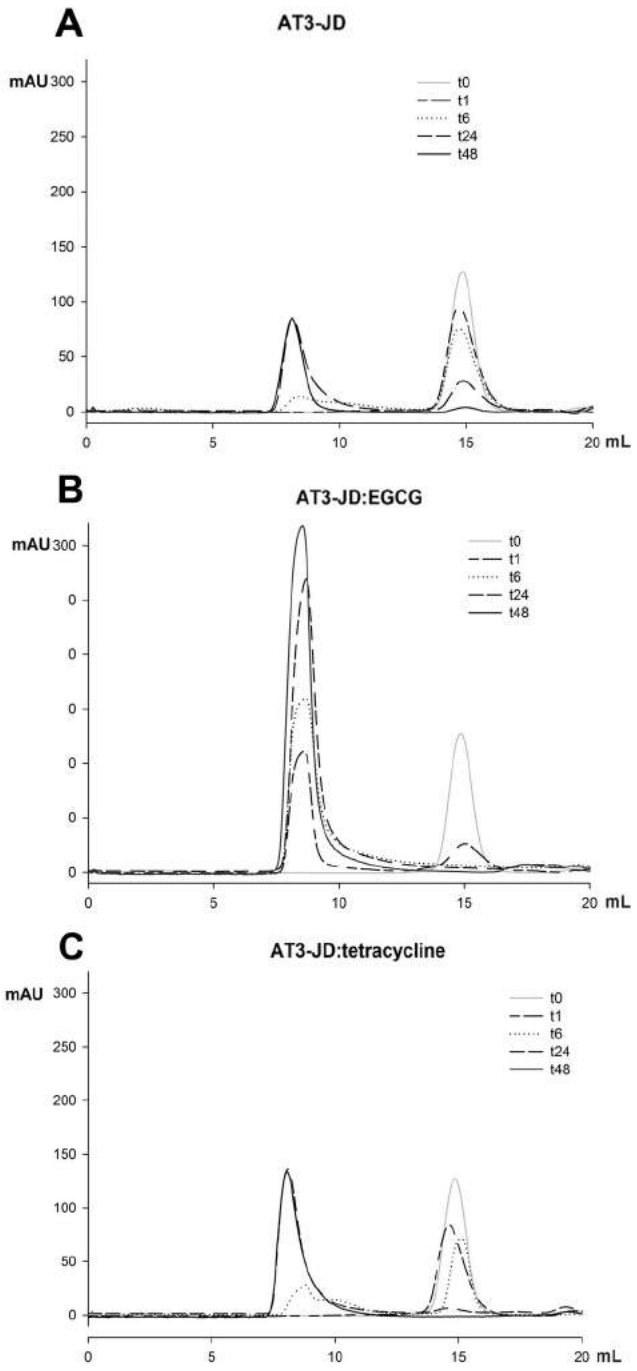

Figure 3. SEC profiles of JD incubated with EGCG or tetracycline. An amount of 500 μg of: A) JD, B) JD/EGCG 1:5, and C) JD/tetracycline 1:5 was loaded onto a Superose 12 10:300 GL column equilibrated in phosphate buffered saline solution after the indicated incubation times.

minima correspond to the absorption maxima.[35] In agreement with previous FTIR characterization of the JD,[12,36] the second derivative spectrum of the native protein (Figure 4B) displayed a major component at approximately $\tilde{\nu}=1635\ cm^{-1}$ that, along with the component at around $\tilde{\nu}=1690\ cm^{-1}$, can be assigned to the native intramolecular β-sheet structures. The component at about $\tilde{\nu}=1657\ cm^{-1}$ occurs in the spectral region of α-helical and random coil structures. During incubation at 37 °C in PBS solution, the amide I peaks of the native protein decreased in intensity and two new components appeared in the spectra at approximately $\tilde{\nu}=1693$ and $1623\ cm^{-1}$ (Figure 4B), which were assigned to the formation of intermolecular β-sheet structures in the protein aggregates.[12] A different behavior was observed in the presence of EGCG (JD/compound 1:5) in comparison with JD alone. Indeed, the second derivative components of the native protein decreased in intensity immediately after EGCG addition, and the peak at about $\tilde{\nu}=1635\ cm^{-1}$ appeared to be downshifted to approximately $\tilde{\nu}=1630\ cm^{-1}$, in the typical spectral region of intermolecular β-sheet structures of protein aggregates (Figure 4C). Very similar spectral changes were previously observed for the full-length expanded AT3 in the presence of EGCG.[13] The presence of an almost constant peak at about $\tilde{\nu}=1630\ cm^{-1}$ suggests that EGCG is able to redirect JD aggregation from the fibril-formation process to off-pathway aggregates. JD second derivative spectra collected at different incubation times in the presence of tetracycline at a JD/compound molar ratio of 1:5 (Figure 4D) indicate that tetracycline does not prevent JD misfolding and aggregation.

However, the final aggregates obtained in the presence of this compound displayed a minor reduction in intensity of the intermolecular β-sheet component, which also occurred at slightly higher wavenumbers compared with the JD alone as shown in Figure 4E, where the second derivative spectra of the pellets obtained after 312 h of protein incubation at 37 °C are reported. In contrast, pellets obtained after incubation with EGCG confirmed the aforementioned downshift to approximately $\tilde{\nu}=1630\ cm^{-1}$, which is indicative of an off-pathway aggregation mode. The time courses of the intensities of native and intermolecular β-sheet structures in the JD aggregates are reported in Figure 4F. Noteworthy, under our conditions, JD misfolding and aggregation at 37 °C in the presence of EGCG was almost completed after an incubation period of 1–2 h, whereas it took about 48 h in the presence of tetracycline, the latter being a pattern essentially indistinguishable from that of the control sample. These results suggest that, unlike tetracycline, EGCG binds to the native JD, leading to the formation of misfolded, aggregation-prone intermediates that are off-pathway of fibrillogenesis.

NMR spectroscopy highlights different interaction modes of EGCG and tetracycline with the JD

Recently, we have extensively exploited STD NMR spectroscopy[37–40] to characterize the binding of several natural[24,31,41,42] and synthetic ligands[43–47] to amyloid oligomers, thus demonstrating the reliability and versatility of this technique. Moreover, Melacini and co-workers validated STD NMR methods in characterizing the amyloid oligomer interaction with soluble proteins (in particular Aβ peptide oligomers)[48,49] and in also mapping peptide early self-association events.[50] In general, when an STD NMR experiment is acquired on a mixture containing the target protein and a potential ligand, the detection of NMR signals of the test molecule in the STD spectra is a clear-cut evidence of an interaction. Here, we have employed STD NMR experiments to investigate the nature of the interac-

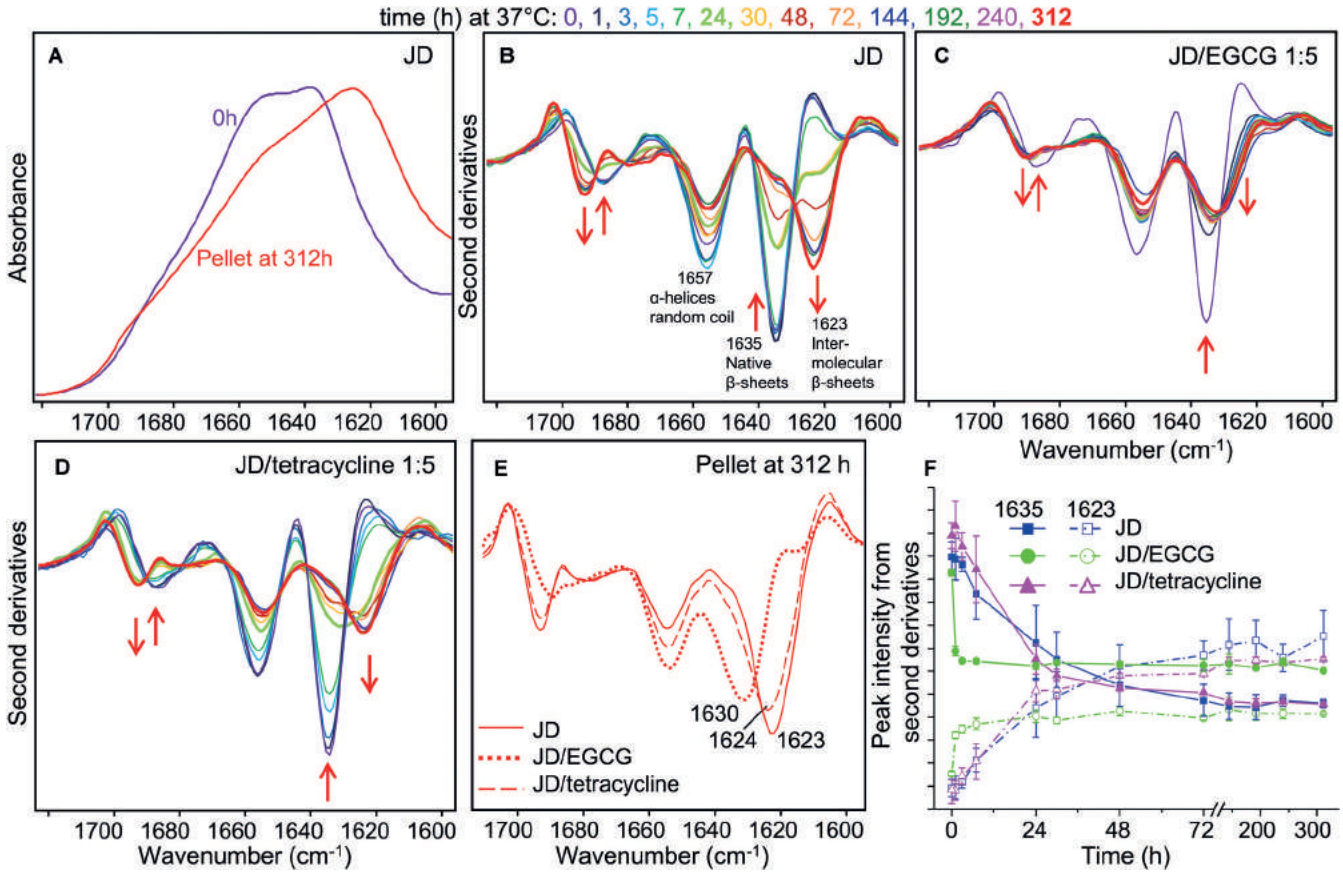

Figure 4. JD misfolding and aggregation studied by using FTIR spectroscopy. A) ATR/FTIR absorption spectra of freshly purified JD and of the pellet collected after incubation of the protein at 37 °C for 312 h. Spectra are reported in the amide I spectral region. B) Second derivatives of the absorption spectra of the JD (150 μM) collected at different incubation times at 37 °C. The assignment of the main components to protein secondary structures are reported. Arrows point to the spectral changes occurring at increasing incubation time. C) Second derivatives of the absorption spectra of 150 μM JD incubated in the presence of 750 μM EGCG (i.e., JD/EGCG 1:5) and otherwise under the conditions reported for panel B. D) Second derivatives of the absorption spectra of 150 μM JD incubated in the presence of 750 μM tetracycline (i.e., JD/tetracycline 1:5) and otherwise under the conditions reported for panel B. E) Second derivative spectra of the pellet collected from a solution of JD incubated in isolation for 312 h at 37 °C, or JD in the presence of EGCG, or of tetracycline. The positions of the main peak, due to β-sheet structures, is indicated. Spectra are shown after normalization at the peak around $\tilde{\nu}=1515$ cm^{-1} of tyrosines to compensate for possible differences in the protein content. F) Time course of the components at $\tilde{\nu}=1635$ and 1623 cm^{-1} (assigned to native JD β-sheets and to intermolecular β-sheet structures of the protein aggregates, respectively) reported for either the JD alone, or incubated in the presence of EGCG or tetracycline. The intensities are taken from the second derivative spectra after normalization of the tyrosine peak approximately appearing at $\tilde{\nu}=1515$ cm^{-1}.

tions of EGCG and tetracycline with both JD monomers and oligomers at the atomic level.

To a solution containing 1.5 mM EGCG or tetracycline in PBS solution, pH 7.2 at 5 °C, an aliquot of monomeric JD was added to a final concentration of 7 μM. Under these conditions, the monomeric state is preserved for at least one day. This is a time suitable for the acquisition of several STD spectra at different saturation times. The same experiments were performed after a pre-incubation period of 5 d at 37 °C of the sole JD. This treatment promotes protein aggregation, with resulting enrichment in JD soluble oligomers, as supported by SEC analysis (Figure S3 in the Supporting Information). STD spectra (Figure 5) unambiguously highlighted a different binding mode by the two compounds. In fact, EGCG resonances appear in both STD spectra depicted in Figure 5A (spectra 2 and 4, recorded in the presence of the JD monomer or the oligomer, respectively), whereas the tetracycline signals are only detected in the STD spectrum recorded in the presence of protein oligomers (Figure 5B, spectrum 4). Thus, the sole EGCG is capable of interacting with the monomeric form, which might, at least in part, account for the different effects of the two compounds in affecting oligomerization.

The binding epitopes identified on either compounds (Figure 6; Figures S4 and S5 in the Supporting Information for the corresponding STD build-up curves) indicate that the whole ligand structure is involved in the receptor recognition process, which is in agreement with previous findings concerning EGCG interaction with AT3Q55 oligomers[24] and tetracycline binding to Aβ oligomers.[31]

In this latter case, we reported in particular the formation of supramolecular colloidal particles presenting a disordered and non-homogeneous internal structure that justifies the absence of a specific ligand binding epitope. We hypothesize the formation of similar supramolecular complexes also in the presence of JD oligomers.

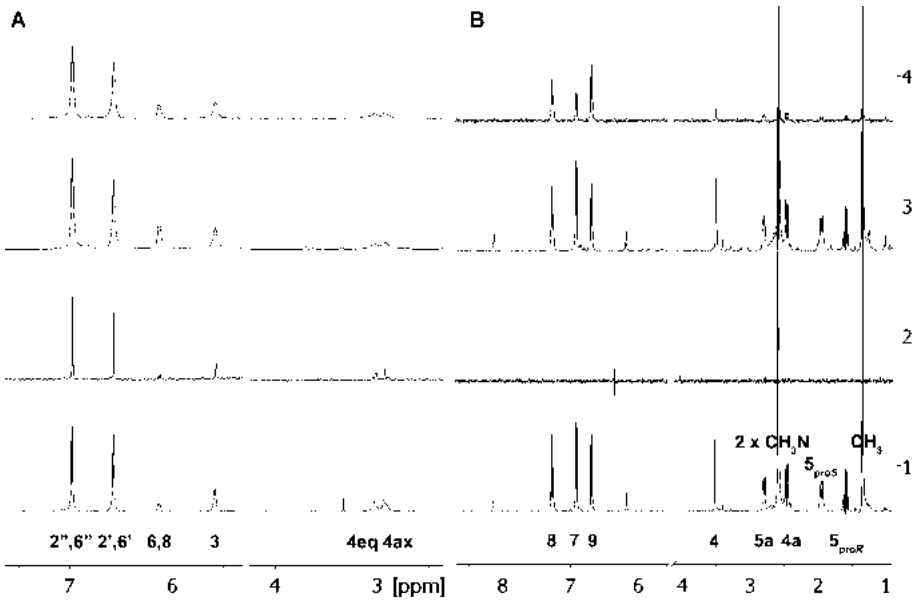

Figure 5. STD NMR characterization of EGCG and tetracycline binding to the JD monomer and oligomers. A) 1) ^{1}H NMR spectrum of a mixture containing JD (7 μM) immediately after purification and 1.5 mM EGCG. 2) STD NMR spectrum of the same mixture investigated in spectrum 1 at a saturation time of 3 s. 3) ^{1}H NMR spectrum of a mixture containing JD (7 μM) five days after purification and 1.5 mM EGCG. 4) STD NMR spectrum of the same mixture investigated in spectrum 3 at a saturation time of 3 s. B) 1) ^{1}H NMR spectrum of a mixture containing JD (7 μM) immediately after purification and 1.5 mM tetracycline. 2) STD NMR spectrum of the same mixture investigated in spectrum 1 at a saturation time of 3 s. 3) ^{1}H NMR spectrum of a mixture containing JD (7 μM) five days after purification and 1.5 mM tetracycline. 4) STD NMR spectrum of the same mixture investigated in spectrum 3 at a saturation time of 3 s. All samples were dissolved in PBS solution, pH 7.2, 5 °C. The spectrometer frequency was 600 MHz. The EGCG H2 signal is overlapped by water resonance. Ligand proton assignment is reported under spectra A1 for EGCG and B1 for tetracycline. All the spectra were recorded at 600 MHz.

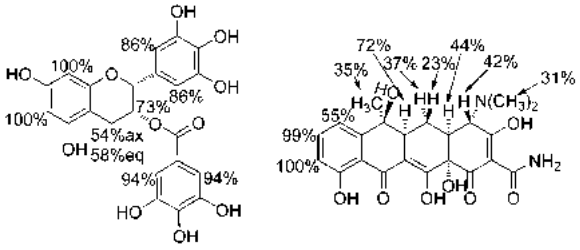

Figure 6. Binding epitopes of EGCG and tetracycline calculated for the interaction with the JD oligomers. In each case, the largest absolute STD effect has been scaled to 100%. The EGCG H2 signal is overlapped by water resonance and thus its STD effect was not calculated.

To provide a complementary insight into the nature of the EGCG interaction with the JD monomers, titration of the ^{15}N-labelled protein with increasing ligand concentrations was performed, and the changes in the protein NMR fingerprint were monitored by acquisition of ^{15}N-SOFAST-HMQC spectra (Figure 7).[51]

First, a SOFAST-HMQC spectrum was acquired on a sample containing 0.3 mM ^{15}N-labelled JD dissolved in PBS solution, pH 6.5 at 25 °C, to verify the match with the backbone amide assignments previously published.[52] Then, the protein was titrated with EGCG (JD/compounds ratios 1:0.5, 1:1, 1:2, 1:3, and 1:4) and the corresponding SOFAST-HMQC spectra were collected (Figure 7). The most significant variation observed is the intensity of the protein cross-peaks, which decreased at each step of titration. This decay correlated with the appearance of a white pellet at the bottom of the NMR tube, occurring after each addition of the ligand, diagnostic of the precipitation of a certain amount of sample. This suggests that the main effect induced by EGCG probably consists in a conformational change of the JD, as already observed by FTIR spectroscopy (Figure 4), which, in turn, promotes fast protein aggregation and precipitation.

The protein sample stability over time in the absence of EGCG was assessed by comparing the SOFAST-HMQC spectra of the JD recorded immediately after purification (Figure 7 A) and after an incubation period of 20 h (which is longer than a full titration experiment) at 25 °C (Figure 7 F). In particular, the protein sample was split into two aliquots, one being employed for the titration experiments (Figures 7 A–E), the other being incubated at 25 °C in the absence of EGCG (Figure 7 F). The spectra given in Figures 7 A and F are identical, supporting the stability of the protein under these experimental conditions.

Thus, protein precipitation is a direct consequence of EGCG addition to the JD sample.

From the comparison of spectra A and C in Figure 7 we derived that, for a protein/ligand molar ratio of 1:1, the amino acid residues most affected by signal broadening are those colored blue in Figure 7 G. They map to the six-stranded antiparallel β-sheet constituting the "core" of the C-terminal subdomain of the JD. Thus, we can infer that the EGCG-induced processes of misfolding and self-aggregation of the JD start in this structural region.

Also, small chemical shift deviations (CSDs) were observed, mainly assigned to residues belonging to the α-helical hairpin moiety (Figure 7 H, pink color). This is a structural motif endowed with high conformational flexibility, likely playing a key role in molecular-recognition and interaction/aggregation processes.[53,54]

Notably, even at high JD/compound ratios and after significant protein precipitation, the ligand resonances were not visible in the ^{1}H NMR spectra of the mixture (Figure S6 in the Supporting Information). This suggests that the stoichiometry of the JD/compound complex should be higher than 1:1 and that at least a part of the ligand precipitates together with the protein aggregates.

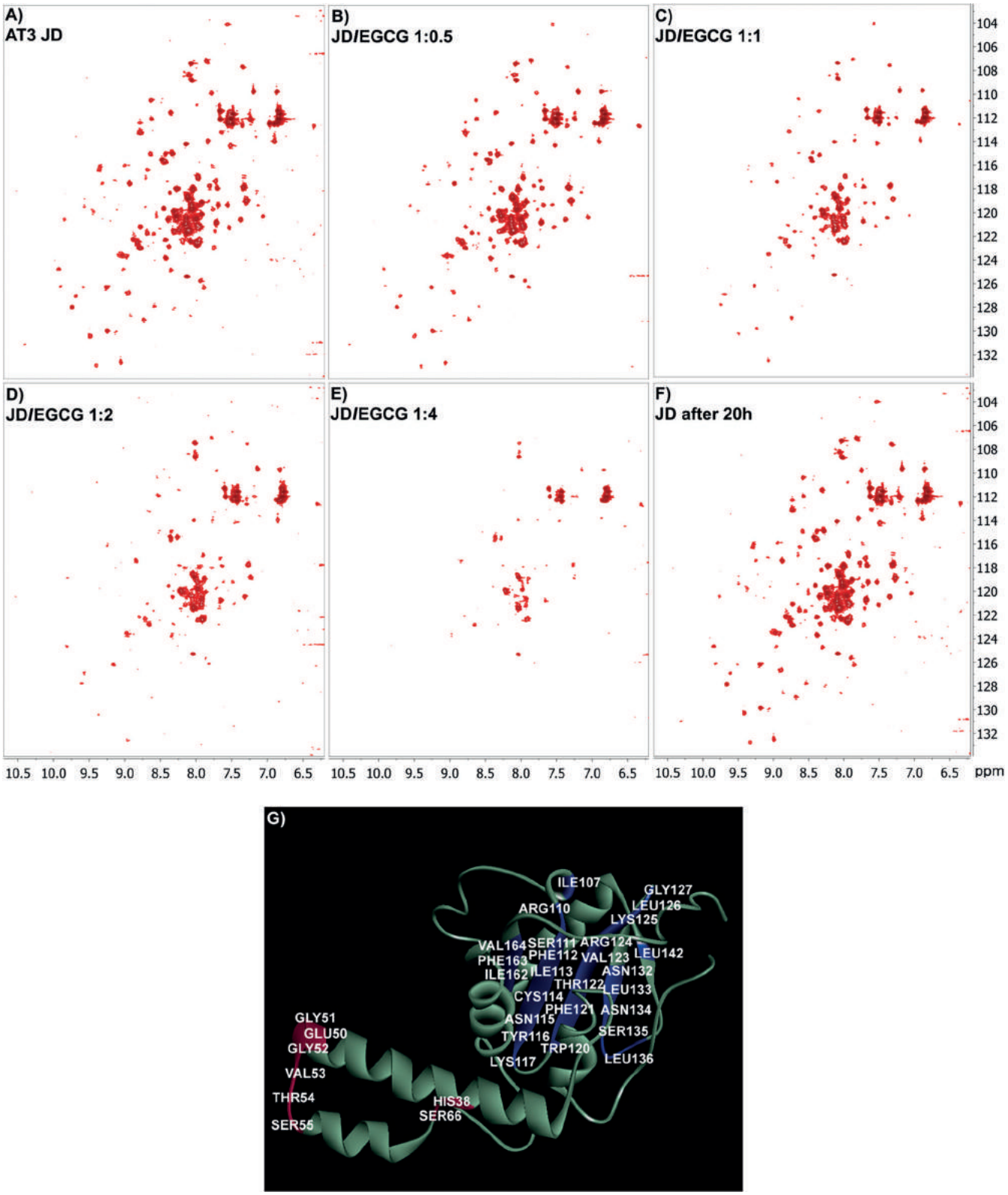

Figure 7. ^{15}N-SOFAST-HMQC titration experiments for the characterization of the EGCG interaction with the JD monomer. The ^{15}N-SOFAST-HMQC spectra were recorded in a solution containing: A) 0.3 mM ^{15}N-JD in PBS solution, pH 6.5 at 25 °C; B) 0.3 mM ^{15}N-JD and 0.15 mM EGCG in PBS solution, pH 6.5 at 25 °C; C) 0.3 mM ^{15}N-JD and 0.3 mM EGCG in PBS solution, pH 6.5 at 25 °C; D) 0.3 mM ^{15}N-JD and 0.6 mM EGCG in PBS solution, pH 6.5 at 25 °C; E) 0.3 mM ^{15}N-JD and 1.2 mM EGCG in PBS solution, pH 6.5 at 25 °C, F) 0.3 mM ^{15}N-JD in PBS solution, pH 6.5, after an incubation period of 20 h at 25 °C. All the spectra were recorded at 600 MHz. G) Residues affected by either signal broadening (blue) or chemical shift perturbation (pink) mapped on the structure of the monomeric JD (PDB ID: 1ZYB).

This is also supported by the dramatic reduction in the diffusion coefficient of EGCG when co-incubated with JD in large stoichiometric excess to JD (JD/EGCG 1:30), as measured by NMR diffusion-ordered spectroscopy (DOSY). The diffusion coefficient of EGCG in the free state (1.5 mM, PBS solution, pH 7.4, 25 °C) was 4.98 m^2s^{-1}, whereas after addition of 50 μM JD, it dropped to 1.96 m^2s^{-1} (reduction of 61%), which supports the existence of an equilibrium free/bound state of the ligand molecules. In the ^{1}H NMR spectra recorded on the same sample prepared for the DOSY acquisition, the EGCG resonances were visible only because of the large ligand stoichiometric excess.

SPR provides evidence of weak JD–EGCG interaction

We performed SPR analyses to determine the binding affinity of the JD–EGCG and JD–tetracycline complexes. In particular, we studied the real time association and dissociation of EGCG or tetracycline to/from JD (Figures 8A and B) coupled directly to the sensor chip CM5 by monitoring the binding and release of EGCG or tetracycline to and from the chip.

In the case of EGCG, the experiments provided evidence of compound binding to the JD. A good fitting was obtained by using the Langmuir 1:1 and BIA evaluation 4.1 software (BIAcore). As the presence of multiple binding sites for EGCG would yield an undistinguishable curve, the K_D value reported in the caption of Figure 8 should be regarded as an apparent one.

No interaction was determined by using tetracycline as an analyte (Figure 8C), which is suggestive of a much lower affinity toward the monomer compared to EGCG, which is in accordance with the NMR data (Figure 5).

Conclusion

In a previous work, we investigated the capability of EGCG and tetracycline to contrast amyloid aggregation and toxicity of full-length expanded variants of AT3.[13] We observed a significant protective effect by both compounds, but also demonstrated substantially different mechanisms of action. Actually, in the presence of EGCG, off-pathway, SDS-resistant soluble aggregates arose, whereas tetracycline did not produce major alterations in the structural features of the aggregates compared with the control, but substantially increased their solubility.

We have thus undertaken the present work to provide insight into how either compound precisely interact with AT3. To this end, we have taken advantage of NMR spectroscopy to identify the individual moieties of the protein and compounds involved in the interaction. However, we have examined their effects on the aggregation of the sole N-terminal JD, as the C-terminal disordered domain would severely hinder NMR measurements.

Our results show that both EGCG and tetracycline affect JD aggregation in a fashion qualitatively similar to that they exert on the full-length, expanded AT3. Most notably, NMR experiments have enabled us to also identify the individual binding epitopes on either compound, which show that the whole ligand structure participates in the protein binding. This points to a nonspecific interaction mode, as also supported by the K_D values assessed by SPR analysis. Not less important, we have also shown that EGCG is able to bind both the monomeric and the oligomeric form of the JD, whereas tetracycline only interacts with the oligomeric one. A possible concern regarding the effects of the two compounds assayed is that they might sequester functional AT3 with a resulting loss of function. However, this should not result in any detrimental effect, as previous work showed that knock-out mice were viable and fertile and did not present a reduced life span.[55]

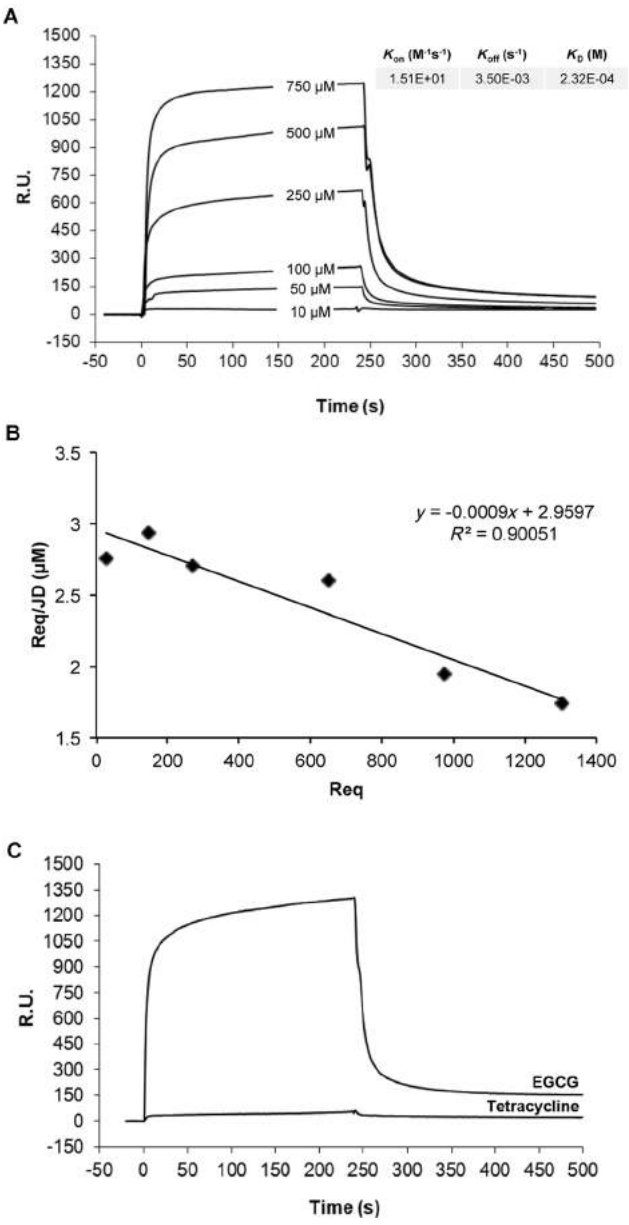

Figure 8. Association/dissociation kinetics for the binding between JD and EGCG. A) JD was immobilized on the sensor chip and the indicated concentrations of EGCG were flowed onto the chip surface. B) The R_{eq} values obtained for each given EGCG concentration were used to generate the Scatchard plot. C) Overlay of the BIAcore sensograms showing the different binding capacity of EGCG and tetracycline (injected at a concentration of 750 μM) for the JD, immobilized on the surface of the sensor chip.

In conclusion, our results suggest that the JD in isolation is a suitable model for assessing the effect of potential antiamyloid agents on AT3, which should significantly speed up research designed for this purpose. This work also provides a more in-depth understanding of the interaction mode between AT3 and the compounds under investigation, which might provide hints to rationally design more effective variants thereof.

Experimental Section

JD purification

The JD-encoding gene was cloned in a pET21-a vector and the protein was expressed in *Escherichia coli* BL21 Tuner (DE3) pLacI (*E. coli* B F$^-$ ompT hsdSB (rB$^-$ mB$^-$) gal dcm lacY1(DE3) pLacI (CamR); Novagen, Germany) as a His-tagged protein. Cells were grown at 37 °C in LB low salt-ampicillin medium, induced with 0.2 mM isopropylthio-β-D-galactoside (IPTG) at OD_{600} 0.8 for 2 h at 30 °C. Protein purification was performed as previously described for the expanded form.[13] To express the ^{15}N-labeled JD, cells were grown at 37 °C in 2 L of LB low salt-ampicillin in ^{15}N-free medium. At OD_{600} 0.7, the cells were centrifuged for 30 min at 5000 *g*. The pelleted cells were resuspended in isotopically labeled minimal medium (3 g L^{-1} KH_2PO_4, 6 g L^{-1} $Na_2HPO_4{\cdot}7H_2O$, 0.12 g L^{-1} $MgSO_4$, 0.2 g L^{-1} NaCl, 1 g L^{-1} $^{15}NH_4Cl$, 0.4% glucose), then incubated to allow the recovery of growth and clearance of unlabeled metabolites. After 1 h, protein expression was induced with 1 mM IPTG for 2 h at 30 °C.[56] Purification of the labeled protein was performed according to the same protocol as for the unlabeled protein.

SDS-PAGE and densitometry analysis of the soluble protein fraction

The purified JD (150 μM) was incubated at 37 °C in PBS solution in the presence or absence of EGCG or tetracycline (Sigma–Aldrich, USA) at a protein/compound molar ratio of 1:5. JD aliquots at different times of incubation (0, 1, 3, 6, 24, 48, and 72 h) were centrifuged at 14000 *g* for 15 min and 3 μL of the supernatants were subjected to SDS-PAGE. The gels were stained with IRDye Blue Protein Stain (LiCor, USA), scanned at 700 nm with the Odyssey Fc System (LiCor) and analyzed with the Image Studio software (LiCor).

SEC analysis

The purified JD (150 μM) was incubated at 37 °C in PBS solution in the presence or absence of EGCG or tetracycline at a protein/compound molar ratio of 1:5. Aliquots of the protein samples (500 μg) were withdrawn at different times of incubation (0, 1, 6, 24, and 48 h) and loaded onto a Superose 12 10:300 GL gel filtration column (GE Healthcare, Life Sciences, UK), pre-equilibrated with PBS solution (25 mM potassium phosphate, pH 7.2, 150 mM NaCl), and eluted at a flow rate of 0.5 mL min^{-1}.

Fourier transform infrared (FTIR) spectroscopy

FTIR analyses were performed following the experimental procedures already optimized and described in previous FTIR characterizations of JD[12, 36] and of expanded AT3.[12, 13] In particular, a sample (600 μL) of the purified JD (150 μM in PBS solution) was incubated in the test tube at 37 °C in the presence or absence of EGCG or tetracycline at a protein/compound molar ratio of 1:5. An aliquot (3 μL) was taken at different times of incubation and deposited on the diamond element of the device for measurements in the attenuated total reflection (ATR) mode. The Golden Gate (Specac, USA) device with a single reflection diamond crystal was employed. The FTIR spectrum was collected after solvent evaporation, which took place in about 1 min. The formation of a semi-dry film was expected following this procedure.[57] ATR/FTIR spectra were collected by using a Varian 670-IR spectrometer (Varian Australia Pty Ltd, Mulgrave VIC, Australia) equipped with a nitrogen-cooled mercury cadmium telluride detector under the following conditions: 2 cm^{-1} spectral resolution, 25 kHz scan speed, 1000 scans co-addition, and triangular apodization. The ATR/FTIR spectra of a PBS solution and of the two compounds at a concentration of 600 μM in PBS solution were also collected at each incubation time at 37 °C and were subtracted from the protein spectra.[13] Second derivatives of the spectra were obtained, after the smoothing of the measured spectra by the Savitzky–Golay algorithm, by using the software Resolutions Pro (Varian Australia Pty Ltd, Mulgrave VIC, Australia).

NMR spectroscopy

NMR experiments were recorded on a Varian 400 MHz Mercury or a Bruker 600 MHz Avance III spectrometer equipped with a QCI cryo-probe, with a *z*-axis gradient coil. EGCG and tetracycline were dissolved in PBS solution, pH 7.2 and, for ligand–receptor interaction experiments based on ligand observation, an aliquot of the protein solution, dissolved in the same buffer, was added to reach the final concentration required. Conversely, for experiments based on protein observation, small aliquots of a 12 mM EGCG solution in PBS solution, pH 6.5, were added to a sample containing the ^{15}N-labelled JD, with a final maximum dilution of the initial protein concentration of 10%. Sodium azide (0.05%; w/v) was added to the sample to prevent protein degradation by bacteria. Basic sequences were employed for ^1H NMR, STD NMR, ^{15}N-SOFAST-HMQC spectroscopic and diffusion experiments.

Solvent suppression was performed by excitation sculpting. ^1H NMR spectra were acquired with a number of transients ranging from 8 and 256 and 2 s recycle delay. For the STD NMR experiments, a train of Gaussian-shaped pulses each of 50 ms was employed to saturate selectively the protein envelope; the total saturation time of the protein envelope was varied between 3 and 0.15 s, 1024 scans; acquisitions were performed at 5 °C. ^{15}N-SOFAST-HMQC experiments were acquired with a number of transients ranging from 8 and 32, and 640 increments; acquisitions were performed at 25 °C. Diffusion experiments were acquired employing an array of 30 spectra for each experiment (128 scans, with 2 s recycle delay) varying the gradient strength from 3.33 to 19.4 G cm^{-2}. The lengths of and delays between the gradient pulses were optimized depending on the experimental conditions and ranged between 0.002 and 0.005 s and 0.2–0.7 s, respectively; acquisitions were performed at 25 °C. Data fitting and diffusion coefficient determinations were performed by using the software Dosytoolbox (http://personalpages.manchester.ac.uk/staff/mathias.nilsson/software.htm)

Surface plasmon resonance (SPR)

Surface plasmon resonance experiments were carried out with a BIAcore X system (GE Healthcare). JD and AT3Q55 proteins were coupled to a carboxymethylated dextran surface of two different CM5 sensor chips by using amine coupling chemistry at surface densities of 5000 and 4000 resonance units, respectively, by injecting 60 μL of each protein at the concentration of 50 μg mL^{-1} resuspended in 10 mM sodium acetate buffer, pH 4 (flow rate of

5 μL min^{-1}). A reference cell was saturated with 1 M ethanolamine, pH 8.5. Different concentrations of EGCG, diluted in the running buffer (10 mM 4-(2-hydroxyethyl)-1-piperazineethanesulfonic acid (HEPES), pH 7.4, 150 mM NaCl, 3 mM ethylenediaminetetraacetic acid (EDTA), 0.005% v/v Surfactant P20), were tested twice over the surface of sensor chip CM5 for 4 min (40 μL injections at flow rate of 10 μL min^{-1}). Surface regeneration was accomplished by injecting 50 mM NaOH (30 s contact) two or three times. The interaction rate constants were calculated by simultaneous fitting of the binding curves obtained with different concentrations of analyte, by using the BIAevaluation 4.1 software (BIAcore).

Acknowledgements

This work was supported by grants from the Regione Lombardia, Italy (Network-Enabled Drug Design) and the Fondazione Regionale per la Ricerca Biomedica (FRRB). The financial support of the MIUR grant SysBioNet – Italian Roadmap for ESFRI Research Infrastructure – to SYSBIO is also greatly acknowledged. We acknowledge the University of Milano-Bicocca (Fondo Grandi apparecchiature) for the acquisition of the FTIR spectrometer Varian 670-IR and the NMR Bruker Avance III 600 MHz spectrometer.

Keywords: aggregation inhibitors · epigallocatechin-3-gallate · Josephin domain · molecular recognition · tetracyclines

[1] Y. Trottier, Y. Lutz, G. Stevanin, G. Imbert, D. Devys, G. Cancel, F. Saudou, C. Weber, G. David, L. Tora, *Nature* **1995**, *378*, 403 – 406.
[2] Y. Kawaguchi, T. Okamoto, M. Taniwaki, M. Aizawa, M. Inoue, S. Katayama, H. Kawakami, S. Nakamura, M. Nishimura, I. Akiguchi, *Nat. Genet.* **1994**, *8*, 221 – 228.
[3] B. T. Koshy, H. Y. Zoghbi, *Brain Pathol.* **1997**, *7*, 927 – 942.
[4] H. L. Paulson, S. Das, P. B. Crino, M. K. Perez, S. C. Patel, D. Gotsdiner, K. H. Fischbeck, R. N. Pittman, *Ann. Neurol.* **1997**, *41*, 453 – 462.
[5] Q. S. Padiath, A. K. Srivastava, S. Roy, S. Jain, S. K. Brahmachari, *Am. J. Med. Genet. Part B Neuropsychiatr. Genet. Off. Publ. Int. Soc. Psychiatr. Genet.* **2005**, *133B*, 124 – 126.
[6] L. Masino, V. Musi, R. P. Menon, P. Fusi, G. Kelly, T. A. Frenkiel, Y. Trottier, A. Pastore, *FEBS Lett.* **2003**, *549*, 21 – 25.
[7] L. Masino, G. Nicastro, R. P. Menon, F. Dal Piaz, L. Calder, A. Pastore, *J. Mol. Biol.* **2004**, *344*, 1021 – 1035.
[8] M. K. M. Chow, A. M. Ellisdon, L. D. Cabrita, S. P. Bottomley, *Biol. Chem.* **2004**, *279*, 47643 – 47651.
[9] A. M. Ellisdon, B. Thomas, S. P. Bottomley, *J. Biol. Chem.* **2006**, *281*, 16888 – 16896.
[10] A. L. Robertson, S. J. Headey, H. M. Saunders, H. Ecroyd, M. J. Scanlon, J. A. Carver, S. P. Bottomley, *Proc. Natl. Acad. Sci. USA* **2010**, *107*, 10424 – 10429.
[11] L. Masino, G. Nicastro, A. De Simone, L. Calder, J. Molloy, A. Pastore, *Biophys. J.* **2011**, *100*, 2033 – 2042.
[12] A. Natalello, A. M. Frana, A. Relini, A. Apicella, G. Invernizzi, C. Casari, A. Gliozzi, S. M. Doglia, P. Tortora, M. E. Regonesi, *PLoS One* **2011**, *6*, e18789.
[13] M. Bonanomi, A. Natalello, C. Visentin, V. Pastori, A. Penco, G. Cornelli, G. Colombo, M. G. Malabarba, S. M. Doglia, A. Relini, M. E. Regonesi, P. Tortora, *Hum. Mol. Genet.* **2014**, *23*, 6542 – 6552.
[14] J. V. Higdon, B. Frei, *Crit. Rev. Food Sci. Nutr.* **2003**, *43*, 89 – 143.
[15] C. S. Yang, Z. Y. Wang, *J. Natl. Cancer Inst.* **1993**, *85*, 1038 – 1049.
[16] F. Jiang, G. Dusting, *J. Curr. Vasc. Pharmacol.* **2003**, *1*, 135 – 156.
[17] A. Higuchi, K. Yonemitsu, A. Koreeda, S. Tsunenari, *Toxicology* **2003**, *183*, 143 – 149.
[18] K. Rezai-Zadeh, G. W. Arendash, H. Hou, F. Fernandez, M. Jensen, M. Runfeldt, R. D. Shytle, J. Tan, *J. Brain Res.* **2008**, *1214*, 177 – 187.
[19] J. Bieschke, J. Russ, R. P. Friedrich, D. E. Ehrnhoefer, H. Wobst, K. Neugebauer, E. E. Wanker, *Proc. Natl. Acad. Sci. USA* **2010**, *107*, 7710 – 7715.
[20] N. Ferreira, I. Cardoso, M. R. Domingues, R. Vitorino, M. Bastos, G. Bai, M. J. Saraiva, M. R. Almeida, *FEBS Lett.* **2009**, *583*, 3569 – 3576.
[21] D. E. Ehrnhoefer, M. Duennwald, P. Markovic, J. L. Wacker, S. Engemann, M. Roark, J. Legleiter, J. L. Marsh, L. M. Thompson, S. Lindquist, P. J. Muchowski, E. E. Wanker, *Hum. Mol. Genet.* **2006**, *15*, 2743 – 2751.
[22] M. Li, A. E. Hagerman, *J. Agric. Food Chem.* **2014**, *62*, 3768 – 3775.
[23] D. E. Ehrnhoefer, J. Bieschke, A. Boeddrich, M. Herbst, L. Masino, R. Lurz, S. Engemann, A. Pastore, E. E. Wanker, *Nat. Struct. Mol. Biol.* **2008**, *15*, 558 – 566.
[24] E. Sironi, L. Colombo, A. Lompo, M. Messa, M. Bonanomi, M. E. Regonesi, M. Salmona, C. Airoldi, *Chem. Eur. J.* **2014**, *20*, 13793 – 13800.
[25] M. Domercq, C. Matute, *Trends Pharmacol. Sci.* **2004**, *25*, 609 – 612.
[26] G. Forloni, M. Salmona, G. Marcon, F. Tagliavini, *Infect. Disord.: Drug Targets* **2009**, *9*, 23 – 30.
[27] I. Cardoso, M. J. Saraiva, *FASEB J.* **2006**, *20*, 234 – 239.
[28] K. Ono, M. Yamada, *J. Neurochem.* **2006**, *97*, 105 – 115.
[29] S. Giorgetti, S. Raimondi, K. Pagano, A. Relini, M. Bucciantini, A. Corazza, F. Fogolari, L. Codutti, M. Salmona, P. Mangione, L. Colombo, A. De Luigi, R. Porcari, A. Gliozzi, M. Stefani, G. Esposito, V. Bellotti, M. Stoppini, *J. Biol. Chem.* **2011**, *286*, 2121 – 2131.
[30] G. Forloni, L. Colombo, L. Girola, F. Tagliavini, M. Salmona, *FEBS Lett.* **2001**, *487*, 404 – 407.
[31] C. Airoldi, L. Colombo, C. Manzoni, E. Sironi, A. Natalello, S. M. Doglia, G. Forloni, F. Tagliavini, E. Del Favero, L. Cantù, F. Nicotra, M. Salmona, *Org. Biomol. Chem.* **2011**, *9*, 463 – 472.
[32] L. Unione, S. Galante, D. Díaz, F. J. Cañada, J. Jiménez-Barbero, *Med. Chem. Commun.* **2014**, *5*, 1280 – 1289.
[33] S. Sang, M. J. Lee, Z. Hou, C. T. Ho, C. S. Yang, *J. Agric. Food Chem.* **2005**, *53*, 9478 – 9484.
[34] A. Barth, *Biochim. Biophys. Acta Bioenerg.* **2007**, *1767*, 1073 – 1101.
[35] H. Susi, D. M. Byler, *Methods Enzymol.* **1986**, *130*, 290 – 311.
[36] A. Apicella, A. Natalello, A. M. Frana, A. Baserga, C. S. Casari, C. E. Bottani, S. M. Doglia, P. Tortora, M. E. Regonesi, *Biochimie* **2012**, *94*, 1026 – 1031.
[37] M. Mayer, B. Meyer, *Angew. Chem. Int. Ed.* **1999**, *38*, 1784 – 1788; *Angew. Chem.* **1999**, *111*, 1902 – 1906.
[38] R. Caraballo, H. Dong, J. P. Ribeiro, J. Jiménez-Barbero, O. Ramström, *Angew. Chem. Int. Ed.* **2010**, *49*, 589 – 593; *Angew. Chem.* **2010**, *122*, 599 – 603.
[39] a) A. Palmioli, E. Sacco, C. Airoldi, F. Di Nicolantonio, A. D'Urzo, S. Shirasawa, T. Sasazuki, A. Di Domizio, L. De Gioia, E. Martegani, A. Bardelli, F. Peri, M. Vanoni, *Biochem. Biophys. Res. Commun.* **2009**, *386*, 593 – 597; b) C. Airoldi, S. Sommaruga, S. Merlo, P. Sperandeo, L. Cipolla, A. Polissi, F. Nicotra, *Chem. Eur. J.* **2010**, *16*, 1897 – 1902; c) C. Airoldi, S. Sommaruga, S. Merlo, P. Sperandeo, L. Cipolla, A. Polissi, F. Nicotra, *ChemBioChem* **2011**, *12*, 719 – 727.
[40] C. Airoldi, S. Giovannardi, B. La Ferla, J. Jiménez-Barbero, F. Nicotra, *Chem. Eur. J.* **2011**, *17*, 13395 – 13399.
[41] C. Airoldi, E. Sironi, C. Dias, F. Marcelo, A. Martins, A. P. Rauter, F. Nicotra, J. Jimenez-Barbero, *Chem. Asian J.* **2013**, *8*, 596 – 602.
[42] A. R. Jesus, C. Dias, A. M. Matos, R. F. M. deAlmeida, A. S. Viana, F. Marcelo, R. T. Ribeiro, M. P. Macedo, C. Airoldi, F. Nicotra, A. Martins, E. J. Cabrita, J. Jiménez-Barbero, A. P. Rauter, *J. Med. Chem.* **2014**, *57*, 9463 – 9472.
[43] C. Airoldi, C. Zona, E. Sironi, L. Colombo, M. Messa, D. Aurilia, M. Gregori, M. Masserini, M. Salmona, F. Nicotra, B. La Ferla, *J. Biotechnol.* **2011**, *156*, 317 – 324.
[44] C. Airoldi, F. Cardona, E. Sironi, L. Colombo, M. Salmona, A. Silva, F. Nicotra, B. La Ferla, *Chem. Commun.* **2011**, *47*, 10266 – 10268.
[45] C. Airoldi, F. Cardona, E. Sironi, L. Colombo, M. Salmona, I. Cambianica, F. Ornaghi, G. Sancini, F. Nicotra, B. La Ferla, *Pure Appl. Chem.* **2013**, *85*, 1813 – 1823.
[46] S. Merlo, E. Sironi, L. Colombo, F. Cardona, A. M. Martorana, M. Salmona, B. La Ferla, C. Airoldi, *ChemPlusChem* **2014**, *79*, 835 – 843.
[47] C. Airoldi, S. Mourtas, F. Cardona, C. Zona, E. Sironi, G. D'Orazio, E. Markoutsa, F. Nicotra, S. G. Antimisiaris, B. La Ferla, *Eur. J. Med. Chem.* **2014**, *85*, 43 – 50.
[48] J. Milojevic, A. Raditsis, G. Melacini, *Biophys. J.* **2009**, *97*, 2585 – 2594.
[49] J. Milojevic, A. G. Melacini, *Biophys. J.* **2011**, *100*, 183 – 192.

[50] H. Huang, J. Milojevic, G. Melacini, *J. Phys. Chem. B* **2008**, *112*, 5795 – 5802.
[51] P. Schanda, E. Kupce, B. Brutscher, *J. Biomol. NMR* **2005**, *33*, 199 – 211.
[52] G. Nicastro, L. Masino, T. A. Frenkiel, G. Kelly, J. McCormick, R. P. Menon, A. Pastore, *J. Biomol. NMR* **2004**, *30*, 457 – 458.
[53] G. Nicastro, R. P. Menon, L. Masino, P. P. Knowles, N. Q. McDonald, A. Pastore, *Proc. Natl. Acad. Sci. USA* **2005**, *102*, 10493 – 10498.
[54] D. Sanfelice, A. De Simone, A. Cavalli, S. Faggiano, M. Vendruscolo, A. Pastore, *Biophys. J.* **2014**, *107*, 2932 – 2940.
[55] P. M. Switonski, A. Fiszer, K. Kazmierska, M. Kurpisz, W. J. Krzyzosiak, M. Figiel, *Neuromolecular Med.* **2011**, *13*, 54 – 65.
[56] J. Marley, M. Lu, C. Bracken, *J. Biomol. NMR* **2001**, *20*, 71 – 75.
[57] E. Goormaghtigh, V. Raussens, J. M. Ruysschaert, *Biochim. Biophys. Acta Rev. Biomembr.* **1999**, *1422*, 105 – 185.

Received: August 5, 2015
Published online on ■■ ■■, 0000

FULL PAPER

Molecular Recognition

M. Bonanomi, C. Visentin, A. Natalello, M. Spinelli, M. Vanoni, C. Airoldi, M. E. Regonesi,* P. Tortora*

■■ – ■■

How Epigallocatechin-3-gallate and Tetracycline Interact with the Josephin Domain of Ataxin-3 and Alter Its Aggregation Mode

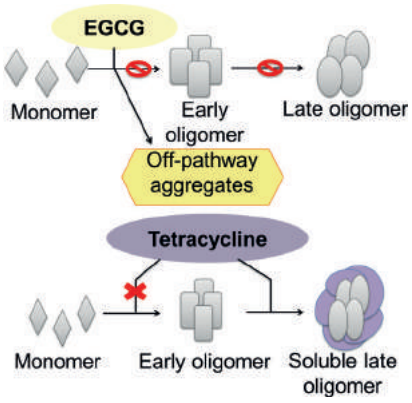

All roads are nontoxic: Epigallocatechin-3-gallate (EGCG) and tetracycline affect the aggregation of the Josephin domain of ataxin-3 in a very different way (see figure).

CHEMISTRY
A European Journal

Supporting Information

How Epigallocatechin-3-gallate and Tetracycline Interact with the Josephin Domain of Ataxin-3 and Alter Its Aggregation Mode

Marcella Bonanomi,[a] Cristina Visentin,[a] Antonino Natalello,[a, b, c] Michela Spinelli,[a, d] Marco Vanoni,[a, c, d] Cristina Airoldi,*[a, c, d] Maria E. Regonesi,*[a, c] and Paolo Tortora[a, c]

chem_201503086_sm_miscellaneous_information.pdf

Supporting Information

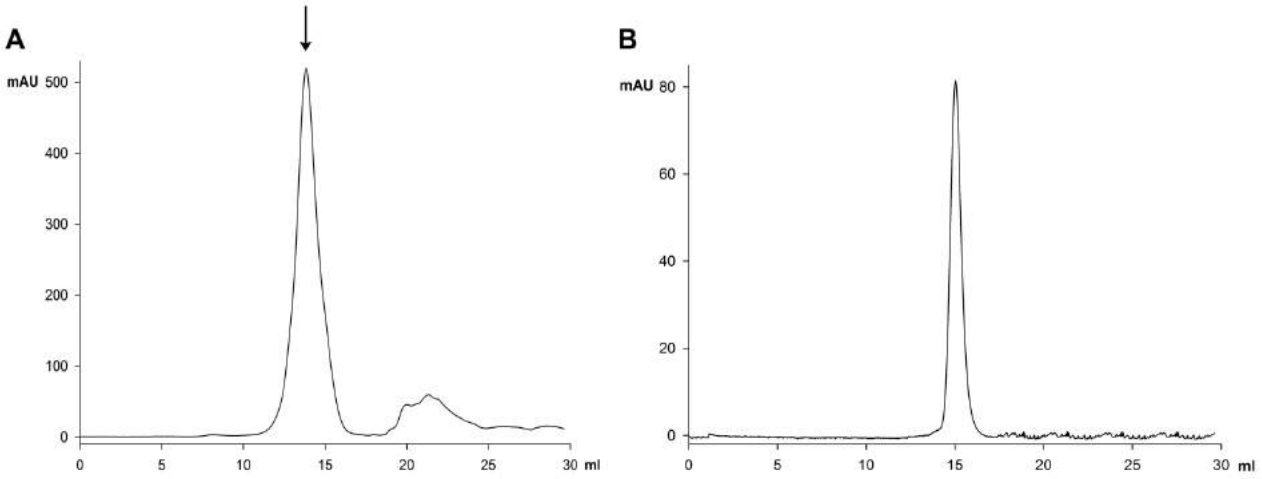

Figure S1. SEC profiles of JD (A) 6 mg His-tagged JD were loaded onto a Superose 12 10/300 GL column equilibrated in PBS buffer. The arrow indicates the peak corresponding to JD monomeric form. (B) 300 µg monomeric JD were reloaded onto the same column.

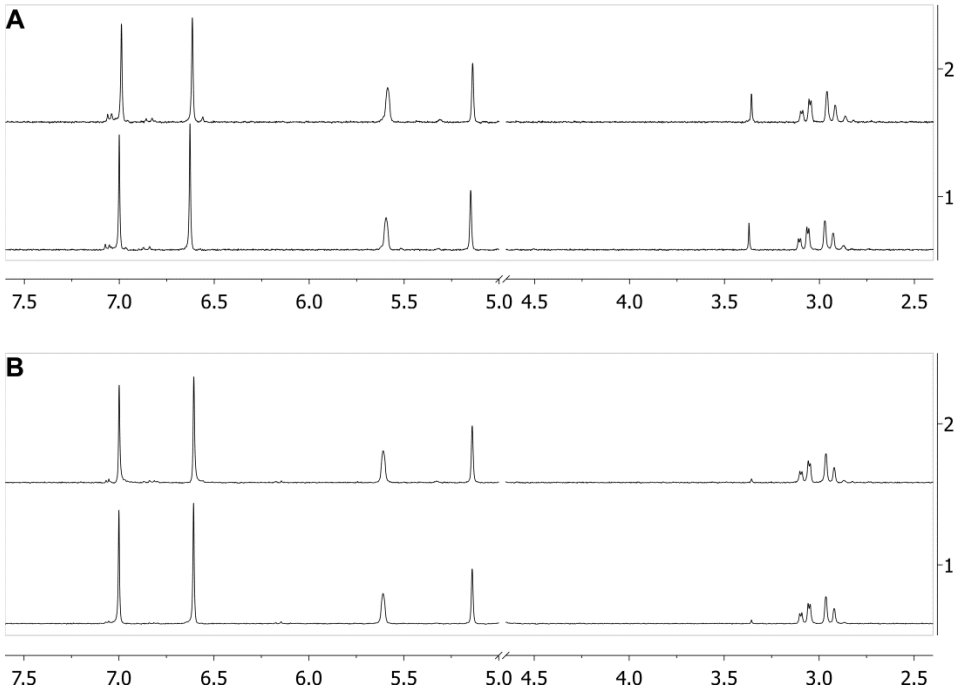

Figure S2. ^{1}H-NMR monitoring of EGCG stability at 37 °C, pH 7.4 or 6.5. ^{1}H-NMR spectra were recorded on a solution containing 2 mM EGCG dissolved in PBS, pH 7.4 (**A**) or 6.5 (**B**) immediately after dissolving the compound (1) or after 72 h (2) of incubation at 37 °C. No significant changes of compound resonances were observed.

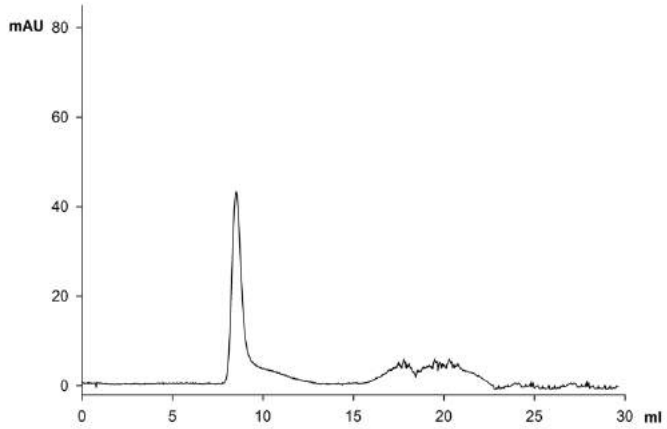

Figure S3. SEC profiles of aggregated JD. 300 µg JD were loaded onto a Superose 12 10/300 GL column equilibrated in PBS buffer after a 6-d incubation.

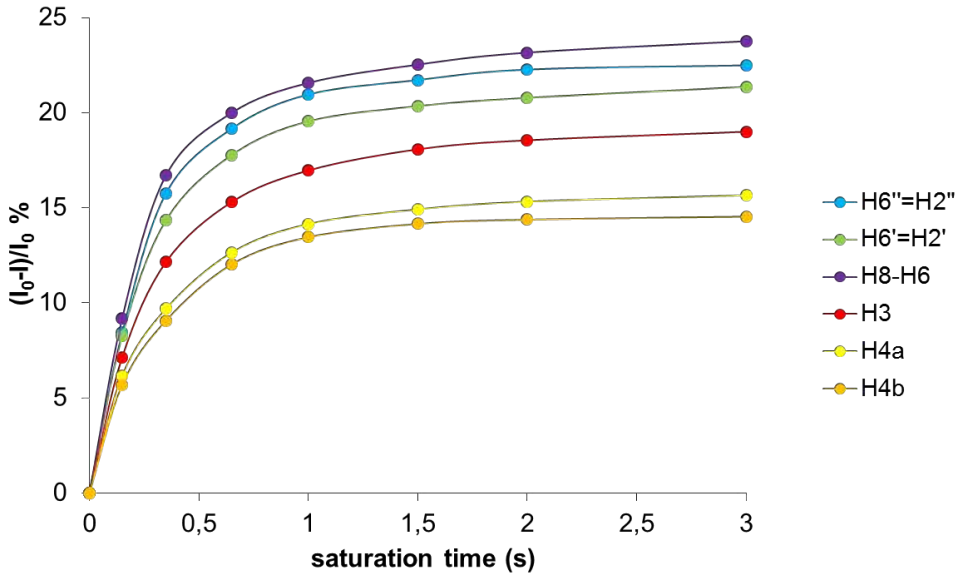

Figure S4. STD NMR characterization of EGCG/JD oligomer interaction. Fractional STD effect for each non-overlapping signal of EGCG was calculated by $(I_0\text{-}I)/I_0$, in which $(I_0\text{-}I)$ is the peak intensity in the STD NMR spectrum and I_0 is the peak intensity in the off-resonance spectrum.

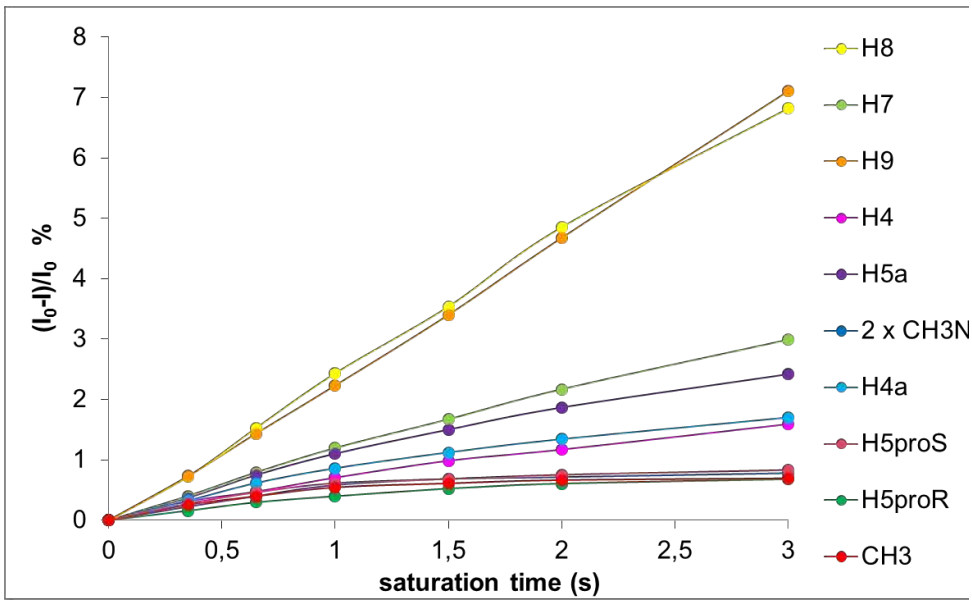

Figure S5. STD NMR characterization of tetracycline/JD oligomer interaction. Fractional STD effect for each signal of tetracycline was calculated by $(I_0\text{-}I)/I_0$, in which $(I_0\text{-}I)$ is the peak intensity in the STD NMR spectrum and I_0 is the peak intensity in the off-resonance spectrum.

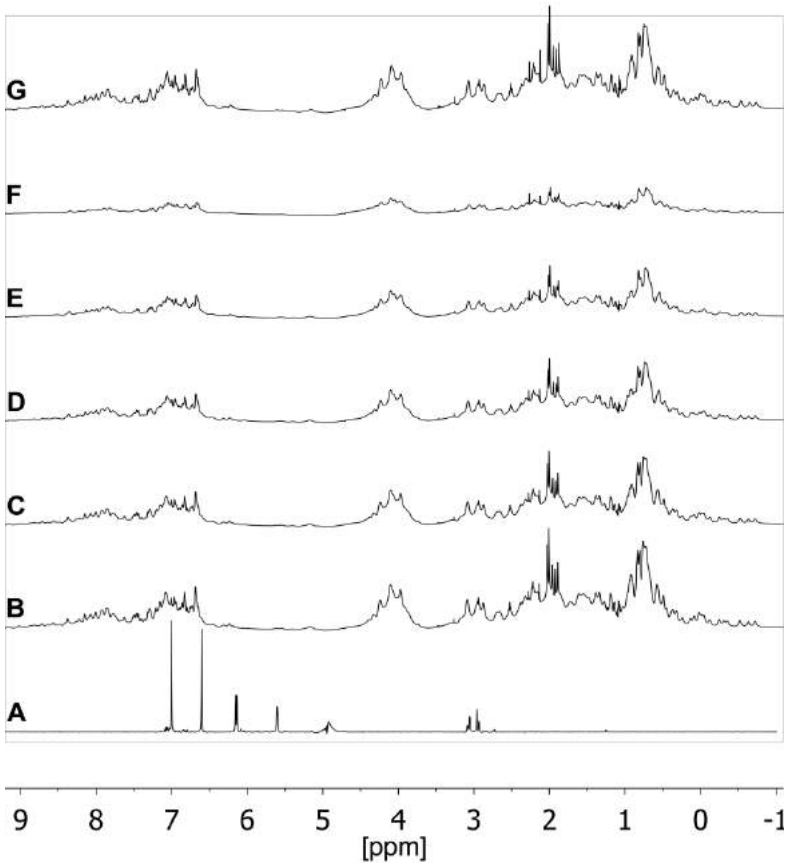

Figure S6. 1H-NMR titration experiments for the characterization of EGCG interaction with JD monomer. 1H-NMR spectra recorded in a solution containing (A) 1 mM EGCG, in PBS, pH 6.5 at 25 °C; (B) 0.3 mM ^{15}N-JD in PBS, pH 6.5 at 25 °C; (C) 0.3 mM ^{15}N-JD and 0.15 mM EGCG in PBS, pH 6.5 at 25 °C; (D) 0.3 mM ^{15}N-JD and 0.3 mM EGCG in PBS, pH 6.5 at 25 °C; (E) 0.3 mM ^{15}N-JD and 0.6 mM EGCG in PBS, pH 6.5 at 25 °C; (F) 0.3 mM ^{15}N-JD and 1.2 mM EGCG in PBS, pH 6.5 at 25 °C; (G) 0.3 mM ^{15}N-JD in PBS, pH 6.5, after a 20-h incubation at 25 °C. All the spectra were acquired with 128 transients.

PLOS | ONE

RESEARCH ARTICLE

The Toxic Effects of Pathogenic Ataxin-3 Variants in a Yeast Cellular Model

Marcella Bonanomi[1], Cristina Visentin[1], Gaetano Invernizzi[1¤], Paolo Tortora[1,2]*, Maria Elena Regonesi[2,3]

1 Department of Biotechnologies and Biosciences, University of Milano-Bicocca, Milan, Italy, **2** Milan Center of Neuroscience (NeuroMI), Milan, Italy, **3** Department of Statistics and Quantitative Methods, University of Milano-Bicocca, Milan, Italy

¤ Current address: Department of Biology, University of Copenhagen, Copenhagen N, Denmark
* paolo.tortora@unimib.it

Citation: Bonanomi M, Visentin C, Invernizzi G, Tortora P, Regonesi ME (2015) The Toxic Effects of Pathogenic Ataxin-3 Variants in a Yeast Cellular Model. PLoS ONE 10(6): e0129727. doi:10.1371/journal.pone.0129727

Academic Editor: Salvador Ventura, Universitat Autònoma de Barcelona, SPAIN

Received: November 21, 2014

Accepted: May 12, 2015

Published: June 8, 2015

Data Availability Statement: All relevant data are within the paper and its Supporting Information files.

Funding: This work was supported by grants from Regione Lombardia, Italy (Network-Enabled Drug Design), from Fondazione Cariplo, Italy (progetto Nobel: Network Operativo per la Biomedicina di Eccellenza in Lombardia). The funders had no role in study design, data collection and analysis, decision to publish, or preparation of the manuscript

Competing Interests: The authors have declared that no competing interests exist.

Abstract

Ataxin-3 (AT3) is a deubiquitinating enzyme that triggers an inherited neurodegenerative disorder, spinocerebellar ataxia type 3, when its polyglutamine (polyQ) stretch close to the C-terminus exceeds a critical length. AT3 variants carrying the expanded polyQ are prone to associate with each other into amyloid toxic aggregates, which are responsible for neuronal death with ensuing neurodegeneration. We employed *Saccharomyces cerevisiae* as a eukaryotic cellular model to better clarify the mechanism by which AT3 triggers the disease. We expressed three variants: one normal (Q26), one expanded (Q85) and one truncated for a region lying from the beginning of its polyQ stretch to the end of the protein (291Δ). We found that the expression of the expanded form caused reduction in viability, accumulation of reactive oxygen species, imbalance of the antioxidant defense system and loss in cell membrane integrity, leading to necrotic death. The truncated variant also exerted a qualitatively similar, albeit milder, effect on cell growth and cytotoxicity, which points to the involvement of also non-polyQ regions in cytotoxicity. Guanidine hydrochloride, a well-known inhibitor of the chaperone Hsp104, almost completely restored wild-type survival rate of both 291Δ- and Q85-expressing strains. This suggests that AT3 aggregation and toxicity is mediated by prion forms of yeast proteins, as this chaperone plays a key role in their propagation.

Introduction

The expansion of an unstable translated CAG repeat causes at least ten dominantly inherited neurodegenerative disorders known as polyglutamine (polyQ) diseases. These include Huntington disease, spinal and bulbar muscular atrophy, dentatorubropallidoluysian atrophy, and seven autosomal dominant spinocerebellar ataxias (SCA1, 2, 3, 6, 7, 12 and 17) [1–3]. In all these diseases, a polyQ stretch expanded beyond a critical threshold leads to misfolding of the respective protein, its aggregation into large intracellular inclusions, cytotoxicity and finally dysfunction and demise of specific neurons [4]. The loss of function resulting from misfolding might also be involved in the mechanisms of pathogenesis [5,6]. Machado-Joseph disease,

otherwise known as spinocerebellar ataxia type-3 (SCA3), is the most common form of autosomal dominantly-inherited ataxia, and characterized by pyramidal symptoms associated in varying degrees with a dystonic-rigid extrapyramidal syndrome or peripheral amyotrophy [7,8]. The gene causatively associated with SCA3 is *atxn3*, which encodes a polyQ-containing protein known as ataxin-3 (AT3) [9]. This is a conserved and ubiquitous protein with a wide distribution in the brain, although different regions present varying expression levels [10]. AT3 is composed of a structured globular N-terminal domain, the Josephin domain (JD), which displays ubiquitin hydrolase activity, followed by a disordered C-terminal tail containing two ubiquitin-interacting motifs (UIMs) and the polyQ stretch of variable length, whose expansion beyond a certain threshold triggers SCA3 [11,12]. To date, the mechanism by which polyQ-expanded AT3 leads to SCA3 pathogenesis has not been fully clarified. It has been largely reported that the polyQ expansion induces transition to aggregation-prone conformations [13–15]. As for most amyloid-forming proteins, several pathways may drive the conversion of the soluble protein to amyloid aggregates, although small aggregates and oligomers are the species responsible for cytotoxicity [16–19]. It has been suggested that the soluble amyloid oligomers have common mechanisms of toxicity [20], for example being able to destabilize the cellular membrane or to sequester quality control system components and transcription factors, causing proteotoxic stress and transcriptional dysregulation [21–23]. Consequently, this investigation is aimed at clarifying the mechanisms underlying AT3 aggregation and how the different protein variants exert their cytotoxicity. To provide insight into this issue, we have used the budding yeast *Saccharomyces cerevisiae*, an eukaryotic model organism widely used in studies on neurodegenerative diseases [24] including the case of polyQ toxicity and aggregation [25] despite the lack of any AT3 homologous in yeast. Nevertheless, most processes involved in neurodegenerative disorders such as apoptosis and necrosis [26], mitochondrial damage, oxidative stress, protein aggregation and degradation can be analyzed within yeast [27]. Models of protein aggregation disorders in *S. cerevisiae* have provided new insight into Parkinson's disease [28,29], amyotrophic lateral sclerosis [30,31], and Huntington's disease [32–34]. Also, nucleocytoplasmic shuttling activity of AT3 has been investigated, which showed active import and export from the nucleus [35]. Here, we have characterized the mechanisms of toxicity exerted by AT3 variants: one normal (AT3-Q26), one expanded-pathological (AT3-Q85), and one truncated for a region lying from the beginning of its polyQ stretch to the end of the protein (AT3-291Δ). Normal AT3 variants have polyQs in the range 10–51; expanded, pathogenic ones, 55–87 [36]. All the proteins were expressed in fusion with the green fluorescent protein (GFP) at the C-terminus. First, we have shown that the expression of the expanded form causes a significant viability reduction compared with the normal, wild type strain. We have demonstrated that the toxicity is associated with an accumulation of reactive oxygen species (ROS), an increase of catalase (CAT) activity, an alteration in the balance of reduced glutathione (GSH) and an induction of necrosis. We have assayed the truncated variant to assess the role of the protein context in polyQ toxicity. Actually, we have previously demonstrated the toxic effects of this truncated form in *Escherichia coli* [37]. Here, we demonstrate an effect also on yeast cell growth and some markers of toxicity in a way comparable to that of the full-length, expanded form. This implies that AT3 regions outside the polyQ tract could also determine its pathological features.

Materials and Methods

Yeast strains and plasmids

Experiments were carried out in W303 (*MATα can1-100 ade2-1 his3-11, 15 trp1-1 ura3-1 leu23,112*) yeast strain. p426GALhtt103QGFP plasmid (Addgene) [38] was digested with

BamHI restriction enzyme to excise huntingtin gene. AT3-Q26, AT3-Q85 and AT3-291Δ genes were digested with *BamHI* and the resulting fragments were subcloned into the digested plasmid in frame with GFP protein at the C-terminus. Transformation of yeast was performed by the lithium acetate method [39]. Yeast cells transformed with the p426GAL empty vector were used as a control.

Yeast growth conditions

Cells were grown overnight in selective media containing glucose (2%), washed three times in sterile water and diluted to an OD_{600} of 0.1 in selective media containing 2% galactose as inducer of AT3 expression. Analyses were performed after 16, 24 or 48 h of induction, unless otherwise noted.

Confocal microscopy analysis of protein aggregation

Fluorescence microscopy was performed to detect protein aggregation using a Leica Mod. TCS-SP2 confocal microscope (Leica Microsystem, Wetzlar, Germany) and the fluorescence of GFP was excited with the 488 nm line.

Clonogenic growth assay

About 100 cells derived from the overnight cultures were grown in the presence or the absence of one of the following: i) 100 μM tetracycline, ii) 100 μM epigallocatechin-3-gallate (EGCG), iii) 5 mM guanidine hydrochloride (GuHCl). Then, cultures were washed in water, spread on a plate with selective medium containing glucose as the sole carbon source and on another plate with selective medium containing galactose as the sole carbon source. The colony-forming ability was plotted as the ratio of the number of cells grown on galactose to those grown on glucose and expressed as percentage.

Filter trap assay and dot blot analysis

For each strain, 1 ml of culture was harvested after 24 h of induction. Total protein extracts were obtained as previously described [40] and the concentration in different samples were determined by the Bradford assay (Coomassie Plus Protein Assay Reagent, Thermo Scientific, Rockford, IL, USA). Equal amounts of the different samples were subjected to either a filter trap assay or dot blot analysis as previously described [41], using an anti-AT3 Z46 rabbit polyclonal primary antibody [42] and anti-rabbit fluorescent secondary antibody (Donkey anti-rabbit IRDye 800 CW, Li-Cor, Lincoln, USA). Dot blots were also performed, using OC antibodies that specifically recognize soluble fibrillar oligomers [43]. Western blotting was performed using primary anti-AT3 Z46 and anti-rabbit fluorescent secondary antibody. Membranes were imaged using a LiCor Odyssey Fc scanner.

MTT assay

The MTT [3-(4,5-dimethylthiazoyl-2-yl) 2,5-diphenyltetrazolium bromide] assay was performed as described by Teparić [44] with minor modifications. The assay quantifies the capability of actively respiring cells to reduce the water-soluble MTT to an insoluble purple formazan. Cells from 1 ml of culture were harvested and resuspended in 0.4 ml 5 μg/mL MTT. The mixture was incubated at room temperature under shaking for 2 h. Then, cells were harvested and resuspended in 1 ml acid 2-propanol (0.04 M HCl in 2-propanol). The suspension was shaken for 10 min and then centrifuged at 7000 x *g* for 10 min. OD_{540} of the supernatant was measured. Data were expressed as percentage of MTT reduction with respect to the control.

ROS assay

H_2O_2 levels were monitored using the Red Hydrogen Peroxide Assay Kit (Enzo Life Sciences) according to the manufacturer's protocol. Cells from 3 ml of culture were harvested and resuspended in lysis buffer (20 mM phosphate buffer, 5 mM EDTA, 0.2 mM PMSF, pH 7.2). Cells were broken using glass beads (0.5 mm diameter) by vortexing five times for 1 min with intervals of 1 min on ice. Cell debris was pelleted and the supernatants used for the test. The conversion of red peroxidase substrate to resorufin was determined measuring OD_{576}. Data were expressed as fold increase with respect to the empty vector strain level.

Determination of glutathione levels

Reduced (GSH) and total glutathione content was determined by the method of Boyne and Ellman [45], using 5,5'-dithio-bis(2-nitrobenzoic acid) (DTNB). 10 ml of cells culture were harvested, washed twice with PBS (25 mM potassium phosphate, 150 mM NaCl, pH 7.2) to remove any trace of growth medium, and resuspended in ice-cold 5% perchloric acid. Cells were then broken with glass beads as described above and incubated on ice for 15 min. Cell debris and proteins were pelleted at 18,000 x *g* for 15 min at 4°C and the supernatant neutralized with 100 mM sodium phosphate, 5 mM EDTA, pH 7.5. To assess GSH levels, 600 μM Ellman reagent was added to samples and OD_{412} measured. To assess total glutathione, the neutralized supernatants were incubated at 37°C for 10 min in the presence of 1 U/ml of glutathione reductase and 0.2 mM NADPH and then the GSH content was determined. GSH concentration was determined using a GSH standard curve. Data were expressed as the ratio of GSH to total glutathione content in percentage.

Antioxidant enzyme activity determination

CAT activity was determined as described by Shangari [46] by measuring the rate of H_2O_2 decomposition with the ferrous oxidation. 3 ml of cell culture were harvested and resuspended in hypotonic lysis buffer (10 mM HEPES, 1.5 mM $MgCl_2$, 10 mM KCl, 0.5 mM DTT, 0.2 mM PMSF, pH 7.9) and broken as described above. Data were expressed as fold increase with respect to the empty vector strain level.

Superoxide dismutase (SOD) activity was measured using the protocol of enzymatic assay described by Sigma [47]. 3 ml of cell culture were harvested and resuspended in lysis buffer (20 mM phosphate buffer, 5 mM EDTA, 0.2 mM PMSF, pH 7.2) and broken as described above. Data were expressed as fold increase with respect to empty vector strain level.

Propidium iodide staining

500 μl of cell culture of induction were harvested after 48 h and resuspended in 250 μl of PBS, incubated for 30 min in the dark with 10 μg/ml of propidium iodide (PI). Then, cells were applied to a microscopic slide and observed using a Leica Mod. TCS-SP2 confocal microscope (Leica Microsystem, Wetzlar, Germany). PI fluorescence was excited with the 488 nm line. As a positive control, cells were treated for 15 min with 70% ethanol prior to incubation with PI. Data were expressed as percentage of PI-positive cells.

Statistical analysis

All experiments were done at least in triplicate. Data are presented as means ± standard error of fold increase or percentage. Values were compared by the Student t test. $P < 0.05$ was considered significant.

Results

A yeast model of ataxin-3 toxicity

To provide insight into the mechanisms of AT3 cytotoxicity in a eukaryotic system, we expressed three variants in *S. cerevisiae*, i.e. a wild type and a pathogenic one, carrying 26 (AT3-Q26) and 85 (AT3-Q85) consecutive glutamines respectively, and a variant truncated for a region lying from the beginning of its polyQ stretch to the end of the protein (AT3-291Δ). All constructs were in fusion with GFP at the C-terminus, under the control of the GAL1 promoter and induced by galactose (Fig 1A). Dot blot analysis of whole cell lysates did not show any significant difference in expression among the three variants at different times of induction, nor did the expression level decline significantly with time (Fig. A in S1 File, panel A). SDS-PAGE analysis confirmed the presence of the three variants and their expression levels (Fig. A in S1 File, panel B).

AT3-Q85 expression leads to the formation of SDS-insoluble aggregates

It has been reported that polyQ expansion in AT3 leads to the formation of intracellular SDS-insoluble aggregates [48]. To check whether this also occurs in our model yeast, we exploited protein constructs in fusion with GFP to monitor their distribution in cells by confocal microscopy analysis (Fig 1B). The results show that the expression of the wild type and of the truncated forms resulted in the appearance at all times from the induction of a largely diffused cytoplasmic fluorescence. In contrast, the expanded variant formed intracellular inclusions starting from 16 h (Fig 1B). Filter trap analysis on whole protein extracts of the three strains at 24 h of induction provided clear evidence in support of a qualitative difference between AT3-Q85 inclusions and those generated by the two other forms, in that the sole AT3-Q85 gave rise to SDS-insoluble aggregates (Fig 1C). To provide more information regarding the nature of such aggregates, we also performed dot blots using OC antibodies that specifically recognize soluble fibrillar oligomers [43]. A strong signal was apparent until 24 h in the case of yeast cell lines expressing AT3-291Δ and AT3-Q85, which faded at the latest time (48 h), suggestive of oligomer evolution into further aggregation forms (Fig 1D). The weak background signal detected under all other conditions, including cells transformed with the vector alone, may be accounted for by amyloidogenic, prion-like yeast proteins, as further outlined in the Discussion.

AT3-291Δ and AT3-Q85 expression impairs cell growth

To check whether the expression of the AT3 variants under investigation results in cytotoxicity, we first analyzed their effect on yeast survival rate by a clonogenic assay. Briefly, cells were pregrown in a medium that repressed expression of the AT3 variants. Then, a fixed amount of cells was plated in parallel onto two different media: without and with inducer (glucose and galactose, respectively) and incubated at 30°C. Their colony-forming ability was determined under either condition (Fig 2A). Results revealed a significant growth-inhibitory effect of AT3-Q85 expression. The AT3-291Δ-expressing strain also showed a decrease in growth capability, although statistically non-significant (Fig 2A).

A significant cytotoxic effect in yeast strains expressing both pathological and truncated variants was also detected by the MTT assay (Fig 2B).

As an alternative approach to assess the effect of the expression of the AT3 variants on yeast survival, we determined the generation time, which yielded results consistent with those of the clonogenic assay. In particular, AT3-Q85 expression resulted in a small but statistically significant increase in duplication time compared to the control (i.e., a yeast cell line transformed with the vector: fig. B in S1 File).

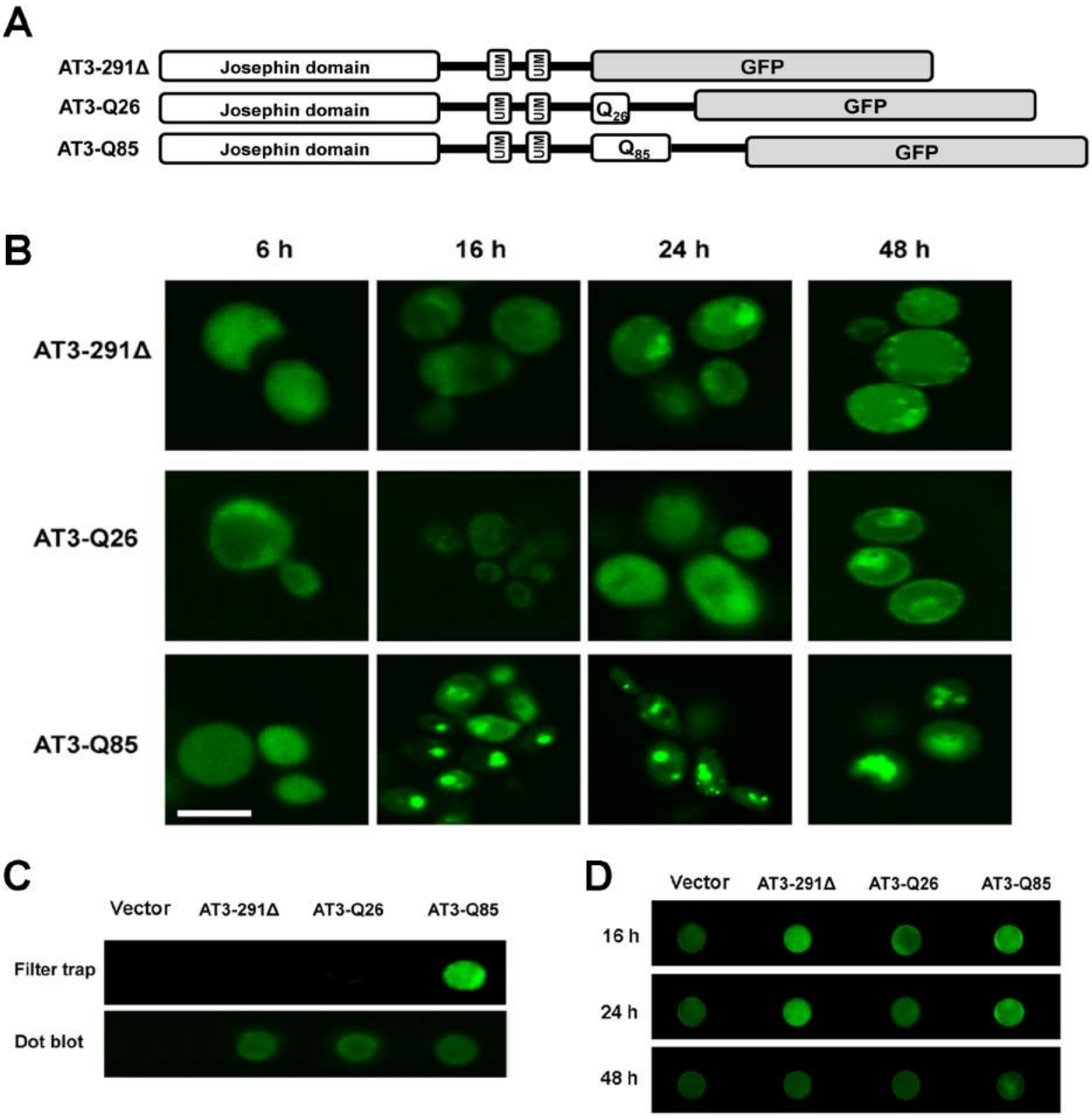

Fig 1. Morphological analysis of AT3 aggregation. A) Sequence and domain organization of the AT3 variants under investigation. UIM: ubiquitin interacting motif, GFP: green fluorescent protein. B) Cells expressing the indicated AT3-GFP fusion proteins were analyzed by fluorescence microscopy (Scale bar: 10 μm) at the indicated times of induction. C) Whole protein extracts of the three strains after 24 h of induction were subjected to filter trap analysis to detect SDS-insoluble aggregates. The immunodecoration was performed using anti-AT3 antibody and anti-rabbit fluorescent secondary antibody. Dot-blot analysis was performed as a loading control. D) Whole protein extracts of *S. cerevisiae* strains expressing the AT3 variants were subjected to dot blot at different times after induction and immunodetected using OC antibody and anti-rabbit fluorescent secondary antibody.

doi:10.1371/journal.pone.0129727.g001

In our previous experimentation, we observed that EGCG and tetracycline reduce AT3 toxicity in both a COS-7 cell line and a transgenic *Caenorhabditis elegans* strain [49]. Thus, as a further validation of our yeast cellular model, we also assayed the effects of these compounds. As expected, they both exerted an almost complete suppression of AT3 toxicity (Fig. C in S1 File).

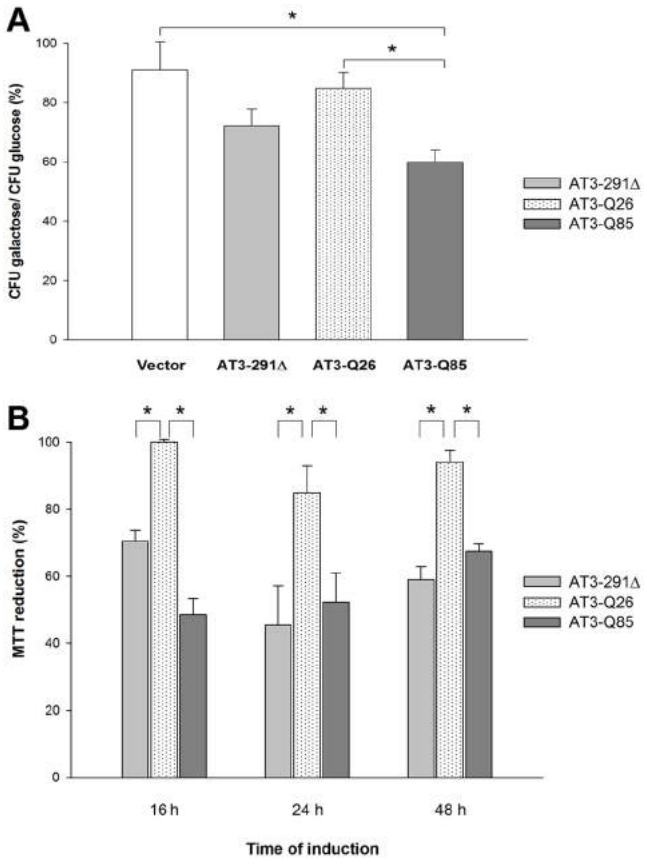

Fig 2. Effect of the AT3 variants expression on cell growth and toxicity. A) Clonogenic assay: about 100 cells from the different cultures were spread onto either glucose or galactose plates and their colony-forming ability expressed as percentage ratio of cells grown under inducing (galactose) *versus* non-inducing (glucose) conditions. Bars represent standard errors and are derived from at least three independent experiments ($P < 0.05$). B) MTT assay: the experiment was performed on cultures after the indicated induction times. Data are expressed as percentage ratio of MTT reduction *versus* the control (empty vector). Bars represent standard errors and are derived from at least three independent experiments ($P < 0.05$).

doi:10.1371/journal.pone.0129727.g002

AT3-291Δ and AT3-Q85 toxicity is likely to be mediated by the action of the molecular chaperone Hsp104

A previous report showed that the deletion of the molecular chaperone Hsp104 in yeast significantly suppresses the aggregation of an artificial polyQ-carrying protein (103Q) [32]. Furthermore, it is well known that Hsp104 is also required for prion maintenance [50]. These findings point to the involvement of yeast prion protein in polyQ toxicity, as also supported by its substantial reduction following prion-encoding gene deletion [32,51]. This prompted us to check the effect of GuHCl on AT3 toxicity, as this compound in the millimolar range is capable of inhibiting Hsp104 [32,50,52]. Actually, GuHCl pretreatment almost completely restored wild-type survival rate of both AT3-291Δ- and AT3-Q85-expressing strains (Fig 3), which confirms a role for Hsp104 and possibly for prion protein in AT3 toxicity.

AT3-291Δ and AT3-Q85 expression induces oxidative stress

Besides quantifying cytotoxicity, MTT assay is a marker of mitochondrial stress. To assess whether the growth inhibitory effect observed in the presence of mutant AT3 forms may be

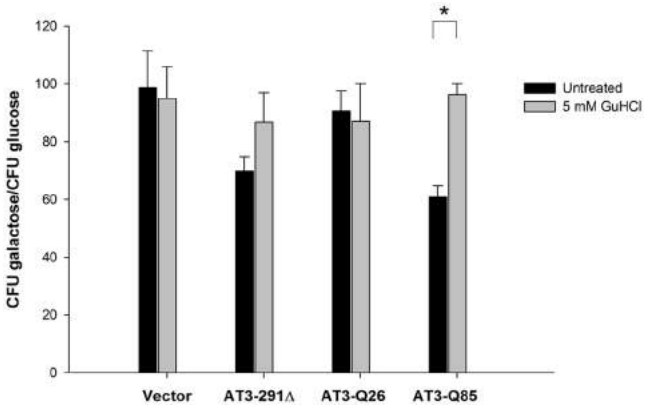

Fig 3. GuHCl restores normal cell growth. About 100 cells grown in the presence or in the absence of 5 mM GuHCl were spread onto either glucose or galactose plates and their colony-forming ability expressed as percentage ratio of cells grown under inducing (galactose) versus non-inducing (glucose) conditions. Bars represent standard errors and are derived from at least three independent experiments ($P < 0.05$).

doi:10.1371/journal.pone.0129727.g003

ascribed to increased oxidative stress, we first evaluated ROS levels in the three strains. We found that already 16 h after induction, H_2O_2 levels were significantly higher in yeast expressing AT3-Q85 and AT3-291Δ compared to AT3-Q26 (1.9 and 1.4 fold increase, respectively) (Fig 4A). At 24 h, the increase was significant only for the strain expressing the expanded form (1.6-fold increase) and, at the latest time, the levels of the three strains were comparable. We then assessed glutathione redox state in the yeast strains at different induction times, by determining the ratio of reduced (GSH) to total glutathione content. Results indicate that at 16 h after induction the ratio in the AT3-Q85 strain underwent a small but statistically significant decrease (by about 1.2 fold), unlike the AT3-291Δ strain that did not show any significant variation at all times assayed (Fig 4B).

The activity of antioxidant enzymes is increased in strains expressing AT3-291Δ and AT3-Q85

Enzymatic components in the antioxidant defense system play critical role(s) against oxidative stress. For this reason, we measured CAT and SOD activities to determine whether the detected increase in ROS levels may induce changes in the activity of certain antioxidant enzymes. Our results revealed markedly increased activity of CAT at 16 h of induction in the yeast expressing AT3-Q85 and AT3-291Δ compared to AT3-Q26 (1.5 and 1.7 fold, respectively) (Fig 5A). At 24 h, the increase was significant only for the expanded form (1.5 fold) and at 48 h there were no appreciable differences. As regards SOD, we observed a significant activity increase in the AT3-291Δ strain at 24 and 48 h of induction (1.4 and 1.3 fold, respectively), whereas in the case of AT3-Q85 a significant increase (1.5 fold) was detected only at 48 h of incubation (Fig 5B).

AT3-Q85 expression affects membrane integrity but does not induce apoptosis

To assess whether the expression of the pathological AT3 variant causes membrane damage, we performed propidium iodide (PI) staining, a membrane impermeable dye that binds to double-stranded DNA with resulting fluorescence enhancement. We observed that close to 10% of AT3-Q85-expressing cells took up the dye after 48 h of induction, which is over three-fold compared with the control strain (empty vector) and over two-fold compared with the wild type AT3-expressing strain, indicating loss of plasma membrane integrity and cell necrosis. In

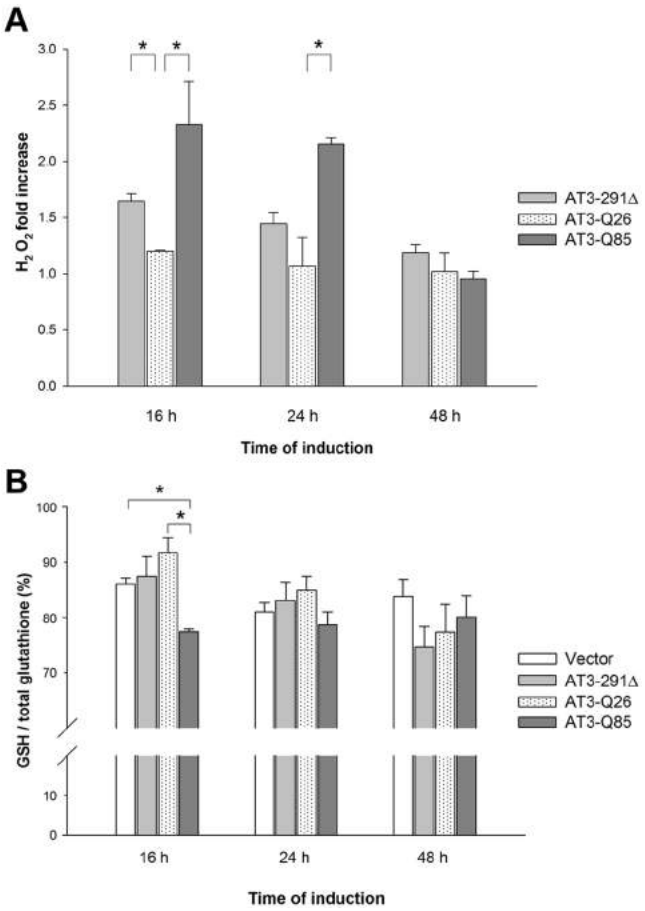

Fig 4. Oxidative stress level in cells expressing AT3 variants. A) ROS levels: intracellular H_2O_2 levels were determined using the Red Hydrogen Peroxide Assay Kit. The conversion of red peroxidase substrate to resorufin was determined by measuring the absorbance at 576 nm. Data were expressed as fold increase with respect to the empty vector strain level. Bars represent standard errors and are derived from at least three independent experiments ($P < 0.05$). B) Glutathione levels: GSH and total glutathione content was determinate using the Ellman reagent. Data were expressed as the ratio of GSH to total glutathione content in percentage. Bars represent standard errors and are derived from at least three independent experiments ($P < 0.05$).

doi:10.1371/journal.pone.0129727.g004

contrast, the percentage of PI-positive AT3-Q26- and AT3-291Δ-expressing cells were similar to control cells (Fig 6). Finally, we evaluated cytochrome *c* release from mitochondria in order to verify the presence of apoptotic cells [53]. AT3-expressing strains did not show any significant difference in the amount of cytochrome *c* released at any time (Fig. D in S1 File).

Discussion

S. cerevisiae has been long exploited as a model system to investigate the molecular mechanisms underlying neurodegenerative diseases [24]. This became possible thanks to the development of yeast genetic tools, as well as the high conservation of fundamental biological processes and pathways associated with neurodegeneration, including protein folding, cellular trafficking and secretion [54] It is noteworthy that about one-fifth of yeast genes are members of orthologous gene families associated with human diseases [55]. We therefore took advantage of the yeast model to study the mechanisms of toxicity related to the expression of AT3, the protein responsible for SCA3. We employed three AT3 variants: a wild type and an expanded one, carrying 26

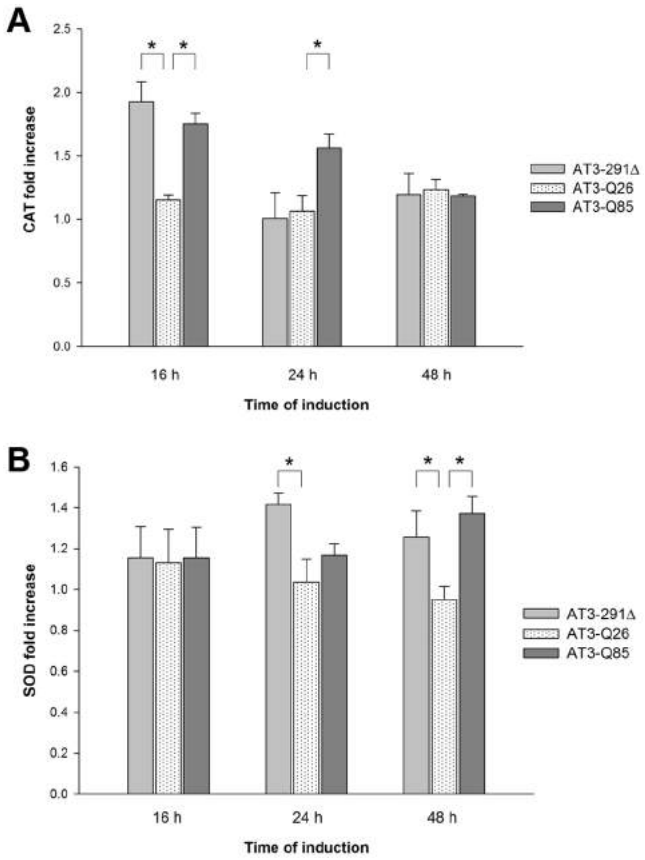

Fig 5. Antioxidant enzyme activity determination. A) CAT activity: the rate of H_2O_2 decomposition was determined using the ferrous oxidation assay and absorbance was measured at 560 nm. Data are expressed as fold increase with respect to the empty vector strain level. Bars represent standard errors and are derived from at least three independent experiments ($P < 0.05$). B) SOD activity was determined as the rate of reduction of oxidized cytochrome *c* at 550 nm. Data are expressed as fold increase with respect to the empty vector strain level. Bars represent standard errors and are derived from at least three independent experiments ($P < 0.05$).

doi:10.1371/journal.pone.0129727.g005

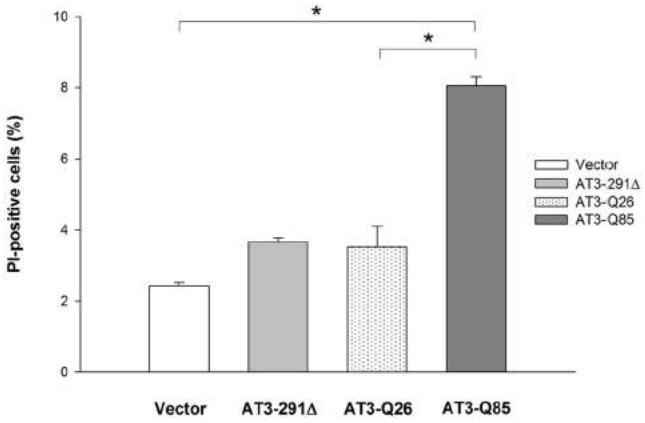

Fig 6. Propidium iodide staining of AT3-expression strains. After a 48-h induction, PI positive cells were counted from > 300 cells from different field views. Bars represent standard errors and are derived from at least three independent experiments ($P < 0.05$).

doi:10.1371/journal.pone.0129727.g006

(AT3-Q26) and 85 (AT3-Q85) consecutive glutamines, respectively, and a variant truncated for a region lying from the beginning of its polyQ stretch to the end of the protein (AT3-291Δ). All proteins were expressed in fusion with GFP at the C-terminus. By employing such fusion proteins not only could we monitor their aggregation, but also express the expanded AT3 variant, whose authentic form proved to be otherwise refractory to expression. It should be noted, on the other hand, that AT3-Q26 in fusion with GFP did not significantly affect any parameter under investigation, which clearly substantiates the idea that AT3-Q85 toxicity is independent of GFP.

We demonstrated that the expression of the expanded form induces a significant growth-inhibitory effect. Although statistically non-significant, the AT3-291Δ-expressing strain also exerted some effect, supporting the hypothesis that the polyQ-harboring context is also involved in fibrillogenesis and in protein toxicity, as confirmed by the MTT assay. Noteworthy, a toxic effect by AT3 variants truncated in the disordered, C-terminal domain, including the polyQ stretch, was previously demonstrated in both *Escherichia coli* [37] and mice either homozygous or heterozygous for the truncated AT3-259Δ, which developed severe motor coordination dysfunction and altered behavior, followed by premature death [56]. Thus, the capability of truncated variants to trigger toxic effects is a well-established phenomenon that develops irrespective of the biological milieu.

A hallmark of SCA3 pathology is the presence of amyloid aggregates in the brain. Through fluorescence microscopy analysis, we showed the formation of aggregation *foci* in the AT3-Q85-expressing strain starting from 16 h after induction. This phenotype should be accounted for by the intrinsic properties of the protein, rather than by its overexpression, as substantiated by the fact that AT3-Q26- and AT3-291Δ-expressing strains did not show any such aggregates, although the three variants were expressed at similar levels. Filter trap analysis showed that SDS-insoluble aggregates only arose from the expanded variant after a 24 h-induction (Fig 1C), whereas at 16 h no such aggregates were generated by any of the AT3 forms (data not shown), in agreement with a previous study [37]. This suggests that intracellular aggregates observed at 16 h are pre-fibrillar species rather than SDS-insoluble mature fibrils. Thus, the fact that the aggregation patterns of AT3-291Δ and AT3-Q85 are somewhat different from each other, suggests that the toxicity mechanisms must also differ, at least to some extent.

To further clarify the mechanisms of AT3 toxicity, we checked the effect of GuHCl on cell growth using the clonogenic assay. GuHCl is a well-known inhibitor of the yeast chaperone Hsp104 [32,50,52], which in turn has been implicated in prion maintenance [50]. GuHCl treatment almost completely restored normal cell growth in AT3-Q85 and AT3-291Δ strains. This strongly supports the idea that Hsp104 promotes AT3 aggregation and toxicity by propagating prion forms of yeast proteins, such as [PSI^+] or [PIN^+] [32,50,52]. We suggest that such forms might act to seed AT3 aggregation, thus substantially accelerating the process and boosting toxicity. Noteworthy, the toxicity of the truncated form, although devoid of the polyQ tract, was also mitigated.

MTT assays highlighted a significant toxic effect induced by the expanded and truncated variants, unlike the wild type. Thus, seeking for mechanisms of toxicity, we assessed possible oxidative stress. Indeed, it is known that amyloid aggregates may boost reactive oxygen species (ROS), which in turn results from mitochondrial dysfunction [57]. We found that, already 16 h after induction, H_2O_2 levels were significantly higher in yeast expressing AT3-Q85 and AT3-291Δ, compared to AT3-Q26. At 24 h, the increase was significant only for the expanded form and, at the latest time, the levels of the three strains were comparable. However, this pattern may due to culture aging, which implies progressive ROS-induced cellular damage in all organisms [58], including yeast [59]. Actually, H_2O_2 level underwent a substantial increase at the latest time (48 h) independent of the toxic effects of the AT3 variants, as detected in the empty vector strain (data not shown). This likely overshadowed the effects related to protein toxicity,

which prevented the possibility to investigate them at the latest time. Thus, our results provide evidence that oxidative stress is implicated in AT3 toxicity and suggest its involvement in the early events occurring at the onset of disease. Alterations in the antioxidant defense system were also demonstrated by the imbalance of the ratio reduced (GSH) to total glutathione. In fact, this was significantly lower in cells expressing AT3-Q85 with respect to the two other strains, whilst total glutathione was not affected by protein expression (data not shown).

To further dissect the mechanisms that mediate the altered redox status in our model, we examined the cellular enzymatic defense system against oxidative stress by assaying CAT and SOD levels. Our results revealed markedly increased activity of CAT at 16 h after induction in the yeast expressing AT3-Q85 and AT3-291Δ compared to AT3-Q26. At 24 h, the increase was significant only for the expanded form. Similar to the case of H_2O_2, SOD levels at 48 h also substantially increased in the control strain (empty vector), and concurrently no apparent toxic effect of protein expression was detectable at that time. In contrast, SOD levels kept essentially constant in the control strain, but significantly increased in the AT3-291Δ strain at both 24 and 48 h of induction, whereas in the case of AT3-Q85 the increase was significant at 48 h only. Previous investigations evaluated oxidative stress biomarkers in SCA3 mammalian cells [60] and patients [61]. In either case, a drop in reduced thiols was detected, in keeping with our results. However, data regarding the level of antioxidant enzymes in diseased cells/patients compared to the controls are conflicting, as CAT was increased in patients, similar to our yeast model, whereas in mammalian cells both CAT and SOD dropped compared to the controls. We have no obvious explanation for such discrepancy, although the decline in CAT and SOD activity in cell cultures might be accounted for as a consequence of oxidative damage [60].

Summarizing, in the AT3-Q85-expressing strain an increase in ROS levels was paralleled by a fast GSH drop and a significant increase in CAT activity, whereas SOD activity increased only after 48 h of induction. The observed pattern may be possibly accounted for by the failure of AT3-Q85 and AT3-291Δ strains to effectively degrade excess of H_2O_2 by thiol groups, although there seems to be a compensatory mechanism that increases CAT and SOD levels compared to the control. Moreover, these data suggest that the appearance of SDS-soluble aggregates at 16 h (Fig 1B and 1C) induces mitochondrial damage, increases in ROS species and a consequent imbalance of the antioxidant defense system. These findings are in line with the hypothesis that oligomeric and pre-fibrillar species formed at the initial stages of the aggregation process are those responsible for cellular toxicity. Moreover, expression of AT3-291Δ also showed a toxic effect, albeit milder than that of the expanded form, which also is likely to be related to its proven capability to form oligomeric species [37].

Another toxicity mechanism involved in neurodegenerative diseases is the direct interaction of amyloid aggregates with lipid membranes and their consequent permeabilization [62–64]. This prompted us to perform PI-staining analyses. Our data show that close to 10% of AT3-Q85-expressing strain underwent loss of plasma membrane integrity and cell necrosis after 48 h of induction. In contrast, neither the AT3-291Δ strain nor the one expressing wild-type protein showed any necrosis marker. Based on our data, the causal relationship between the toxic effects resulting from AT3-Q85 expression and membrane damage cannot be precisely established. It is possible that both ROS and AT3 oligomeric forms affect membrane integrity, as observed in previous reports [65–67].

No apotosis was observed in our yeast model using the cytochrome c assay, although we previously reported the capability of the aggregates formed *in vitro* by AT3-291Δ and AT3-Q55 to induce apoptosis in rat cerebellar granule neurons when added to cell medium. This apparent contradiction is probably due to different experimental strategies, as in the yeast model the protein was expressed in the intracellular environment and targeted by the cellular defense system, whereas in the case of rat neurons it was added to the medium.

In conclusion, this work shows that *S. cerevisiae* is a suitable model to study the mechanisms of SCA3 pathogenesis. Actually, not only did our investigations in yeast detect the toxicity of both expanded and truncated AT3, in keeping with data collected in other cellular milieus [37,65] and animal models [56], but could also reveal differences in behavior between the two forms, in terms of aggregation patterns *in vivo* and toxicity. Thus, it is plausible that such differences also rely upon qualitatively different cellular mechanisms, which might justify the milder phenotype of the truncated form compared to the expanded one. In any case, our results strongly support the idea that AT3 toxicity could be correlated with the formation of oligomeric and pre-fibrillar aggregates that cause oxidative stress in the short-term, whereas long-term effects might affect cell membrane integrity, at least in the case of the expanded form.

Supporting Information

S1 File. This file contains methods, figures and captions of: A) expression level quantification of the AT3 variants; b) growth rates assessed by duplication time; c) the effects of EGCG and tetracycline on colony-forming abilities of AT3 expressing strains; d) cytochrome C release assay.
(ZIP)

Acknowledgments

We would like to thank Dr. Sergio Giannattasio (Institute of biomembrane and bioenergetics, CNR Bari, Italy) for the gift of the polyclonal antibody against the mitochondrial protein acetohydroxyacid reductoisomerase (Ilv5p).

Author Contributions

Conceived and designed the experiments: PT MER MB GI. Performed the experiments: MB CV. Analyzed the data: PT MER MB CV GI. Contributed reagents/materials/analysis tools: PT MER. Wrote the paper: PT MER MB CV.

References

1. Gatchel JR, Zoghbi HY. Diseases of unstable repeat expansion: mechanisms and common principles. Nat Rev Genet. 2005; 6: 743–755. doi: 10.1038/nrg1691 PMID: 16205714
2. Orr HT, Zoghbi HY. Trinucleotide repeat disorders. Annu Rev Neurosci. 2007; 30: 575–621. doi: 10.1146/annurev.neuro.29.051605.113042 PMID: 17417937
3. Zoghbi HY, Orr HT. Glutamine repeats and neurodegeneration. Annu Rev Neurosci. 2000; 23: 217–247. doi: 10.1146/annurev.neuro.23.1.217 PMID: 10845064
4. Duennwald ML. Polyglutamine misfolding in yeast: toxic and protective aggregation. Prion. 2011; 5: 285–290. doi: 10.4161/pri.18071 PMID: 22052348
5. Zuccato C, Ciammola A, Rigamonti D, Leavitt BR, Goffredo D, Conti L, et al. Loss of huntingtin-mediated BDNF gene transcription in Huntington's disease. Science. 2001; 293: 493–498. doi: 10.1126/science.1059581 PMID: 11408619
6. Zuccato C, Tartari M, Crotti A, Goffredo D, Valenza M, Conti L, et al. Huntingtin interacts with REST/NRSF to modulate the transcription of NRSE-controlled neuronal genes. Nat Genet. 2003; 35: 76–83. doi: 10.1038/ng1219 PMID: 12881722
7. Ranum LP, Lundgren JK, Schut LJ, Ahrens MJ, Perlman S, Aita J, et al. Spinocerebellar ataxia type 1 and Machado-Joseph disease: incidence of CAG expansions among adult-onset ataxia patients from 311 families with dominant, recessive, or sporadic ataxia. Am J Hum Genet. 1995; 57: 603–608. PMID: 7668288
8. Riess O, Rüb U, Pastore A, Bauer P, Schöls L. SCA3: neurological features, pathogenesis and animal models. Cerebellum Lond Engl. 2008; 7: 125–137. doi: 10.1007/s12311-008-0013-4

9. Kawaguchi Y, Okamoto T, Taniwaki M, Aizawa M, Inoue M, Katayama S, et al. CAG expansions in a novel gene for Machado-Joseph disease at chromosome 14q32.1. Nat Genet. 1994; 8: 221–228. doi: 10.1038/ng1194-221 PMID: 7874163
10. Trottier Y, Cancel G, An-Gourfinkel I, Lutz Y, Weber C, Brice A, et al. Heterogeneous intracellular localization and expression of ataxin-3. Neurobiol Dis. 1998; 5: 335–347. doi: 10.1006/nbdi.1998.0208 PMID: 10069576
11. Masino L, Musi V, Menon RP, Fusi P, Kelly G, Frenkiel TA, et al. Domain architecture of the polyglutamine protein ataxin-3: a globular domain followed by a flexible tail. FEBS Lett. 2003; 549: 21–25. PMID: 12914917
12. Burnett B, Li F, Pittman RN. The polyglutamine neurodegenerative protein ataxin-3 binds polyubiquitylated proteins and has ubiquitin protease activity. Hum Mol Genet. 2003; 12: 3195–3205. doi: 10.1093/hmg/ddg344 PMID: 14559776
13. Bevivino AE, Loll PJ. An expanded glutamine repeat destabilizes native ataxin-3 structure and mediates formation of parallel beta-fibrils. Proc Natl Acad Sci U S A. 2001; 98: 11955–11960. doi: 10.1073/pnas.211305198 PMID: 11572942
14. Chow MKM, Paulson HL, Bottomley SP. Destabilization of a non-pathological variant of ataxin-3 results in fibrillogenesis via a partially folded intermediate: a model for misfolding in polyglutamine disease. J Mol Biol. 2004; 335: 333–341. PMID: 14659761
15. Williams AJ, Paulson HL. Polyglutamine neurodegeneration: protein misfolding revisited. Trends Neurosci. 2008; 31: 521–528. doi: 10.1016/j.tins.2008.07.004 PMID: 18778858
16. Uversky VN. Mysterious oligomerization of the amyloidogenic proteins. FEBS J. 2010; 277: 2940–2953. doi: 10.1111/j.1742-4658.2010.07721.x PMID: 20546306
17. Campioni S, Mannini B, Zampagni M, Pensalfini A, Parrini C, Evangelisti E, et al. A causative link between the structure of aberrant protein oligomers and their toxicity. Nat Chem Biol. 2010; 6: 140–147. doi: 10.1038/nchembio.283 PMID: 20081829
18. Bucciantini M, Giannoni E, Chiti F, Baroni F, Formigli L, Zurdo J, et al. Inherent toxicity of aggregates implies a common mechanism for protein misfolding diseases. Nature. 2002; 416: 507–511. doi: 10.1038/416507a PMID: 11932737
19. Lajoie P, Snapp EL. Formation and toxicity of soluble polyglutamine oligomers in living cells. PloS One. 2010; 5: e15245. doi: 10.1371/journal.pone.0015245 PMID: 21209946
20. Kayed R, Head E, Thompson JL, McIntire TM, Milton SC, Cotman CW, et al. Common structure of soluble amyloid oligomers implies common mechanism of pathogenesis. Science. 2003; 300: 486–489. doi: 10.1126/science.1079469 PMID: 12702875
21. Demuro A, Mina E, Kayed R, Milton SC, Parker I, Glabe CG. Calcium dysregulation and membrane disruption as a ubiquitous neurotoxic mechanism of soluble amyloid oligomers. J Biol Chem. 2005; 280: 17294–17300. doi: 10.1074/jbc.M500997200 PMID: 15722360
22. Kayed R, Sokolov Y, Edmonds B, McIntire TM, Milton SC, Hall JE, et al. Permeabilization of lipid bilayers is a common conformation-dependent activity of soluble amyloid oligomers in protein misfolding diseases. J Biol Chem. 2004; 279: 46363–46366. doi: 10.1074/jbc.C400260200 PMID: 15385542
23. Schaffar G, Breuer P, Boteva R, Behrends C, Tzvetkov N, Strippel N, et al. Cellular toxicity of polyglutamine expansion proteins: mechanism of transcription factor deactivation. Mol Cell. 2004; 15: 95–105. doi: 10.1016/j.molcel.2004.06.029 PMID: 15225551
24. Khurana V, Lindquist S. Modelling neurodegeneration in Saccharomyces cerevisiae: why cook with baker's yeast? Nat Rev Neurosci. 2010; 11: 436–449. doi: 10.1038/nrn2809 PMID: 20424620
25. Duennwald ML. Yeast as a platform to explore polyglutamine toxicity and aggregation. Methods Mol Biol Clifton NJ. 2013; 1017: 153–161. doi: 10.1007/978-1-62703-438-8_11 PMID: 23719914
26. Braun RJ, Büttner S, Ring J, Kroemer G, Madeo F. Nervous yeast: modeling neurotoxic cell death. Trends Biochem Sci. 2010; 35: 135–144. doi: 10.1016/j.tibs.2009.10.005 PMID: 19926288
27. Porzoor A, Macreadie IG. Application of yeast to study the tau and amyloid-β abnormalities of Alzheimer's disease. J Alzheimers Dis JAD. 2013; 35: 217–225. doi: 10.3233/JAD-122035 PMID: 23396350
28. Cooper AA, Gitler AD, Cashikar A, Haynes CM, Hill KJ, Bhullar B, et al. Alpha-synuclein blocks ER-Golgi traffic and Rab1 rescues neuron loss in Parkinson's models. Science. 2006; 313: 324–328. doi: 10.1126/science.1129462 PMID: 16794039
29. Gitler AD, Chesi A, Geddie ML, Strathearn KE, Hamamichi S, Hill KJ, et al. Alpha-synuclein is part of a diverse and highly conserved interaction network that includes PARK9 and manganese toxicity. Nat Genet. 2009; 41: 308–315. doi: 10.1038/ng.300 PMID: 19182805
30. Johnson BS, McCaffery JM, Lindquist S, Gitler AD. A yeast TDP-43 proteinopathy model: Exploring the molecular determinants of TDP-43 aggregation and cellular toxicity. Proc Natl Acad Sci U S A. 2008; 105: 6439–6444. doi: 10.1073/pnas.0802082105 PMID: 18434538

31. Johnson BS, Snead D, Lee JJ, McCaffery JM, Shorter J, Gitler AD. TDP-43 is intrinsically aggregation-prone, and amyotrophic lateral sclerosis-linked mutations accelerate aggregation and increase toxicity. J Biol Chem. 2009; 284: 20329–20339. doi: 10.1074/jbc.M109.010264 PMID: 19465477

32. Meriin AB, Zhang X, He X, Newnam GP, Chernoff YO, Sherman MY. Huntington toxicity in yeast model depends on polyglutamine aggregation mediated by a prion-like protein Rnq1. J Cell Biol. 2002; 157: 997–1004. doi: 10.1083/jcb.200112104 PMID: 12058016

33. Duennwald ML, Jagadish S, Muchowski PJ, Lindquist S. Flanking sequences profoundly alter polyglutamine toxicity in yeast. Proc Natl Acad Sci U S A. 2006; 103: 11045–11050. doi: 10.1073/pnas.0604547103 PMID: 16832050

34. Duennwald ML, Lindquist S. Impaired ERAD and ER stress are early and specific events in polyglutamine toxicity. Genes Dev. 2008; 22: 3308–3319. doi: 10.1101/gad.1673408 PMID: 19015277

35. Macedo-Ribeiro S, Cortes L, Maciel P, Carvalho AL. Nucleocytoplasmic shuttling activity of ataxin-3. PloS One. 2009; 4: e5834. doi: 10.1371/journal.pone.0005834 PMID: 19503814

36. Matos CA, de Macedo-Ribeiro S, Carvalho AL. Polyglutamine diseases: the special case of ataxin-3 and Machado-Joseph disease. Prog Neurobiol. 2011; 95: 26–48. doi: 10.1016/j.pneurobio.2011.06.007 PMID: 21740957

37. Invernizzi G, Aprile FA, Natalello A, Ghisleni A, Penco A, Relini A, et al. The relationship between aggregation and toxicity of polyglutamine-containing ataxin-3 in the intracellular environment of *Escherichia coli*. PloS One. 2012; 7: e51890. doi: 10.1371/journal.pone.0051890 PMID: 23251648

38. Krobitsch S, Lindquist S. Aggregation of huntingtin in yeast varies with the length of the polyglutamine expansion and the expression of chaperone proteins. Proc Natl Acad Sci U S A. 2000; 97: 1589–1594. PMID: 10677504

39. Gietz D, Jean A St, Woods RA, Schiestl RH. Improved method for high efficiency transformation of intact yeast cells. Nucleic Acids Res. 1992; 20: 1425. PMID: 1561104

40. Alberti S, Halfmann R, Lindquist S. Biochemical, cell biological, and genetic assays to analyze amyloid and prion aggregation in yeast. Methods Enzymol. 2010; 470: 709–734. doi: 10.1016/S0076-6879(10)70030-6 PMID: 20946833

41. Natalello A, Frana AM, Relini A, Apicella A, Invernizzi G, Casari C, et al. A major role for side-chain polyglutamine hydrogen bonding in irreversible ataxin-3 aggregation. PloS One. 2011; 6: e18789. doi: 10.1371/journal.pone.0018789 PMID: 21533208

42. Shehi E, Fusi P, Secundo F, Pozzuolo S, Bairati A, Tortora P. Temperature-dependent, irreversible formation of amyloid fibrils by a soluble human ataxin-3 carrying a moderately expanded polyglutamine stretch (Q36). Biochemistry. 2003; 42: 14626–14632. doi: 10.1021/bi0352825 PMID: 14661975

43. Kayed R, Head E, Sarsoza F, Saing T, Cotman CW, Necula M, et al. Fibril specific, conformation dependent antibodies recognize a generic epitope common to amyloid fibrils and fibrillar oligomers that is absent in prefibrillar oligomers. Mol Neurodegener. 2007; 2: 18. doi: 10.1186/1750-1326-2-18 PMID: 17897471

44. Teparić R, Stuparević I, Mrsa V. Increased mortality of *Saccharomyces cerevisiae* cell wall protein mutants. Microbiol Read Engl. 2004; 150: 3145–3150. doi: 10.1099/mic.0.27296-0 PMID: 15470095

45. Boyne AF, Ellman GL. A methodology for analysis of tissue sulfhydryl components. Anal Biochem. 1972; 46: 639–653. PMID: 4623507

46. Shangari N, O'Brien PJ. Catalase activity assays. Curr Protoc Toxicol Editor Board Mahin Maines Ed—Chief Al. 2006; Chapter 7: Unit 7.7.1–15. doi: 10.1002/0471140856.tx0707s27

47. McCord JM, Fridovich I. Superoxide dismutase. An enzymic function for erythrocuprein (hemocuprein). J Biol Chem. 1969; 244: 6049–6055. PMID: 5389100

48. Ellisdon AM, Thomas B, Bottomley SP. The two-stage pathway of ataxin-3 fibrillogenesis involves a polyglutamine-independent step. J Biol Chem. 2006; 281: 16888–16896. doi: 10.1074/jbc.M601470200 PMID: 16624810

49. Bonanomi M, Natalello A, Visentin C, Pastori V, Penco A, Cornelli G, et al. Epigallocatechin-3-gallate and tetracycline differently affect ataxin-3 fibrillogenesis and reduce toxicity in spinocerebellar ataxia type 3 model. Hum Mol Genet. 2014; 23: 6542–6552. doi: 10.1093/hmg/ddu373 PMID: 25030034

50. Chernoff YO, Lindquist SL, Ono B, Inge-Vechtomov SG, Liebman SW. Role of the chaperone protein Hsp104 in propagation of the yeast prion-like factor [psi+]. Science. 1995; 268: 880–884. PMID: 7754373

51. Cushman-Nick M, Bonini NM, Shorter J. Hsp104 suppresses polyglutamine-induced degeneration post onset in a drosophila MJD/SCA3 model. PLoS Genet. 2013; 9: e1003781. doi: 10.1371/journal.pgen.1003781 PMID: 24039611

52. Osherovich LZ, Weissman JS. Multiple Gln/Asn-rich prion domains confer susceptibility to induction of the yeast [PSI(+)] prion. Cell. 2001; 106: 183–194. PMID: 11511346

53. Giannattasio S, Atlante A, Antonacci L, Guaragnella N, Lattanzio P, Passarella S, et al. Cytochrome c is released from coupled mitochondria of yeast en route to acetic acid-induced programmed cell death and can work as an electron donor and a ROS scavenger. FEBS Lett. 2008; 582: 1519–1525. doi: 10.1016/j.febslet.2008.03.048 PMID: 18396162

54. Miller-Fleming L, Giorgini F, Outeiro TF. Yeast as a model for studying human neurodegenerative disorders. Biotechnol J. 2008; 3: 325–338. doi: 10.1002/biot.200700217 PMID: 18228539

55. Heinicke S, Livstone MS, Lu C, Oughtred R, Kang F, Angiuoli SV, et al. The Princeton Protein Orthology Database (P-POD): a comparative genomics analysis tool for biologists. PloS One. 2007; 2: e766. doi: 10.1371/journal.pone.0000766 PMID: 17712414

56. Hübener J, Vauti F, Funke C, Wolburg H, Ye Y, Schmidt T, et al. N-terminal ataxin-3 causes neurological symptoms with inclusions, endoplasmic reticulum stress and ribosomal dislocation. Brain J Neurol. 2011; 134: 1925–1942. doi: 10.1093/brain/awr118 PMID: 21653538

57. Lashuel HA, Hartley D, Petre BM, Walz T, Lansbury PT Jr. Neurodegenerative disease: amyloid pores from pathogenic mutations. Nature. 2002; 418: 291. doi: 10.1038/418291a PMID: 12124614

58. Harman D. Free Radical Theory of Aging: An Update. Ann N Y Acad Sci. 2006; 1067: 10–21. doi: 10.1196/annals.1354.003 PMID: 16803965

59. Denoth Lippuner A, Julou T, Barral Y. Budding yeast as a model organism to study the effects of age. FEMS Microbiol Rev. 2014; 38: 300–325. doi: 10.1111/1574-6976.12060 PMID: 24484434

60. Yu Y-C, Kuo C-L, Cheng W-L, Liu C-S, Hsieh M. Decreased antioxidant enzyme activity and increased mitochondrial DNA damage in cellular models of Machado-Joseph disease. J Neurosci Res. 2009; 87: 1884–1891. doi: 10.1002/jnr.22011 PMID: 19185026

61. Pacheco LS, da Silveira AF, Trott A, Houenou LJ, Algarve TD, Belló C, et al. Association between Machado-Joseph disease and oxidative stress biomarkers. Mutat Res. 2013; 757: 99–103. doi: 10.1016/j.mrgentox.2013.06.023 PMID: 23994570

62. McLaurin J, Chakrabartty A. Characterization of the interactions of Alzheimer beta-amyloid peptides with phospholipid membranes. Eur J Biochem FEBS. 1997; 245: 355–363. PMID: 9151964

63. Lindgren M, Hammarström P. Amyloid oligomers: spectroscopic characterization of amyloidogenic protein states. FEBS J. 2010; 277: 1380–1388. doi: 10.1111/j.1742-4658.2010.07571.x PMID: 20148961

64. Jayasinghe SA, Langen R. Membrane interaction of islet amyloid polypeptide. Biochim Biophys Acta. 2007; 1768: 2002–2009. doi: 10.1016/j.bbamem.2007.01.022 PMID: 17349968

65. Pellistri F, Bucciantini M, Invernizzi G, Gatta E, Penco A, Frana AM, et al. Different ataxin-3 amyloid aggregates induce intracellular Ca(2+) deregulation by different mechanisms in cerebellar granule cells. Biochim Biophys Acta. 2013; 1833: 3155–3165. doi: 10.1016/j.bbamcr.2013.08.019 PMID: 24035922

66. Richter C. Biophysical consequences of lipid peroxidation in membranes. Chem Phys Lipids. 1987; 44: 175–189. PMID: 3311416

67. Butterfield DA, Castegna A, Lauderback CM, Drake J. Evidence that amyloid beta-peptide-induced lipid peroxidation and its sequelae in Alzheimer's disease brain contribute to neuronal death. Neurobiol Aging. 2002; 23: 655–664. PMID: 12392766

The polyglutamine protein ataxin-3 enables normal growth under heat shock conditions in the methylotrophic yeast *Pichia pastoris*

Marcella Bonanomi ‡‖, Valentina Roffia §‖, Antonella De Palma §, Alessio Lombardi‡, Francesco Antonio Aprile ¶, Cristina Visentin‡, Paolo Tortora‡†*, Pierluigi Mauri§*, Maria Elena Regonesi‡†

From the ‡ Department of Biotechnology and Biosciences, University of Milano-Bicocca, 20126 Milan (Italy); § Institute for Biomedical Technologies, National Research Council, 20090, Milan, Italy; ¶ Department of Chemistry, University of Cambridge, Cambridge CB2 1EW, United Kingdom; † Milan Center of Neuroscience (NeuroMI), 20126 Milano (Italy).

‖ These authors contributed equally to this work.

* To whom correspondence should be addressed: Paolo Tortora, Department of Biotechnology and Biosciences, University of Milano-Bicocca, 20126 Milan (Italy); Tel.: +39 02 6448 3401; E-mail: paolo.tortora@unimib.it. Pierluigi Mauri, Institute for Biomedical Technologies, National Research Council, 20090, Milan, Italy; Tel.: +39 02 26422728; E-mail: pierluigi.mauri@itb.cnr.it.

Summary

The protein ataxin-3 triggers neurodegeneration in humans when its polyglutamine stretch close to the C-terminus exceeds a critical threshold. Ataxin-3 consists of the globular N-terminal Josephin domain, followed by a disordered C-terminal one. For this protein, a role as a transcriptional regulator and as a ubiquitin hydrolase has been proposed, the latter being involved in handling proteins destined for degradation. Here, we report that, when expressed in the yeast Pichia pastoris, full-length ataxin-3 enabled almost normal growth at 37°C, well above the optimum of 30°C. The Josephin domain in isolation was also effective but significantly less, whereas a catalytically inactive variant was completely ineffective. MudPIT proteome analysis demonstrated persistent upregulation of mitochondrial energy metabolism enzymes during growth at 37°C in the strain expressing full-length, functional ataxin-3, compared with a control strain (transformed with the empty vector). Concurrently, at 37°C intracellular ATP in the transformed strain was even higher than at 30°C, whereas a control strain displayed ATP depletion. Elevated ATP was paralleled by upregulation of enzymes involved in protein biosynthesis and biosynthetic pathways, as well as of several stress-induced proteins. These effects required ubiquitin hydrolase activity of ataxin-3. We suggest that they mostly result from mechanisms of transcriptional regulation.

Introduction

Ataxin-3 (ATX3) is one among several proteins containing stretches of consecutive glutamines that are responsible for different, albeit related, neurodegenerative diseases in humans, when their size exceeds a critical threshold (1-3). ATX3 triggers the Machado-Joseph

EGCG and related phenol compounds redirect the amyloidogenic aggregation pathway of ataxin-3 towards non-toxic aggregates and prevent toxicity in neural cells and *Caenorhabditis elegans* animal model

Cristina Visentin[a], Marcella Bonanomi[a], Antonino Natalello[a], Giulia Filippi[a], Francesca Pellistri[b], Elena Gatta[b], Amanda Penco[b], Annalisa Relini[b], Luca De Gioia[a], Cristina Airoldi[a,c], Maria E. Regonesi[a,c*], Paolo Tortora[a,c].

[a] Department of Biotechnologies and Biosciences, University of Milano-Bicocca, 20126 Milan, Italy
[b] Department of Physics, University of Genoa, 16146 Genoa, Italy
[c] Milan Center of Neuroscience (NeuroMI), 20126 Milano (Italy).

ABSTRACT

The protein ataxin-3 (ATX3) triggers an amyloid-related neurodegenerative disease when its polyglutamine stretch is expanded beyond a critical threshold. We formerly demonstrated that the polyphenol epigallocatechin-3-gallate (EGCG) could redirect amyloid aggregation of a full-length, expanded ATX3 (ATX3-Q55) towards non-toxic, soluble, SDS-resistant aggregates. Here, we have characterized other related phenol compounds, although smaller in size, i.e., (–)-epicatechin gallate (ECG), and gallic acid (GA). We analyzed the aggregation pattern of ATX3-Q55 and of the N-terminal globular Josephin domain (JD) by assessing time course of soluble protein, as well its structural features by FTIR and AFM, in the presence and the absence of the mentioned compounds. All of them redirected the aggregation pattern towards soluble, SDS-resistant aggregates. They also prevented the appearance of ordered side-chain hydrogen bonding in ATX3-Q55, which is the hallmark of polyQ-related amyloids. Molecular docking analyses on the JD highlighted interactions in its aggregation-prone region by all three compounds, thus accounting for their capability to prevent amyloidogenesis. However, a decreasing number of interactions, in the order EGCG>EGC>GA, was detected. Saturation transfer difference NMR experiments also confirmed EGCG and EGC binding to monomeric JD. ATX3-Q55 preincubation with any of the three compound prevented its calcium-influx-mediated cytotoxicity towards neural cells. Finally, all the phenols significantly reduced toxicity in a transgenic *Caenorhabditis elegans* strain expressing an expanded AT3. Although GA is somewhat less effective than the other compounds, it has a much simpler structure and a higher chemical stability, so it is more suitable for controlled conjugation to nanodevices.